Failure prediction of steel components under the coupled effect of excessive plastic deformations and pitting corrosion

Mohammad Ali Mahdavipour

Mohammad Ali Mahdavipour

Failure prediction of steel components under the coupled effect of excessive plastic deformations and pitting corrosion

Doctoral dissertation for the degree of Doctor of Philosophy (Ph.D.)

University of Agder

Faculty of Engineering and Science

2022

Preface

This thesis presents the scientific contributions of the author in the field of civil and structural engineering. It is organized as an article-based thesis that consists of five appended papers prepared by the author and co-workers, which are currently published or in the process of being published. In addition, synopsis chapters are referenced to outline how the research was conducted in order to provide a continuous and coherent description of the entire process.

The work described in this thesis has been carried out at the University of Agder, Faculty of Engineering Sciences during 2018–2022. It has been conducted under the supervision of my principal supervisor, Associate Professor Dmitry Vysochinskiy, and co-supervisor Associate Professor Zhiyu Jiang, both of whom are from the University of Agder. This thesis has been submitted in partial fulfillment of the requirements for the degree of Doctor of Philosophy (Ph.D.).

Acknowledgments

Summary

Nowadays, modern computers have made advanced computational resources accessible to analysts engaged in the field of structural engineering. Through these advancements, the role of numerical modeling has increasingly become more significant in both research and engineering projects. In addition, improved testing facilities and measuring instruments like digital image correlation (DIC) have made material testing more informative than before, and engineers can calibrate more complicated material models to simulate complex phenomena such as plasticity and fracture.

All developed testing and numerical modeling techniques come together to form a numerical failure assessment framework for steel structures. Due to the distinct advantages of numerical modeling over full-scale testing, this framework is well-developed in many applications (e.g., elastic analyses). However, in many other applications, numerous involved phenomena and their interactions with each other, as well as additional factors (e.g., corrosion), call for more development both in material testing and numerical techniques to customize the framework to better suit the final application.

This thesis has focused on the failure assessment of steel components under the coupled effect of extensive plasticity and pitting corrosion. A framework was developed based on experimental material calibration and stochastic numerical modeling approaches.

To establish the assessment framework, a large portion of this thesis has been devoted to material scale testing and modeling, in which an alternative approach was proposed to calibrate ductile fracture criterion (i.e., void growth model) based on the DIC technique. The proposed method makes calibration feasible for welding and heat-affected zones and mitigates the inaccuracies typically associated with the common calibration process.

In addition, the failure of practical steel members with pitting corrosion under excessive plastic deformations was predicted on the component scale. In this connection, proper details in finite element modeling, such as element type, mesh size, and material model, must be selected appropriately to take advantage of the computational ability and to determine the stress and strain fields on the microstructural scales. These finite element models must also consider the pitting corrosion uncertainties and be applicable to complicated geometries. Based on these two objectives, this thesis aimed to investigate existing finite element

techniques and to propose improvements accordingly. For this purpose, the corrosion uncertainties were explicitly involved in developing the concept of fracture-based fragility curves at the component level. This was done through micromechanics-based modeling of different random pitting morphologies at a given intensity level of pitting corrosion. In this connection, a mesh carving technique with distinct features was introduced and validated to implement the random pitting morphologies into numerical models. The proposed fragility curves resulting from the failure assessment framework can address the effect of pitting corrosion in terms of the probability of failure, which is an important parameter for the risk-based corrosion management in steel structures located in corrosive environments.

Furthermore, the accurate prediction of localized material behavior due to pitting corrosion needs to be efficiently linked to component scales. For this purpose, this thesis discusses relevant challenges and proper solutions in terms of applying the micromechanical modeling to a large-scale and complicated geometry, e.g., a steel beam-to-column joint. In this connection, two-level numerical modeling was proposed as a solution to reduce the complexity of the problem for a practical structural application.

In general, this thesis provides a developmental path from a material to a component scale to establish a failure assessment framework and to push different aspects of it towards the final application that is predicting the effect of pitting corrosion in steel structures under extreme loads. Based on the outcomes of such a framework, decision-makers can utilize risk management methods and assess the most critical scenarios in terms of principal criteria, e.g., health and safety, economy, and environment, and accordingly update protection and retrofit plans to extend lifetime of the steel structures.

Summary in Norwegian

Moderne datasystemer gjør at betydelige beregningsressurser er tilgjengelig for analytikere innenfor konstruksjonsteknikk. Som følge av dette blir numerisk modellering stadig viktigere i både forsknings og ingeniørprosjekter. I tillegg har forbedrede testfasiliteter og måleinstrumenter som DIC (Digital Image Correlation) gjort materialtesting mer informativ enn før, og ingeniører kan kalibrere mer kompliserte materialmodeller for å simulere komplekse fenomener som plastisitet og brudd.

Utviklede testmetoder og numeriske modelleringsteknikker kan sammen danne et numerisk rammeverk for å vurdere faren for sammenbrudd i stålkonstruksjoner. På grunn av de tydelige fordelene med numerisk modellering fremfor fysisk fullskala testing, er det numeriske rammeverket godt utviklet for mange bruksområder (f.eks. elastiske analyser). I mange andre applikasjoner krever imidlertid mange involverte fenomener og deres interaksjoner med hverandre, samt tilleggsfaktorer (f.eks. korrosjon), mer utvikling både innen materialtesting og numeriske teknikker for å tilpasse rammeverket for å passe bedre til det endelige bruksområdet.

Denne avhandlingen har satt søkelys på vurdering av sammenbrudd av stålkomponenter under den kombinerte effekten av omfattende plastisitet og gropkorrosjon. Et rammeverk for å vurdere risikoen for brudd ble utviklet basert på eksperimentell materialkalibrering og stokastiske numeriske modelleringsmetoder.

For å etablere rammeverket, har en stor del av denne avhandlingen vært dedikert til testing på materialnivå og modellering, der en alternativ tilnærming ble foreslått for å kalibrere duktilt bruddkriterium (VGM) ved hjelp av DIC. Den foreslåtte metoden gjør det mulig å kalibrere materialmodeller for sveiser og varmepåvirkede soner og redusere unøyaktighetene som vanligvis er forbundet med den vanlige kalibreringsprosessen.

I tillegg ble sammenbrudd av stålelementer utsatt for gropkorrosjon og store plastiske deformasjoner modellert på komponentnivå. I denne forbindelse må riktige detaljer implementeres i finite element-modelleringen, slik som elementtype, elementstørrelse og materialmodell for å utnytte beregningsevnen og for å bestemme spennings- og tøyningsfeltene på de mikrostrukturelle nivåene. Disse finite element modellene må også ta hensyn til usikkerheter knyttet til gropkorrosjon og være anvendelige på kompliserte geometrier. Basert på disse to

målene, tok denne avhandlingen sikte på å undersøke eksisterende finite element-teknikker og foreslå passende forbedringer. For dette formålet ble usikkerhetene knyttet til korrosjon eksplisitt benyttet i utviklingen av konseptet med bruddbaserte kurver for å predikere sannsynligheten for sammenbrudd på komponentnivå. Dette ble gjort gjennom mikromekanikk-basert modellering av forskjellige tilfeldige grop-morfologier ved et gitt intensitetsnivå av gropkorrosjon. I denne forbindelse ble en mesh carving-teknikk med distinkte funksjoner introdusert og validert for å implementere de tilfeldige grop-morfologiene i numeriske modeller. De foreslåtte kurvene som er et resultat av rammeverket for vurdering av faren for sammenbrudd kan adressere effekten av gropkorrosjon når det gjelder denne sannsynligheten, som er en viktig parameter for risikobasert korrosjonshåndtering i stålkonstruksjoner i korrosive miljøer.

Videre må den nøyaktige predikeringen av lokal materialadferd på grunn av gropkorrosjon være effektivt knyttet til komponentnivå. For dette formålet diskuterer denne avhandlingen relevante utfordringer og løsninger når det gjelder bruk av den mikromekaniske modelleringen på komponent/sammenføynings nivå og med komplisert geometri, for eksempel en stål-bjelke-til-søyle-forbindelse. To-nivå numerisk modellering ble foreslått som en løsning for å redusere kompleksiteten til problemet i praktiske konstruksjoner.

I sin helhet, presenterer denne avhandlingen utviklingen fra material- til komponentnivå for å etablere et rammeverk for vurdering av sammenbrudd og for å drive ulike aspekter av det mot det endelige bruksområdet som er modellering av effekten av gropkorrosjon i stålkonstruksjoner under ekstremlast. Basert på resultatene av et slikt rammeverk, kan beslutningstakere bruke risikostyringsmetoder og vurdere de mest kritiske scenariene i forhold til hovedkriterier, for eksempel helse og sikkerhet, økonomi og miljø, og følgelig oppdatere inspeksjon og vedlikeholdsplaner for å forlenge levetiden av stålkonstruksjoner.

Contents

List of figures

xvii

List of papers

This thesis consists of synopsis chapters and the following papers referred to in the text by their Roman numerals (e.g., P(II)).

I. Mahdavipour M.A., Ding S., Vysochinskiy D. 2019. *Performance of welded flange plate joints between steel beams and box columns without continuity plates*. Cape Town: The Seventh International Conference on Structural Engineering, Mechanics and Computation (SEMC).

II. Mahdavipour M.A., Vysochinskiy D. 2020. *Effect of the joint strength on the performance of ordinary moment-resisting frames under a progressive collapse situation.* XI International Conference on Structural Dynamics (EURODYN). Athens, Greece: European Association for Structural Dynamics.

III. Mahdavipour M.A., Vysochinskiy D. (under review). 2022. *A DIC-based alternative approach to calibrate ductile fracture criterion*. Journal of Engineering Mechanics.

IV. Mahdavipour M.A., Vysochinskiy D. 2022. *Developing fracture-based fragility curves for steel components in corrosive environments*. Journal of Structural Engineering. 10.1061/(ASCE)ST.1943-541X.0003299.

V. Mahdavipour M.A., Vysochinskiy D. 2022. *Micromechanical modeling of corroded steel joints under excessive plastic deformations*. Journal of Performance of Constructed Facilities. 10.1061/(ASCE)CF.1943-5509.0001706.

Besides these papers, an extra paper was also published during my Ph.D. studies that is not referred to in the thesis.

VI. Mahdavipour M.A., Eslami A., Jehel P. 2020. *Seismic evaluation of ordinary RC buildings retrofitted with externally bonded FRPs using a reliability-based approach*. Composite Structures, 232: 111567.

Author's contribution

P(I): "Performance of welded flange plate joints between steel beams and box columns without continuity plates"

Mahdavipour, as the first author, developed the idea and structural details proposed in this paper. The first author also modeled joints in Abaqus, post-processed the results, and prepared the manuscript. Ding and Vysochinskiy contributed to the manuscript with valuable comments, and suggestions, and editing of the manuscript.

P(II): "Effect of the joint strength on the performance of ordinary moment-resisting frames under a progressive collapse situation"

Mahdavipour as the first author developed the idea and designed the studied frame. The first author also performed the uniaxial tensile tests and calibrated the ductile damage model. Finally, the first author modeled joint sub-assemblage in Abaqus, post-processed the results, and prepared the manuscript. Vysochinskiy contributed to the manuscript with valuable comments, suggestions, and editing.

P(III): " A DIC-based alternative approach to calibrate ductile fracture criterion"

Mahdavipour as the first author developed the idea of using DIC to calibrate the material model. In this connection, the first author conducted experimental and numerical studies to support the idea. The first author also developed a user subroutine to implement the fracture criterion in Abaqus models. Finally, Mahdavipour analyzed the results and prepared the manuscript. Vysochinskiy contributed to the manuscript with valuable comments, suggestions, and editing.

P(IV): "Developing fracture-based fragility curves for steel components in corrosive environments"

Mahdavipour as the first author reviewed the literature and developed the idea of fracture-based fragility curves for steel components in corrosive environments. The first author also developed a meshing technique to implement the pit geometry into numerical models in Abaqus. Finally, the first author analyzed models, post-processed the results, and prepared the manuscript. Vysochinskiy contributed to the manuscript with valuable comments, suggestions, and editing.

P(V): "Micromechanical modeling of corroded steel joints under excessive plastic deformations"

Mahdavipour as the first author reviewed the literature, formed the idea, and developed numerical models in Abaqus to support the idea. The first author also analyzed the models, post-processed the results, and prepared the manuscript. Vysochinskiy contributed to the manuscript with valuable comments, suggestions, and editing.

1. Introduction

This introduction begins with a background about the general context that the thesis aims contribute to. It also reviews the research significance of the thesis by describing some of the practical motivations behind the prediction of failure of steel components under the coupled effect of excessive plastic deformations and pitting corrosion.

1.1 Background

1.1.1 Failure prediction of steel structures

Mild steel is a ductile material that can withstand extensive plastic deformations before fracture. Figure 1.1 shows a typical stress–strain behavior of mild steel when it is tested under tensile loads. The considerable fracture strain and significant toughness (area under the curve) indicate the ability of mild steel to absorb energy and deform plastically without fracturing [1]. To utilize this wide range of material behavior, realistic material characterization is essential to predict the failure of steel components. Subsequently, based on the predicted failure, minimum requirements and design configuration can be prescribed to ensure the proper functionality of a component and the safety of the global structure.

In general, the term "failure" as used in this thesis refers to a situation in which a load-bearing component in a structural system ceases to perform its intended function to transfer loads to other connected elements [1]. In steel structures, component failure can be associated with various levels of material behavior highlighted in Figure 1.1, ranging from elastic to extensive plastic deformations. For components under monotonic loads, buckling of a slender component under compression loads is a failure with elastic material behavior, while ductile fracture of a tensile member is associated with considerable plastic material behavior.

This change of behavior from elastic region to plastic and finally fracture also typically alters the scale of failure from a global to a very local scale. For the aforementioned examples, elastic buckling of a slender component can be characterized as a global instability failure, while ductile fracture is a highly localized material failure. This transition from elastic to large plastic behavior, and from a global to local perspective, can significantly affect the selection of the methods used to predict failure. It is worth mentioning that in some failure modes, the local material failure can occur under elastic or limited plastic loads, e.g., high-cycle fatigue or cleavage fracture.

1
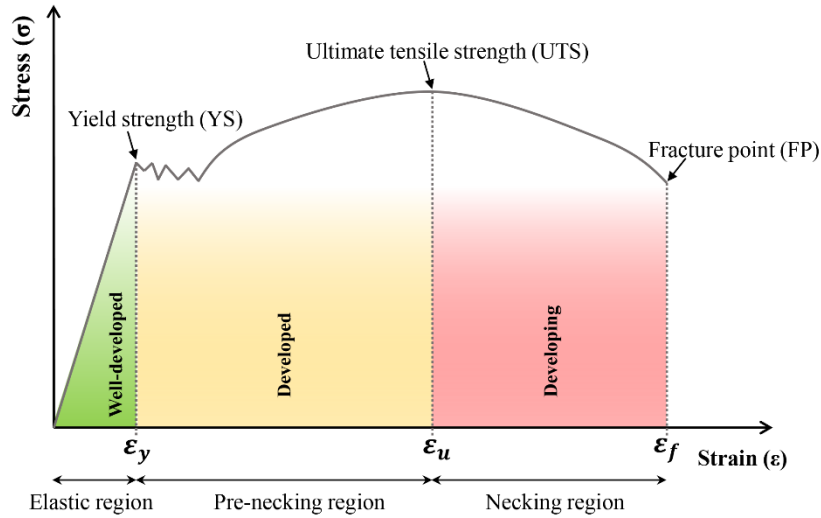
Figure 1.1. Typical stress–strain curve of mild steel with the current development status of the numerical modeling in practical engineering.

In this connection, design codes provide user-friendly, simplified, and empirical-based approaches to predict failure, mainly in relation to more frequent and predictable cases. At the same time, highly uncertain phenomena (e.g., corrosion or weld defects) in real-world structures can affect structural performance and lead to complicated failures that cannot be generalized by a simplified empirical approach that is mainly established based on a limited database of large scale-tests [2]. Therefore, design codes prescribe preventive requirements in such cases to avoid challenging failures. For example, steel design codes [3, 4] address the plastic design and allow controlled plastification in the protected zone to dissipate input energy and to withstand external actions by assuming these zones as defect-free zones [5]. To fulfill this assumption, they also define acceptable local defects and minimum material toughness and impose strict inspections and testing procedures to reduce the chance of a complicated failure due to defects and uncertain material behavior.

However, past practical experience indicated that these quality control procedures did not work perfectly in many cases, or they lost their efficiency over time (e.g., coating for corrosion). For this reason, engineers need a complementary numerical modeling framework to assess failure in steel components when they are out of defined range or are subject to extreme and stochastic external actions not intended in the regular design. In this regard, well-developed numerical models can help to analyze test results and extrapolate them so as to explain the reasons behind the failure of steel structures [2].

In general, numerical modeling is a rapid prototyping approach [6] based on computer-based modeling (e.g., finite element analysis (FEA)) that allows engineers to test, analyze, and design various structural systems as if they are physical prototypes. The distinct advantages of numerical modeling over physical prototyping (large-scale tests) have motivated both industrial and research communities to derive as much benefit as possible in running their businesses. These advantages are:

Broad applicability: Numerical modeling can be applied to a wide range of structures under various external conditions. It can be utilized to assess the performance of a global system by using developed macro models or to predict extremely local responses by micromechanics-based models. Thanks to rapid advancements in computer technology, numerical modeling can now be used for prototyping large structures like ships [7] or tall buildings using a PC, whereas, in many cases, physical testing required large laboratories with rigid reaction walls and floors and expensive testing and measurement facilities, as shown in Figure 1.2. In addition, multiphysics problems in which interactions between different environments are under investigation can hardly be tested physically. Therefore, numerical modeling plays a critical role in prototyping these problems.

Considerable flexibility: Due to financial limitations, a small number of specimens with limited ranges of size and configuration are usually used to carry out physical prototyping. Consequently, the outcomes are more or less subjective and are valid for similar applications. For example, the American Institute of Steel Construction (AISC) 358-16 [8] prescribes some size limitations for prequalified steel connections, as the code is mainly based on experimental studies. In contrast, various influential parameters (size, material, loading, etc.) can be involved in numerical modeling and modified for more investigations. This ability is advantageous when time-variant problems like the aging effect are under investigation [9]. In those cases, engineers can continuously update numerical models for the current deterioration state and predict the structural responses for future events.

Reliability: Physical testing is usually done in a deterministic way due to the limitation in the number of specimens. In contrast, numerical modeling can be coupled with probabilistic models to evaluate the reliability of structures considering different sources of uncertainties [10]. In such studies, several iterations of analysis can be easily carried out by changing the parameters in the

finite element models to involve different sources of uncertainties associated with the geometry, loads, materials, and environmental conditions.

Cost saving: Numerical modeling is significantly cheaper and more available compared to physical testing. Various businesses that may vary in size and financial level can afford a numerical package based on their area of expertise.

Figure 1.2. Extensive laboratory resources are required for large-scale structural tests: A steel beam-to-column connection tested by the International Institute of Earthquake Engineering and Seismology [11].

Despite the above-mentioned advantages, numerical modeling does not mean a complete deviation from physical testing. In other words, in numerical modeling, computer-based simulations must be fed by precise material models that are calibrated by proper material testing and calibration procedures. Therefore, the testing focus is changing from large-scale component tests to more novel and accurate material testing and modeling. The more complex the material behavior, the more detailed and complicated modeling methods and calibration techniques must become.

Figure 1.1 also highlights the current developmental status of numerical modeling in practical engineering for three distinct regions: elastic, pre-necking, and necking. As this figure shows, numerical modeling is currently well-developed and widely used in many applications in structural engineering where the elastic behavior of the structure is expected, e.g., models to analyze and design steel structures under gravity loads. In such models, steel elastic behavior is entirely characterized by Hooke's law based on Young's modulus (E) and Poisson's ratio (ν) [2]. Furthermore, in some other applications, the elastic analysis responses of

the structures are modified based on the code procedures to approximate the global nonlinear responses. For example, most of the seismic codes [4, 12] allow engineers to run the elastic analysis of the structures and evaluate the global nonlinear responses based on modification factors such as the response modification coefficient (R) and the displacement amplification factor (C_d).

In many other applications, structural components are supposed to sustain a controlled plastification in which the strain is typically less than the ultimate tensile strength (UTS) shown in Figure 1.1. In these components, a constitutive model with more parameters (e.g., yield strength, hardening model) is required to more accurately describe the plastic behavior. Since plastic deformations are associated with damage on the microstructural scale [13], uncertainties in the plastic region are more considerable than in the elastic region. Many codes and guidelines prescribe the modeling procedures [14, 15] and specified material plastic characteristics [16] needed to simulate the material nonlinearity. When a macro model is employed, simplified material behaviors, like an elastic-perfectly plastic model or an elastic-linear plastic model, are often acceptable. On the other hand, for more detailed capacity analyses where local responses of steel components are under investigation, true stress–strain data from uniaxial tensile tests is preferred. These stress–strain relationships are illustrated in Figure 1.3.
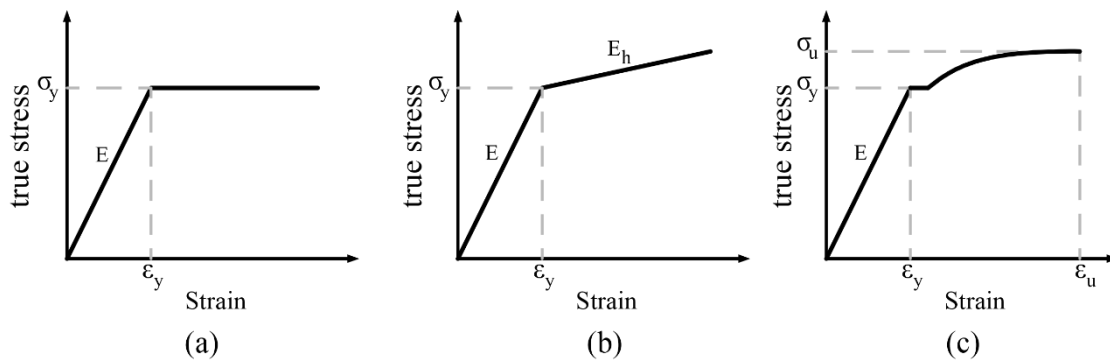
Figure 1.3. Various presentations of steel stress–strain curve up to UTS point: a) elastic-perfectly plastic model, b) an elastic-linear plastic model, c) true stress–strain data.

The material behavior for strains greater than ε_u (at UTS) is even more complicated due to the interaction between geometrical and material nonlinearities, extensive damage accumulation, stress triaxiality, and strain localization followed by material failure (fracture). Since the micromechanical processes of void growth and coalescence are dominant mechanisms in steel ductile fracture, many aspects of numerical modeling are still under development to analyze the relationship between small-scale material behavior and practical

5

applications. It must be emphasized that plastic deformation beyond ε_u is not a conventional intention of the design but can occur due to accidental extreme events like a progressive collapse, a collision, or an explosion. In these applications, detailed simulations of local responses are essential to capture the effect of strain localizations and stress risers and to predict the fracture initiation properly.

To predict this failure mode (i.e., ductile fracture of components), numerical models must be fed with adequate and accurate constitutive model and fracture criteria according to material type, loading rate, temperature, etc. Since prediction errors can be caused by both the inherent properties of the model and inaccurate calibrations, it is useful to distinguish between an adequate and an accurate model (an adequate material model refers to a model that can appropriately simulate different phenomena involved in the physical process of steel plasticity and ductile fracture, while an accurate model is an adequate model that has been properly calibrated and applied).

So far, many studies have been conducted to develop different material models and numerical techniques for post-necking and ductile fracture modeling; however, more efforts are required to predict the ductile failure of steel structures under uncertain and complex conditions, such as structures located in corrosive environments.

1.1.2 Failure of corroded steel structures

In a corrosive environment, corrosion as an additional factor can affect the failure of steel structures by strength degradation (general corrosion) or extensive stress and strain localization (pitting corrosion). The latter is one of the main forms of corrosion that initiates and propagates locally in steel structures located in a corrosive environment [17, 18]. Due to the number of parameters involved, the nature of the pitting corrosion and its characteristics are extremely stochastic [17, 18]. The penetration rate, depth, shape, and location of pits are all dependent on various environmental and material factors, including pH and chloride concentration, erosive environment, surface direction, metallurgical properties, surface roughness, temperature, UV radiation, and repeated wetting and drying (particularly in the splash zone of offshore structures) [17, 19].

On the other hand, the pitting corrosion rate and the pitting depth are independent of the metal thickness [20]. As a result, the consequences of pitting corrosion could be more serious for steel structures with thinner walls where corrosion can affect a large portion of metal thickness in a short time.

In corrosion science, a long-term evolution rule for different types of corrosion (i.e., general and pitting corrosion) is provided for a specific environment. Accordingly, the probability distributions of the corrosion characteristics, e.g., pit depth and shape, are estimated with respect to exposure times [21-25]. Figure 1.4 illustrates an example of pit depth evolution by the exposure time measured for mild steel located in coastal seawater by Melchers [22].
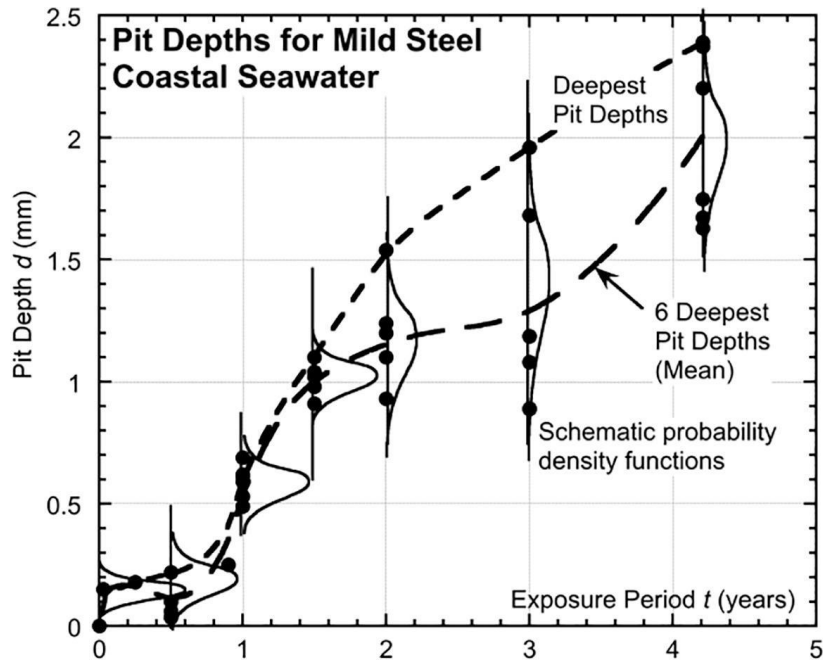
Figure 1.4. Pit depth evolution rule measured for mild steel located in coastal seawater (from Melchers [22] with permission).

This data can be obtained by examining a historical survey of the corrosion properties (coating records, corrosion morphology, environmental situations, etc.) of the current or a similar structure located in a comparable environment [19]. Alternatively, experimental studies in the natural or artificial environment (salt spray test [26]) can be employed in cases lacking historical data. Based on the historical corrosion database and empirical corrosion modeling or complementary numerical analyses to model pitting corrosion kinetics [27, 28], the statistical properties of corrosion parameters can be estimated with respect to the time of exposure. In this connection, various corrosion evolution rules from simple linear [29] and bilinear [29] models to multiphase models [30] have been developed. Some of these models are reviewed in [28, 31]. It is worth mentioning that the corrosion science and its procedures used to calibrate the pitting corrosion evolution rule are out of the scope of this thesis.

1.1.2.1 Overview of standards and guidelines

Due to the complexity of the corrosion phenomenon, current codes and guidelines [15, 32-34] mainly address the corrosion in the design phase structures by prescribing standardized protection methods to avoid corrosion for predetermined service life. They also define the maximum allowable thickness diminution in existing structures due to corrosion without quantifying the failure [35, 36]. A review of the definition of corrosion intensity presented by these codes indicates that they have ignored influential parameters of pitting corrosion for ductile fracture. For example, DNVGL-CG-0172 and DNVGL-CG-0182 [35, 36] mainly define the allowable thickness diminution based on the degree of pitting without considering pit aspect ratio and possible interactions between pits. Therefore, the specified acceptable thicknesses might primarily intend to prevent common failure modes like fatigue or buckling rather than ductile fracture.

1.1.2.2 Modeling of pitting corrosion under plastic deformations

The localized behavior of pits boosts the complexity in the simulation of the ductile fracture when it goes to application. In material modeling, pits act as notches that magnify stress triaxiality and localize plastic strains. The result is an accelerated failure of the components due to a higher rate of ductile fracture initiation. This notch effect must be adequately addressed in the failure prediction of corroded steel components under extreme loads. In numerical techniques, considering the stochastic nature of corrosion and its local effect is challenging. For this purpose, an efficient implementation approach of pitting corrosion in the geometry of the components is required. Therefore, the discretization of random pitting morphology with a reasonable computational time is also necessary. In addition, the time-dependent aspect of corrosion calls attention to the life cycle assessment in which the performance of structures is continuously updated based on the current corrosion status. Considering the possible number of components in a structural system, using an updatable numerical technique can be beneficial in terms of modeling cost. In such an updatable framework, new features in the corroded surface can be implemented without redoing all modeling procedures.

The first important parameter to implement pits on a steel member is the shape of the pits. As Table 1.1 shows, various assumptions and idealizations about pitting corrosion morphology have been made to implement pits in finite element models. Previous studies [37, 38] showed that when corrosion pits are significantly developed into the thickness of members, the pits can be simplified by semi-

ellipsoids. Many researchers used this pit shape as an acceptable shape, particularly for mild steel in the marine environment [39-45].

As illustrated in Figure 1.5, besides the coordinates (*x* and *y*), one needs to specify pit depth (*d*) and aspect ratio (*AR*) to characterize a pit by a semi-ellipsoidal geometry. *AR* is defined as the ratio between the pit width (*w*) and the pit depth (*AR=w/d*).

In addition to pit characteristics, the intensity of the pitting pattern also affects the performance of steel components. One of the widely used parameters that provides information about the intensity of pits is the degree of pitting (DOP), which is the ratio of the corroded area (A_c) to the total area of the original member (A_t) [28, 40, 46] and can be written as follows:

$$DOP(\%) = \frac{A_c}{A_t} \times 100\% \qquad (1.1)$$
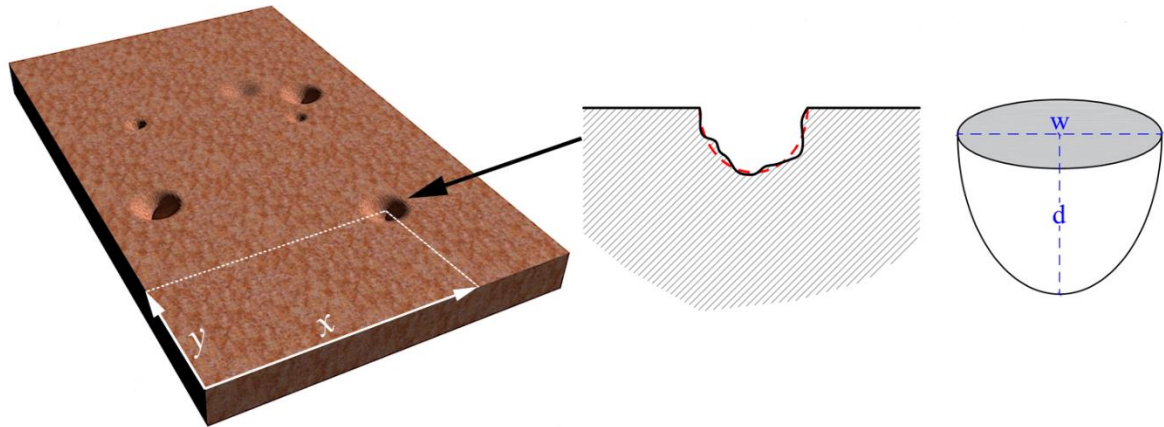
Figure 1.5. The geometry of a well-penetrated pit resembles a semi-ellipsoid.

Depending on the geometry of the pits, they can increase the plastic strain and stress triaxiality [39, 43, 45, 47-49]. These two parameters are known as influential parameters that accelerate ductile fracture initiation in metals [50, 51].

The open literature related to the corrosion of steel structures mainly covers the numerical models and the influencing factors on structural degradation in terms of ultimate strength [28], while the ductile fracture and deformability of structural components under extreme events have been poorly documented. Table 1.1 summarizes recent studies on the numerical modeling of steel components with pitting corrosion under extensive plastic deformations.

Table 1.1. Recent studies on the numerical modeling of ductile fracture of steel components with pitting corrosion.
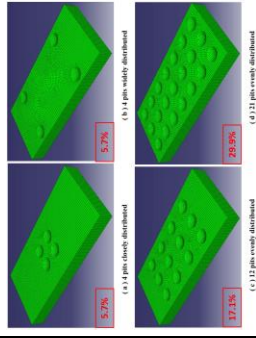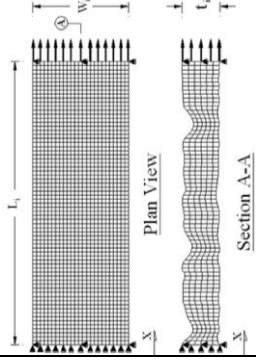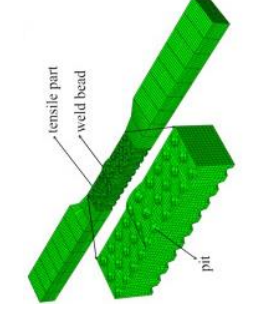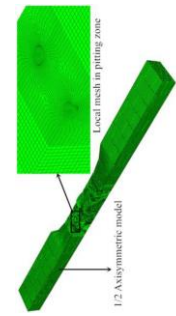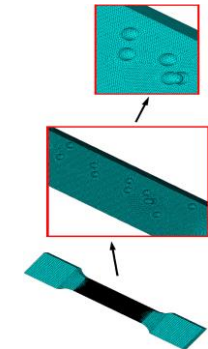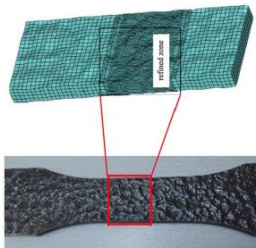
Reference	Xu et al. [37]	Appuhamy et al. [52]	Ahmmad and Sumi [53]	Yu [54]
Year	2016	2011	2010	2009
Component type	Double-sided corroded butt-welded plates	Double-sided corroded steel plates	Double-sided corroded steel plates	Axial and biaxial tensile single-sided corroded steel plates
Pit morphology	Hemispherical	Scan of the actual corroded surface	Conical	Semi-oblate spheroid
Fracture model	Stress modified critical strain	Stress modified critical strain	Not modeled	A strain-based model
Software	Abaqus/Explicit	LUSAS	LS-DYNA	Abaqus
Description				
Element type (size)	Reduced integration brick element (1 mm)	Hexahedral solid element with eight nodes	Hexahedral solid element with eight nodes (0.5 × 1 × 2 mm)	Hexahedral solid element with twenty nodes (0.25 mm)
Pitting pattern	Ordered pitting distribution	Distribution from tests	Distribution from tests	Ordered pitting distribution
Updatable model	No	No	No	No

Table 1.1. Recent studies on the numerical modeling of ductile fracture of steel components with pitting corrosion (continued).

Reference	Wang et al. [56]	Wang et al. [39]	Zhao et al. [41]	Songbo et al. [55]
Year	2017	2018	2020	2021
Component type	Double-sided corroded steel plates	Single-sided corroded butt-welded plates	Single-sided corroded mild steel plates	Double-sided corroded mild steel plates
Pit morphology	Scan of the actual corroded surface	Semi-ellipsoidal	Cylindrical, conical, or ellipsoidal and hemispherical shapes	Scan of the actual corroded surface
Fracture model	Void growth model and stress modified critical strain	A simplified fracture criterion	No fracture model	Stress modified critical strain
Software	ANSYS	Abaqus/Explicit	ANSYS	Not reported
Description				
Element type (size)	Hexahedral solid element with eight nodes (0.75 mm)	Reduced integration brick element (one-tenth of pit depth)	Tetrahedral elements for the corroded domain (0.5 mm)	Hexahedral solid element with eight nodes (0.1 mm)
Pitting pattern	Distribution from tests	Ordered pitting distribution	Random pitting distribution	Distribution from tests
Updatable model	No	No	No	No

The studies referenced in Table 1.1 investigated the effect of different characteristics of pits on the strength and ductility of steel components numerically and experimentally. Studies [37, 39] on butt-welded steel joints indicated strength and ductility reduction when the pitting corrosion was developed. Pit location, distribution, and geometry (i.e., pit depth and aspect ratio) were the most important factors that caused ductility degradation by local ductile fracture initiation and propagation [37, 39]. Numerical studies [39, 42, 55] also showed that the interaction of pits can change the notch geometry in a way that increases the stress triaxiality ratio and changes strain distribution so that ductile fracture can initiate with a smaller elongation. It is evident that by increasing the DOP the interaction between pits is more likely because of closer proximity. On the other hand, as illustrated in Figure 1.6, for an identical DOP, the various random pitting patterns can cause different interaction scenarios that must be properly addressed in the failure prediction of steel components for future corrosion.
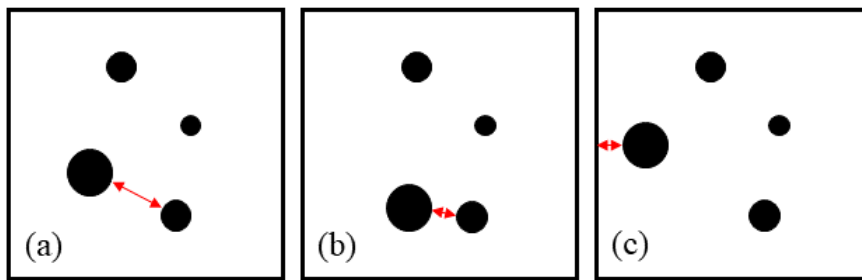
Figure 1.6. Various random pitting patterns with the same DOP can cause different interaction scenarios: a) no significant interaction, b) interaction between pits, c) interaction between pits and edges of the plate.

Also, to determine the critical section for probable fracture initiation, the pitting corrosion factor was defined as the ratio of maximum pit depth to the average thickness at a corroded section [57]. Thus, sections with larger pitting corrosion factors are potential sections for fracture initiation.

Despite the above-mentioned remarkable findings on the effect of pitting corrosion on ductile fracture of steel components, none of the studies listed in Table 1.1 proposed a systematic numerical approach to deal with the stochastic feature of pitting corrosion for the prediction of failure. Some of these numerical models [41, 53] were performed without a fracture criterion in their numerical models. As a result, these numerical models were limited to the plastic behavior of steel without explicit implementation of fracture. Many other of these studies [37, 39, 54] used predefined ordered pitting distributions in their numerical studies. Such numerical models cannot address the random nature of pitting corrosion properly, as they use

predefined pit distributions. Predefined pit distributions cannot model all possible scenarios of pit interactions because of fixed proximities between pits. On the other hand, studies [52, 53, 55, 56] that used real corroded morphologies of tested specimens based on scanning techniques only assessed the failure of current corrosion morphology. These studies did not develop a systematic approach for the prediction of possible failure scenarios of future corrosion. In addition, all the studies listed in Table 1.1 used numerical models limited to simple plates; however, in most applications, the effect of pitting corrosion must be considered in the failure prediction of complicated steel components like steel joints.

In large-scale practical components, in most cases, no adequate information is available on the effect of localized corrosion on overall member performance. Large-scale tests are also less informative in this regard due to the uncertain nature of the future pitting corrosion. In addition, in-service testing for a current pitting morphology is impossible for a component involved in an existing structure. Therefore, the need for numerical modeling as an assessment tool is significant in this topic. Such a numerical failure assessment framework should include some features as follows:

1. To calculate the stress and strain distribution in the corroded domain, numerical models must accurately take the three-dimensional effect of pits into account. Therefore, a high-resolution discretization of the corrosion geometry must be utilized in such numerical models to correctly predict the local responses on the pits and consider the interaction between them.

2. To predict the structural failure properly, numerical models must be fed by adequate and accurate constitutive model and fracture criterion of the involved materials (i.e., base metal, weld, and heat-affected zone).

3. The proposed numerical framework must have a linking ability between material scale and structural scale. Therefore, it must be extendable to complicated geometries like steel connections at a reasonable computational cost and without numerical difficulties.

4. Because of the stochastic and time-dependent nature of corrosion in steel material, the failure assessment framework must consider the uncertainties associated with pitting corrosion in the process of failure prediction so that the result can be used through a comprehensive risk-based corrosion management framework [19].

5. The numerical models used in the failure prediction must be progressively updatable and include the possibility to be coupled with real-time

monitoring systems or periodic inspections to ensure long-term structural integrity and safety based on life-cycle assessments [19]. In this connection, it is essential that numerical models be modifiable for sequential loads and corrosions.

1.2 Objective and scope

The present thesis addresses the numerical failure assessment framework to predict the failure of the steel components under the coupled effect of pitting corrosion and excessive plastic deformations. The thesis and the appended papers aim to improve the numerical modeling framework by modifying the procedure of material model calibration toward a more applicable and accurate calibration approach. This assembly also emphasizes linking small-scale micromechanics-based modeling and large-scale component modeling to predict the failure of the steel components under such complicated and extreme scenarios. The uncertainties and time-dependent nature of pitting corrosion are involved in the proposed failure assessment framework to provide a realistic representation of pitting corrosion in the process of failure prediction. To achieve the above-mentioned objectives, five scientific papers were written, as described in Table. 1.2. These papers cover material characterization and modeling, structural failure under excessive plastic deformations, and numerical modeling of the interaction between excessive plastic deformations and pitting corrosion.

Table 1.2. Relation between the objectives of the appended papers and the general objective of the thesis.

		Paper	Objective	Contribution
Steel components under extensive plastic deformations	Material and structural failures	P(I)	Using numerical models to investigate the optimal configuration of steel beams and box columns joint under extensive cyclic plastic deformations.	Scrutinizing the role of numerical modeling in failure prediction of steel components under extensive plastic deformations.
		P(II)	Using numerical models to investigate the effect of the joint strength on the performance of ordinary moment-resisting steel frames under a progressive collapse situation based on a calibrated ductile damage model.	Investigating the role of material testing and modeling in failure prediction of steel components under extensive plastic deformations.
		P(III)	Proposing an alternative DIC-based approach to calibrate the constitutive model and fracture criterion for weld and heat-affected zone (HAZ) metals and mitigate calibration errors associated with the common calibration process.	Improving steel ductile fracture modeling for the assessment of the corroded components by an alternative calibration approach.
	Interaction between pitting corrosion and extensive plastic deformations	P(IV)	Developing the concept of fracture-based fragility curves at the component level by micromechanics-based modeling to take the stochastic and time-dependent nature of pitting corrosion into account for the integrity evaluation during risk-based corrosion management studies.	Implementing the random nature of the pitting corrosion to consider different interaction scenarios between pitting corrosion and extensive plastic deformations. Propose a rational failure evaluation approach to quantify the failure for life-cycle assessments.
		P(V)	Employing two-level numerical modeling to reduce the complexity involved in the modeling of pitting corrosion in complicated geometries.	Linking micromechanics-based modeling and large-scale component modeling.

1.3 Industrial applications

1.3.1 Examples of extreme events in corrosive environments

According to the Norwegian Petroleum Safety Authority (PSA), 115 ship-to-platform collisions have been reported on the Norwegian continental shelf in the period 1982–2010 with various degrees of severity [58]. Among these collisions, 26 more recent ones occurred between 2002 to 2010 without casualties; however, significant economic consequences were reported [58]. As Figure 1.7 shows, four collisions occurred on average between ships and platforms annually. One of the recent collisions reported publicly is the collision between supply vessel PSV Sjøborg and Statfjord A platform that occurred in 2019. The vessel lost its position during loading/discharging operation and collided with the lifeboat structure, as shown in Figure 1.8. The accident was ranked with the highest degree of severity (Red1) according to Equinor's classification matrix [59]. The consequences, like damage to the lifeboat structure by fracture of some structural members, were reported. Although the collision did not impair the structural integrity of the platform, 218 people were evacuated from the platform by helicopter [59]. This event could have led to more dramatic consequences if more severe damage on lifeboats occurred with an explosion and fire on the platform.

So far, different types of platforms and infrastructures like bridges [60], offshore wind turbines [61], oil platforms [62], and fish farms [63] have been studied for such collision scenarios.

Besides the ship collision, many infrastructures are prone to experience various other extreme events like different types of collisions, element removal due to a localized fire, an explosion in industrial facilities caused by gas pipe fracture, or a leakage of combustible liquids [64], and also impacts from dropped objects [65]. For instance, Figure 1.9 illustrates the topside structure of a jetty with corroded joints that experienced a column removal. Although these accidents could be different by unit type, geography, and accident type [23, 24], the final structural consequences can be similar, causing plastic deformations beyond the intended design limits.

16
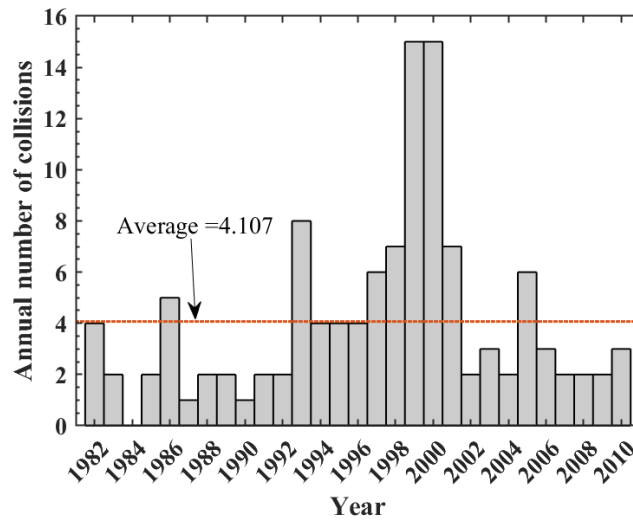
Figure 1.7. Ship-to-platform collision statistics for the Norwegian continental shelf in the period 1982–2010 [58].

Figure 1.8. Sjøborg supply vessel collided with the Statfjord A platform and caused damage to the lifeboat structure in 2019 [59, 66].
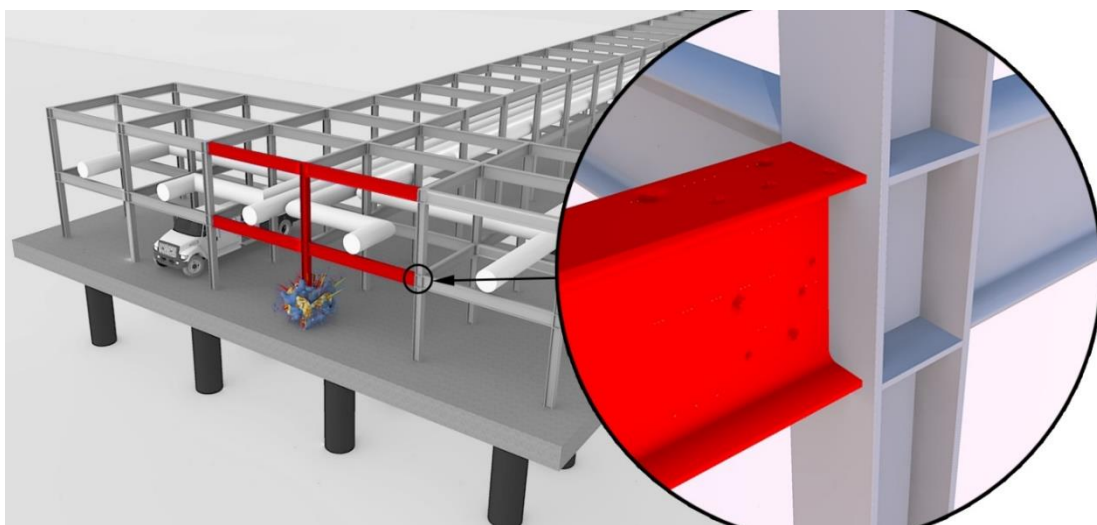
Figure 1.9. An illustration of the topside structure of a jetty subjected to column removal and pitting corrosion.

17

Figure 1.10. A corroded steel beam-to-column connection.

On the other hand, based on the reports, a significant percentage of the world offshore facilities are past their theoretical design life [19]. Many of these constructed steel facilities are subjected to pitting corrosion [19] (see Figure 1.10 as an example). Depending on the characteristics, pits can accelerate ductile fracture in metals [50, 51]. Ductile fracture initiation at the root or wall of a corrosion pit can be followed by ductile tearing that pushes the crack front at high-stress levels and increases the chance of failure by cleavage fracture and unstable crack propagation [39, 67]. As a result, the effect of pitting corrosion must be appropriately addressed in steel structures as an adverse factor to the structural integrity. The owners and authorities must continuously demonstrate the integrity and safety of these facilities against extreme loads by considering the impact of corrosion. This demonstration can be performed through a comprehensive risk-based corrosion management consisting of two phases: evaluating the structural integrity of currently corroded components and predicting the structural failures for potential future corrosion to keep these facilities in operation for a prolonged life beyond their design [19].

1.3.2 Risk-based corrosion management

Based on recommended practice, risk-based corrosion management is a process to identify, assess, and prioritize the failure risks due to corrosion in order to minimize, inspect, and control the probability of disastrous events [19].

Based on this definition, quantifying the probability of components failure and their consequences to the whole system plays a central role in performing risk-based corrosion management [19]. Centered on such evaluated failure probabilities, the risk managers can identify the potential threats and consequences

of the current and future corrosion to the structural integrity. Accordingly, they can choose proper treatment techniques to retrofit existing structures to fulfill principal criteria, e.g., health and safety, economy, environment, etc. [19]. Table 1.3 shows an example of a risk matrix in which the risk level is determined based on the probability of failure and classified consequences of failure. It is worth mentioning that in risk-based corrosion management, assessments should cover both the risk of failure in local components and the sequent risk of global collapse [68]. For this purpose, the collapse probability of the global system due to a given component failure can be identified based on a conditional probability written as follows:

$$P_{global\ collapse} = P(global\ failure|component\ failure)$$ (1.2)

Furthermore, the risk evaluation of failure in the design phase of new structures subjected to corrosion is also essential to facilitate an optimal selection of corrosion prevention, inspection, and monitoring methods.

The tasks included in risk-based corrosion management are typically performed in a life-cycle assessment, as schematically shown in Figure 1.11. First, based on a periodic inspection plan, the current corrosion status is obtained for critical zones. Then, based on numerical simulations, the failure of components based on the current status is evaluated. This evaluation can lead to an urgent remedy for extensively deteriorated components. Otherwise, the component failure and global collapse are predicted for future corrosion scenarios in terms of probability. Based on these probabilities of failure and predefined risk matrix (see Table 1.3 as an example), risk managers identify the possible life extension without repair or prescribe a retrofit plan. Since the defined life extension and the intensity of future corrosion are correlated, the process can be iterative to achieve an optimal solution.

Table 1.3. An example of a risk matrix to define risk level based on the probability of failure (adapted from [68]).

	The consequence of failure (CoF)				Probability of failure				
CoF	**Personnel**	**Pollution**	**Economy**	**Reputation**	**1**	**2**	**3**	**4**	**5**
1	Classification according to no. of injuries and fatalities	Classification according to, e.g., tons of spill to sea (of various types)	Classification according to loss in million NOK, (e.g., due to repair and lost production)	Specific classification to be defined	L	L	L	L	M
2					L	L	L	M	M
3					L	M	M	M	H
4					M	M	H	H	H
5					M	H	H	V	VH
Risk levels: L= low; M= Medium; H= High; VH= Very High									
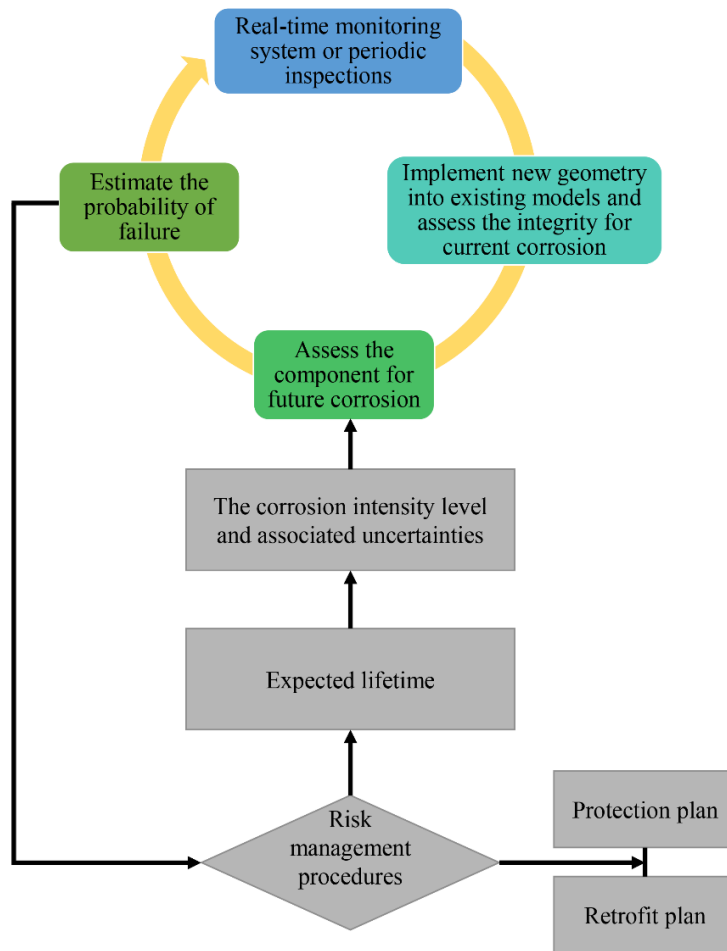
Figure 1.11. Overview of life-cycle assessment of steel components subjected to corrosion.

2. Fracture modeling in structural steel

2.1 Fracture modes of steel structures

In general definition, a fracture is a forced separation of material into two or more parts. As a result, fracture forms new free surfaces in the material matrix. Based on the material microstructure, applied stress states, temperature, and environmental conditions, fracture in steel can occur in various modes, ranging from stable ductile fracture to abrupt unstable brittle fracture [69-71]. Therefore, to develop an adequate and accurate fracture criterion, the dominant mechanism behind these fracture modes must be understood correctly. This thesis focuses on ductile fracture mode based on microvoid nucleation, growth, and coalescence mechanisms caused by extensive plastic deformations. Other mechanisms such as cleavage, ductile-to-brittle transition, and intragranular fracture mechanisms are briefly reviewed to provide a thorough perspective regarding fracture.

2.1.1 Ductile fracture

Ductile fracture is one of the main material failure modes of steel structures accompanied by large-scale plasticity [72]. In contrast to brittle modes (i.e., cleavage and intergranular fracture) that have an extremely random nature, extensive plasticity before final material failure makes ductile fracture more predictable. This predictability enables engineers to avoid it successfully in the design phase under expected loads. Three sequential mechanisms driven by plastic deformation are responsible for ductile fracture initiation [70, 71]:

Void nucleation: Depending on the applied stress, the interfacial bonds between secondary particles or inclusions in the steel matrix can be broken, and a void nucleates around the secondary particle as described in Figure 2.1(b) [70, 71]. If these second-phase particles are strongly bonded to the matrix, void nucleation typically controls the fracture properties of the material; otherwise, void growth and coalescence mechanisms, as described in the following, control the behavior [70].

Based on continuum theory, Argon et al. [73] proposed that decohesion stress (σ_c) at a cylindrical particle can be approximated by summing the hydrostatic stress (σ_m) and the equivalent von Mises stress ($\bar{\sigma}$) as follows [74]:

$$\sigma_c = \sigma_m + k\bar{\sigma} + C \frac{l_0}{R_0} \qquad (2.1)$$

Where k is a geometrical factor, l_0 is the distance between particles, R_0 is the particle radius, and C is a numerical coefficient [74]. In addition, σ_m is the average of the principal stresses along three orthogonal axes calculated as follows:

$$\sigma_m = \frac{\sigma_1 + \sigma_2 + \sigma_3}{3} \tag{2.2}$$

In this equation σ_1, σ_2 and σ_3 are principal stress components. In addition, $\bar{\sigma}$ as equivalent von Mises stress can be calculated based on these stress components by the following expression:

$$\bar{\sigma} = \sqrt{\frac{(\sigma_1 - \sigma_2)^2 + (\sigma_2 - \sigma_3)^2 + (\sigma_3 - \sigma_1)^2}{2}} \tag{2.3}$$

The model proposed by Argon et al. [73] showed consistency with experimental observations that in a triaxial tensile stress field, the void nucleation can happen more quickly. Some other models [75, 76] were also established based on dislocation-particle interactions in crystalline materials that are mainly applied for particles with a diameter smaller than one μm [70]. More details about these models are provided in [70, 74].

Void growth: As illustrated in Figure 2.1(b), after nucleation, applied stress and plastic strain cause the nucleated voids to grow. It is widely demonstrated in the literature [50, 51, 70, 77-79] that the void growth rate strongly depends on the stress triaxiality (η) that is defined as the ratio of the hydrostatic stress (σ_m) to the equivalent von Mises stress ($\bar{\sigma}$) as follows:

$$\eta = \frac{\sigma_m}{\bar{\sigma}} \tag{2.4}$$

Void coalescence: The voids are small and independent of each other at the early stage of plastic deformations. Due to increasing plastic strain, the voids grow, and the ligament lengths between neighboring voids decrease, and they interact [71]. Eventually, plastic strain is concentrated along a particular plane of voids due to necking instabilities and deformation localization caused by the void growth, and suddenly a macroscopic fracture surface is formed, as described in Figure 2.1(b) [70, 71]. The coalescence process typically corresponds to an abrupt change in the slope of the local stress-strain curve [72].

This type of fracture is often observed in uniaxial tensile tests. As shown in Figure 2.1(a), fracture morphology typically shows a cup-and-cone shape, consisting of a flat plane at the central region and a shear lip around it [70]. Due to the higher

stress triaxiality ratio at the center of the specimen, the void growth and coalescence occur at a higher rate [70]. The higher stress triaxiality allows the ductile mechanism of microvoid growth and coalescence to occur around large particles. This is compatible with the final fracture surface, which is usually coarsely dimpled at the center, as shown in Figure 2.1(d). On the other hand, due to low triaxiality and strain concentration in 45° deformation bands formed in the neck area, nucleation occurs around small particles in the lip (shear lip) [70]. Since the distribution of smaller particles is denser, the voids interact more significantly in this area [70]. The final consequence is a rapid coalescence and failure at the lip by a smoother and more shiny surface. Figure 2.2 present the fracture surface of mild steel under a scanning electron microscope with a low magnification. As it is apparent, only the fractured surface at the center of the specimen has a clear dimpled surface due to coarser nucleated voids. In contrast, dimples in shear lips are small, and to make dimples visible, a larger magnification is required.
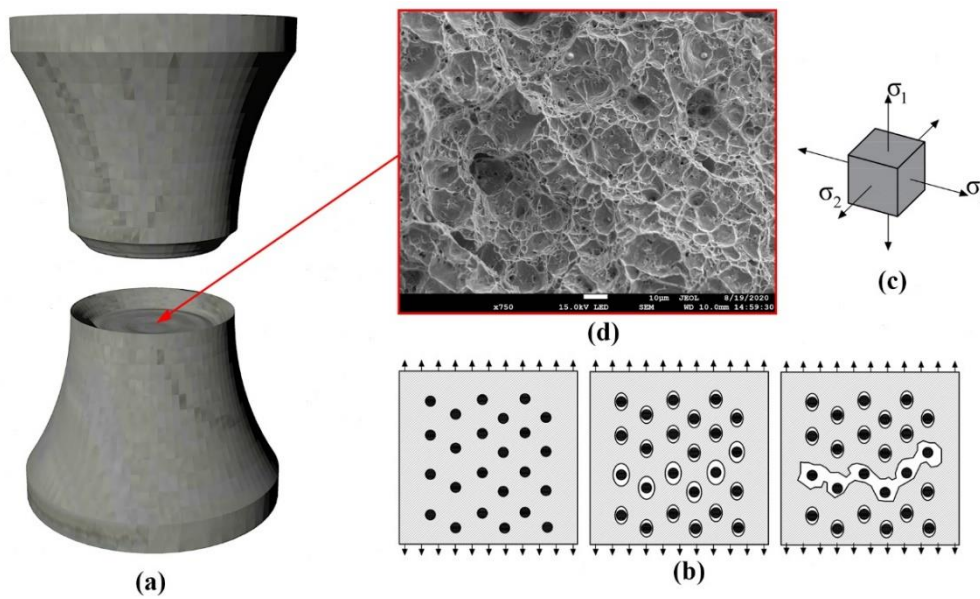
Figure 2.1. Ductile fracture of round bar tensile specimen: a) the cup-and-cone fracture surface, b) void nucleation, growth, and coalescence, c) high-level stress triaxiality at the canter, d) Coarsely dimpled appearance of the fractured surface at the center for S355J2 steel.

The large plastic deformations before ductile fracture provide a good energy absorption capacity and significant warnings before the total failure of structures. Therefore, it is a desirable fracture mode in the design of steel structures under extreme loads.
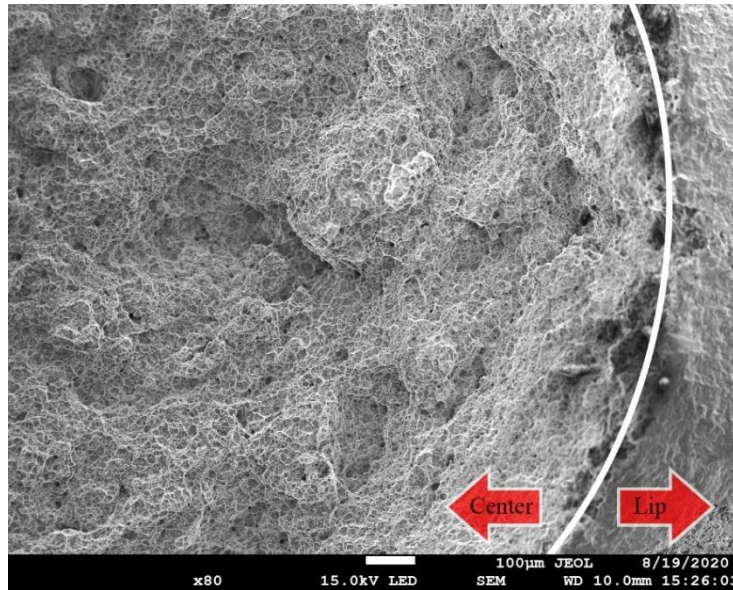
Figure 2.2. The fracture surface at the center of the mild steel tensile specimen has larger dimples than the shear lip.

2.1.2 Cleavage fracture

Brittle fracture in metal usually refers to failures resulting from rapid crack propagation due to cleavage fracture or intergranular fracture [70]. From the microstructure perspective, cleavage fracture occurs due to a sudden separation of material along a crystallographic plane with a dense atomic structure with a limited number of active slip systems [70, 72]. This plane in metals with body-centered cubic (BCC) crystal structure like ferritic steel is (100) plane [70]. It is worth mentioning that the fracture path is transgranular, as illustrated in Figure 2.3(a). Since there could be a mismatch between plane orientation in neighboring grains, the orientation of the cleavage plane changes to adapt a new plane when it crosses grain boundaries [72]. This step forms patterns called "rivers", as observed by fractography.

On a macroscopic scale, shiny and faceted fracture surface normal to the maximum principal stress is formed in the cleavage fracture. In fracture mechanics terminology, this corresponds to mode I of fracture.

Cleavage fracture requires stress larger than the cohesive strength of the material at the atomic level [70]. In this connection, sharp local discontinuity, like microscopic cracks, can act as local stress raisers and nucleate a crack. In mild steel, cleavage usually initiates at grain boundary carbides. In such situations, any plastic deformation is enclosed to the surrounding area of the crack tip, so there may be little sign of large-scale plasticity [69].

24

Once the crack nucleates, two potential scenarios can happen. The crack can remain sharp, and applied loads push the crack front at high-stress levels causing rapid propagation and failure. The other possible scenario is that the crack is arrested at surrounding grains or in a steep stress gradient ahead of the macroscopic crack so that total fracture of the specimen or structure does not occur [70].

Cleavage fracture toughness is extremely uncertain because of the random location of the critical fracture-triggering particles [70]. Therefore, two identical specimens made from the same material may exhibit quite different toughness values because the distance between the critical fracture-triggering particles and the crack tip is different [70]. That is why many stochastic approaches for micromechanical modeling of cleavage have been developed. For more details about relevant mathematical models of cleavage fracture, please refer to Anderson [70] and Brocks [80].

Although cleavage fracture is known as a brittle fracture, it can also be preceded by ductile crack growth (also called ductile tearing), as shown in Figure 2.4 [70].

(a)   (b)
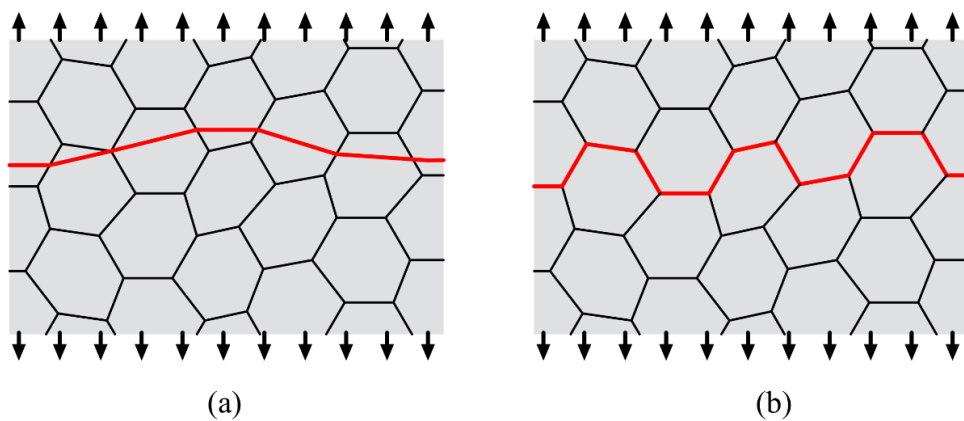
Figure 2.3. Schematic illustration of two fracture mechanisms in metal: a) cleavage (transgranular) fracture, b) intergranular fracture

(a)   (b)   (c)
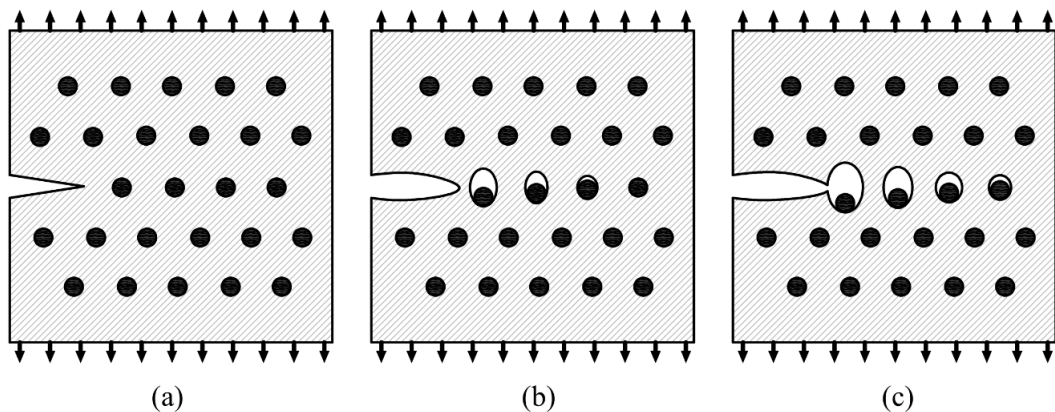
Figure 2.4. Schematic illustration of cleavage fracture preceded by ductile crack propagation.

2.1.3 Intergranular fracture

As described, ductile metals typically exhibit ductile fracture by the coalescence of voids formed at inclusions and second-phase particles or brittle fracture by transgranular cleavage. In both cases, metals do not fail along grain boundaries [70]. There are some special situations in which cracks can form and propagate along grain boundaries, as illustrated in Figure 2.3(b) [70]. This mode of fracture is named intergranular fracture. Precipitation of a brittle phase on the grain boundary, environmentally assisted cracking, intergranular corrosion, and grain boundary cavitation and cracking at high temperatures are some mechanisms for intergranular fracture [70]. For more details, refer to Anderson [70].

2.2 Modeling of ductile fracture

The topic of ductile fracture has been studied for more than 50 years; however, modeling ductile fracture in structural applications and predicting consequent failures in steel structures subjected to plastic deformations is still an open research issue. This phenomenon is complex due to uncertainties related to physical micromechanisms of ductile fracture and challenges in proper modeling and interpreting them in structural applications [81, 82].

Before the review of ductile fracture modeling, it is important to distinguish between continuum approaches and traditional fracture mechanics. Both these approaches are concerned with the behavior of the damage medium to evaluate the failure of metallic structures; however, their procedure of dealing with the problem is quite different [83].

In continuum approaches, defects exist on a microscopic scale in the form of microvoids and microcracks that are assumed to be continuously distributed within the material [83]. Thus, the physical and mechanical properties of damaged material depend on the distribution of the micro-defects. In contrast, traditional fracture mechanics deals with a pre-existing macrocrack, where stress singularity exists at the crack tips with significant stress concentration [83]. Figure 2.5 schematically describes the position of two approaches in evaluating the fracture in metallic structures.
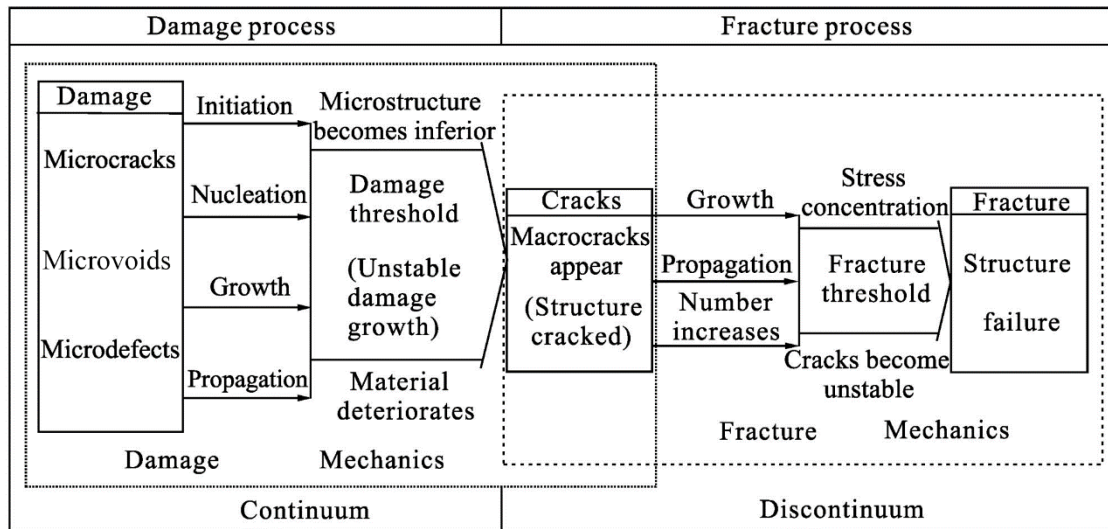
Figure 2.5. The position of continuum approaches and traditional fracture mechanics approaches to assess fracture in metallic structures (adapted from [83]).

It is widely accepted in related literature [71, 84-86] that the traditional fracture mechanics approaches such as stress intensity factor (K_I), J-integral (J_I), and crack tip opening displacement (CTOD) are not adequate to predict ductile fracture in large-scale plastification. Because these models are generally developed based on elastic or small-scale yielding on the tip of an existing crack, micromechanisms of ductile fracture are not explicitly considered in their formulation [71].

In addition, traditional fracture mechanics use the energy release rate as the main parameter that is related to the stress state, while in reality, the stress and strain state governs ductile fracture [70, 71]. Therefore, traditional fracture mechanics is an indirect means of quantifying fracture toughness and is unable to capture the physical ductile fracture process [71]. Moreover, in these approaches, a single geometry-independent parameter (e.g., K_I, J_I, or CTOD) is assumed to characterize the entire stress and strain field around the crack tip [70, 87, 88]. This assumption also cannot always remain true, especially in situations of nonhardening materials under fully plastic conditions, because the near-tip fields depend on the configuration [70, 71]. Hence, ensuring that sufficient constraint exists at the crack tip is important for the validity of single-parameter fracture mechanics [70]. In fact, the material in the near-tip field will contract perpendicular to the major stress axis [89]. This contraction is constrained by the surrounding material and induces an additional triaxial stress state in the crack tip, which promotes fracture initiation [89]. The amount of constraint effect depends directly on the specimen configuration [89]. The constraint effect is low in a small specimen due to a small

amount of surrounding material in the crack tip. In contrast, the constraint effect is high in large specimens because of the larger volume of the surrounding material [89].

All these limitations motivated the research community to develop direct stress and strain field approaches for more realistic simulation of ductile fracture under situations such as large-scale yielding. Such approaches would aim to capture the stress and strain interaction and their influence on the microstructural features, which cause fracture. However, such modeling is extremely computationally intensive and could not be performed when traditional fracture mechanics were more common. Today, computers can model the stress and strain fields at the microstructural level using extremely detailed finite element analyses.

These developed models that use stress and strain fields directly to predict fracture can be classified based on different terms. They can be classified as coupled and uncoupled models. In uncoupled models, the damage does not affect the constitutive equation, while in coupled models, the plastic flow and damage flow are coupled within the potential function to produce the softening effect [72, 83]. In addition, models can be divided into abrupt or continuous models. In the later, the fracture status is checked based on a continuous evaluation and integration of plastic strain and triaxiality through the loading history (e.g., void growth model and continuum damage mechanic). In contrast, in abrupt models, only an instantaneous check of involved parameters with critical values is done, such as Johnson and Cook (J-C) [79] and Stress Modified Critical Strain model (SMCS) [90]. Continuous models are more accurate when an involved parameter like triaxiality changes sharply; however, they need more computational resources compared to the abrupt models because of the continuous integration. In another common categorization, ductile fracture models can be sorted based on their physical foundation into two main categories: empirical criteria and micromechanics-based criteria.

2.2.1 Empirical criteria of ductile fracture

Empirical criteria phenomenologically calculate accumulated damage based on equivalent plastic strain adjusted by a proper triaxiality function to describe macroscopically observable degradation effects [80]. Bai et al. [91]; Bao and Wierzbicki [77]; Johnson and Cook [79]; Norris Jr et al. [92]; Marino et al. [93]; Hooputra et al. [94], Cockcroft and Latham [95] are some examples of well-known empirical models. In addition, some recent advanced empirical fracture models

(e.g., Bai and Wierzbicki [96]) can consider the effect of the Lode parameter (ξ), which is a function of the third invariant of the deviatoric stress tensor. However, the increasing number of parameters in models raises the problem of their experimental identification. In some cases, the parameters cannot be directly calculated from measured data or need specimens with special configurations that are uncommon in structural application [80, 81]. In addition, previous studies on tensile fracture demonstrated that the effect of the Lode parameter is negligible for the high positive triaxiality (i.e., $\eta > 0.33$) that is the case of tensile fracture [84, 96]. This region is highlighted in Figure 2.6.
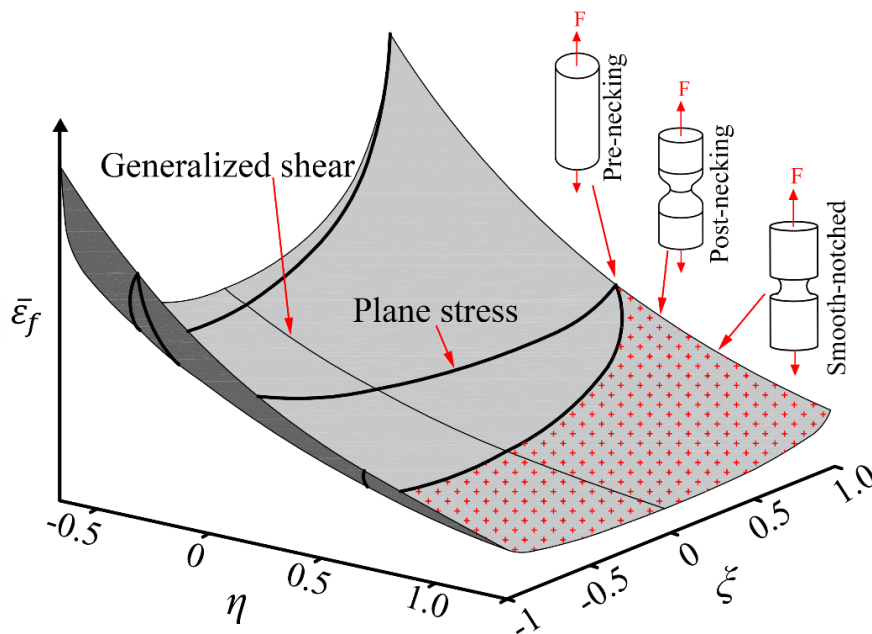
Figure 2.6. Fracture strain is a function of stress triaxiality (η) and Lode parameter (ξ) (The effect of ξ can be neglected when $\eta > 0.33$).

2.2.2 Micromechanics-based criteria

Micromechanics-based criteria have been developed based on the physical evolution of void growth and coalescence mechanisms. Several mathematical models to simulate these physical mechanisms have been proposed. Void growth models [50, 51, 90], Gurson-based models [97-100], and models based on continuum damage mechanics [101-103] are the most widely referenced. It is worth mentioning that in many widely used steel materials, void growth and coalescence govern the fracture process [71]. Therefore, some of these popular micromechanics-based models only consider these two mechanisms as the main

cause of the fracture and neglect the void nucleation that absorbs a small portion of the total damage [84].

2.2.2.1 Void growth model (VGM)

McClintock [50] proposed an equation for the growth of single cylindrical voids in elastic-perfectly plastic material under plastic strain. Similar studies were carried out on spherical voids by Rice and Tracey [51]. Both studies identified that the void growth rate is exponentially related to the stress triaxiality ratio (η). According to Rice and Tracey's result, the void growth rate for a spherical void can be defined as:

$$\frac{dR}{R} = C e^{1.5\frac{\sigma_m}{\sigma_y}}.d\bar{\varepsilon}_p \qquad (2.5)$$

Where R is the radius of a spherical void, $d\bar{\varepsilon}_p$ is the incremental form of equivalent plastic strain obtained as follows:

$$d\bar{\varepsilon}_p = \sqrt{\frac{2}{3}d\bar{\varepsilon}_p{}^{ij}.d\bar{\varepsilon}_p{}^{ij}} \qquad (2.6)$$

Where $d\bar{\varepsilon}_p{}^{ij}$ denotes the incremental form of strain components. It is worth mentioning that Eq. 2.5 is limited to elastic perfectly plastic materials. To account for hardening behavior, the yield stress (σ_y) replaced by the equivalent von Mises stress ($\bar{\sigma}$) [104] as follows:

$$\frac{dR}{R} = C e^{1.5\frac{\sigma_m}{\bar{\sigma}}}.d\bar{\varepsilon}_p \qquad (2.7)$$

In this equation, the exponent of 1.5 was obtained based on theoretical derivations done by Rice and Tracey [51, 90]. Also, C is a material-dependent parameter that controls the void growth rate.

Then fracture is physically postulated to initiate when the size of voids exceeds a critical value [90]. Based on this postulation, the VGM fracture criterion can be formulated mathematically by the following expression [90]:

$$VGI = \int_0^{\bar{\varepsilon}_p} e^{1.5\eta}.d\bar{\varepsilon}_p > VGI_{critical} \qquad (2.8)$$

The left-hand side of this expression is known as the Void Growth Index (VGI) that is an explicit integration of stress triaxiality ratio (η) with respect to equivalent plastic strain ($\bar{\varepsilon}_p$) over the loading history. The critical void growth index

($VGI_{critical}$) on the right-hand side is assumed to be a material property that can be calibrated based on the test results of Smooth-Notched Tensile (SNT) specimens and complementary finite element analyses [90]. The radius of the notch can change the stress triaxiality ratio at the notch section. The VGM model is well-known in structural engineering; however, it has some disadvantages listed as follows:

- The material parameter ($VGI_{critical}$) cannot be directly measured by material testing [82]. As a result, complementary finite element models are required to calibrate the model.
- The model is uncoupled, and damage softening is not modeled.
- The model needs more computational resources than abrupt models (e.g., SMCS) due to the continuous integration of strain and stress over the loading history.

More related literature and details about calibration procedures of VGM and its applications are provided in P(III).

2.2.2.2 Porous solid plasticity (Gurson-based)

The Gurson-based models have been developed based on the porous plasticity constitutive model, which considers the effect of ductile damage by progressively shrinking the yield surface [81, 82, 97]. Porous plasticity is based on the fact that metals are not ideally dense but contain cavities at the microscale growing with hydrostatic tension [80]. The original Gurson model [97] was derived through modeling of a single spherical cavity in a cubic rigid-plastic matrix, where a perfect plastic von Mises homogeneous material was assumed. In this model, the only dimensional microstructural feature is the void volume fraction or porosity (f) [72]. The yield surface is given by the following equation:

$$g\left(\bar{\sigma}, \sigma_m, \sigma_y, f\right) = (\frac{\bar{\sigma}}{\sigma_y})^2 + 2fcosh\left(\frac{3}{2}\frac{\sigma_m}{\sigma_y}\right) - 1 - f^2 = 0 \qquad (2.9)$$

where σ_y is the yield strength. By assuming $f = 0$, the Gurson model is identical to von Mises yield surface for an incompressible material [70]. Eq. 2.9 clearly shows that larger porosity (f) shrinks the yield surface and produces the softening effect.

The original Gurson model was based on the void growth stage only, and the proposed yield surface could not represent coalescence and fracture. In addition, it

was demonstrated by unit cell simulations that void growth rates were not accurately predicted in the original form [72]. Therefore, many researchers have proposed various modifications to this model over the years. The most widely used modification was proposed by Tvergaard and Needleman [100], known as the Gurson-Tvergaard-Needleman (GTN) model. Tvergaard and Needleman [100] replaced yield strength σ_y by the flow stress $\sigma_p(\bar{\varepsilon}_p)$ of the matrix material. When von Mises yield criterion and isotropic hardening are used, the flow stress will be equal to equivalent von Mises stress. In addition, this modification introduced an equivalent porosity (f^*) to model void coalescence [100]. Further, additional parameters $(q_1, q_2$ and $q_3)$ were used to describe void growth rate more accurately as observed in unit cell calculations [100]. The modified yield surface is written as follows:

$$g\left(\bar{\sigma}, \sigma_m, \sigma_p, f^*\right) = (\frac{\bar{\sigma}}{\sigma_y})^2 + 2q_1 f^* \cosh\left(\frac{3q_2}{2}\frac{\sigma_m}{\sigma_p}\right) - 1 - q_3 f^{*2} = 0 \quad (2.10)$$

Based on the GTN formulation, the yield surface exhibits a hydrostatic stress dependence in contrast to classical plasticity [70]. In addition, unlike the Rice and Tracey model [51], the GTN model contains a failure criterion. Ductile fracture is postulated to initiate due to a plastic instability that produces a band of localized deformation [70]. However, the model is unable to predict the necking instability between voids due to neglecting discrete voids [70]. Similar to the void growth rate proposed by Rice and Tracy, the porosity evolution rule in GTN shows an exponential trend with respect to stress triaxiality [70, 84].

The model has gained its reputation in the research community; however, the model has been found to have disadvantages in applied fracture prediction, including [71, 81, 82]:

- A large number of material parameters must be calibrated and fitted for a single material [71, 81, 82]. Identification of these parameters requires some expert knowledge; the results may be user-dependent, and there is no standard for this procedure [80].
- The material parameters are not physically based and cannot be directly measured by material testing [82].
- Damage softening increases the mesh sensitivity of the model compared to uncoupled models [105].

More details about the GTN model and parameters identification can be found in [100].

2.2.2.3 Continuum damage mechanics (CDM)

Continuum damage mechanics (CDM) is another approach to simulate ductile fracture. This approach has been mainly developed from the concept of a macroscopic damage variable proposed by Kachanov [101]. Based on thermodynamics theories Chaboche [102] and Lemaitre [106] formulated the constitutive equations of CDM. Lemaitre assumed that macroscopic crack initiated when the damage variable (D) reached a critical value (D_c). One of the well-known CDM-based models is the Rousselier model [107]. Although the Rousselier model was developed from different bases, it has a similar yield surface formulation to the Gurson model given by:

$$g\left(\bar{\sigma}, \sigma_m, \sigma_p, D\right) = \frac{1}{1-D}\frac{\bar{\sigma}}{\sigma_p} + c\frac{\sigma_1}{\sigma_p}Dexp\left(\frac{1}{1-D}\frac{\sigma_m}{\sigma_1}\right) - 1 = 0 \qquad (2.11)$$

Where c and σ_1 are adjustable parameters. When the Rousselier model is properly calibrated, it can provide predictions as accurate as the Gurson model with the advantage of better capturing localization [72].

Different direct and indirect methods were proposed to measure the damage evolution of material in respect to plastic strain [108]. Direct measurement typically uses the measurement of the density variation by micrographic pictures to estimate the damage parameter. Indirect measurements can be destructive such as the measurement of the variations of the elasticity modulus, or non-destructive such as the measurement of the micro-hardness variation and of the electrical potential [108]. In the most common method, D is identified based on the decrease of Young's modulus through cycles of loading and unloading tests [108].

Different CDM-based formulations have been proposed so far to improve the application of CDM; however, these models also show limitations in practice [81, 82] as follows:

- Selection and measurement of damage evolution rule can be challenging and expensive due to many loading and unloading testing cycles.
- Damage evolution rules are often validated only with experimental data obtained under uniaxial stress. Therefore, the validity of parameters in a multiaxial stress state is not always guaranteed.

- Similar to the porosity models, the CDM formulations are also subjected to high mesh sensitivity due to the coupled effect of plasticity and damage that causes softening.

Although micromechanics-based ductile fracture models are based on physical micromechanisms of fracture behavior of steel and can provide an accurate prediction of fracture initiation, many of them require rigorous calibration and implementation procedures because of numerous involved material parameters (e.g., Gurson models) or using a coupled damage and plasticity models (e.g., CDM models). Based on the literature, among these physical-based models, VGM is more conventional and has been successfully used in civil and structural engineering applications. Numerous studies [85, 90, 109-111] demonstrated that VGM is an adequate model for the prediction of ductile fracture under tensile monotonic loads (i.e., $\eta > 0.33$) in which the void growth and coalescence are the governing fracture mechanisms, and the effect of Lode parameter (ξ) is fairly small compared to the damage from the hydrostatic stress.

On the other hand, VGM has only one calibration parameter ($VGI_{critical}$) that makes the calibration process less complicated than some other models like Gurson-Tvergaard-Needleman (GTN) [81]. As a result, VGM offers a good compromise between adequacy and complexity. In addition, this model uses the history of strain and stress to evaluate the fracture so that it would be a proper model for situations with large geometry or triaxiality variation in ductile materials [71].

Based on the above-mentioned advantages, in this thesis, the VGM was selected as a micromechanics-based fracture criterion and was studied comprehensively through P(III) and applied in P(IV) and P(V) to establish a failure assessment framework for steel components with pitting corrosion under excessive plastic deformations.

2.2.3 Representative volume element

In classical mechanics, a material element is defined as an infinitesimal neighborhood of a material point that its volume $dV = dxdydz \rightarrow 0$ [80]. Material properties and responses (stress and strain) are assumed as homogeneous in this volume. By this definition, micromechanics-based models face a challenge to express the constitutive equations based on quantities that characterize the microstructure and its properties because these quantities can be significantly different in the neighborhood.

To solve this problem, the representative volume element (RVE) is defined as a material volume that can be considered statistically representative for the microstructure of the material and represents the neighborhood of a material point [80]. RVE can contain a number of cavities, cracks, particles, or inclusions [80]. Then, the constitutive behavior is described on a mesoscale (also called a unit cell) by mesoscopic stress and strain fields defined by averaging over the RVE. The RVE size must be small enough to avoid smoothing of high gradients but large enough to represent an average of the microstructural properties [112]. For experimental purposes and numerical analysis of metals, a volume of 0.1 mm^3 is recommended [112].

With a similar idea, characteristic length parameter (ℓ^*) is defined to make ductile fracture modeling feasible. The ductile fracture behavior of materials is significantly affected by the characteristic microstructural length, which may be related to the average voids spacing [113]. To quantify ductile fracture initiation as a global behavior and release from single point behavior, a length-scale parameter needs to be defined to collect multiple single-material point failures [71]. Thus, a characteristic length parameter (ℓ^*) is specified. In fact, the occurrence of the ductile fracture is triggered once the fracture criterion exceeds the critical value over the characteristic length. The choice and determination of this length scale are based on microstructural measurements (based on fractography) as well as finite element analyses [71]. This parameter was reported from 0.1 to 0.4 mm for structural steel [90, 110].

3. Methodology

3.1 Overall methodology

Figure 3.1 illustrates the final failure assessment framework proposed in this thesis, which consists of experimental and numerical techniques to predict the failure of steel components under the coupled effect of excessive plastic deformations and pitting corrosion.
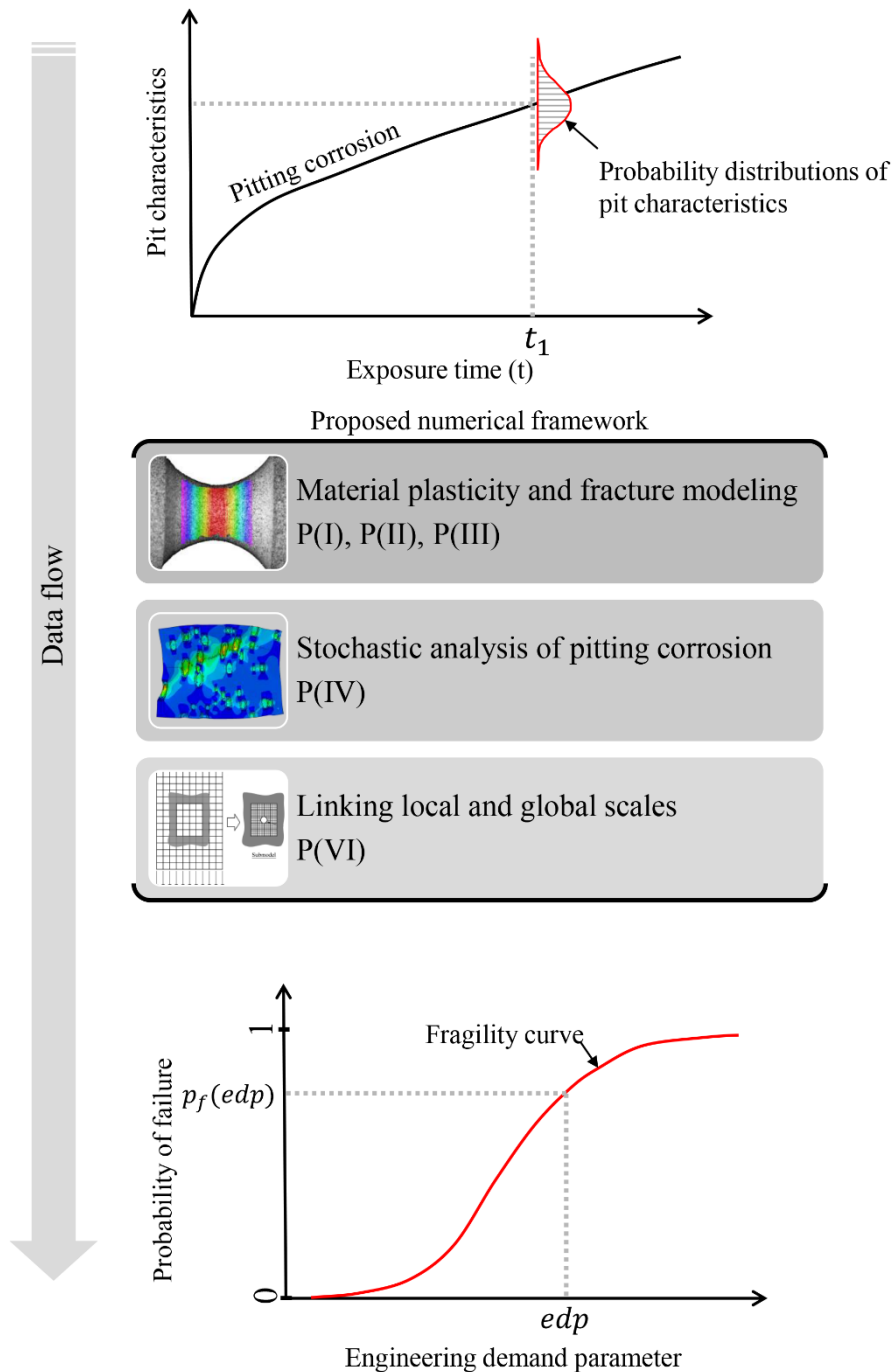
Figure 3.1. Outline of the investigation methodology.

37

Based on this figure, the input of the framework is a long-term evolution rule of pitting corrosion associated with the probability distributions of the corrosion characteristics, e.g., pit depth and aspect ratio. By giving this input data, the numerical framework is supposed to produce fracture-based fragility curves as the final result, which provides the probability of failure of a component with respect to a determined demand parameter, e.g., axial elongation.

Therefore, the proposed framework is responsible for linking inputs and outputs by performing stochastic numerical analyses in which the material fracture and ductile failure of the components are predicted by finite element techniques while considering the stochastic implementation of the pitting morphology. It is again worth mentioning that experimental studies are almost uninformative on this topic, and numerical studies play a prominent role in scrutinizing the effect of random pitting corrosion and predicting possible failure scenarios.

Based on this overview, the employed numerical framework requires a stochastic pit implementation technique to apply random morphologies on steel components at a reasonable computational cost to take advantage of the computational ability and determine the stress and strain fields at the corroded domains.

The framework also needs adequate and accurate constitutive and fracture models of mild steel to predict the ductile fracture initiation and possibly propagation in the studied components. Furthermore, this material modeling must be applicable to all involved materials, i.e., base metal, weld and HAZ. Finally, the numerical framework must be extendable to larger components such as steel joints with complicated geometries. Each of these three main features was studied through different publications, which are appended to this thesis.

For this purpose, to predict the ductile fracture of mild steel, an alternative calibration approach for the ductile fracture criterion based on techniques, was proposed. This calibrated material model was employed to develop a stochastic modeling technique of pitting corrosion and introduce the idea of fracture-based fragility curves. Finally, to extend the numerical models to large-scale applications, the challenges and solutions regarding evaluating the failure in practical steel components with complicated geometries were addressed by linking large and local scales.

3.2 The material model calibration approach

Due to numerous involved factors (e.g., pit locations and characteristics, the interaction between pits, etc.), the ductile fracture initiation locus is unknown

under random pitting corrosion. Therefore, a micromechanics-based fracture criterion is necessary to assess the structural integrity under these conditions. In contrast to traditional fracture mechanics that rely on a predefined crack or defect, micromechanics-based models can be used without such an assumption about the fracture locus.

As presented in Chapter 2, the void growth model (VGM) as a micromechanics-based model possesses unique features that make it interesting for structural applications. However, the model still requires the development of a reliable and advanced calibration procedure.

As a common approach, uniaxial tensile tests are used for the calibration of the constitutive model and notched tensile specimens are used for the calibration of the VGM parameter (i.e., $VGI_{critical}$). However, using standard uniaxial specimens is not practical when the constitutive model of a weld or HAZ metal in a perpendicular direction to the weld line is intended due to the finite length of the material.

In addition, the common calibration process of the VGM relies on complementary finite element modeling. Therefore, the calibration accuracy substantially depends on the applied constitutive model and other numerical properties (e.g., mesh size, element type, etc.). In this connection, using standard uniaxial specimens for calibrating constitutive models can increase the potential of nonunique calibration due to the inhomogeneous stress state and its interaction with geometrical nonlinearity (necking) in large plastic strains [114]. It was demonstrated that different combinations of material parameters can produce the same goodness of fit between numerical and experimental force-displacement curves, while the local responses such as plastic strains can be varied up to 50% compared to the actual material strain [114]. Moreover, calibrating a pressure-independent constitutive model by uniaxial specimens and applying it for notched specimens with different stress triaxialities ignores the possible effect of hydrostatic pressure [96, 115-118]. In addition to these points, using the material model calibrated by the common approach to simulate notched specimens can add the error of natural variation in steel material properties and increase the uncertainties associated with testing and measuring facilities (testing and measuring must be done for both uniaxial and notched specimens).

Therefore, an alternative approach was proposed to increase the applicability of the VGM and also enhance the calibration accuracy of the model. In the proposed approach, both the constitutive model and the VGM are calibrated simultaneously

on notched specimens using digital image correlation full-field strain measurement. For this purpose, a two-segment exponential function was employed to simulate the hardening evolution rule, as depicted in Figure 3.2. Previous studies on similar hardening models (e.g., two-term Voce model [119] or extended Voce hardening) showed that using more segments for the hardening rule provides more flexibility in calibration and more accurate matching between experimental and numerical results [120-124]. As illustrated in Figure 3.2(c), these two segments of the hardening evolution function ($H(\bar{\varepsilon}_p)$) intersect each other at a point that is named the transitional strain ($\varepsilon_{(Trans)}$). This strain hardening evolution function can be written as follows:

$$H(\bar{\varepsilon}_p) = \begin{cases} k_1 e^{-n_1 \bar{\varepsilon}_p} & for \ \ \bar{\varepsilon}_p \leq \varepsilon_{(Trans)} \\ k_2 e^{-n_2 \bar{\varepsilon}_p} & for \ \ \bar{\varepsilon}_p \geq \varepsilon_{(Trans)} \end{cases} \tag{3.1}$$

where k_1 and n_1 and k_2 and n_2 are considered as material calibration parameters for the first and second segments, respectively. These parameters can be adjusted based on an iterative optimization process to find the best match between numerical and experimental force-displacement curves. In accordance with the form of the force-displacement curves for the smooth-notched specimens, the transitional strain ($\varepsilon_{(Trans)}$) was phenomenologically assumed to be equal to the strain corresponding to the cap point of the curves measured by DIC. This assumption is consistent with Zhang et al. [125]'s findings that the true strain at maximum load is independent of the notch geometry.

As shown in Figure 3.2(b), for smooth-notched round bar specimens there is only one strain value in the minimum section due to axisymmetric geometry. However, for double-edge-notched flat specimens, the strain will be distributed non-uniformly over the notch cross section. Thus, the strain measured by DIC must be averaged as the transitional strain (see Figure 3.2(b)).

Figure 3.3 illustrates the progressive iterative optimization process used to calibrate the material parameters for two segments of the hardening rule. First of all, the elastic modulus and yield stress of each specimen were estimated by assuming a simple elastic-perfectly plastic constitutive model. Then, as also shown in Figure 3.3(a), k_1 and n_1 were adjusted based on a simple shifting and reducing of initial boundaries in the space of the variables until the mean absolute percentage error (MAPE) becomes smaller than an acceptable error (e.g., 1%

matching error in this thesis). MAPE is calculated based on the force-displacement curves that resulted from the test and FEM as follows:

$$MAPE = \frac{1}{N} \sum_{i=1}^{N} \left| \frac{F_{test} - F_{FEM}}{F_{test}} \right| \qquad (3.2)$$

where F_{test} and F_{FEM} are experimental and numerical forces for a given displacement point. N also denotes the number of displacement points where the curves are discretized for comparison, and it was assumed to be 25 points for each segment (50 points for the overall curve).

Once the iterations were converged to a solution for the first segment, the plastic flow curve was fixed for the first segment up to the transitional strain $(\varepsilon_{(Trans)})$. Then, the material parameters k_2 and n_2 were adjusted for the second segment using a similar approach, as described in Figure 3.3(b). Once the second segment was calibrated, the whole plastic flow curve was determined for the specimen, as shown in Figure 3.3(c).

Conversely, as illustrated in Figure 3.4, for the common approach, the constitutive model for uniaxial specimens can be obtained directly based on the test results up to the ultimate tensile strength point (before necking). For this purpose, the true uniaxial strain can be expressed as [13]:

$$\varepsilon^t = ln\,(1 + \varepsilon^e) \qquad (3.3)$$

In addition, by presuming the volume constancy and uniform distribution of strain along the gauge length, the true stress also can be calculated by [13]:

$$\sigma^t = \sigma^e(1 + \varepsilon^e) \qquad (3.4)$$

where σ^t and ε^t are true uniaxial stress and strain, respectively. σ^e and ε^e also refer to the engineering values of stress and strain.
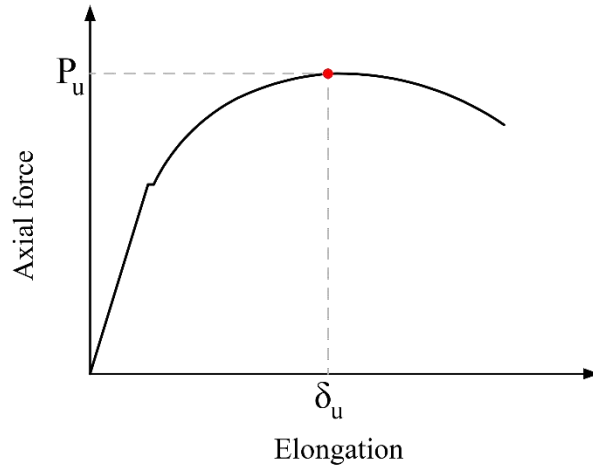
(a) Force-elongation curve
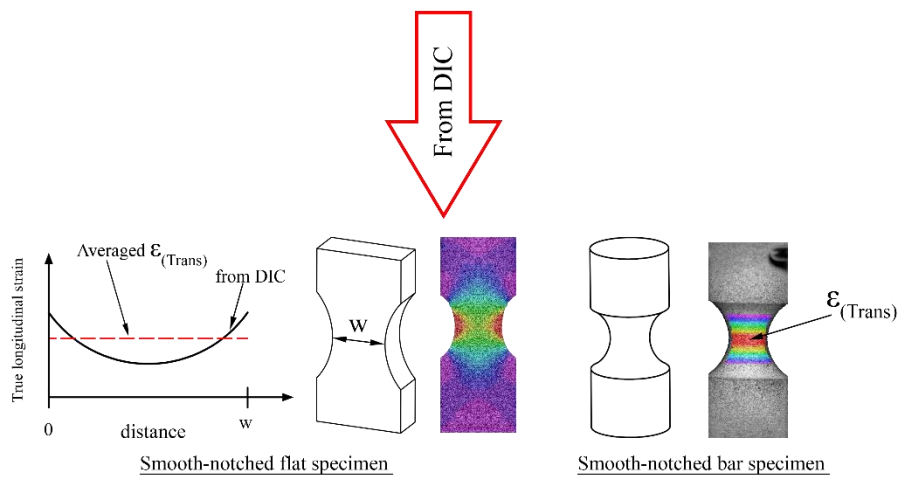
(b) Transitional strain at the ultimate point
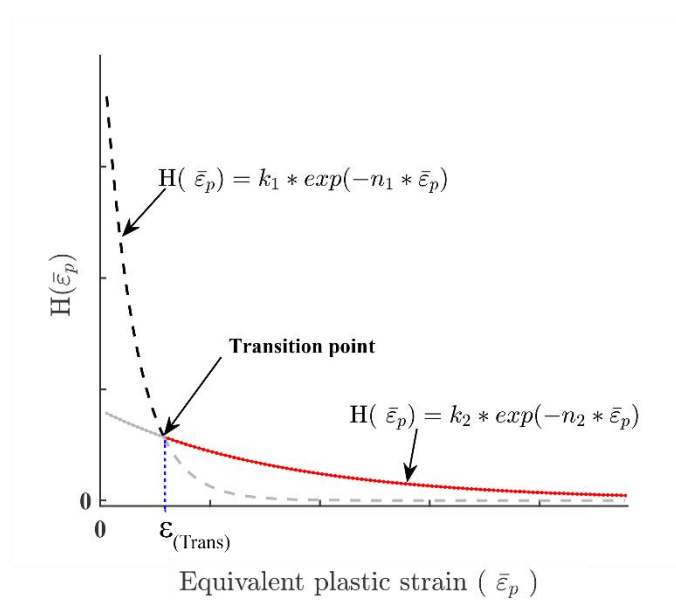
(c) Two-segment exponential strain hardening

Figure 3.2. An alternative approach for calibrating the constitutive model based on notched specimens proposed in P(III).
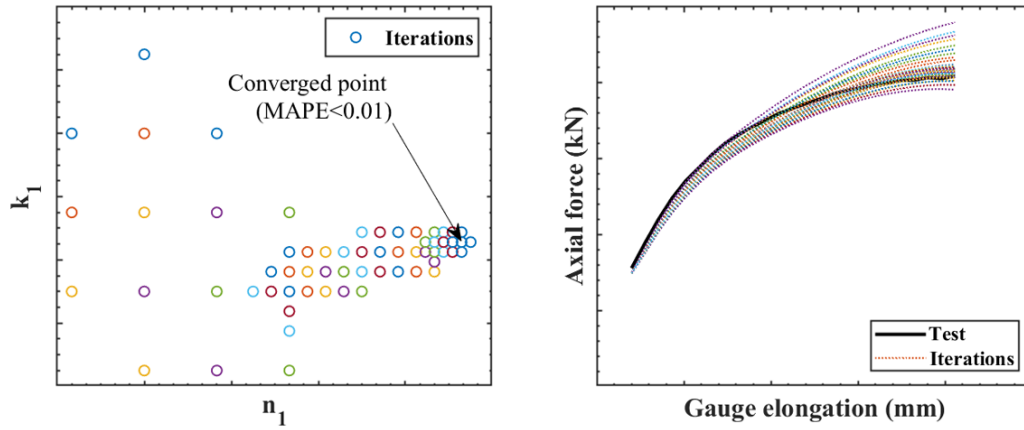
a) First segment fitting
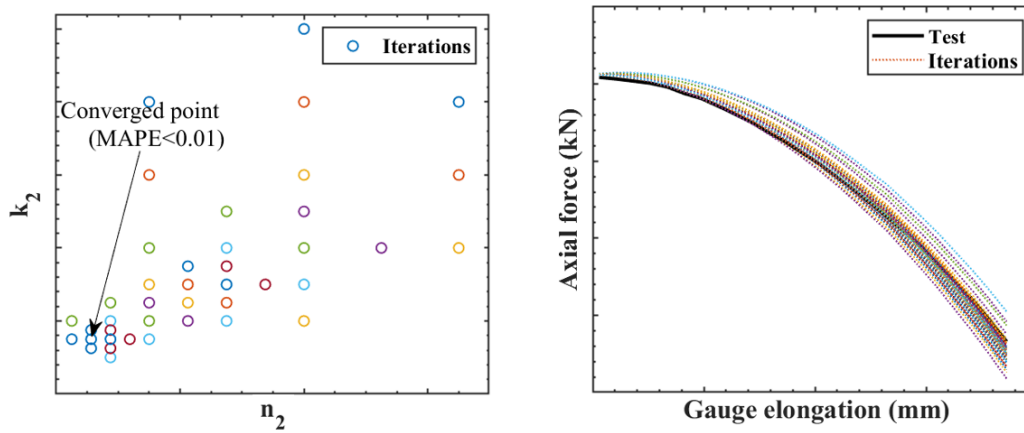
b) Second segment fitting
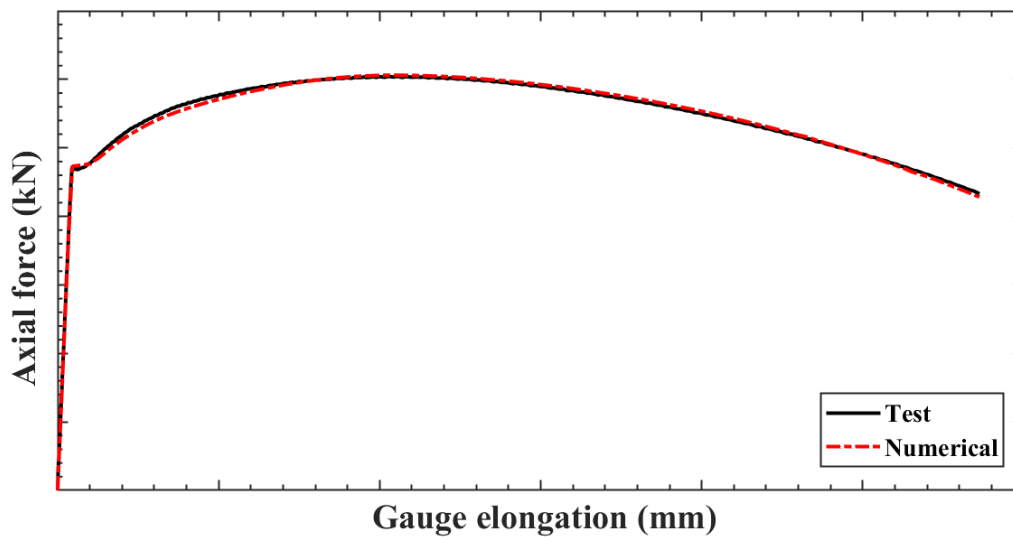
c) Overall fitted curve

Figure 3.3. The iterative optimization process used in the calibration of the two-segment hardening rule based on the mean absolute percentage error (MAPE) for notched specimens.
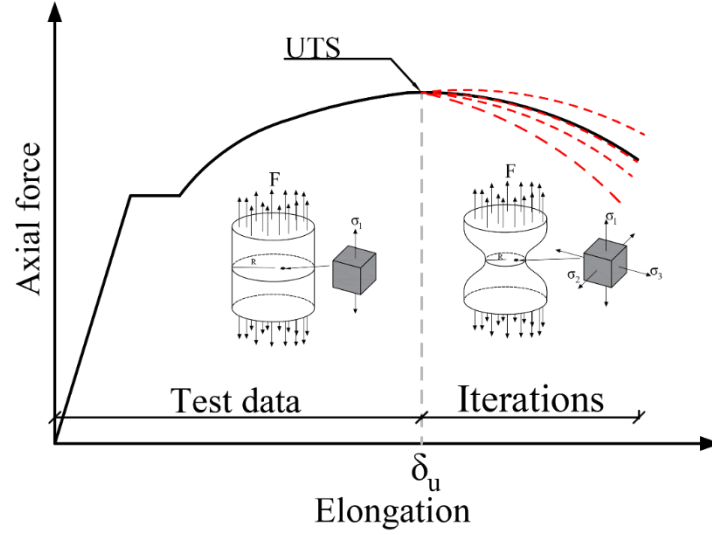
Figure 3.4. An illustration of the calibration process of a material constitutive model based on uniaxial specimens.

However, these assumptions are not valid for the post-necking region. Therefore, the hardening rule must be calibrated for the post-necking region by a similar iterative optimization process used for notched specimens, as illustrated in Figure 3.4. The hardening rule for the post-necking region can be written as an exponential function with two parameters as follows:

$$H(\bar{\varepsilon}_p) = k_0 e^{-n_0 \bar{\varepsilon}_p} \tag{3.5}$$

where calibration parameters k_0 and n_0 are selected in the calibration process. It is worth mentioning that this exponential form of hardening evolution, which has been proposed by Voce [119], can provide a better fit for materials when the stress reaches a saturation stress at large strains [126, 127] and when compared to unsaturated models like Hollomon's power law [128].

Because of the extensive iterative optimization process used in the calibration of the constitutive model, the computational effort could be considered the most challenging issue. Therefore, a solution established on an adaptive meshing technique [129] was employed to reduce the mesh sensitivity in numerical models and utilize a larger mesh size to reduce the computational time of the calibration process.

The mesh size is more important when an explicit solver is employed in which the stable time increment is directly connected to the minimum size of the elements. This adaptive technique combines the features of pure Lagrangian and Eulerian analyses [129]. For this purpose, over a specified time interval, it creates a new mesh and remaps the solution variables from the old mesh to the new mesh with

44

an advection process to maintain the quality of the mesh and avoid a large element distortion in the necked area, as depicted in Figure 3.5.

(a)   *(b)*   *(c)*
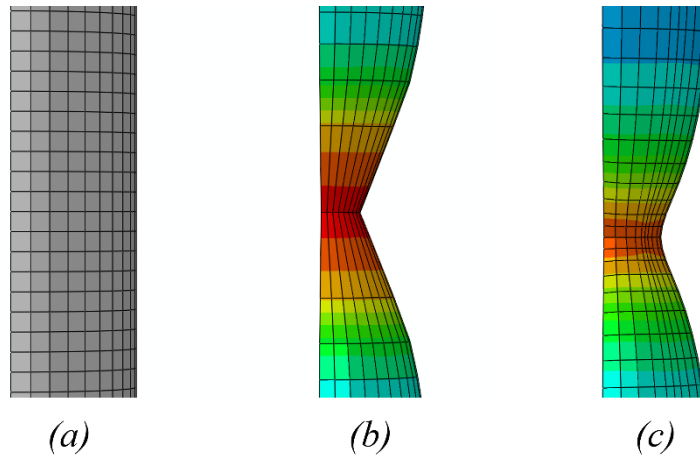
Figure 3.5. Mesh quality and element distortion of standard uniaxial round bar specimens in the neck area: a) undeformed mesh, b) deformed mesh without adaptive meshing technique and c) deformed mesh with adaptive meshing technique (for 0.5 mm of initial mesh size).

3.2.1 Material study

The proposed failure assessment framework was validated through numerical and experimental case studies that were presented in the appended papers. All these studies concentrated on the S355J2 steel grade, which is known as a variant of S355 that absorbs a minimum of 27J of energy at low temperatures (-20°C) based on the V-notch impact tests (Charpy impact test). This grade is one of the most-used steel grades for industrial and offshore applications. Table 3.1 presents the chemical composition and basic mechanical properties of S355J2 based on EN 10025–2:2004 [16]. This table provides the material properties only for thicknesses smaller than 40 mm that were used in this thesis. For other thicknesses, the reader can refer to [16].

Table 3.1. Chemical composition and basic mechanical properties of S355J2 [16].

Notation	C max. (%)	Mn max. (%)	Si max. (%)	P max. (%)	S max. (%)	Cu max. (%)	Minimum yield strength (MPa)	Tensile strength (MPa)	Minimum fracture elongation* (%)	Notch impact test	
				Nominal thickness						Temperature Min. (°C)	Absorbed energy (J)
S355J2	t≤40			All thicknesses			t≤16	16<t ≤40	3< t ≤100	3< t ≤40	-20	27
	0.20	1.60	0.55	0.030	0.030	0.55	355	345	470–630	22		
* Elongation is measured based on a gauge length equal to 5.65 times the square root of the gauge area ($5.65\sqrt{s_0}$).												

To demonstrate the applicability of the proposed approach for calibration of the constitutive model and the VGM, the calibration was performed on two sets of material specimens in both the round and flat configurations. For this purpose, round bar specimens were taken from a 16 mm S355J2, while flat specimens were taken from an IPE 200 steel beam with the same material. All specimens were taken in the rolling direction.

In addition, the test setup and displacement rate were different for these two sets. For round bar specimens, the tests were carried out by a 30 kN machine (see Figure 3.6) with a 0.02 mm/s displacement rate, while for the flat specimens a 0.1 mm/s displacement rate was imposed by a 250 kN testing machine, as described in P(III). Figure 3.7 shows the uniaxial and notched specimens in the round configuration. Tables 3.2 and 3.3 also present the test matrix of uniaxial and notched round bar specimens, respectively. As these tables show, six uniaxial and nine smooth-notched tensile specimens with three different notch radius sizes (NR=12 mm, 6 mm and 3 mm) were tested. The same information can be found in P(III) for the flat configuration.
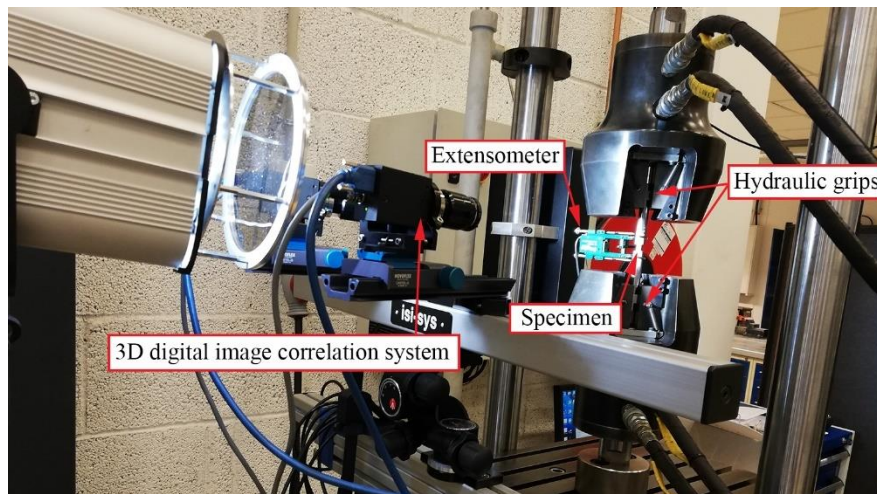
Figure 3.6. Test setup configuration for round bar specimens.

For numerical simulation of the tested specimens, one quarter of their geometry was modeled due to symmetry. C3D8R eight-node brick elements with a reduced integration point were used to discretize the geometry of the specimens. The only integration point of the C3D8R element is located at the middle of the element [31]. To calibrate the constitutive model, the uniform gauge length of the uniaxial specimens and the notches in the notched specimens were meshed with the 0.5 mm mesh size. In addition, an extra 0.2 mm mesh size was employed to investigate the mesh sensitivity of the models. The mesh configurations for these specimens are

presented in Figures 3.8 and 3.9. Once the models were used to calibrate the VGM, the mesh size in the notches was selected as 0.2 mm, which is comparable with the characteristic length (ℓ^*) of the mild steel [90, 110].

As described before, to ensure the mesh quality in the strain-localized places (necks in the uniaxial tensile specimens and notches in the notched specimens), mesh size was controlled and updated during the analyses by using the adaptive meshing technique.

When the calibration of the constitutive model and VGM criterion was carried out based on both the proposed and common approaches, their accuracy was validated by predicting the failure of four pull-plate tests with the configurations illustrated in Figure 3.10. More details of the numerical models employed to simulate ductile fracture initiation and propagation in the pull-plate tests are provided in P(III).

It is worth mentioning that to implement the VGM as a fracture criterion, USDFLD and VUSDFLD user subroutines were developed for Abaqus implicit and explicit solvers, respectively. These codes are appended to this thesis for further application.
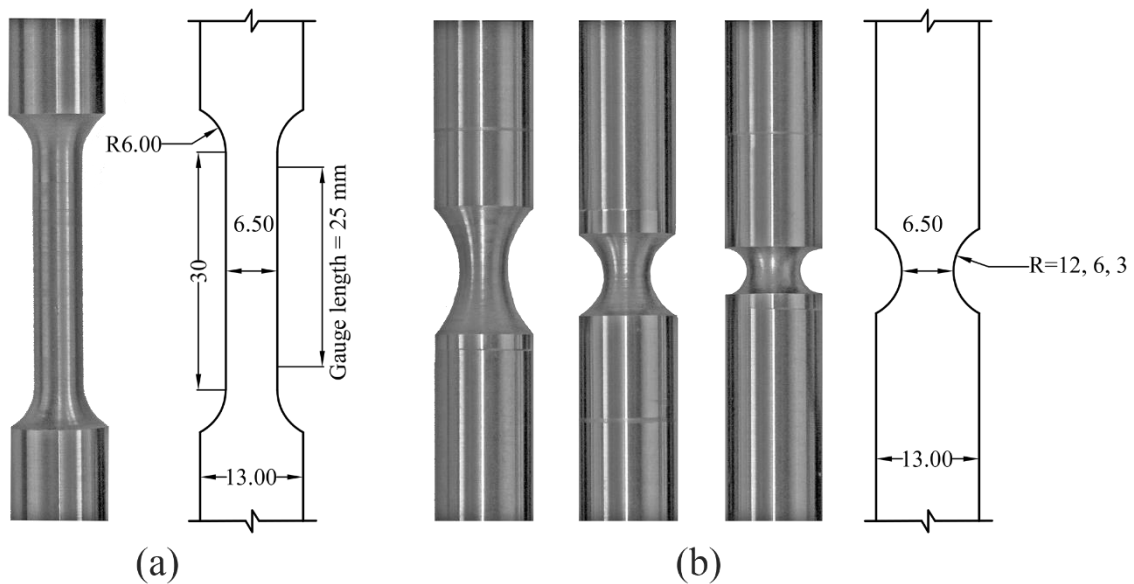
Figure 3.7. The geometry of round bar specimens taken from a 16 mm plate (S355J2): a) uniaxial tensile specimen and b) smooth-notched tensile specimens with 12 mm, 6 mm and 3 mm notch radius sizes (all dimensions are in mm and the total length of the specimens was 170 mm).
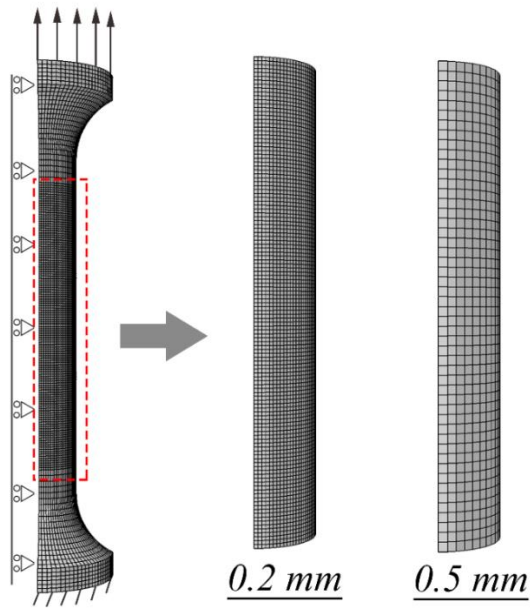
Figure 3.8. Mesh configurations used for uniaxial specimens' discretization with 0.2 mm and 0.5 mm element sizes.
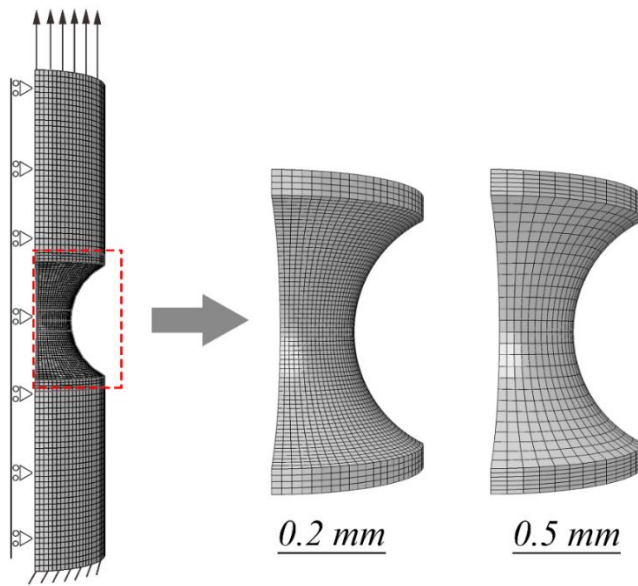
Figure 3.9. Mesh configurations used for smooth-notched specimens' discretization with 0.2 mm and 0.5 mm element sizes.

Table 3.2. Uniaxial round bar tensile specimens test matrix.

Specimen	Nominal diameter* (mm)	Gauge length (mm)	Elastic modulus (MPa)	Yield stress (MPa)	Ultimate true stress (MPa)	Ultimate true strain (mm/mm)
U1			213966	442.7	629.2	0.148
U2			187685	427.1	603.8	0.139
U3	6.5	25	210804	448.8	628.0	0.140
U4			202943	444.4	628.9	0.142
U5			198961	458.6	631.8	0.133
U6			201015	457.8	633.0	0.139
* The actual diameters were measured for each specimen individually.						

Table 3.3. Smooth-notched round bar tensile specimens test matrix.

Specimen	Nominal notch diameter* (mm)	Radius of notch (mm)	Gauge length (mm)
HR12(1)		12	
HR12(2)		12	
HR12(3)**		12	
HR6(1)		6	
HR6(2)	6.5	6	25
HR6(3)		6	
HR3(1)		3	
HR3(2)		3	
HR3(3)		3	
* The actual diameters were measured for each specimen individually. ** This test failed due to an incorrectly selected data logger channel.			
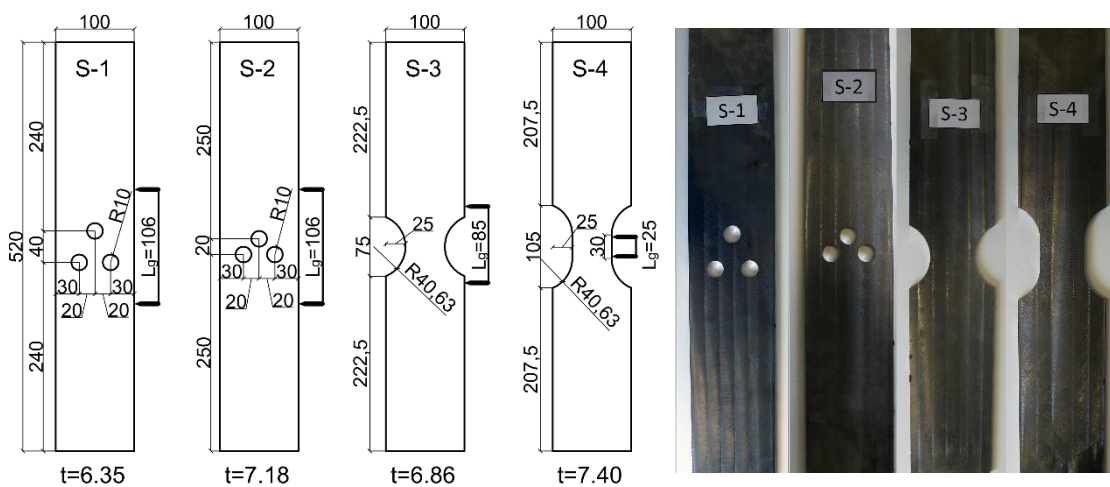
Figure 3.10. Configuration of the pull-plate test specimens tested and simulated by calibrated numerical models.

3.3 Stochastic analysis of pitting corrosion

When the integrity of steel structures is under assessment for future pitting corrosion, the stochastic and time-variant natures of corrosion in steel material must be addressed properly to assess the probability of failure. In P(IV), the concept of fracture-based fragility curves was developed at the component level to consider these random effects on the probability of failure for steel components.

Fracture-based fragility curves can be obtained by micromechanics-based modeling of different randomly generated pitting morphologies for a predefined intensity level of pitting corrosion. Pitting morphologies also can be created randomly based on the probability distributions of pit characteristics at a certain time of exposure. Figure 3.1 schematically presents a fracture-based fragility curve as the outcome of the stochastic analyses.

Based on the definition of fragility curves, the probability of failure for a determined engineering demand parameter (edp_1) can be written as follows:

$$F(edp_1) = P_f(EDP > edp_1 | IM = im_1)$$ (3.6)

where $F(edp_1)$ implies the probability of failure when engineering demand parameter (EDP) exceeds edp_1. EDP is selected as a structural response quantity that typically controls the failure or damage state of a component [130]. The right-hand term $P_f(EDP > edp_1 | IM = im_1)$ is a cumulative probability distribution function fitted on the failure results obtained from the stochastic analyses of the structural component that was subjected to a set of random pitting morphologies generated for a predefined level of intensity measure ($IM = im_1$) for a given time of exposure (t_1). The intensity measure parameter (IM) defines the severity of future corrosion based on the most influential parameters of pitting corrosion.

3.3.1 Intensity measure of corrosion

Intensity measure is defined as a parameter that indicates the severity of future corrosion in the assessment process. For uniform corrosion, the most important parameter that can specify the intensity of corrosion is the average diminished depth, while in pitting corrosion, using only one parameter cannot adequately address the intensity level of the corrosion.

One of the typical IMs is degree of pitting (DOP), which characterizes the surficial intensity of pits by determining the ratio of the corroded area (A_c) to the total area of the member (A_t) [28, 40, 46], as expressed in Eq. 1.1.

Figure 3.11 illustrates 5%, 10%, and 30% DOP in a rectangular plate. As this figure shows, larger $DOPs$ reduce the pit proximity and increase the likelihood of pit interactions.
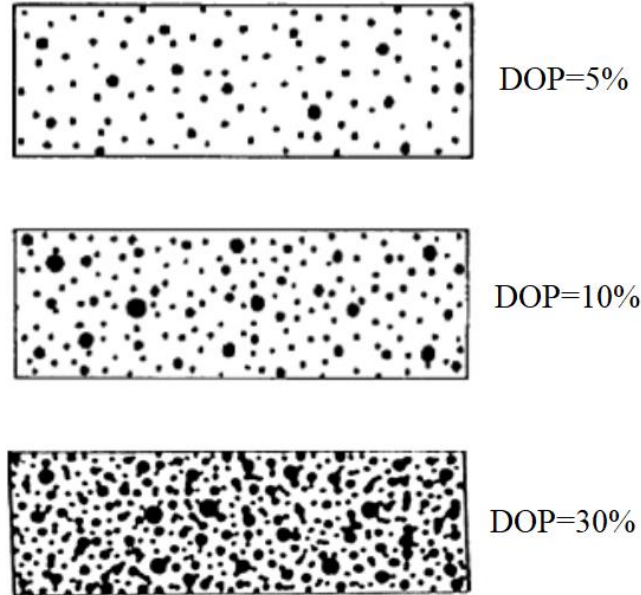
Figure 3.11. Illustration of three different DOPs (adapted from [35]).

In addition, the pit depth was shown as another influential parameter on the deformability of the tensile components [37, 57]. Therefore, in this study, an integrated intensity measure was used that consists of both DOP and average pitting depth (d_{avg}), which can be specified as $IM[DOP, d_{avg}]$. This definition is also consistent with the standard procedures [131, 132] proposed for the rating of pitting corrosion.

3.3.2 Engineering demand parameter

The selection of a proper EDP depends on the kind of load and the probable failure mode of the component [130]. For instance, when the fracture of a tensile member is under investigation, axial elongation controls the failure and can be considered as an EDP. However, for other types of components (e.g., steel joints under bending or a compressive member), the EDP must be selected accordingly. In these components, joint rotation and compressive load can be considered as structural responses that describe the component failure or damage state.

3.3.3 Random pit sampling

By assuming semi-ellipsoid as an acceptable geometry of pits, the characteristics of each pit can be generated through a Monte Carlo random sampling approach. In this approach, the location, depth and aspect ratio parameters of each pit are randomly generated based on their probability distributions. As illustrated in Figure 3.12, this random procedure was repeated for an assumed time of exposure (t_1) so that the intensity of the corrosion is $IM[DOP_{(t_1)}, d_{avg(t_1)}]$. In each iteration, a new pit is generated until the DOP reaches the target value (e.g., 10%).
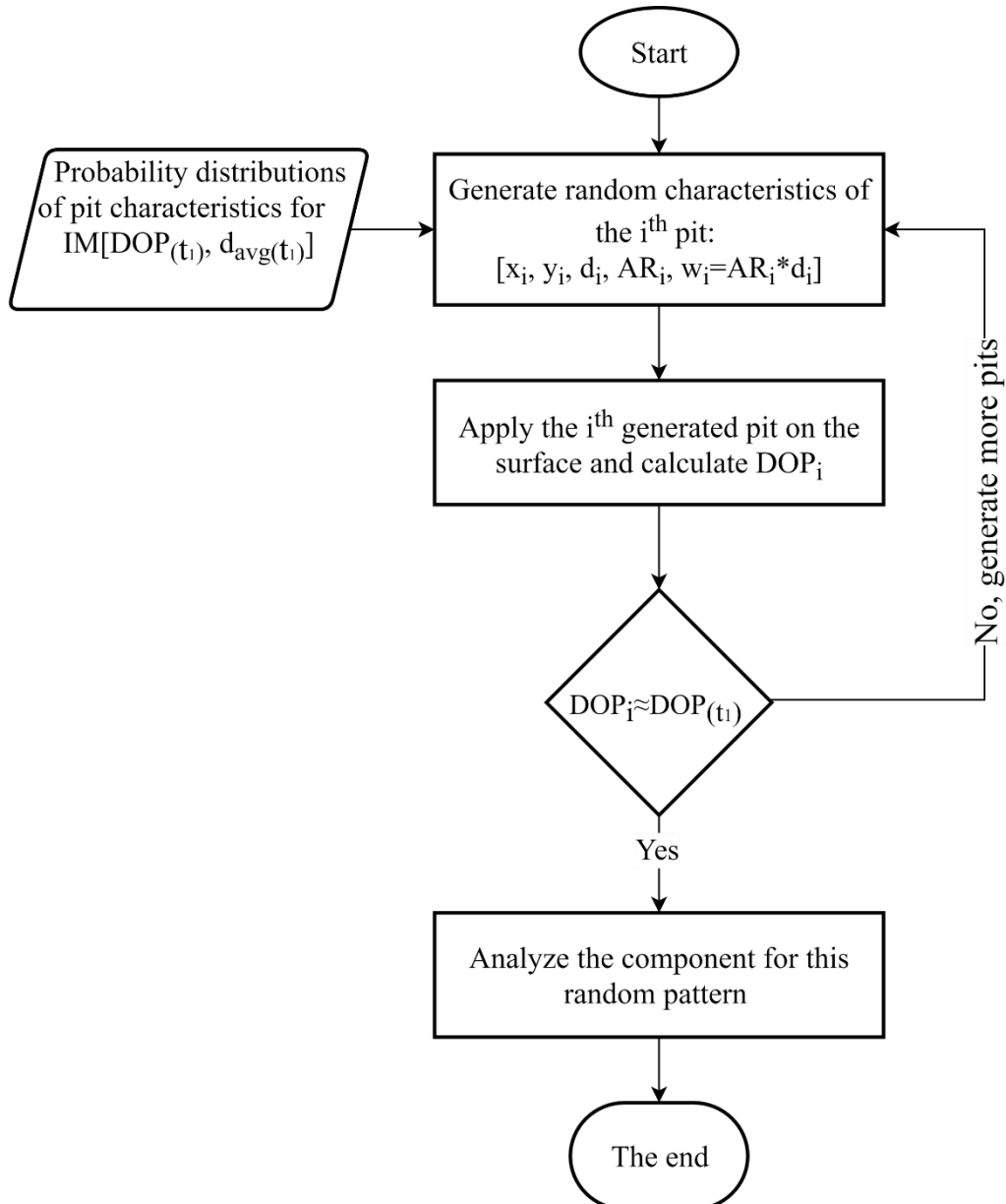
Figure 3.12. The algorithm of random pitting pattern generation for $IM[DOP_{(t_1)}, d_{avg(t_1)}]$.

3.3.4 Discretization of random pitting patterns

The meshing technique and proper type of elements to implement pitting corrosion depend on the type of failure. For steel members under compression loads where the main failure is a global or local buckling, shell elements are adequate [28, 133-135]. Then, the effect of random pitting geometry can be implemented by varying the thickness of the shell element in the location of the pits [28, 133-135]. Conversely, when the component is under tensile load, and the ductile fracture and material separation is the most dominant failure mode, using solid elements with fine mesh is necessary to predict the fracture initiation. In contrast to shell elements, solid elements can sufficiently capture the effect of triaxiality and model different interactional scenarios between pits.

Despite the accuracy of solid elements, implementing a random pattern of semi-ellipsoidal pits in the geometry of components is a demanding task. When the geometry is complicated and hexahedral elements are utilized, the standard meshers provided by numerical software solutions often need manual partitioning and seeding to generate a proper mesh quality. These manual meshing techniques are inefficient for implementing a random pitting morphology with many different random pits. In most cases, these meshing techniques can cause divergence or a poorly meshed geometry. This can prove quite problematic for this thesis in which multiple random patterns are under investigation. One alternative is to use tetrahedral elements that support fully automatic tetrahedral meshers [129]. However, for the same degree of freedom and amount of discretization layers through the thickness of a member, more tetrahedral elements are required for discretization compared to hexahedrons [56].

Moreover, the first-order tetrahedral elements are not accurate enough for structural calculations under large plastic deformations [129]. As a consequence, the second-order formulation must be chosen, which dramatically increases computational demand. In contrast, developed reduced integration hexahedral elements can significantly increase computational efficiency without considerably losing accuracy [129]. Therefore, various attempts have been made to implement random pitting corrosion with hexahedral elements [28, 53, 56]. However, these previously used techniques are mainly developed based on third-party software or code that might be inaccessible to the community. In addition, as mentioned in the previous chapter, these approaches lack some essential features that limit using them in a life-cycle assessment of structures under pitting corrosion.

Therefore, P(IV) proposes a carving technique to implement random pitting patterns into the numerical models. This meshing technique allows the implementation of a random pattern of pits with arbitrary morphology into the geometry of components by using solid hexahedral elements and removing elements from an intact mesh, as depicted in Figure 3.13.
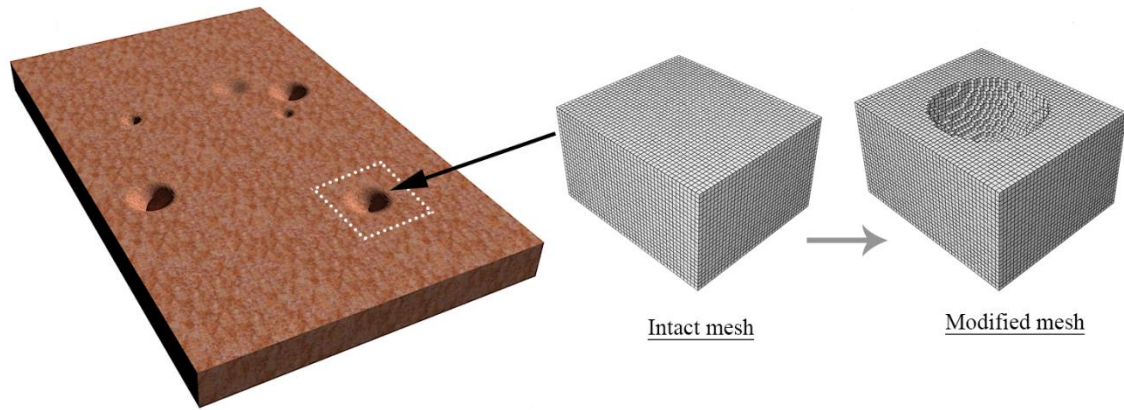
Figure 3.13. An illustration of the mesh carving technique used in P(IV) to implement pit geometry on the intact mesh.

For this purpose, the critical locations of the components were determined and discretized with eight-node brick elements with reduced integration (e.g., C3D8R in Abaqus). Then, the pits were implemented by removing nodes and associated elements located inside the pits that were generated randomly.

The proposed technique possesses some unique features when compared to conventional meshing techniques:

- It can reasonably simulate the three-dimensional local effect of pits.
- It is progressively updatable for new pits or intensified general corrosion so that the corrosion morphology can be modified without redoing all modeling steps.
- Because it is updatable, it can efficiently be coupled with real-time monitoring systems or periodic inspections and assess long-term structural integrity and safety based on life-cycle assessments, as illustrated in Figure 1.11, which was presented in the first chapter.
- The proposed numerical models are adjustable for sequential loads and corrosions.

For the micromechanics-based modeling of the ductile fracture, a fine mesh size comparable with the characteristic length (ℓ^*) of the mild steel is required to calculate the local response and the fractured state accurately [90, 110]. This mesh

refinement must be used over the most critical region of the component due to the unknown locus of the fracture initiation. By using such fine mesh, a stepwise representation of pits created by carving on the intact mesh can predict relatively similar local results compared to pits implemented by geometry. This was tested in P(IV) through a standard mesh sensitivity analysis for a single pit penetrating the component.

3.3.5 Study on single-sided corroded plate

The proposed stochastic numerical approach was employed to analyze steel components under pitting corrosion coupled with excessive plastic deformations. For this reason, a pull plate was selected as a single-sided corroded plate to develop the idea of the fracture-based fragility curves and predict the probability of failure. As Figure 3.14 indicates, the critical area of the specimen was 30 mm uniform length, which was studied for the predefined pitting corrosion intensity measures listed in Table 3.4.

Figure 3.14. The geometry of the intact tensile plate from S355J2 steel material (all dimensions are in mm and the thickness of the plate is 7.4 mm).

Table 3.4. Matrix of predefined levels of intensity measure of pitting corrosion $IM[DOP, d_{avg}]$.

		d_{avg}		
		1 mm	2 mm	3 mm
	5%	IM[5%, 1 mm]	IM[5%, 2 mm]	IM[5%, 3 mm]
DOP	10%	IM[10%, 1 mm]	IM[10%, 2 mm]	IM[10%, 3 mm]
	30%	IM[30%, 1 mm]	IM[30%, 2 mm]	IM[30%, 3 mm]

Random pit generation was executed based on the probability distributions of the pit characteristics adapted from the relevant literature. The position vector (x, y) of each pit center was generated based on uniform distribution [136], as illustrated in Figure 3.15. In this connection, overlapping of the pits was also allowed to implement the intersection of pits and create a larger area of wall thinning. Statistical analyses on naturally and artificially corroded structures showed that the pit depth and aspect ratio follow lognormal distribution [133, 136], as depicted in Figures 3.16(a) and 3.16(b). The average pit depth is a time-dependent parameter evaluated for a specific environment and expected exposure time. As listed in Table 3.4, three different average pit depths were assumed (d_{avg} =1, 2 and 3 mm). The logarithmic standard deviation of the depth of the pits ($\sigma_{\ln(d)}$) was observed from 0.1 to 0.5 without an apparent trend of change during the time of exposure [136]. Therefore, a 0.3 fixed logarithmic standard deviation of pit depth was considered for all average pit depths in this thesis. The *AR* is also time variant, so that during the time of exposure the pit shapes change from shallow-wide pits (*AR*=60) to deep-narrow pits (*AR*=5) [136]. Since the deepest pits are the most influential pits on ductile fracture [37, 39], a 5:1 width-to-depth ratio was assumed as the average aspect ratio (AR_{avg}) with a 0.6 logarithmic standard deviation ($\sigma_{\ln(AR)}$) [136]. It is worth mentioning that the logarithmic standard deviation of *AR* was also reported unchanged during the exposure time [136]. It is also important to emphasize that although the selected averages and standard deviations do not imply a specific real situation, they are reasonable values adopted to expand the methodology into an application. In an actual project, as mentioned before, the target level of pitting corrosion is defined and updated based on the corrosion evolution rule determined for a project, periodic inspections and an expected design life.

For each defined intensity measure, fifty random morphologies were generated based on the above-described probability distributions and applied on the intact mesh of the uniform length by using the carving method, as illustrated in Figure 3.17. All of the generated morphologies were analyzed to predict the failure of the pull plate under the tensile load and boundary conditions shown in Figure 3.17. For this purpose, the elongation in the uniform length was considered as an EDP, and the failure elongation was determined as an elongation in which the strength of the plate dropped sharply.
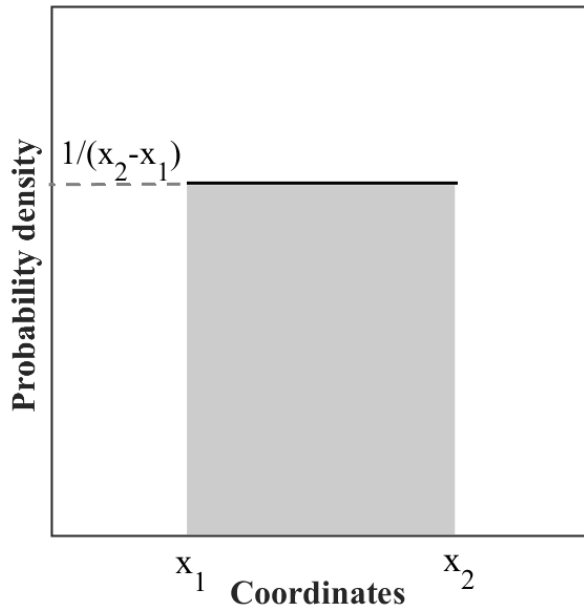
Figure 3.15. Uniform distribution to generate the location of random pit.

(a)

(b)
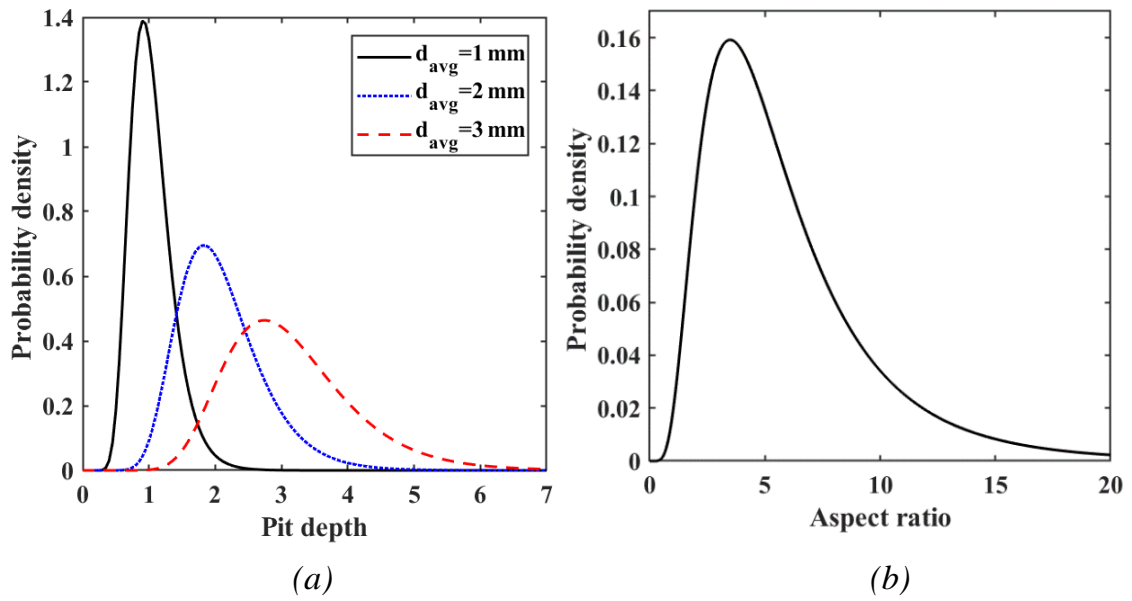
Figure 3.16. Lognormal distribution of pit characteristics: a) pit depth with different average values and b) pit aspect ratio.
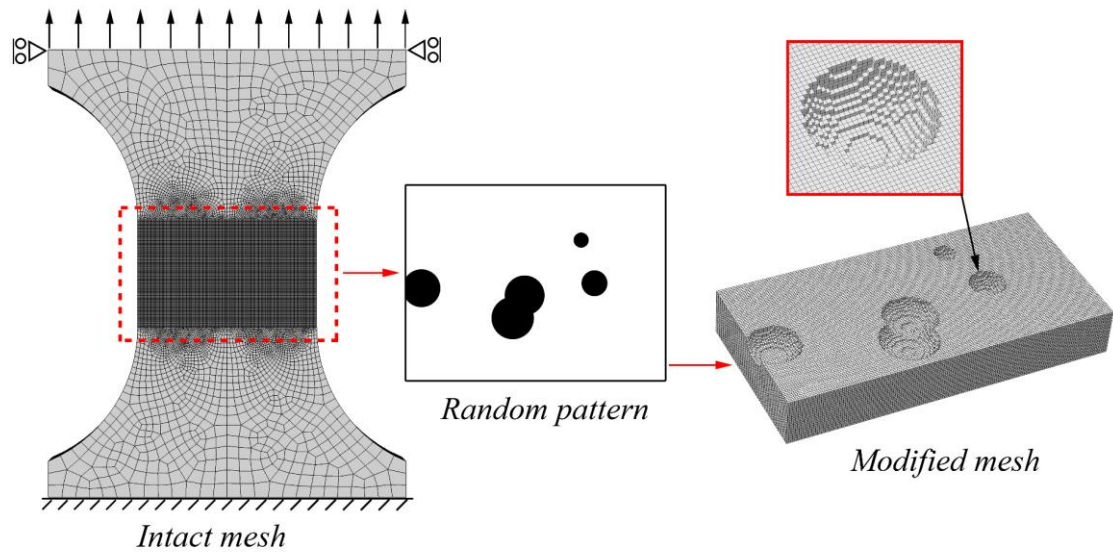
Figure 3.17. Implementation of random pitting morphology by carving on the intact mesh of the uniform length.

3.4 Linking local and global scales

Steel components used in structural systems typically have complicated geometries, especially around joints that are supposed to transfer applied loads to adjacent members. Different types of fasteners (e.g., welds or bolts) and various involved materials (e.g., base metal, bolts, welds, HAZ) intensify the complexity of these problems. In addition, a reduced cross-section area due to bolt holes or weld access holes, and additional stiffness of the adjacent members (constraints), concentrate most of the imposed plastic deformations in steel joints. This plastification typically has a complicated distribution, so that various locations in a steel joint are prone to experience excessive plastic deformations. Conversely, when pitting corrosion is under study in such geometries, micromechanics-based modeling of pitting corrosion in full-scale components is challenging in terms of meshing and computational effort, especially when different scenarios (e.g., various random patterns) must be studied. In this regard, using tetrahedral elements that support fully automatic tetrahedral meshers is computationally inefficient due to the reasons pointed out before. In addition, using refined mesh in a local pitting domain significantly increases the stable time increment for the whole model when an explicit solver is used.

In P(V), a two-level numerical modeling procedure was investigated to deal with complicated geometries and reduce the complexity of the problem. In this technique, as described in Figure 3.18, a nonlinear finite element analysis of the

58

components is performed at the global level without pit implementation. Then, based on the outcomes of this model and submodeling technique, critical regions of the global model were studied for fracture modeling and pit existence. Submodeling is a technique to analyze a local region with a more refined mesh based on the interpolation of the solution from a relatively coarse mesh in the global model [137-141].
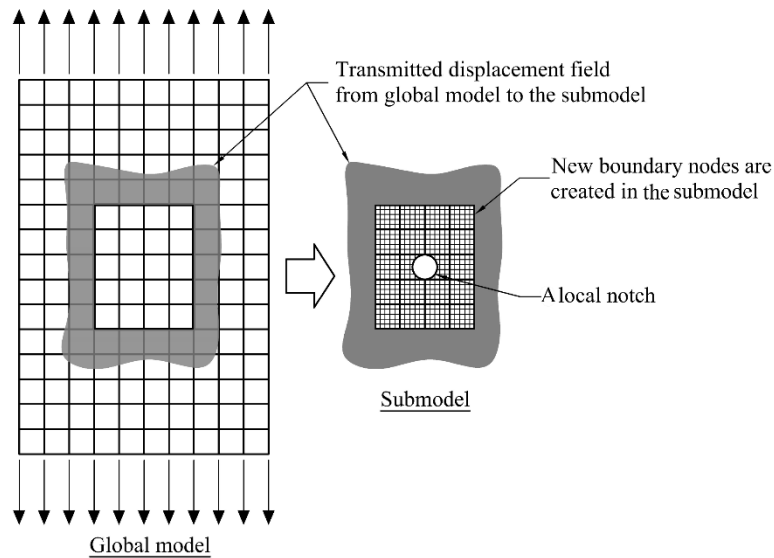
Figure 3.18. An illustration of two-level finite element modeling.

There are two common submodeling techniques. In the displacement-based method, nodal displacements are extracted from the global model and applied as boundary conditions of the submodels. The alternative method is stress-based submodeling in which stresses or tractions from the integration points are transmitted to the submodels as boundary conditions. The displacement-based submodeling method is preferred for large displacement problems because boundary conditions calculated using displacement can converge faster than the stress field [142]. In addition, Narvydas and Puodziuniene [139] demonstrated that displacement-based submodeling is less sensitive to the mesh density of the global model and can provide higher accuracy than the stress-based method.

In P(V), the limitation of this technique and different sources of numerical errors, including discretization and boundary condition errors, were discussed. Discretization errors are inherent in the determination of responses with the finite element method [143]. Since using a fine mesh in submodels is controlled by micromechanics-based modeling, the discretization errors in the submodels might be less critical. As a result, most of the discretization errors originated from the

59

global model and must be restricted to calculate boundary responses accurately for the submodels [141]. This error can be controlled by refining the mesh until further refinement causes no considerable variation in the nodal displacement output of the global model [141, 143].

It is worth mentioning that submodeling is a one-directional boundary condition, exchanging from the global model to the submodel with no feedback from the submodel to the global model [139, 144, 145]. The only link between the submodel and the global model is the transfer of the time-dependent values of the variables to the relevant boundary nodes of the submodel, as illustrated in Figure 3.18. Therefore, for displacement-based submodeling, it is essential to ensure that the stiffness of the submodel is the same as the corresponding region in the global model during the analysis [139]. However, in some cases, the stiffness can be different due to several reasons including mesh refinement, a material separation that is not modeled on the global scale and extensive degradation effects that change the stiffness of the studied area significantly. This change of stiffness must be treated before using the submodeling results or properly addressed in the global model.

As indicated in Figure 3.18, mesh refinement in the submodels also creates additional degrees of freedom at the boundaries that do not exist in the global model [142]. The global solution only provides displacements at the nodes of the original coarse mesh. Consequently, the displacement boundary conditions for new nodes in the submodels must be derived based on the shape function of the original elements in the global model [142]. This interpolation can induce error in the boundary condition of the submodels. However, for areas with a low nonlinear gradient in responses, this error is negligible. Therefore, the global mesh size adequacy must be checked for the proper transmission of displacements into the submodels. In order to evaluate the amount of these errors, the boundary responses of the submodels are compared to the corresponding region in the global model.

All of the above-mentioned errors can be limited by selecting a proper mesh density for global models and submodels through mesh sensitivity analyses.

In this connection, P(V) investigates the application of the two-level numerical modeling through a parametric numerical study performed on a typical welded steel beam-to-column joint with an isolated corrosion pit and under a column removal scenario. Fracture initiation in the joint was studied for different pitting scenarios, which varied in pit location, depth and aspect ratio. Then, the critical

pitting scenarios were identified by comparing the fracture initiation of the corroded joint with the intact joint (uncorroded).

3.5 Study of a full-scale steel joint

A real scale steel joint was numerically investigated for the effect of pitting corrosion under excessive plastic deformations. For this purpose, two-level micromechanics-based simulations were employed to link local and large scales to predict the fracture initiation of the joint. Figure 3.19 shows the joint sub-assemblage composed of two half-span beams and one column that moves vertically in the middle. This configuration has been widely used in different numerical and experimental studies [64] to simulate the effect of an interior column removal scenario. More structural details about the joint are presented in P(V).
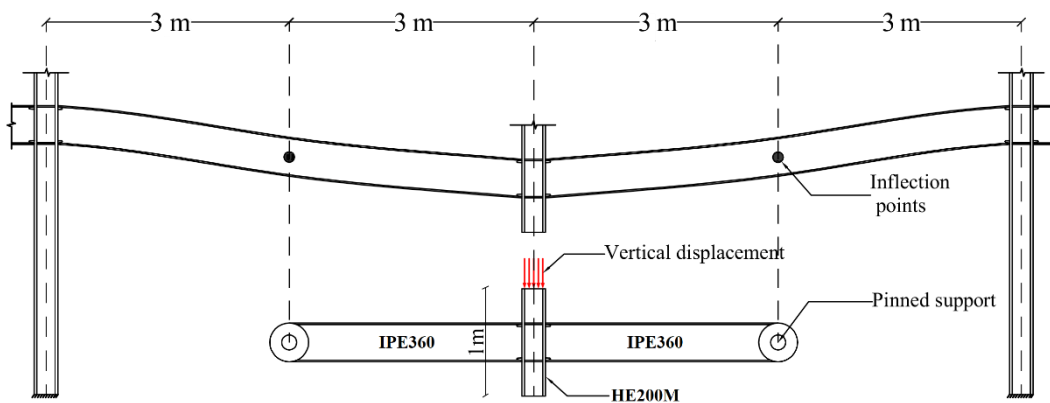
Figure 3.19. The configuration of joint sub-assemblage under a column removal scenario.

The joint was studied for different scenarios of a single pit that was penetrated in critical regions. The critical regions in the flange and the web of the beam were determined based on the equivalent plastic strain demand obtained from the FEA of the intact joint.

All studied pits were classified into three categories based on the pit location relative to the free edge of the web or flange plate. In the edge pit category, the pit cut the free edge of the plates, and it was assumed that the pit center coincided with the edge line. In the near-edge category, the pit penetrates close to the free edge of the plates, so that a ligament is formed between the pit and the edge. In this category, the effect of the edge ligament was studied for three different ligament lengths ($l_e = t/12, t/6$ and $t/4$), where t is the plate thickness. The rest of the pit

scenarios are in the far-edge category in which the pit is located far from the free edges of the plates.

All these pit categories were also examined for different geometrical parameters such as various depth and aspect ratios. Table 3.5 presents the pit characteristics matrix studied in P(V). These isolated pits were moved into critical areas according to the predefined grids shown in Figures 3.20 and 3.21. Based on the above-described pitting matrix, P(V) studied 582 pitting scenarios that differ in terms of location, depth and aspect ratio.

Table 3.5. Isolated pit characteristics matrix.

notation	pit depth (d)	location	pit aspect ratio (AR)	edge ligament length (l_e)
P1	$t/2$	far-edge	2	-
			1	-
			0.5	-
		near-edge	2	$t/12, t/6, t/4$
			1	$t/12, t/6, t/4$
			0.5	$t/12, t/6, t/4$
		edge	2	-
			1	-
			0.5	-
P2	$t/4$	far-edge	2	-
			1	-
			0.5	-
		near-edge	2	$t/12, t/6, t/4$
			1	$t/12, t/6, t/4$
			0.5	$t/12, t/6, t/4$
		edge	2	-
			1	-
			0.5	-
t is 12.7 mm for the flange plate and 8 mm for the web plate.				

(a) edge and far-edge pit   **(b) near-edge pit**
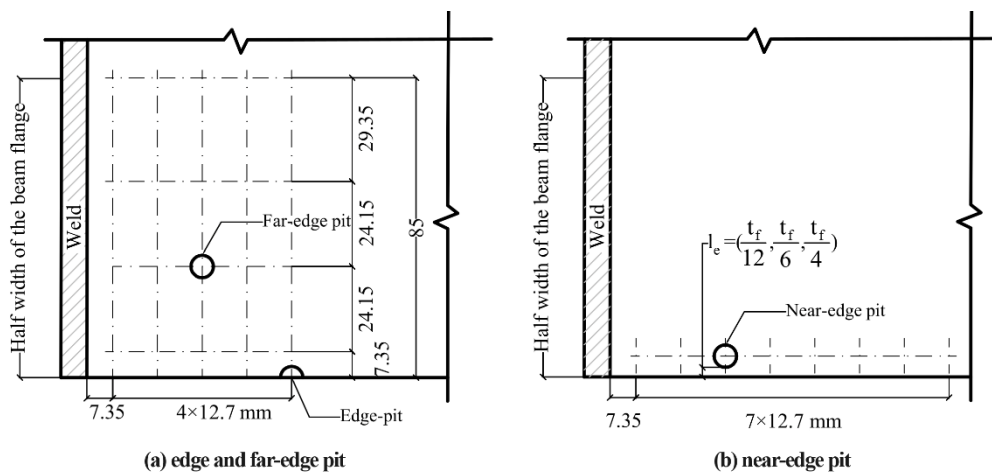
Figure 3.20. Pit location grid on the flange of the beam (all dimensions are in mm).
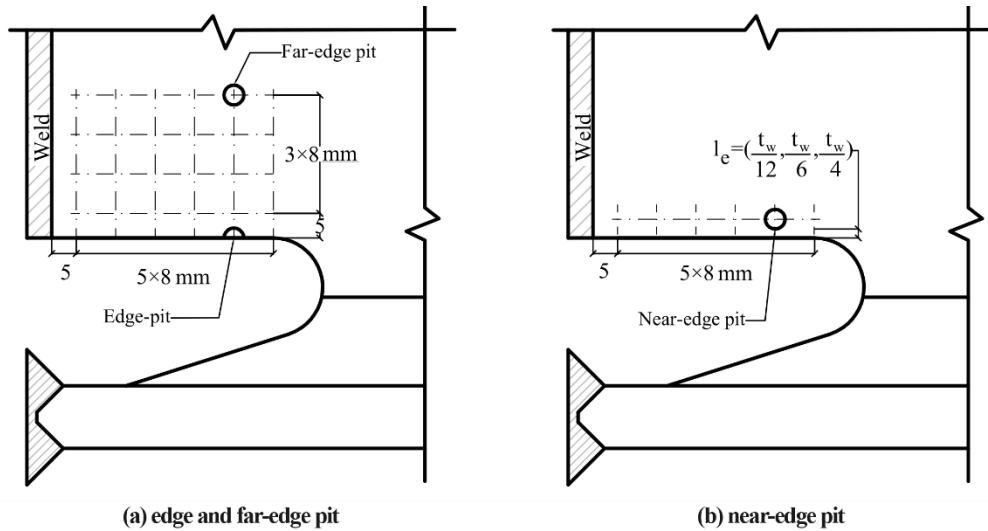
Figure 3.21. Pit location grid on the web of the beam (all dimensions are in mm).

To carry out the submodeling technique and assess the fracture initiation of each pit scenario, the numerical model of the joint was performed in global model and submodels, as described in Figure 3.22. The appropriate mesh size of the global model and submodels was selected based on sensitivity analyses, as presented in P(V). More detailed information about the numerical models and boundary conditions is provided in this paper.

Finally, to assess the degradation of the corroded joint, the joint vertical displacement corresponding to the fracture initiation of the intact submodel (uncorroded) was considered as the benchmark value. Then, the corroded submodels with different described pit scenarios were investigated up to this displacement. By doing so, if a corrosion pit could initiate fracture by a less vertical displacement of the joint, it was considered as a degrading factor in terms of ductile fracture initiation.
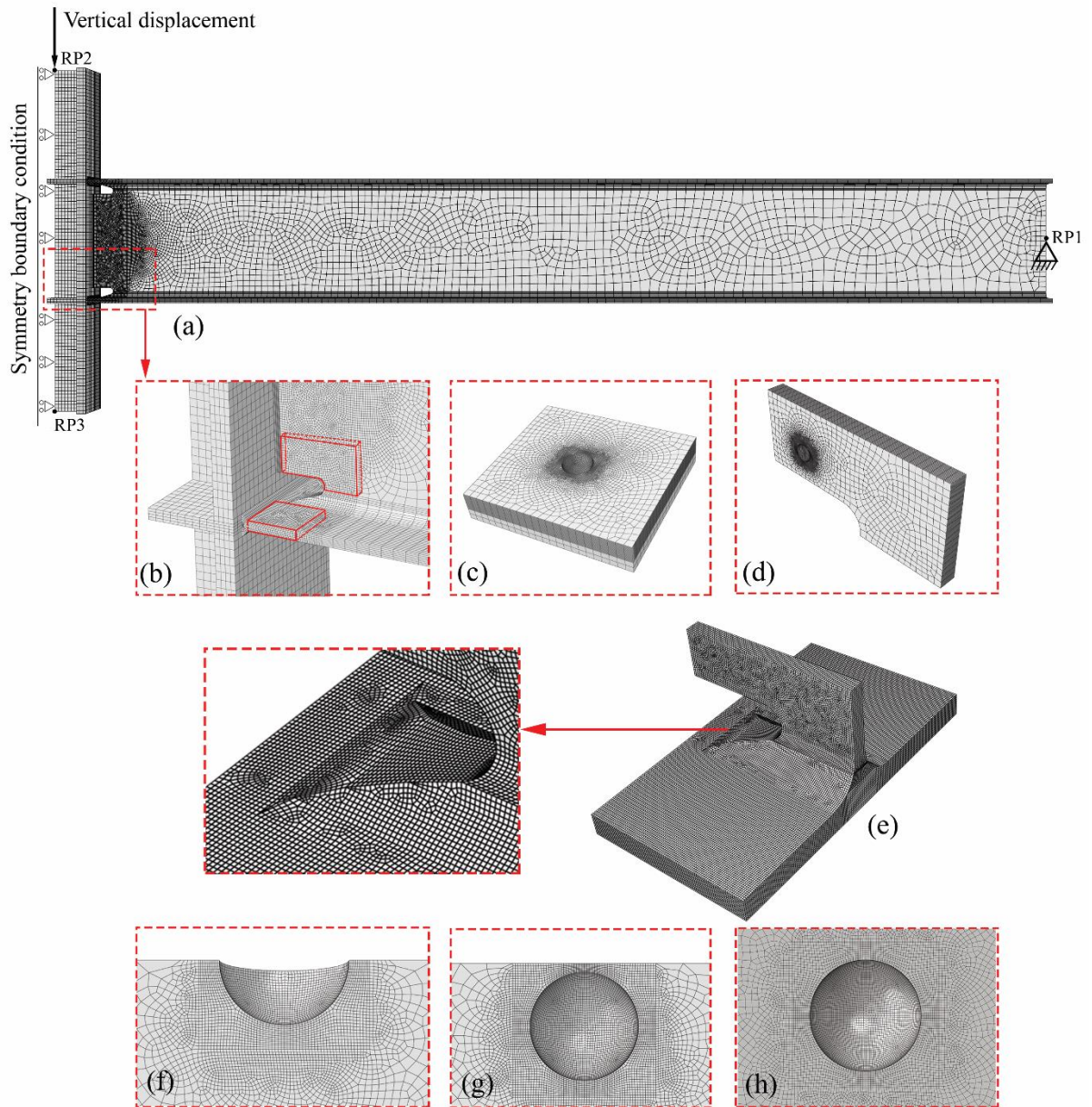
Figure 3.22. Finite element modeling details: a) a global model of the joint and applied boundary conditions, b) mesh refinement in the global model, c) a submodel from the beam flange, d) a submodel from the beam web, e) an intact submodel and mesh configuration, f) mesh configuration of an edge pit, g) mesh configuration of a near-edge pit and h) mesh configuration of a far-edge pit.

4. Results and discussion

4.1 Material calibration results

Since the proposed approach for the calibration of the steel material model relies on the DIC measurement, it is essential to ensure the DIC system is well calibrated and the measurements are accurate for the application. For this purpose, the engineering strain of uniaxial specimens measured by physical and virtual extensometers was compared for both test configurations (i.e., flat and round sets). Examples of this validation are shown in Figure 4.1 for U1 and U5 round bar specimens (see Table 3.2). As this figure indicates, the strains measured by DIC have overlapped the curves obtained from the physical extensometer up to the ultimate tensile point. After the ultimate point and necking, the result is dependent on the gauge length of the extensometers and the curves having diverged. Indeed, defining a virtual extensometer with equal length to a physical extensometer was impossible because of the holding arms of the physical extensometer. Therefore, in the DIC, virtual extensometers were defined with smaller gauge lengths, as expressed in Figure 4.1. Similar validation results can be found for flat specimens in P(III).
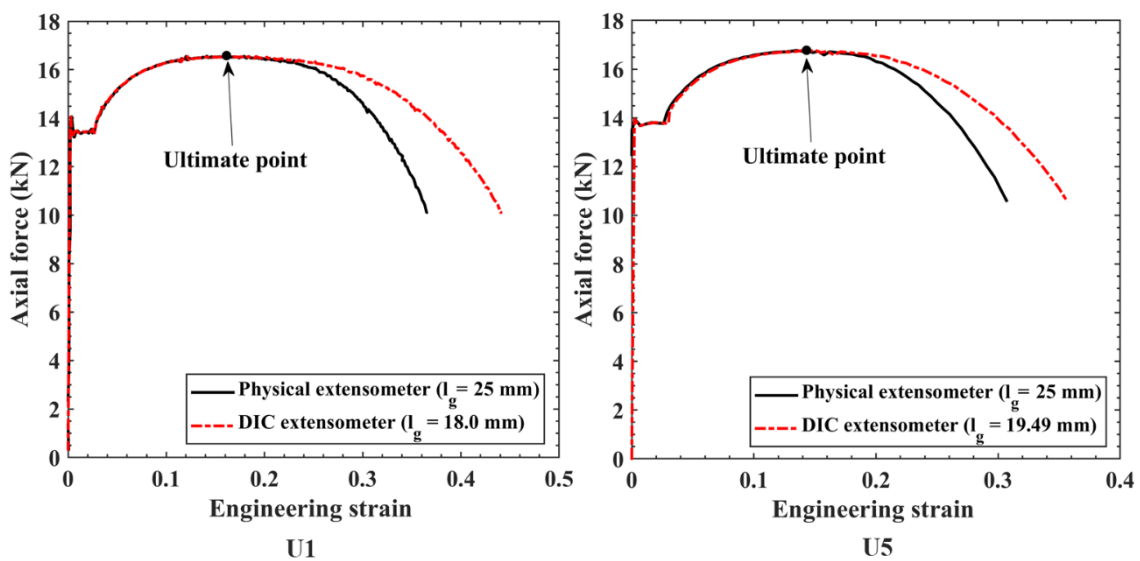
Figure 4.1. The DIC validation for round bar uniaxial specimens U1 and U5.

Figure 4.2 compares the numerical and experimental force-displacement curves of the six tested uniaxial round bar tensile specimens. Similar figures are presented in P(III) for the flat specimens.

These curves demonstrate that for selected steel grades (i.e., S355J2) the exponential post-necking hardening rule can simulate the force-displacement

65

response of the round and flat specimens accurately (MAPE<0.01). The calibrated values of k_0 and n_0 also are shown in this figure.

In addition, a comparison between the numerical curves obtained by the two different mesh sizes (0.5 mm and 0.2 mm) reveals that the force-displacement response of the specimens as a global response is almost nonsensitive to the mesh size. Thus, although using a 0.2 mm mesh size changed the MAPE values slightly, it remained smaller than the predefined accepted value (0.01) for almost all specimens. The same trend can be drawn for the local strain in the neck area. As Figures 4.3 and 4.4 indicate for round and flat uniaxial specimens, using a 0.2 mm mesh size instead of 0.5 mm made a very slight variation on the surface true longitudinal strain at the fracture displacement of the specimens. It can be concluded that a 0.5 mm mesh size along with the adaptive meshing technique can be utilized to reduce the computational time of the calibration process of the constitutive model without a considerable loss of accuracy. However, the obtained numerical fracture strains show large differences from the DIC strains.

As Figures 4.5 and 4.6 show the local strains obtained by DIC and FEM for uniaxial specimens, numerical models could provide an accurate prediction of surface true longitudinal strain at ultimate displacement with a 3.6%–3.7% error on average. In contrast, they predict surface true longitudinal strain at the fracture displacement with a 22%–26% error on average. In other words, despite a good agreement between the numerical and experimental force-displacement curves that show MAPE<0.01, the numerical models could not provide accurate local responses for the after-necking region of the tested uniaxial specimens. It is worth mentioning that true longitudinal strain is the total true plastic and elastic strain along the loading direction. These results confirm the study published by Cooke and Kanvinde [114] in which the non-uniqueness and loss of accuracy of the constitutive model calibration were demonstrated. However, the effect of this inaccuracy on the final fracture criterion calibration must be studied in terms of the fracture prediction of smooth-notched specimens as well as in the evaluation of component failure.
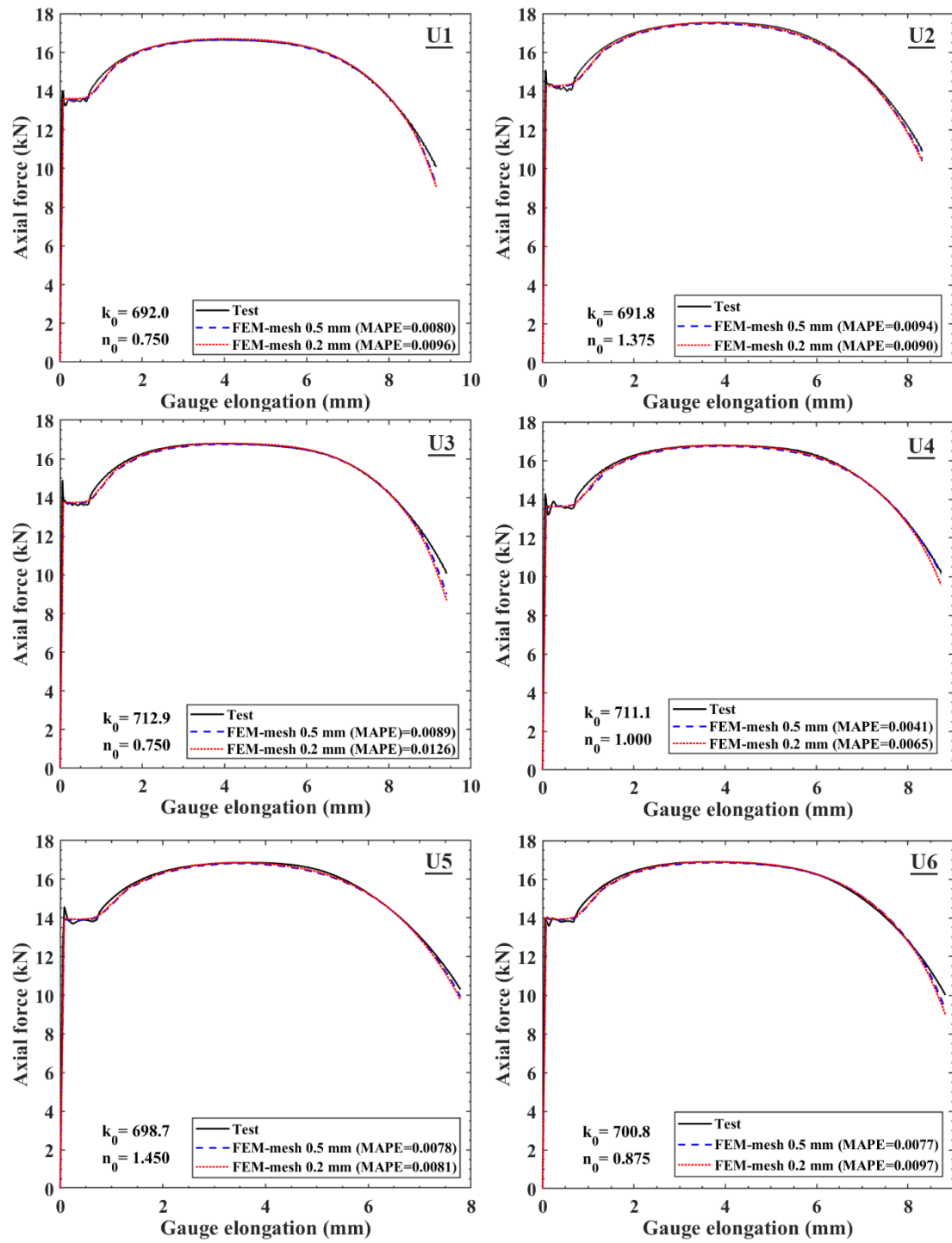
Figure 4.2. Numerical and experimental force-displacement curves for uniaxial round bar specimens.
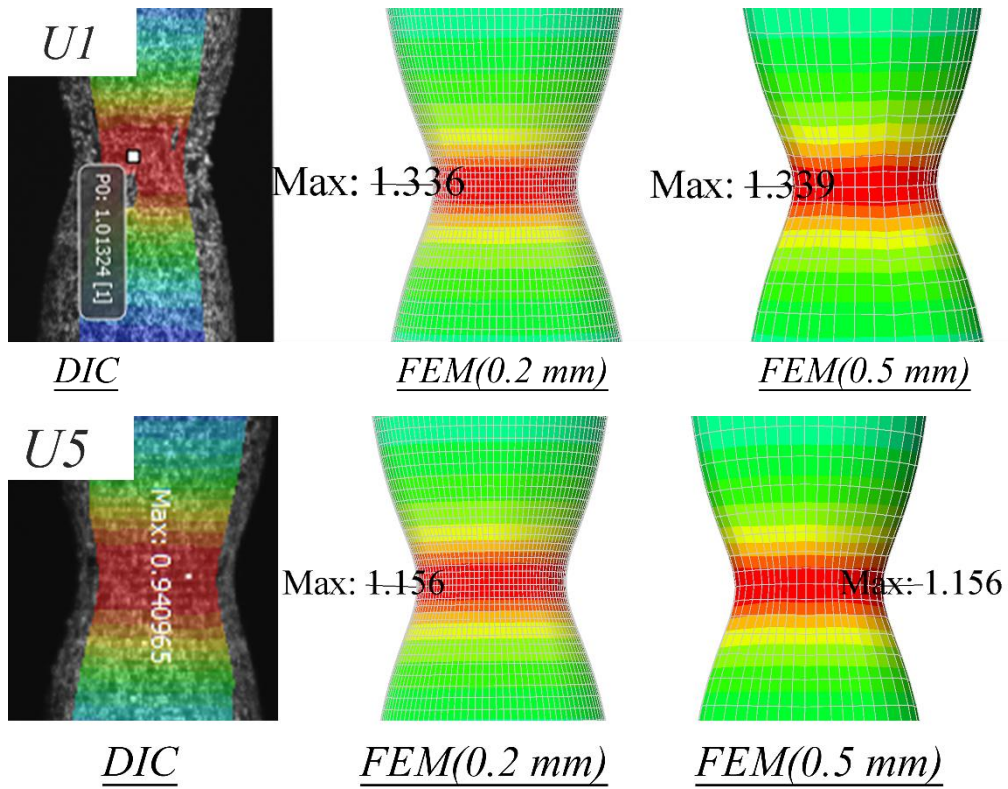
Figure 4.3. The DIC and numerical surface true longitudinal strain at the fracture displacement of uniaxial round bar specimens U1 and U5.
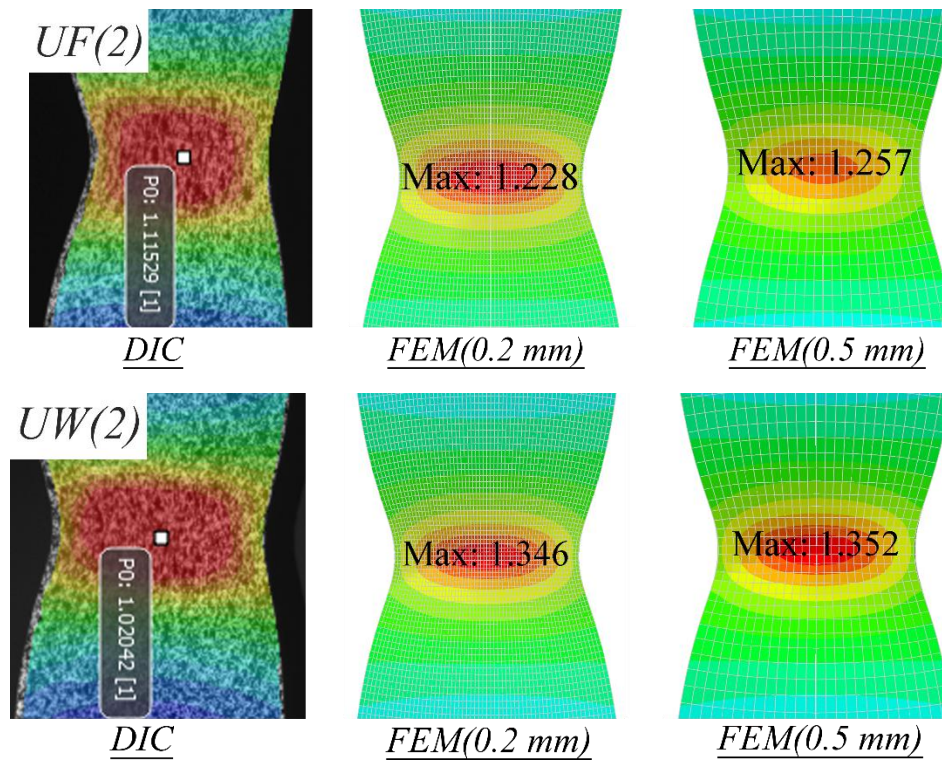
Figure 4.4. The DIC and numerical surface true longitudinal strain at the fracture displacement of uniaxial flat specimens UF(2) and UW(2).

Figure 4.5. The surface true longitudinal strain at the ultimate and fracture displacements of uniaxial round bar specimens.
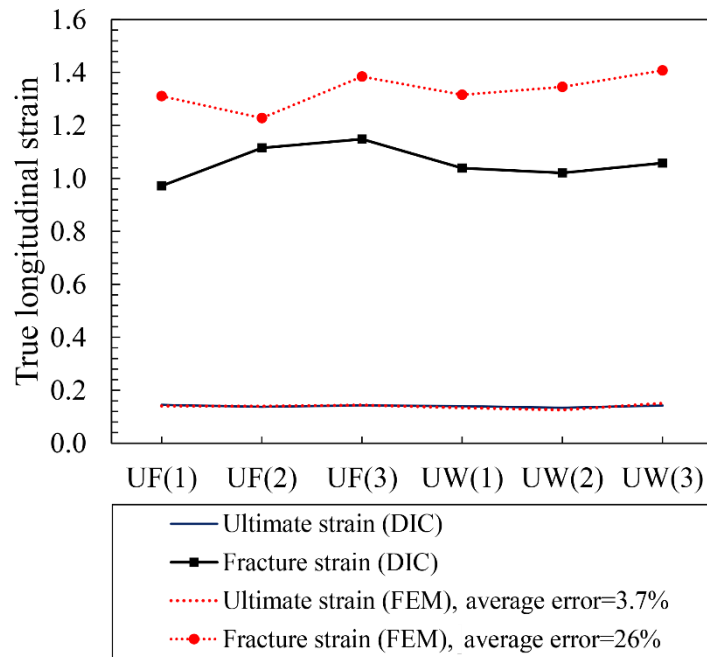
Figure 4.6. The surface true longitudinal strain at the ultimate and fracture displacements of uniaxial flat specimens.

For each notched specimen, the transitional strain ($\varepsilon_{(Trans)}$) was measured by the DIC for the cap point of the corresponding force-displacement curve, as reported in Table 4.1. Figure 4.7 shows the field of true longitudinal strain in the notch area of the tested round bar specimens corresponding to the cap and fracture displacements. This figure indicates that smaller notches exhibited lower fracture

strain due to higher triaxiality. The transitional strain was obtained for the flat specimens by averaging the strain profile at the minimum section of the specimens, as presented in P(III). In addition, for the flat specimens, a sensitivity analysis with respect to $\varepsilon_{(Trans)}$ was conducted; detailed results are provided in P(III). The results of the sensitivity analysis demonstrated that by a ±15% variation in $\varepsilon_{(Trans)}$, the MAPE was changed negligibly, and for almost all specimens, it remained under the maximum allowable value (0.01) defined in the calibration procedure.

Table 4.1. Calibration outputs of the proposed and common calibration approaches for round bar specimens.

Specimen	Hardening parameters (proposed approach)				$\varepsilon_{(Trans)}$ measured by DIC	Total MAPE		$VGI_{critical}$	
	k_1	n_1	k_2	n_2		Proposed approach	Common approach	Proposed approach	Common approach
HR12(1)	4250	14.375	803.5942	2.25	0.183344	0.0085	0.0345	3.38	2.51
HR12(2)	4000	14	823.034	2	0.154843	0.0036	0.0299	3.29	2.69
HR6(1)	4250	14.67188	808.0445	2.25	0.180815	0.0022	0.0318	3.23	2.64
HR6(2)	4250	14.71582	812.4246	2.125	0.165556	0.0048	0.0306	3.20	2.65
HR6(3)	4265.6	14.37598	800.6514	2	0.19751	0.0067	0.0289	3.19	2.76
HR3(1)	4000	14.25	819.1672	2	0.190948	0.0034	0.0323	3.15	2.77
HR3(2)	3750	14	802.593	2.25	0.161231	0.0066	0.0279	3.17	2.68
HR3(3)	3750	14	818.75	1.984375	0.186489	0.0081	0.0266	3.17	2.67
Mean (CV%)	4064.45 (5.5)	14.30 (2.04)	811.0 (1.06)	2.11 (5.98)	0.178 (8.59)	0.0054 (42.3)	0.0303 (8.4)	3.22 (2.3)	2.67 (3.0)

The calibrated parameters of the proposed hardening rule for the smooth-notched round bar specimens are listed in Table 4.1. Figure 4.8 also compares the numerical and experimental force-displacement curves for two-thirds of the smooth-notched round bar specimens as examples. As this figure shows, the numerical models in which the material hardening evolution was calibrated based on the proposed approach showed a close agreement with the experimental curves (0.0054 total MAPE on average). In contrast, although in the common approach the constitutive model was calibrated accurately to simulate the force displacement of the uniaxial specimens, the results for the notched specimens showed deviations from the experiments (0.0303 MAPE on average). Such deviations also can be seen between the experimental and numerical curves obtained by other researchers [3, 5].

As shown in Figure 4.9 for the notch local strain, the common and proposed approaches provided an almost similar fracture strain by a 3.2% and 5.1% error relative to the DIC, respectively. Similarly, for the flat notched specimens, the numerical models based on the common and proposed approaches could predict

DIC strains at the middle of the specimens by a 5.6% and 5.4% error, respectively (see Figure 4.10). As a result, the main difference between the two calibration approaches is evaluating the equivalent stress. Based on the obtained curves and also validation tests, the common method overestimated the equivalent stress in the post-necking region. Figure 4.11 compares the average plastic flow curves, which were calibrated based on two approaches for both flat and round test configurations.
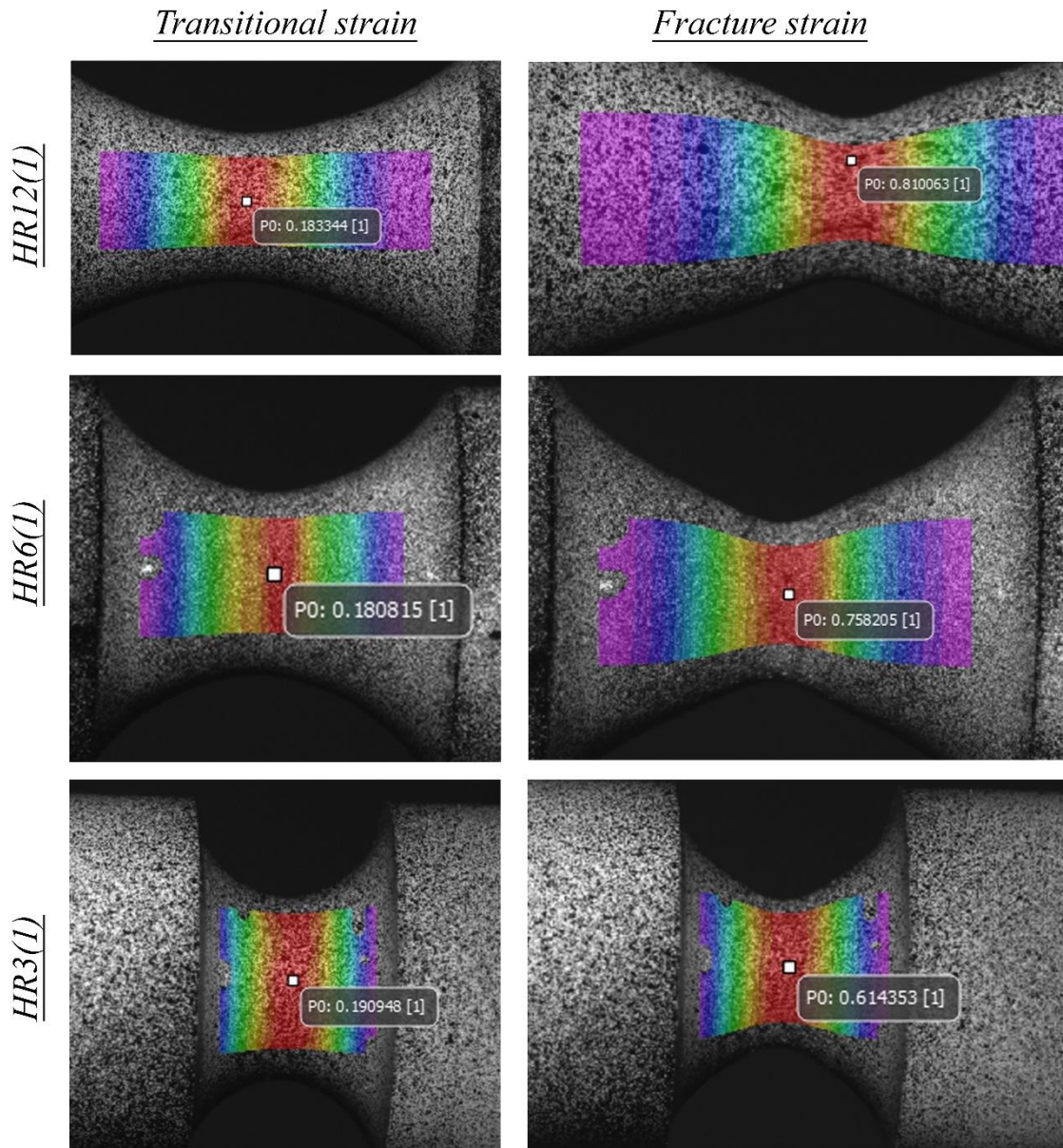
Figure 4.7. Transitional and fracture strains measured by DIC for three smooth-notched round bar specimens.

Once the constitutive model was calibrated by the two described approaches, the VGI for the material points of each notched specimen was calculated based on Eq.

71

2.8 by using the developed user subroutines. Table 4.1 lists the calibrated $VGI_{critical}$ for round bar specimens based on constitutive models that resulted from the proposed and common approaches. These values were the maximum VGI at the notch section in a displacement corresponding to the test fracture displacement (Δ_f). For all smooth-notched round bar and flat specimens, the maximum VGI occurred at the center of the specimen except for the double-edge-notched flat specimens with a 3 mm notch radius, which the fracture initiated at a point between the center and the notch root.

As Table 4.1 shows, the mean value of the $VGI_{critical}$ calibrated by the proposed approach for the round set is 3.22, which is about 21% more than the average $VGI_{critical}$ calibrated by the common approach (2.67). P(III) shows a more significant difference for the flat set, so that the $VGI_{critical}$ calibrated based on the proposed approach was about 48% more than the $VGI_{critical}$ obtained by the common approach. These results can be understood as the nonunique calibration of the VGM and demonstrate that the calibration of the VGM and the constitutive model are correlated. In other words, the $VGI_{critical}$ calibrated based on each approach must be used by the corresponding constitutive model to have an accurate prediction of the fracture.

When round bar configuration was used for the specimens, the common and proposed approaches provided almost the same coefficient of variation for the $VGI_{critical}$ (see Table 4.1). In contrast, for flat specimens that lack axisymmetric geometry, the $VGI_{critical}$ calibrated by the common approach exhibited about 18% dispersion, while the proposed approach led to an 8% coefficient of variation. These values demonstrate that the proposed calibration approach is more efficient in reducing calibration errors and uncertainties for the flat configuration rather than the round bar specimens, which provide almost the same statistical results with both approaches. This enhancement of the calibration accuracy was validated to predict the failure of four pull-plate specimens (see Figure 3.10). The detailed validation results are provided in P(III). The comparison between experimental and numerical force-displacement curves demonstrated that the proposed approach could better predict validation tests, particularly in terms of failure force.

Based on the results presented in P(III), the proposed calibration approach was considered as an alternative for the calibration of the VGM. This approach would be particularly useful in cases where the production of uniaxial tension specimens is difficult, e.g., to calibrate the material models of weld and heat-affected zone.
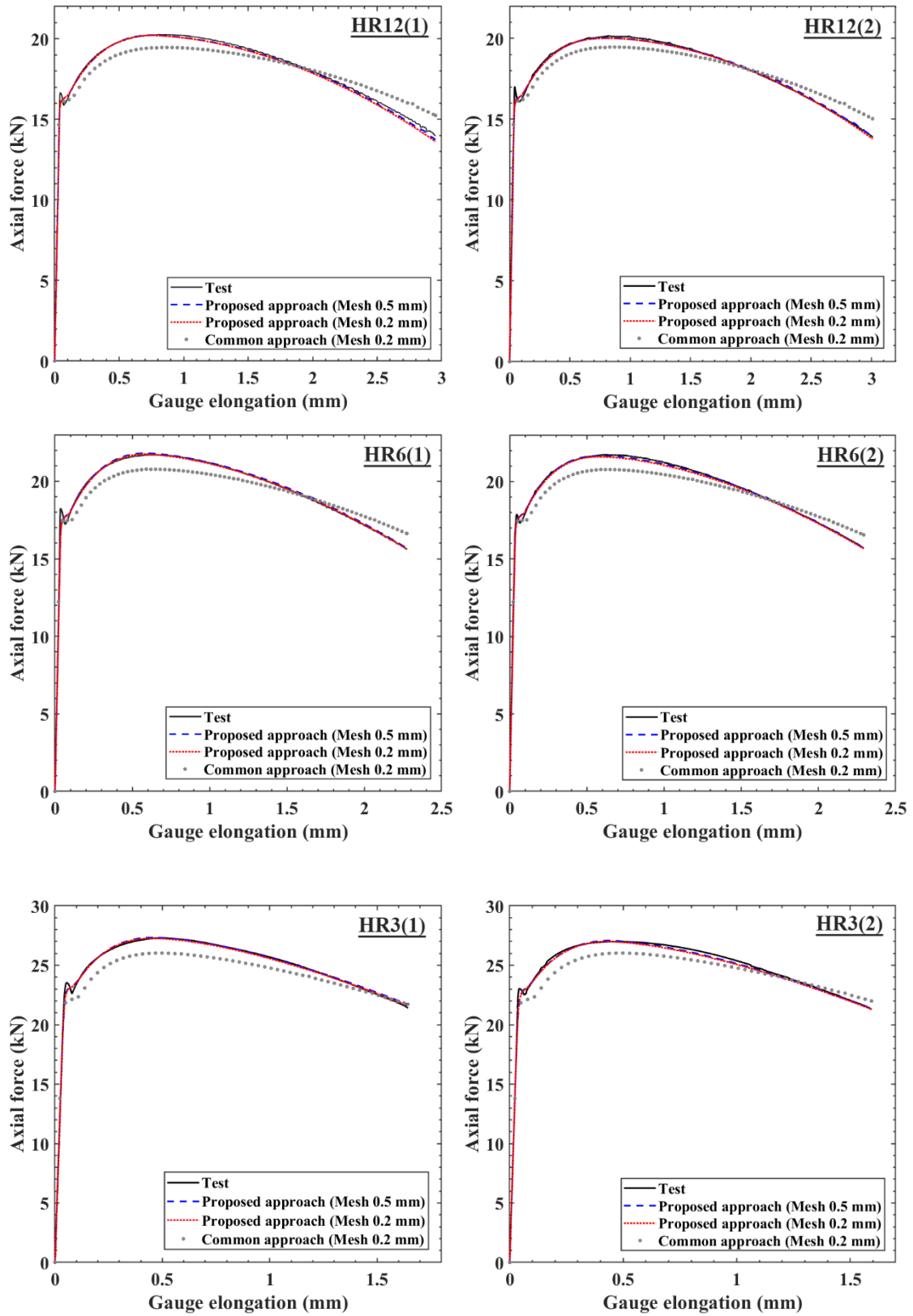
Figure 4.8. Numerical and experimental force-displacement curves of smooth-notched round bar specimens.

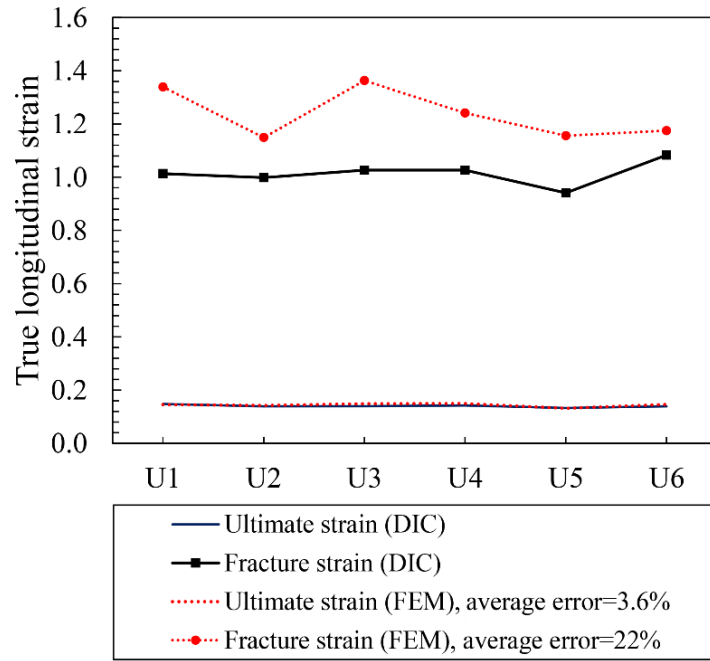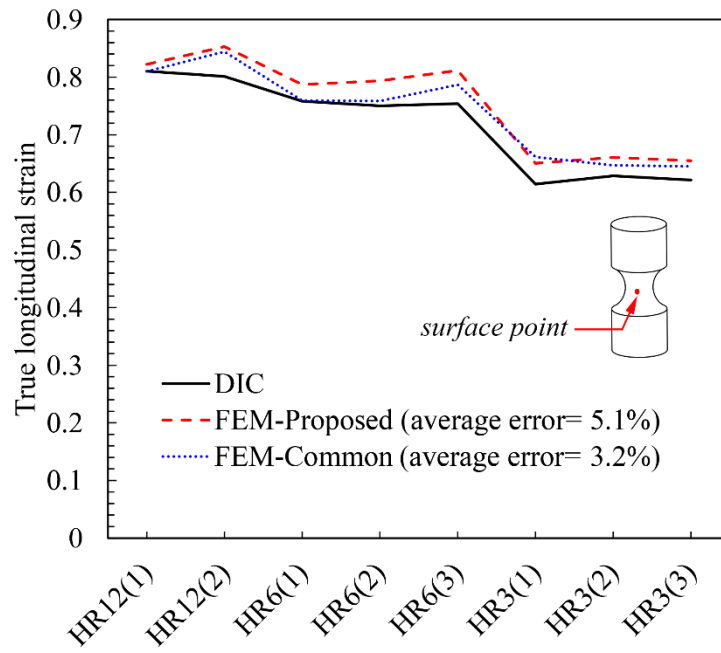*Figure 4.9. The surface true longitudinal strain at the fracture displacement of smooth-notched round bar specimens.*
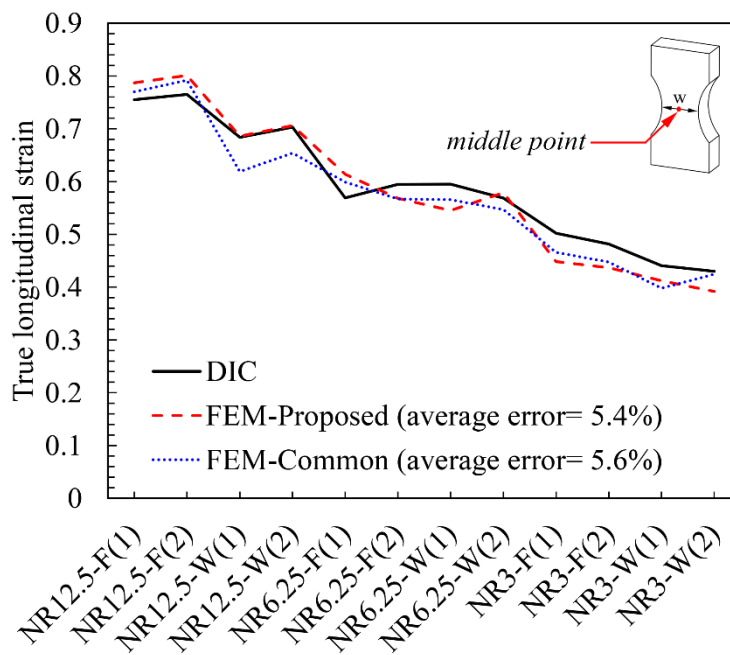
Figure 4.10. The surface true longitudinal strain at the fracture displacement of double-notched flat specimens at the middle point.
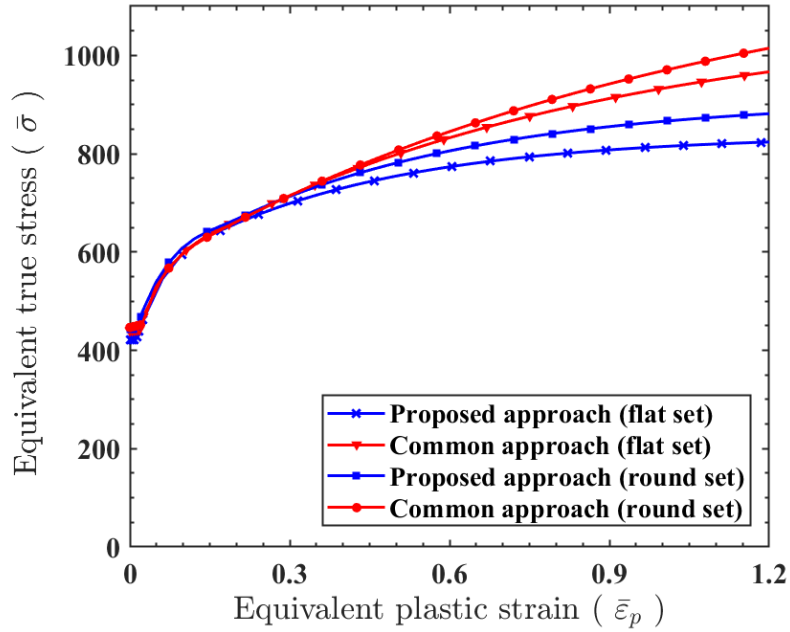
Figure 4.11. Average plastic flow curves calibrated for two sets of specimens based on the proposed and common approaches.

4.2 Stochastic analyses results

To select the size of the intact mesh for the single-sided corroded plate (see Figure 3.14), a standard mesh sensitivity analysis for a single pit with a 3 mm depth penetrated at the center of the plate was carried out and then validated for other pit depths. The pit was implemented by carving on the intact mesh with different sizes (0.7–0.3 mm) in addition to direct implementation of the geometry of the pit, as shown in Figure 4.12. The VGI distribution in the pit was selected as the local response that determines the fracture initiation in the material.

The results presented in Figure 4.12 indicate that by decreasing the mesh size from 0.4 mm to 0.3 mm, the maximum VGI demand changed less than 1%. This slight variation implies that mesh size is converged, and that using a 0.4 mm mesh size is sufficient to discretize the pit and evaluate the local response in the pit domain. Conversely, the element size must also be comparable with the typical characteristic length (ℓ^*) of mild steels, which is reported to be from 0.4 mm to 0.2 mm [90, 110]. Based on these two factors, a 0.3 mm mesh size was selected for the discretization of the intact uniform length of the case study specimen.

Figures 4.12, 4.13 and 4.14 provide the VGI obtained from the carved pits and the pits implemented by geometry for 3 mm, 2 mm and 1 mm depths, respectively. Based on these figures, the maximum VGI obtained from the two approaches shows a 7%–8.7% difference. It must be understood that using an ideal smooth

75

semi-ellipsoidal is a simplification of the overall geometry of the pits. However, the natural pits can have irregular surfaces. Therefore, this difference should not be considered as an absolute error but indicate that the carving pits can predict the local effect of a pit well enough. It is also worth mentioning that although the carved pit could capture the maximum VGI observed in the pit, the VGI distribution fluctuates due to the stepwise nature of the carving approach. Since the maximum VGI controls the fracture initiation, the form of distribution is less influential on the final pit fracture behavior.
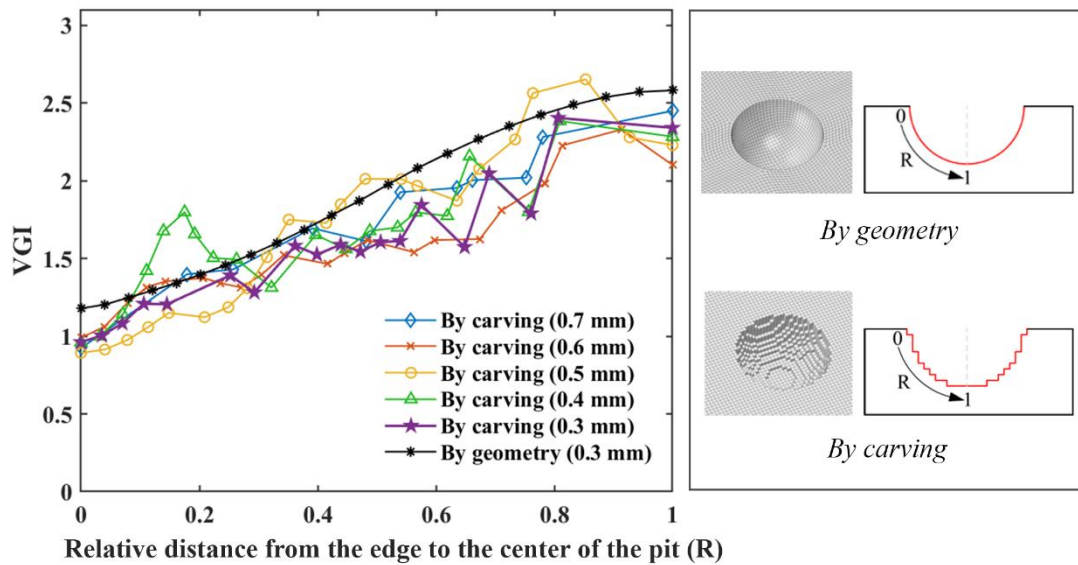
Figure 4.12. Sensitivity of the VGI to the mesh size for a 3 mm single pit carved at the center of the plate (7% difference in the maximum VGI for the 0.3 mm mesh size).
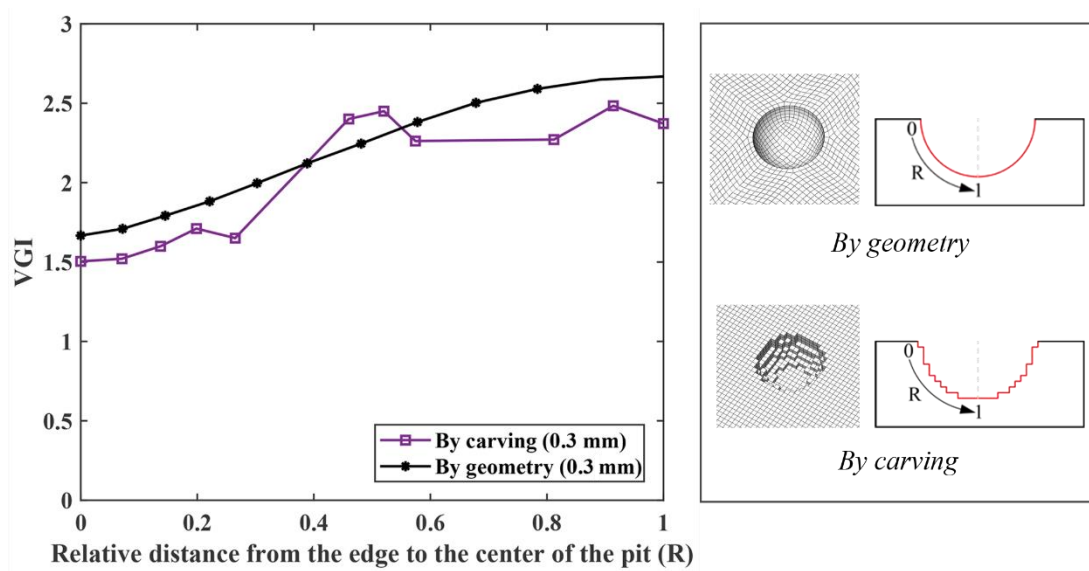
Figure 4.13. VGI evaluation for a 2 mm single pit carved at the center of the plate using the 0.3 mm mesh size (7% difference in the maximum VGI).

76
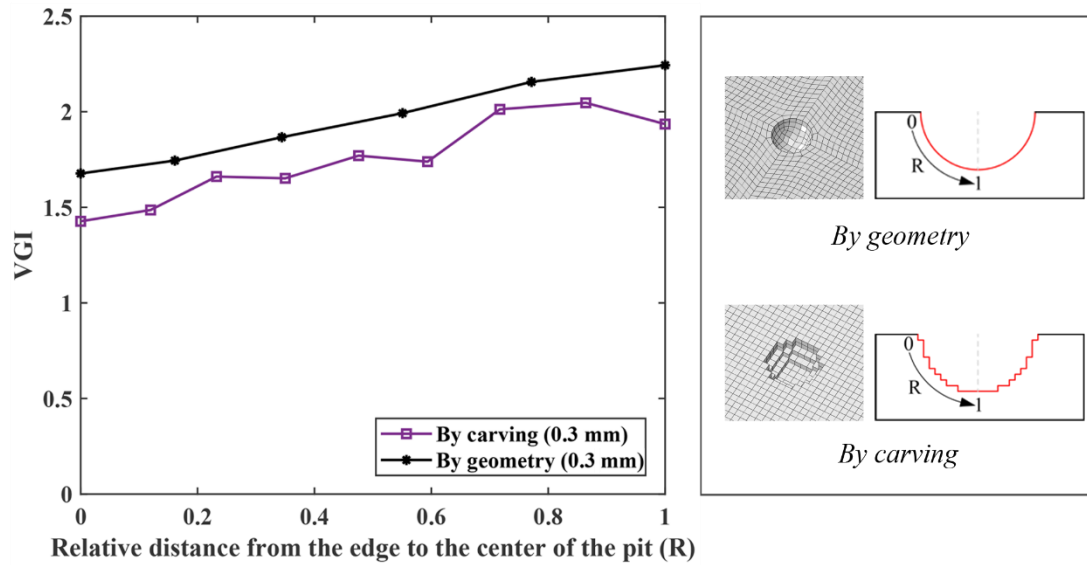
Figure 4.14. VGI evaluation for a 1 mm single pit carved at the center of the plate using the 0.3 mm mesh size (8.7% difference in the maximum VGI).

For each of the nine intensity measures listed in Table 3.4, the intact mesh of the specimen was modified and analyzed for fifty randomly generated pitting morphologies. For example, Figure 4.15 shows carved mesh for some of the random pitting morphologies generated for a 2 mm average pit depth and three different DOPs.

Figures 4.16 and 4.17 show the force-elongation curves for 1 mm and 3 mm average pit depths and different studied DOPs. The ultimate and failure points of each curve are marked in these figures. In addition, the failure elongation of the intact specimen is provided for better comparison.

The variation of the highlighted points indicates that different random pitting morphologies with an identical intensity measure could change the capacity and deformability of the specimen. Statistical parameters for ultimate load and failure elongation are listed in P(IV). The effect of random pitting on the ultimate load and the failure elongation were also discussed in P(IV) based on correlation analyses.

Based on the results, the ultimate load of the specimen was subject to a low rate of dispersion (6.5%), indicating that the details of pitting corrosion have a negligible effect on the ultimate load variation. The average reduction in the ultimate load was also 23.5% at the maximum intensity (i.e., IM[30%, 3mm]). The correlation analyses demonstrated that the ultimate capacity of the specimen is correlated with both the d_{avg} and DOP by -0.52 and -0.72 correlation coefficients, respectively.

Conversely, the failure elongation experienced 12.6%–30.2% dispersion due to a variation of pitting morphology. This dispersion explains the effect of pitting details on the ductility of the specimen by initiating the fracture and propagation in different modes. It is worth mentioning, as shown in Figures 4.16 and 4.17, the corroded specimen exhibited a reduced failure displacement for all analyzed random patterns except a few generated samples in IM[5%,1mm]. Figure 4.18 indicates two of these cases in which patterns with shallow pits occurred outside of the critical area of the specimen. In such patterns, corrosion only increased the flexibility without directly affecting the fracture initiation.

IM[5%, 2mm]   IM[10%, 2mm]   IM[30%, 2mm]
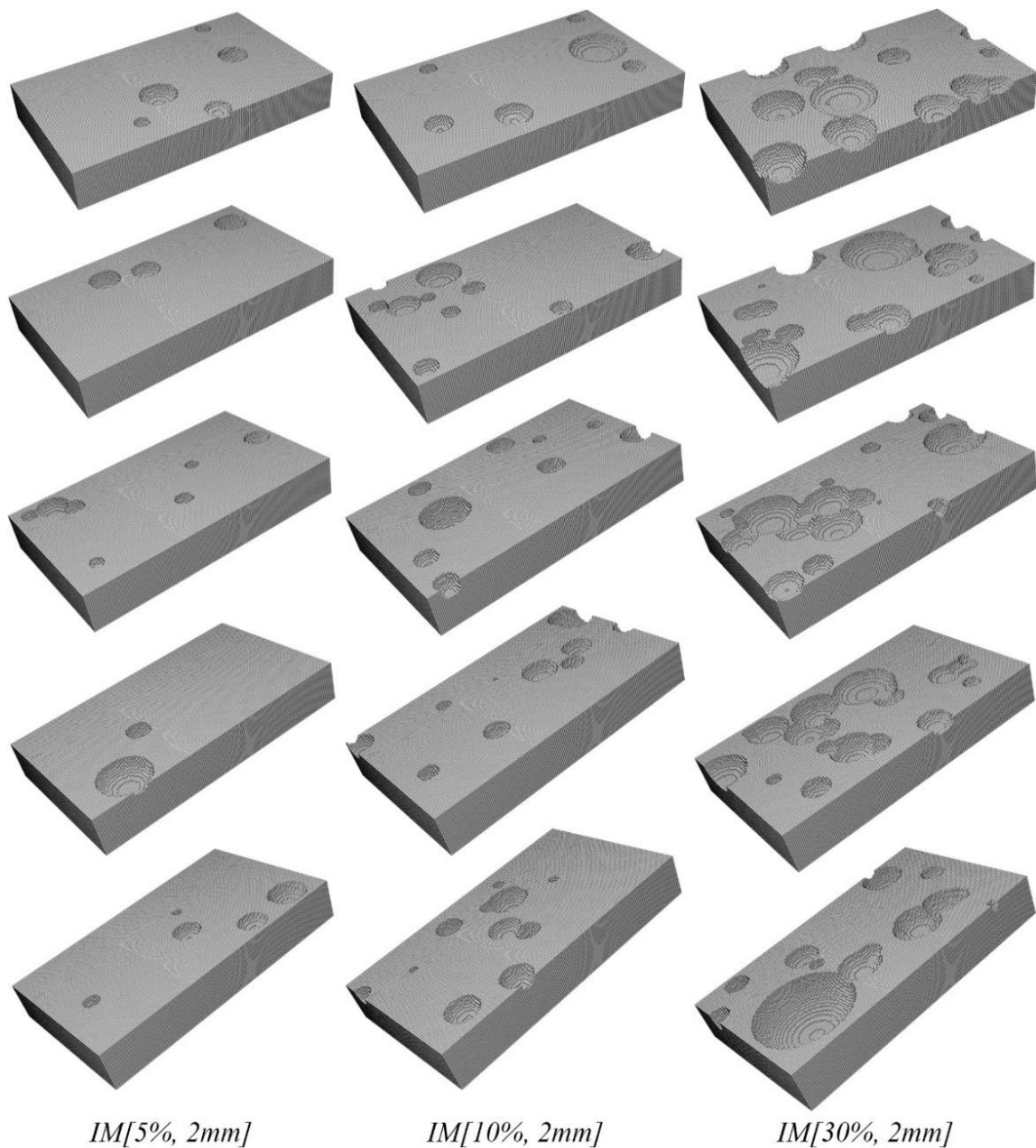
Figure 4.15. Carved mesh for random pitting morphologies generated for a 2 mm average pit depth and three different DOPs.
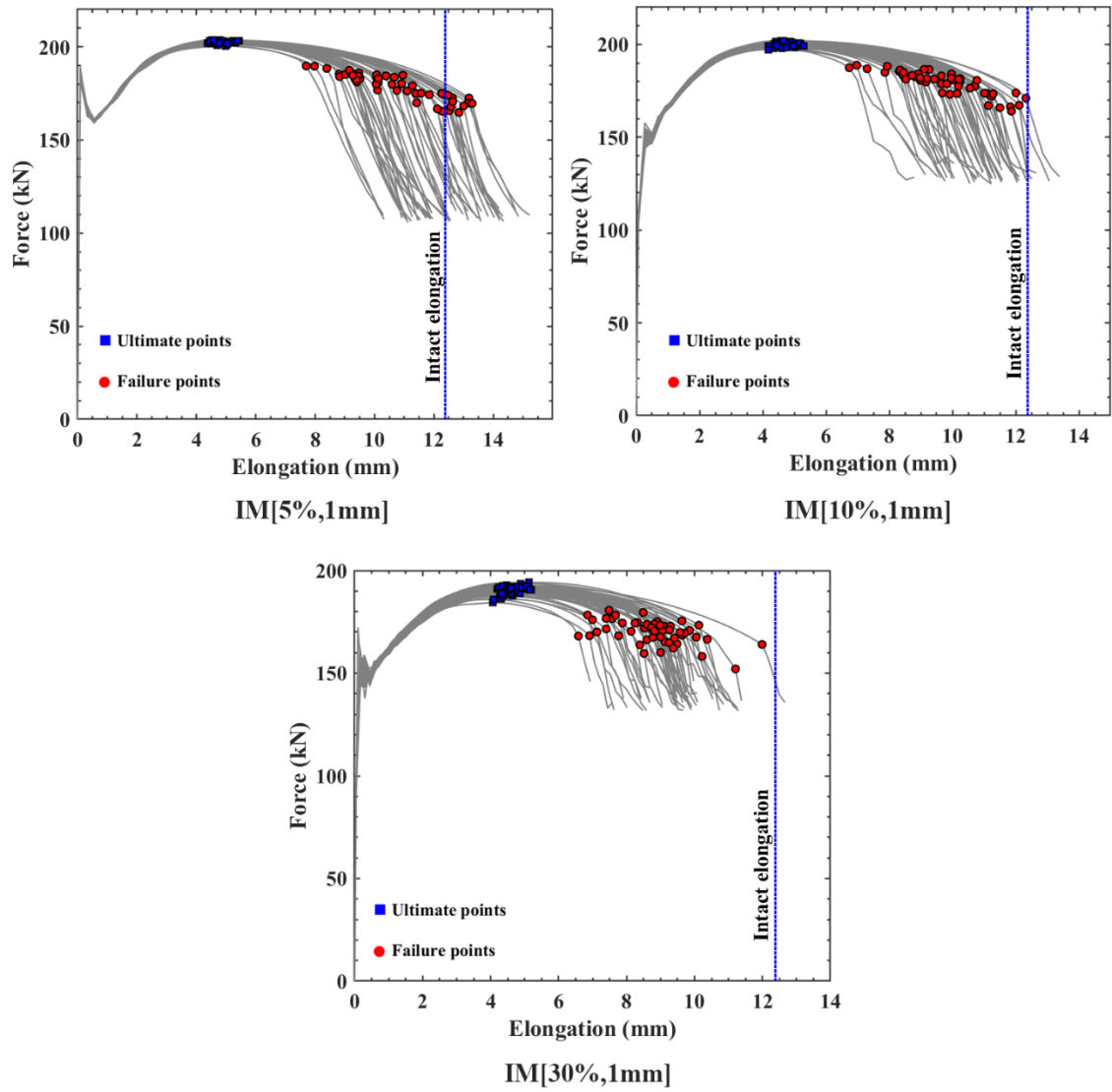
Figure 4.16. Force-elongation curves for a 1 mm average pit depth and different DOPs.
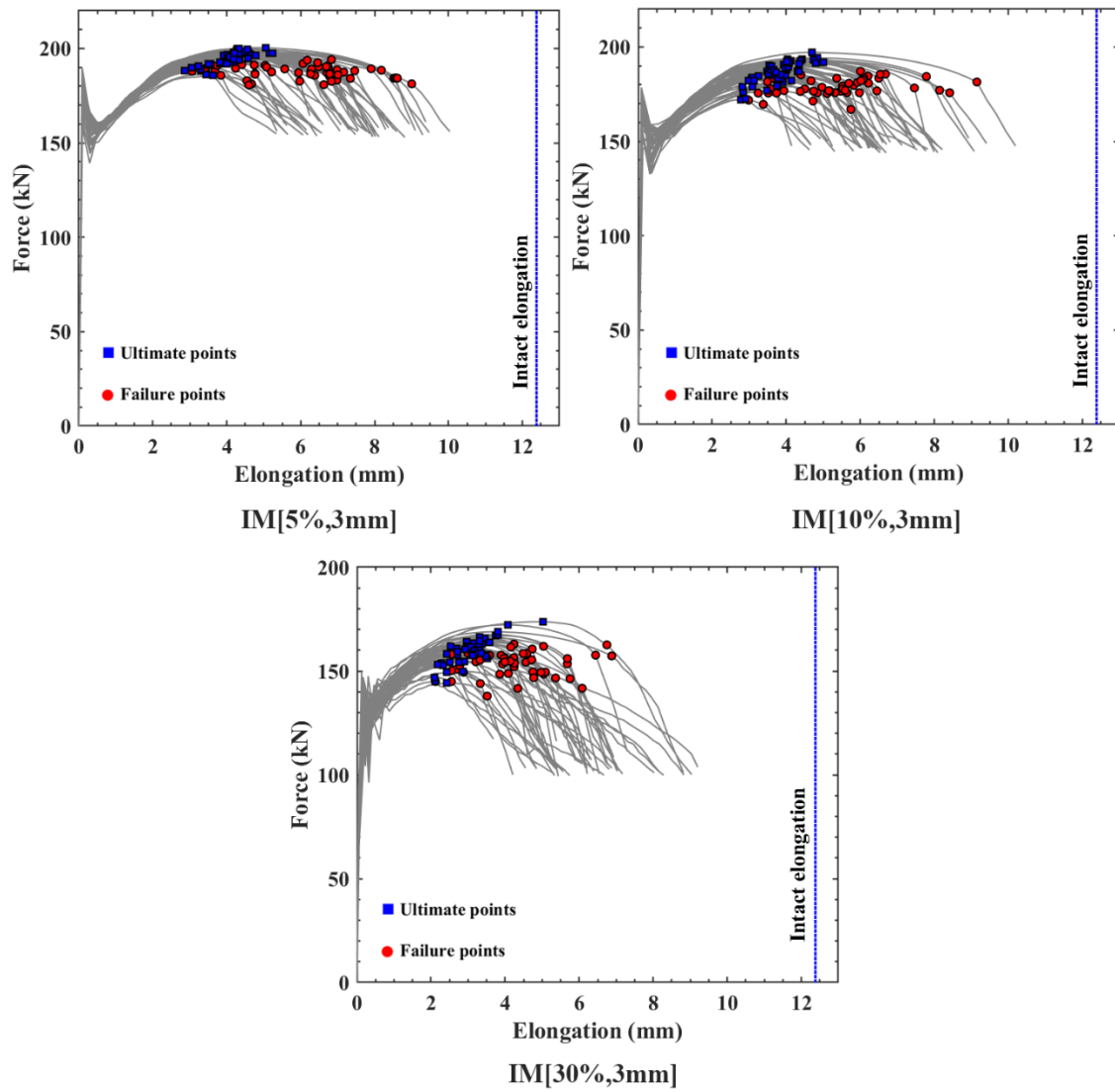
Figure 4.17. Force-elongation curves for a 3 mm average pit depth and different DOPs.
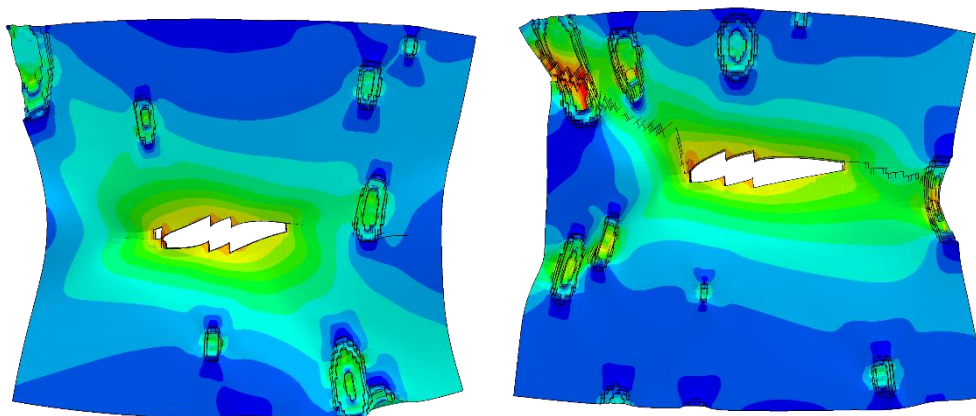
Figure 4.18. Some random patterns in IM[5%, 1 mm] increased the flexibility of the specimen without a direct effect on the fracture initiation.

Figure 4.19 illustrates the most dominant modes in which pitting affected fracture initiation and propagation. The interaction of two pits, the interaction between pits and the edge of the plate, and the existence of a well-penetrated pit are the most dominant modes in which corrosion pits accelerate the ductile fracture initiation. However, by increasing the DOP, the fracture accelerated due to a combination of these modes, which cannot be easily classified into a specific mode.
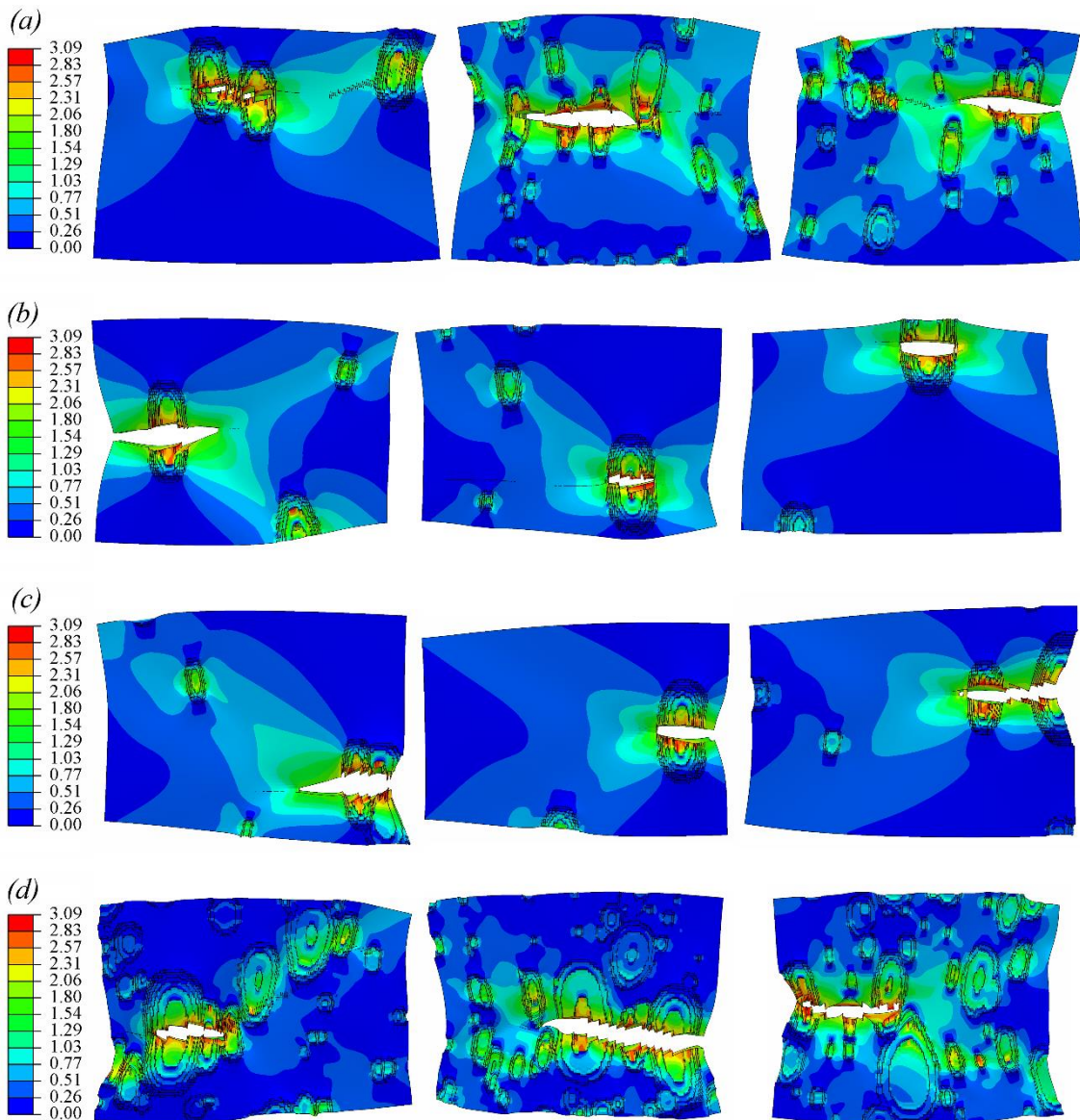
Figure 4.19. Different modes in which pits accelerate the ductile fracture initiation: a) interaction between neighboring pits, b) occurrence of a depth pit, c) interaction between pits and edges of plates and d) a combination of the described modes.

The empirical cumulative distribution function was calculated based on the fifty failure elongations obtained for each intensity measure. Figure 4.20 shows these fragility curves for a given *DOP* and different d_{avg} (1 mm, 2 mm and 3 mm).

Large differences between these curves denote the significant effect of pitting characteristics on the deformability of the specimen.
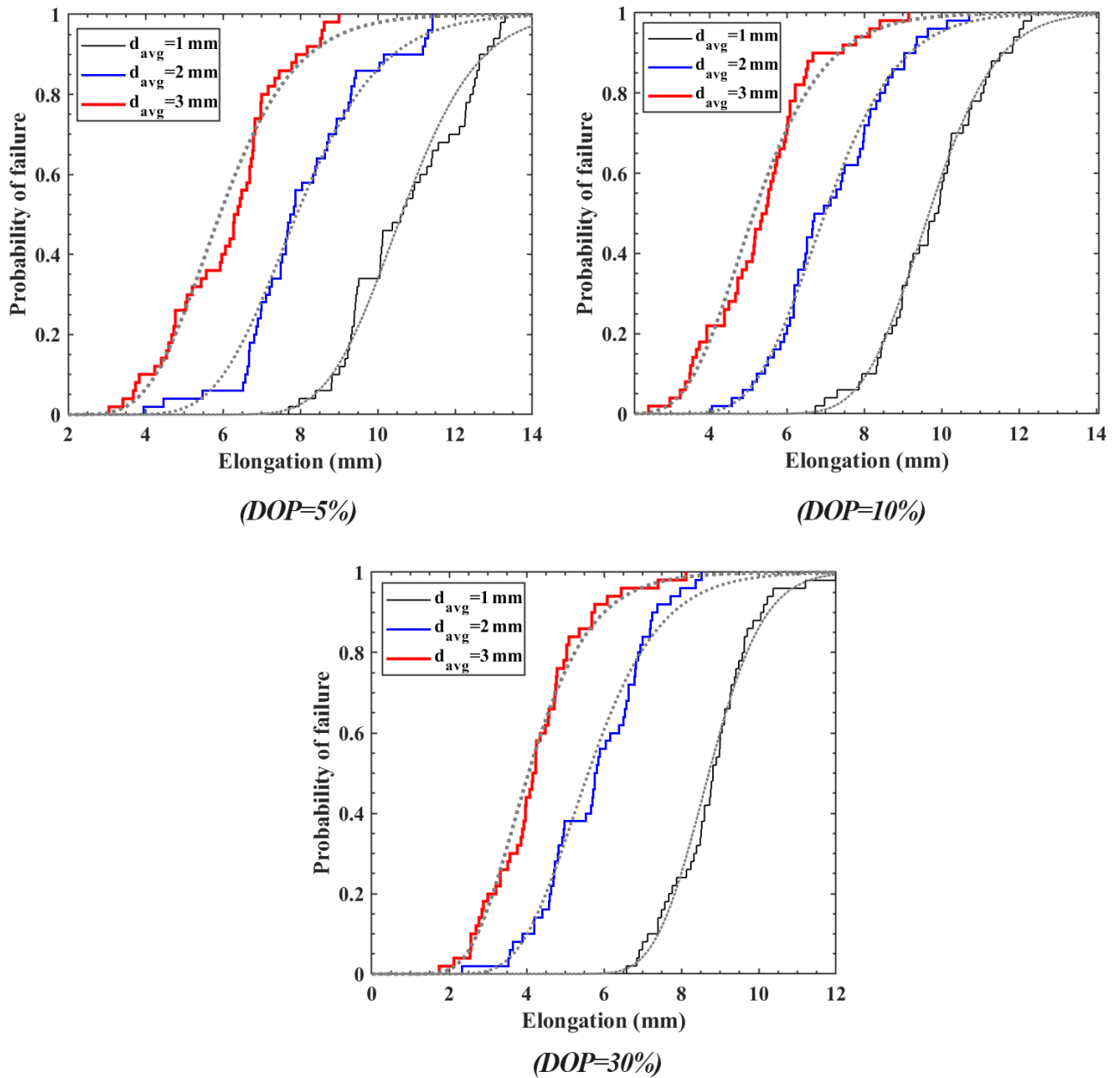
Figure. 4.20. Fragility curves obtained for various DOP and d_{avg} (dotted curves denote fitted lognormal distributions).

The two-sample Kolmogorov–Smirnov (K–S) nonparametric test on the failure elongations indicated that Lognormal distribution can better describe the fragility curves than Normal and two-parameter Weibull distributions. In addition, the effect of the number of random morphologies on the fragility curves was investigated by two-sample K–S tests. As Table 4.2 shows, using twenty random morphologies was sufficient to describe the fragility curves of the studied specimen in all intensities. In this connection, the performed K–S tests did not

reject the null hypothesis that the data from twenty samples were describing the same distributions from fifty samples. However, this number can vary by specimen configuration.

Table 4.2. Two-sample K–S test results for different intensity measures and various amounts of samples compared to the distribution obtained from fifty samples.

	Number of random samples			
Pitting intensity	10	20	30	40
IM[5%, 1 mm]	NR	NR	NR	NR
IM[5%, 2 mm]	NR	NR	NR	NR
IM[5%, 3 mm]	NR	NR	NR	NR
IM[10%, 1 mm]	NR	NR	NR	NR
IM[10%, 2 mm]	R	NR	NR	NR
IM[10%, 3 mm]	R	NR	NR	NR
IM[30%, 1 mm]	NR	NR	NR	NR
IM[30%, 2 mm]	R	NR	NR	NR
IM[30%, 3 mm]	R	NR	NR	NR
NR: Did not reject the null hypothesis (same distributions) R: rejected the null hypothesis (different distributions)				

4.3 Results of the large-scale joint

In P(V), mesh sensitivity analyses were done to select a proper mesh configuration for the submodeling technique. For this purpose, a 3 mm mesh size was examined for the global model with different numbers of layers through the thickness of the plates. As Figure 4.21(a) indicates, by increasing the number of layers from seven to nine, the nodal displacements in the global model (at the boundary of the submodels) only changed by 0.22%. As a result, seven layers were considered to extract the boundary displacements for the submodels. Then, the von Mises stresses in the global model and submodels were compared for a displacement corresponding to the fracture initiation of the intact joint. The curves presented in Figure 4.21(b) show about a 3% difference in boundary stress, which means the mesh refinement and boundary condition errors were negligible for the selected mesh configuration.
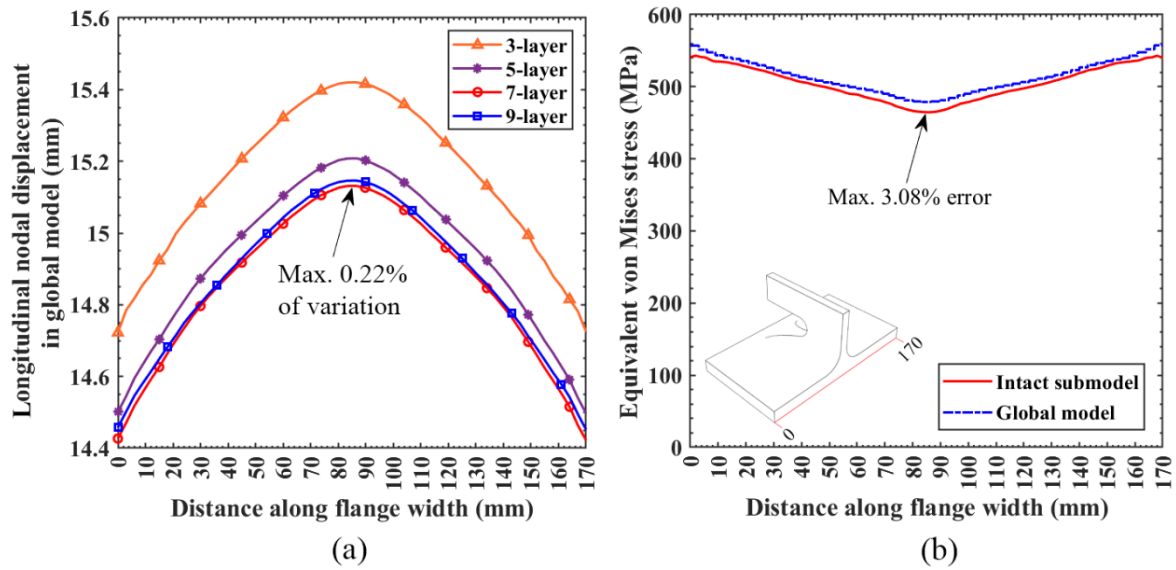
Figure 4.21. Mesh sensitivity analysis results at the boundary of the submodel region: a) longitudinal nodal displacement of the global model converged by using seven layers of elements through the thickness of the plates and b) stress values obtained from the global model and submodel.

The selected joint was studied for all predefined pit scenarios by comparing the joint vertical displacement corresponding to the fracture initiation of the corroded and intact joint. Based on the presented result in P(V), none of the edge pits was fractured before the intact joint fracture. As a result, such pits can be considered noncritical for the ductility of the joint. Far-edge pits close to the butt welds in both the flange and web exhibited the fracture initiation earlier than the intact joint. However, as shown in Figure 4.22, the reduction in fracture displacement was small (11% maximum). As a result, such isolated pits also can be skipped due to their insignificant effect. In contrast, the near-edge pits were identified as the most critical pits that can accelerate the fracture initiation of the joint, particularly when they formed a narrow ligament between the pit and the free edge of the plates. The result shown in Figure 4.23 demonstrates that the fracture initiation displacement of the intact joint could be reduced by about 25% when near-edge pits existed. If the initiated ductile crack propagates in the form of ductile tearing and unstable crack propagation, it can significantly reduce the joint ductility. These results highlight the importance of inspection, monitoring and treatment of near-edge pits or far-edge pits that can change into a near-edge pit during the exposure time.

Regarding geometrical parameters, the results presented in P(V) showed that when the aspect ratio decreased (narrower pit) or the pit's depth increased, there was an increased tendency to fracture.

These results suggest that two-level numerical modeling is a capable technique to facilitate micromechanical simulation of pitting corrosion in complicated components under excessive plastic deformations. Based on this technique, engineers can scrutinize the behavior of corroded real scale joints to find a proper treatment strategy.
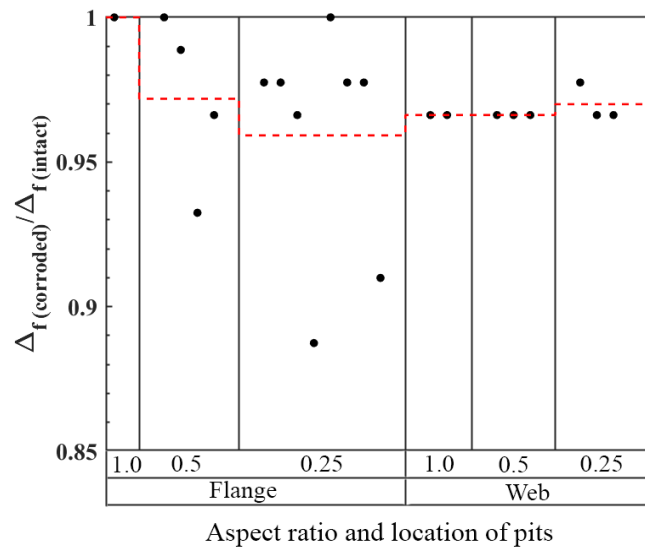
Figure 4.22. The ratio of fracture initiation displacement of the joint subjected to an isolated far-edge pit (the dashed line denotes the average ratio).
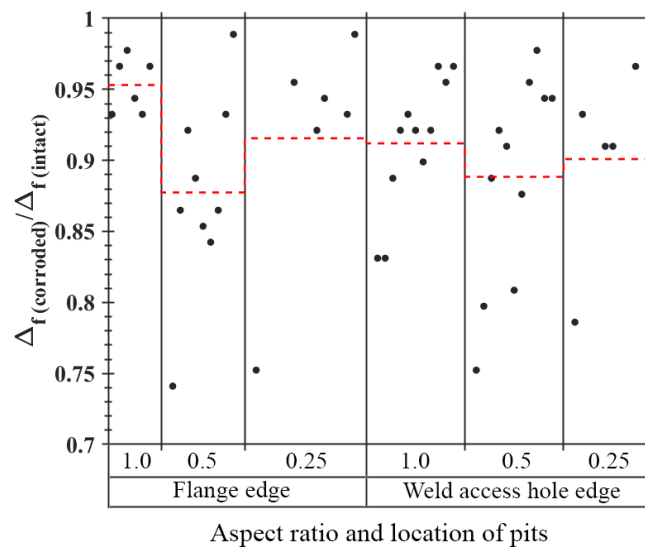
Figure 4.23. The fracture initiation displacement ratio of the joint subjected to an isolated near-edge pit (the dashed line denotes the average ratio).

5. Conclusions, delimitations and future work

5.1 Conclusion

This thesis set out to develop a failure assessment framework, including testing and modeling approaches linking different scales (material and structure) to predict the failure of steel components under the coupled effect of large-scale plasticity and pitting corrosion.

On the material scale, the void growth model (VGM) was chosen as a micromechanics-based ductile fracture criterion. The common calibration approach of the VGM is not well suited to situations where the material length is insufficient, e.g., welds and heat-affected zone. It also can be subjected to various sources of calibration error. This thesis presented an alternative approach to increase the applicability of the VGM and mitigate possible calibration errors. The proposed approach simultaneously calibrates the constitutive model and fracture criterion based on the DIC full-field strain measurement. Based on the results presented in the thesis, the following conclusions were drawn:

- The proposed calibration approach can be used as an appropriate alternative for characterizing the plastic and fracture behavior of weld and HAZ metals. The result showed that both common and proposed approaches similarly predicted the fracture strain in notched specimens with reasonable errors (4.8% on average).

- The proposed calibration approach was successfully used with both round and flat configurations of specimens. However, it led to fewer calibration errors and uncertainties in the flat configuration.

- The proposed approach could better estimate the post-necking equivalent stress compared to the common approach. As a result, it could predict the fracture force of the tested pull-plate specimens more accurately than the common approach.

- Furthermore, because the proposed approach synchronizes the calibration of the constitutive model and fracture criterion, it can accurately capture the correlation between them to address the material variation in probabilistic-mechanical analyses.

In addition to accurate material modeling, the assessment framework requires developed numerical modeling in which the three-dimensional local effects of pits and their stochastic and time-dependent natures are addressed properly.

To explicitly take these factors into account, the concept of a fracture-based fragility curve was developed at the component level by micromechanics-based modeling of different random pitting morphologies. For a predefined intensity level of pitting corrosion, random pitting patterns were generated according to the probability distributions of the pit characteristics (location, depth and aspect ratio). A unique meshing technique was employed to implement these random pitting morphologies in numerical models. This meshing technique was established based on carving the volume of random pits on an intact mesh at the critical zone of components. Analysis of the computed results show the following conclusions:

- The variation of the pitting morphology by a random procedure could meaningfully affect the failure elongation of the tensile steel components due to different modes of triggering ductile fracture initiation. However, the variation of corrosion morphology affected the ultimate capacity of the components slightly.

- Based on the comprehensive sensitivity analysis, it was shown that a mesh size in the range of the steel characteristic length (e.g., 0.3 mm) could reasonably predict the local responses in the carved pits with different penetration depths.

- The correlation analyses on the predicted failure elongations demonstrated that both the degree of pitting (DOP) and average pit depth must be included in the definition of the intensity measure of the pitting corrosion when components are studied under excessive plastic deformations.

- In addition, the proposed mesh carving method is progressively updatable by nature. As a result, current surface morphology can be modified for new penetrated pits or the development of existing pits without redoing all modeling processes. Because of this feature, it can be efficiently coupled with real-time monitoring systems to assess long-term structural integrity and safety based on life-cycle assessments.

Since the proposed fracture-based fragility curves were developed based on micromechanics-based modeling, they encounter difficulties in engineering applications, mainly regarding implementing pitting morphology on large-scale components. Therefore, two-level numerical modeling as a solution was discussed to reduce the complexity of the problem. In this technique, submodels with refined mesh are used to perform micromechanics-based simulations and assess the fracture initiation in steel components for different pitting scenarios based on

boundary conditions extracted from a global model. This approach was applied to study a selected beam-to-column joint under different pitting scenarios, and some important conclusions are noted and summarized below:

- It was concluded that the employed modeling approach is capable of optimally assessing pitting corrosion in complicated components under excessive plastic deformations.

- The results obtained for the moment-resisting joint demonstrated that an isolated pit could initiate ductile fracture of the joint by 25% less joint vertical displacement. However, the level of degradation depended on the pit location and geometry.

- The employed two-level numerical modeling approach can identify the most critical regions of the steel joint for pitting corrosion. Based on these regions, periodic inspections can be performed to ensure structural safety under extreme events.

In general, the compilation of papers presented in this thesis can provide valuable sequential developments from the material to the component level to establish a failure assessment framework and push different parts of it towards the final application, which is predicting the effect of pitting corrosion in steel structures under extreme loads. Based on the outcomes of such an assessment framework, decision-makers can utilize risk management methods and assess the most critical scenarios in terms of principal criteria (e.g., health and safety, economy and the environment) and accordingly prescribe remedies for an expected lifetime.

5.2 Delimitations

Fracture simulation involves many parameters in its numerical models. Taking all of these parameters into consideration is challenging due to the lack of experimental data and uncertainties that affect the analysis. Therefore, it is the analyst's responsibility to select essential features of the studied problem and simplify the problem in the other aspects accordingly based on available tools and resources. Consequently, the following delimitations and simplifications were considered in this thesis:

- The material fracture mode was limited to a tensile monotonic ductile fracture with high positive triaxiality (i.e., $\eta > 0.33$) in which the effect of the Lode parameter is negligible. Other types of fractures that occur in shear

or compressive loads where the Lode parameter is more influential were not discussed.

- All deformations were considered quasi-static so that the material behavior can be assumed to be independent from the strain rate. This assumption is reasonable, particularly for ship collisions that occur at a low speed [7].

- Only base metal was studied for pitting corrosion, and other involved metals such as welds and heat-affected zones were assumed uncorroded.

- All tests and numerical simulations were performed at room temperature. However, for applications with low or high temperatures, the fracture behavior of steel material must be adjusted accordingly.

- All aspects of a physical structure, including material, load and geometry, can be subjected to uncertainties. However, this thesis only investigates the uncertainties related to pitting corrosion.

- Finally, this research considers semi-ellipsoidal shape as pit geometry. Other possible pit geometries, such as narrow crack-shaped pits or phenomena such as corrosion fatigue that increase the chance of brittle fracture, are out of the scope of this thesis.

5.3 Future work

This thesis aimed to create a foundation for a failure assessment framework mainly in terms of material characterization and numerical modeling. However, there is ample space to make it more applicable based on state-of-the-art techniques listed in the following:

- Linking the failure assessment framework to other techniques such as real-time monitoring or inspection techniques to boost the applicability of the framework, particularly within a life-cycle assessment. In this connection, a data-transferring module must be established to transfer corrosion data from the monitoring module to the numerical module.

- Developing a material model calibration procedure based on only a few uniaxial tensile specimens with a small number of iterations by using DIC measurements.

- Involving machine learning methods to reduce the computational time and provide rapid insight into the structural integrity. In this regard, a proper machine learning framework must be trained to estimate the failure of the

components based on the morphology of the corrosion without performing numerical models.

- Developing a demand-capacity framework based on multiscale approaches, e.g., virtual-hybrid simulations to consider a two-directional data transition between the global and components' behavior.

List of references

1. McCormac, J. and S. Csernak, *Structural Steel Design*. 5th Edition ed. 2012: Prentice Hall.
2. Ellobody, E., R. Feng, and B. Young, *Finite element analysis and design of metal structures*. 2013: Elsevier.
3. AISC, *Seismic provisions for structural steel buildings (ANSI/AISC 341-16)*. 2016, American Institute of Steel Construction: Chicago(IL).
4. European Committee for Standardization, *Eurocode 8: Design of structures for earthquake resistance-part 1: general rules, seismic actions and rules for buildings (EN 1998-1)*. 2004: Brussels, Belgium.
5. Bruneau, M., et al., *Ductile design of steel structures*. 2011: McGraw-Hill Education.
6. Chua, C.K., K.F. Leong, and C.S. Lim, *Rapid prototyping: principles and applications*. 2003: World Scientific Publishing Company.
7. Kõrgesaar, M., *Modeling ductile fracture in ship structures with shell elements*, in *Department of Applied Mechanics*. 2015, Aalto University: Finland.
8. AISC, *Prequalified connections for special and intermediate steel moment frames for seismic applications (AISC 358-16)*. 2016, American Institute of Steel Construction: Chicago.
9. Zhang, M., et al., *Comparison of uncertainty models in reliability analysis of offshore structures under marine corrosion*. Structural Safety, 2010. **32**(6): p. 425-432.
10. Lemaire, M., *Structural reliability*. 2013: John Wiley & Sons.
11. IIEES. *IMAX Project* Available from: http://www.iiees.ac.ir/en/.
12. ASCE. *Minimum design loads for buildings and other structures*. 2010. American Society of Civil Engineers.
13. Chung, K. and M.-G. Lee, *Basics of Continuum Plasticity*. 2018: Springer.
14. DNV, *Determination of structural capacity by non-linear FE analysis methods (Recommended Practice No. DNV-RP-C208)*. 2013, Det Norske Veritas GL AS: Oslo.
15. European Committee for Standardization, *Eurocode 3: Design of steel structures - Part 1-8: Design of joints (EN 1993-1-8)*. 2005: European Committee for Standardization,Brussels.
16. European Committee for Standardization, *Standard for hot-rolled structural steel. Part 2 - Technical delivery conditions for non-alloy structural steels (EN 10025-2:2004)*. 2004, CEN: Brussels, Belgium.
17. Bardal, E., *Corrosion and protection*. Engineering Materials and Processes. 2004, London: Springer.
18. Pedeferri, P., *Corrosion Science and Engineering*. Engineering Materials, ed. L. Lazzari and M. Pedeferri. 2018, Switzerland: Springer.
19. DNV GL, *Risk based corrosion management (DNVGL-RP-C302)*. 2015, DNV GL AS.
20. Champion, F., *Metal thickness and corrosion effects*. Metal Industry, 1990. **74**: p. 7-9.

21. Shekari, E., F. Khan, and S. Ahmed, *Probabilistic modeling of pitting corrosion in insulated components operating in offshore facilities.* ASCE-ASME J Risk and Uncert in Engrg Sys Part B Mech Engrg, 2017. **3**(1).

22. Melchers, R.E., *New insights from probabilistic modelling of corrosion in structural reliability analysis.* Structural Safety, 2021. **88**: p. 102034.

23. Melchers, R.E., *Pitting corrosion of mild steel in marine immersion environmentpart 1: maximum pit depth.* Corrosion, 2004. **60**(09).

24. Melchers, R.E., *Pitting Corrosion of Mild Steel in Marine Immersion EnvironmentPart 2: Variability of Maximum Pit Depth, October 2004.* Corrosion, 2004. **60**(10).

25. Melchers, R.E., *Progress in developing realistic corrosion models.* Structure and Infrastructure Engineering, 2018. **14**(7): p. 843-853.

26. ASTM, *Standard practice for operating salt spray (fog) apparatus*, in *ASTM International*. 2019: West Conshohocken, PA.

27. Ansari, T.Q., et al., *Phase-field model of pitting corrosion kinetics in metallic materials.* npj Computational Materials, 2018. **4**(1): p. 1-9.

28. Wang, Y., J.A. Wharton, and R.A. Shenoi, *Ultimate strength analysis of aged steel-plated structures exposed to marine corrosion damage: A review.* Corrosion Science, 2014. **86**: p. 42-60.

29. Southwell, C., J. Bultman, and C. Hummer, *Estimating service life of steel in seawater.* Seawater corrosion handbook, 1979. **87**: p. 374.

30. Melchers, R.E., *Probabilistic models for corrosion in structural reliability assessment—part 2: models based on mechanics.* J. Offshore Mech. Arct. Eng., 2003. **125**(4): p. 272-280.

31. Melchers, R.E., *Predicting long-term corrosion of metal alloys in physical infrastructure.* npj Materials Degradation, 2019. **3**(1): p. 1-7.

32. DNV GL, *Design of offshore steel structures, general-LRFD method (DNVGL-OS-C101).* 2016, DNV GL AS.

33. International Organization for Standardization, *ISO 12944: Paints and varnishes - Corrosion protection of steel structures by protective paint systems - Part 1-8.* 2019.

34. International Organization for Standardization, *Petroleum and natural gas industries-fixed steel offshore structures, ISO 19902.* 2008, International Organization for Standardization.

35. DNV GL, *Thickness diminution for mobile offshore units (DNVGL-CG-0172).* 2015, DNV GL AS.

36. DNV GL, *Allowable thickness diminution for hull structure (DNVGL-CG-0182).* 2016, DNV GL AS.

37. Xu, S., et al., *Effects of corrosion on surface characterization and mechanical properties of butt-welded joints.* Journal of Constructional Steel Research, 2016. **126**: p. 50-62.

38. Duddu, R., *Numerical modeling of corrosion pit propagation using the combined extended finite element and level set method.* Computational Mechanics, 2014. **54**(3): p. 613-627.

39. Wang, H., et al., *Effect of pitting degradation on ductile fracture initiation of steel butt-welded joints.* Journal of Constructional Steel Research, 2018. **148**: p. 436-449.

40. Huang, Y., et al., *Ultimate strength assessment of hull structural plate with pitting corrosion damnification under biaxial compression.* Ocean Engineering, 2010. **37**(17-18): p. 1503-1512.

41. Zhao, Z., et al., *Tensile strength of Q345 steel with random pitting corrosion based on numerical analysis.* Thin-Walled Structures, 2020. **148**: p. 106579.

42. Yan, Y., et al., *A study on the influence of double ellipsoidal pitting corrosion on the collapsing strength of the casing.* Engineering Failure Analysis, 2019. **100**: p. 11-24.

43. Cerit, M., *Numerical investigation on torsional stress concentration factor at the semi elliptical corrosion pit.* Corrosion Science, 2013. **67**: p. 225-232.

44. Zhang, J., Z. Liang, and C. Han, *Effects of ellipsoidal corrosion defects on failure pressure of corroded pipelines based on finite element analysis.* International Journal of Electrochemical Science, 2015. **10**: p. 5036-5047.

45. Cerit, M., K. Genel, and S. Eksi, *Numerical investigation on stress concentration of corrosion pit.* Engineering failure analysis, 2009. **16**(7): p. 2467-2472.

46. Wang, R., H. Guo, and R.A. Shenoi, *Compressive strength of tubular members with localized pitting damage considering variation of corrosion features.* Marine Structures, 2020. **73**: p. 102805.

47. Pidaparti, R.M. and R.R. Patel, *Correlation between corrosion pits and stresses in Al alloys.* Materials Letters, 2008. **62**(30): p. 4497-4499.

48. Ji, J., et al., *Prediction of stress concentration factor of corrosion pits on buried pipes by least squares support vector machine.* Engineering Failure Analysis, 2015. **55**: p. 131-138.

49. Turnbull, A., L. Wright, and L. Crocker, *New insight into the pit-to-crack transition from finite element analysis of the stress and strain distribution around a corrosion pit.* Corrosion Science, 2010. **52**(4): p. 1492-1498.

50. McClintock, F.A., *A criterion for ductile fracture by the growth of holes.* Journal of applied mechanics, 1968. **35**(2): p. 363-371.

51. Rice, J.R. and D.M. Tracey, *On the ductile enlargement of voids in triaxial stress fields.* Journal of the Mechanics and Physics of Solids, 1969. **17**(3): p. 201-217.

52. Appuhamy, J., et al., *Reduction of ultimate strength due to corrosion-A finite element computational method.* International Journal of Engineering (IJE), 2011. **5**(2): p. 194.

53. Ahmmad, M.M. and Y. Sumi, *Strength and deformability of corroded steel plates under quasi-static tensile load.* Journal of marine science and technology, 2010. **15**(1): p. 1-15.

54. Yu, W., *Corrosion effects on the ductile fracture, strength and reliability of membranes, plates and shells*. 2009, University of Michigan.

55. Songbo, R., et al., *Effects of the corrosion pitting parameters on the mechanical properties of corroded steel.* Construction and Building Materials, 2021. **272**: p. 121941.

56. Wang, Y., et al., *Predicting the residual strength and deformability of corroded steel plate based on the corrosion morphology.* Construction and Building Materials, 2017. **152**: p. 777-793.

57. Sheng, J. and J. Xia, *Effect of simulated pitting corrosion on the tensile properties of steel.* Construction and Building Materials, 2017. **131**: p. 90-100.

58. Kvitrud, A. *Collisions between platforms and ships in Norway in the period 2001-2010.* in *International Conference on Offshore Mechanics and Arctic Engineering.* 2011. Rotterdam, The Netherlands.

59. Nygård, B., *learning after platform supply vessel collision with Statfjord A platform.* 2019, Equinor ASA.

60. Sha, Y., J. Amdahl, and C. Dørum, *Numerical and analytical studies of ship deckhouse impact with steel and RC bridge girders.* Engineering Structures, 2021. **234**: p. 111868.

61. Köller, J., J. Köppel, and W. Peters, *Offshore wind energy: research on environmental impacts.* 2006: Springer Science & Business Media.

62. Yu, Z. and J. Amdahl, *A review of structural responses and design of offshore tubular structures subjected to ship impacts.* Ocean Engineering, 2018. **154**: p. 177-203.

63. Yu, Z., et al., *Numerical analysis of local and global responses of an offshore fish farm subjected to ship impacts.* Ocean Engineering, 2019. **194**: p. 106653.

64. Adam, J.M., et al., *Research and practice on progressive collapse and robustness of building structures in the 21st century.* Engineering Structures, 2018. **173**: p. 122-149.

65. DNV, *Recommended practice DNV-RP-C204: Design against accidental loads* 2010, DET NORSKE VERITAS.

66. Equinor. *Collision between supply vessel and Statfjord A.* 2021; Available from: https://www.equinor.com/en/news/sammenstoet-mellom-statfjorda-og-supplyfartoey.html.

67. Petti, J.P. and R.H. Dodds Jr, *Ductile tearing and discrete void effects on cleavage fracture under small-scale yielding conditions.* International Journal of Solids and Structures, 2005. **42**(13): p. 3655-3676.

68. Hokstad, P., et al., *Ageing and life extension for offshore facilities in general and for specific systems.* SINTEF Report for the Petroleum Safety Authority Norway, 2010.

69. Taylor, D., *The theory of critical distances: A new perspective in fracture mechanics.* 2007, UK: Elsevier.

70. Anderson, T.L., *Fracture mechanics: fundamentals and applications.* 2015: CRC press.

71. Kanvinde, A. and G. Deierlein, *Micromechanical simulation of earthquake-induced fracture in structural steel*, in *Rep. No.145.* 2004, The John A. Blume Earthquake Engineering Center: Stanford.

72. François, D., A. Pineau, and A. Zaoui, *Mechanical behaviour of materials: Volume II: fracture mechanics and damage*. Vol. 2. 1998: Springer.

73. Argon, A., J. Im, and R. Safoglu, *Cavity formation from inclusions in ductile fracture.* Metallurgical Transactions A, 1975. **6**(4): p. 825-837.

74. Yip, S., *Handbook of materials modeling: Part A. Methods*. 2007: Springer Science & Business Media.

75. Brown, L. and W. Stobbs, *The work-hardening of copper-silica v. equilibrium plastic relaxation by secondary dislocations.* Philosophical Magazine, 1976. **34**(3): p. 351-372.

76. Goods, S. and L. Brown, *The nucleation of cavities by plastic deformation.* Perspectives in Creep Fracture, 1983: p. 71-85.

77. Bao, Y. and T. Wierzbicki, *On fracture locus in the equivalent strain and stress triaxiality space.* International Journal of Mechanical Sciences, 2004. **46**(1): p. 81-98.

78. Hancock, J. and A. Mackenzie, *On the mechanisms of ductile failure in high-strength steels subjected to multi-axial stress-states.* Journal of the Mechanics and Physics of Solids, 1976. **24**(2-3): p. 147-160.

79. Johnson, G.R. and W.H. Cook, *Fracture characteristics of three metals subjected to various strains, strain rates, temperatures and pressures.* Engineering fracture mechanics, 1985. **21**(1): p. 31-48.

80. Brocks, W., *Plasticity and fracture*. 2018: Springer.

81. Jia, L.-J. and H. Ge, *Ultra-low-Cycle Fatigue Failure of Metal Structures Under Strong Earthquakes*. 2019: Springer.

82. Fernandes, A.A., A.M. de Jesus, and R.N. Jorge, *Monotonic and Ultra-Low-Cycle Fatigue Behaviour of Pipeline Steels: Experimental and Numerical Approaches*. 2018: Springer.

83. Zhang, W. and Y. Cai, *Continuum damage mechanics and numerical applications*. 2010: Springer Science & Business Media.

84. Wen, H., *Predicting ductile fracture in steel connections*. 2016, Colorado State University.

85. Wang, Y., et al., *Fracture prediction of welded steel connections using traditional fracture mechanics and calibrated micromechanics based models.* International Journal of Steel Structures, 2011. **11**(3): p. 351.

86. Kanvinde, A., et al., *Predicting fracture in structural fillet welds using traditional and micromechanical fracture models.* Engineering Structures, 2008. **30**(11): p. 3325-3335.

87. Kanvinde, A., *Predicting fracture in civil engineering steel structures: State of the art.* Journal of Structural Engineering, 2017. **143**(3): p. 03116001.

88. Saxena, A., *Nonlinear fracture mechanics for engineers*. 1998: CRC press.

89. Anderson, T.L., *Effect of crack-tip region constraint on fracture in the ductile-to-brittle transition*, in *NBSIR 84-3001*. 1984, U.S. Department of Commerce.

90. Kanvinde, A. and G. Deierlein, *The void growth model and the stress modified critical strain model to predict ductile fracture in structural steels.* Journal of Structural Engineering, 2006. **132**(12): p. 1907-1918.

91. Bai, Y., Y. Bao, and T. Wierzbicki, *Fracture of prismatic aluminum tubes under reverse straining.* International journal of impact engineering, 2006. **32**(5): p. 671-701.

92. Norris Jr, D., et al., *A plastic-strain, mean-stress criterion for ductile fracture.* Journal of Engineering Materials and Technology, 1978. **100**(3): p. 8.

93. Marino, B., F. Mudry, and A. Pineau, *Experimental study of cavity growth in ductile rupture.* Engineering Fracture Mechanics, 1985. **22**(6): p. 989-996.

94. Hooputra, H., et al., *A comprehensive failure model for crashworthiness simulation of aluminium extrusions.* International Journal of Crashworthiness, 2004. **9**(5): p. 449-464.

95. Cockcroft, M.G. and D.J. Latham, *Ductility and the Workability of Metals.* Journal of the Institute of Metals, 1968. **96**.

96. Bai, Y. and T. Wierzbicki, *A new model of metal plasticity and fracture with pressure and Lode dependence.* International journal of plasticity, 2008. **24**(6): p. 1071-1096.

97. Gurson, A.L., *Continuum theory of ductile rupture by void nucleation and growth: Part I—Yield criteria and flow rules for porous ductile media.* Journal of Engineering Materials and Technology, 1977. **99**(1): p. 14.

98. Tvergaard, V., *Influence of voids on shear band instabilities under plane strain conditions.* International Journal of fracture, 1981. **17**(4): p. 389-407.

99. Tvergaard, V., *On localization in ductile materials containing spherical voids.* International Journal of fracture, 1982. **18**(4): p. 237-252.

100. Tvergaard, V. and A. Needleman, *Analysis of the cup-cone fracture in a round tensile bar.* Acta metallurgica, 1984. **32**(1): p. 157-169.

101. Kachanov, L., *Introduction to continuum damage mechanics.* Vol. 10. 1986: Springer Science & Business Media.

102. Chaboche, J.-L., *Anisotropic creep damage in the framework of continuum damage mechanics.* Nuclear engineering and design, 1984. **79**(3): p. 309-319.

103. Lemaitre, J., *A course on damage mechanics.* 1996: Springer Science & Business Media.

104. d'Escatha, Y. and J. Devaux, *Numerical study of initiation, stable crack growth, and maximum load, with a ductile fracture criterion based on the growth of holes*, in *Elastic-plastic fracture.* 1979, ASTM International.

105. Addessio, F. and J. Johnson, *Rate-dependent ductile failure model.* Journal of applied physics, 1993. **74**(3): p. 1640-1648.

106. Lemaitre, J., *Coupled elasto-plasticity and damage constitutive equations.* Computer methods in applied mechanics and engineering, 1985. **51**(1-3): p. 31-49.

107. Rousselier, G., *Ductile fracture models and their potential in local approach of fracture.* Nuclear engineering and design, 1987. **105**(1): p. 97-111.

108. Lemaitre, J. and J. Dufailly, *Damage measurements.* Engineering Fracture Mechanics, 1987. **28**(5-6): p. 643-661.

109. Kanvinde, A. and G. Deierlein, *Finite-element simulation of ductile fracture in reduced section pull-plates using micromechanics-based fracture models.* Journal of Structural Engineering, 2007. **133**(5): p. 656-664.

110. Liao, F., W. Wang, and Y. Chen, *Parameter calibrations and application of micromechanical fracture models of structural steels.* Structural engineering and mechanics, 2012. **42**(2): p. 153-174.

111. Liao, F., W. Wang, and Y. Chen, *Ductile fracture prediction for welded steel connections under monotonic loading based on micromechanical fracture criteria.* Engineering Structures, 2015. **94**: p. 16-28.

112. Lemaitre, J., *A course on damage mechanics.* 2012: Springer Science & Business Media.

113. Sun, D.-Z. and A. Honig, *Significance of the characteristic length for micromechanical modelling of ductile fracture.* WIT Transactions on Engineering Sciences, 1970. **6**.

114. Cooke, R. and A. Kanvinde, *Constitutive parameter calibration for structural steel: Non-uniqueness and loss of accuracy.* Journal of Constructional Steel Research, 2015. **114**: p. 394-404.

115. Gao, X., et al., *On stress-state dependent plasticity modeling: Significance of the hydrostatic stress, the third invariant of stress deviator and the non-associated flow rule.* International Journal of Plasticity, 2011. **27**(2): p. 217-231.

116. Wilson, C.D., *A critical reexamination of classical metal plasticity.* J. Appl. Mech., 2002. **69**(1): p. 63-68.

117. Pantousa, D. and T. Karavasilis, *Experimental and numerical investigation of the ductile fracture of structural steel at elevated temperatures.* Journal of Constructional Steel Research, 2020: p. 106444.

118. Gao, X., et al., *Effects of the stress state on plasticity and ductile failure of an aluminum 5083 alloy.* International Journal of Plasticity, 2009. **25**(12): p. 2366-2382.

119. Voce, E., *The relationship between stress and strain for homogeneous deformation.* Journal of the Institute of Metals, 1948. **74**: p. 537-562.

120. Hertelé, S., W. De Waele, and R. Denys, *A generic stress–strain model for metallic materials with two-stage strain hardening behaviour.* International Journal of Non-Linear Mechanics, 2011. **46**(3): p. 519-531.

121. Qin, J., et al., *Modeling strain-path changes in aluminum and steel.* International Journal of Solids and Structures, 2017. **117**: p. 123-136.

122. Vysochinskiy, D., *Formability of aluminium alloy subjected to prestrain by rolling*, in *Department of structural engineering.* 2014, Norwegian University of Science and Technology.

123. Khadyko, M., et al., *An experimental–numerical method to determine the work-hardening of anisotropic ductile materials at large strains.* International Journal of Mechanical Sciences, 2014. **88**: p. 25-36.

124. Johannessen, H., et al., *Experimental and numerical study of notched SHS made of different S355 steels.* Journal of Constructional Steel Research, 2021. **182**: p. 106673.

125. Zhang, Z., et al., *A notched cross weld tensile testing method for determining true stress–strain curves for weldments.* Engineering fracture mechanics, 2002. **69**(3): p. 353-366.

126. Tu, S., et al., *Stress–strain curves of metallic materials and post-necking strain hardening characterization: A review.* Fatigue & Fracture of Engineering Materials & Structures, 2020. **43**(1): p. 3-19.

127. Jun, C., F.-g. Li, and Z.-k. SUN, *Tensile stress–strain behavior of metallic alloys.* Transactions of Nonferrous Metals Society of China, 2017. **27**(11): p. 2443-2453.

128. Hollomon, J.H., *Tensile deformation.* Aime Trans, 1945. **12**(4): p. 1-22.

129. Dassault Systèmes, *ABAQUS Analysis User's Manual (Version 6.14).* 2014, Providence, RI: Dassault Systèmes Simulia Corp.

130. Whittaker, A., et al., *Engineering demand parameters for structural framing systems.* Report number: ATC-58-2, 2004. **2**.

131. International Organization for Standardization, *ISO 11463: Corrosion of metals and alloys - Guidelines for the evaluation of pitting corrosion.* 2020.

132. ASTM, *Standard guide for examination and evaluation of pitting corrosion (G46-94).* 2005, ASTM International.

133. Wang, R., R.A. Shenoi, and A. Sobey, *Ultimate strength assessment of plated steel structures with random pitting corrosion damage.* Journal of Constructional Steel Research, 2018. **143**: p. 331-342.

134. Zhao, Z., et al., *Influence of random pitting corrosion on moment capacity of thin-walled circular tubes subjected to compression force.* International Journal of Pressure Vessels and Piping, 2021. **189**: p. 104260.

135. Zhao, Z., et al., *Influence of pitting corrosion on the bending capacity of thin-walled circular tubes.* Journal of the Brazilian Society of Mechanical Sciences and Engineering, 2018. **40**(11): p. 1-12.

136. Xia, M., Y. Wang, and S. Xu, *Study on surface characteristics and stochastic model of corroded steel in neutral salt spray environment.* Construction and Building Materials, 2021. **272**: p. 121915.

137. Mao, K. and C. Sun, *A refined global-local finite element analysis method.* International journal for numerical methods in engineering, 1991. **32**(1): p. 29-43.

138. Marenić, E., I. Skozrit, and Z. Tonković, *On the calculation of stress intensity factors and J-integrals using the submodeling technique.* Journal of pressure vessel technology, 2010. **132**(4).

139. Narvydas, E. and N. Puodziuniene. *Applications of sub-modeling in structural mechanics.* in *Proceedings of 19th International Conference. Mechanika, Kaunas, Lithuania.* 2014.

140. Hirai, I., B.P. Wang, and W.D. Pilkey, *An efficient zooming method for finite element analysis.* International Journal for Numerical Methods in Engineering, 1984. **20**(9): p. 1671-1683.

141. Kardak, A.A., *On an effective submodeling procedure for stresses determined with finite element analysis.* 2015, Louisiana State University.

142. Sun, C. and K. Mao, *A global-local finite element method suitable for parallel computations.* Computers & structures, 1988. **29**(2): p. 309-315.

143. Oñate, E., *Structural analysis with the finite element method. Linear statics: volume 2: beams, plates and shells*. 2013: Springer Science & Business Media.

144. Verma, A.S., et al., *Comparison of numerical modelling techniques for impact investigation on a wind turbine blade.* Composite Structures, 2019. **209**: p. 856-878.

145. Mora, D., et al., *Fracture mechanics analyses of a reactor pressure vessel under non-uniform cooling with a combined TRACE-XFEM approach.* Engineering Fracture Mechanics, 2020. **238**: p. 107258.

Appended codes

USDFLD subroutine developed to implement Void Growth Model fracture criterion in Abaqus/Implicit.

```
C ---------------------subroutine variables -----------------------
      SUBROUTINE USDFLD(FIELD,STATEV,PNEWDT,DIRECT,T,CELENT,
     1 TIME,DTIME,CMNAME,ORNAME,NFIELD,NSTATV,NOEL,NPT,LAYER,
     2 KSPT,KSTEP,KINC,NDI,NSHR,COORD,JMAC,JMATYP,MATLAYO,
     3 LACCFLA)
C
      INCLUDE 'ABA_PARAM.INC'

      CHARACTER*80 CMNAME,ORNAME
      CHARACTER*3  FLGRAY(15)
      DIMENSION FIELD(NFIELD),STATEV(NSTATV),DIRECT(3,3),
     1 T(3,3),TIME(2)
      DIMENSION ARRAY(15),JARRAY(15),JMAC(*),JMATYP(*),
     1 COORD(*)

C -------------------------- Current values of variables -----------------------

C -------------------------- Call current values of PEEQ-----------------------
      CALL GETVRM('PE',ARRAY,JARRAY,FLGRAY,JRCD,JMAC,JMATYP,
     1 MATLAYO,LACCFLA)
C    EPL is element's PEEQ that is ARRAY(7)
      EPL = ARRAY(7)
C -------------------------- Call current values of stress-----------------------
      CALL GETVRM('S',ARRAY,JARRAY,FLGRAY,JRCD,JMAC,JMATYP,
     1 MATLAYO,LACCFLA)

C    Sij is element's stress components
      S11 = ARRAY(1)
      S22 = ARRAY(2)
      S33 = ARRAY(3)
      S12 = ARRAY(4)
      S13 = ARRAY(5)
      S23 = ARRAY(6)

C    Hydrostatic Pressure
      PT = -(ARRAY(1)+ARRAY(2)+ARRAY(3))/3.0

C    Von Mises stress
```

```
      MS = SQRT( 0.5*((ARRAY(1)-ARRAY(2))**2+(ARRAY(1)-ARRAY(3))**2+(AR
     1 RAY(2)-ARRAY(3))**2+6*(ARRAY(4)**2+ARRAY(5)**2+ARRAY(6)**2)))



C    Triaxiality only for tensile elements (MS>0)
      IF(MS .GT. (0))THEN


         TR = -PT/MS
C        Save triaxiality in Solution-dependent state variable (2)
         STATEV(2)=TR
      ELSE
C        For compression element DVGI is zero so triaxiality is not important assume to be 0
         TR=0
         STATEV(2)=TR
      ENDIF


C -----------------------Calculate increment of values------------------------


C    call PEEQ from previous time increment of analysis
      CALL GETVRM('SDV',ARRAY,JARRAY,FLGRAY,JRCD,JMAC,JMATYP,
     1 MATLAYO,LACCFLA)



      IF(EPL .GT. (0))THEN
C        DEPL is the increment in PEEQ
C        STATEV(1) is PEEQ from previous time increment of analysis
         DEPL=ABS(EPL-STATEV(1))
C        Save PEEQ in Solution-dependent state variable (1)
         STATEV(1)=EPL
C        If triaxiality is positive (tension)
         IF (TR .GE. (0))THEN
C        DVGI is the increment in VGI
         DVGI=DEPL*exp(1.5*ABS(TR))
C        save VGI in Solution-dependent state variable (3)
C        STATEV(3) is VGI from previous time increment of analysis
         STATEV(3)=STATEV(3)+DVGI


         ELSE
C        If triaxiality is negative (compression)
C        No change in VGI
         DVGI=0
C        save VGI in Solution-dependent state variable (3)
         STATEV(3)=STATEV(3)+DVGI
         ENDIF
```

102

```fortran
      ELSE
C         If the plastic strain was 0 then the VGI is zero.
C         save VGI in Solution-dependent state variable (3)
          STATEV(3)=0

      ENDIF


C --------------------------- Element removal -----------------------------------

C      If VGI>VGIcritical=3.09 (this value must be calibrated for material)
       IF(STATEV(3) .GT. (3.09))THEN
C         set field variable (1)=1
          FIELD(1) = 1
C         save Solution-dependent state variable (4) =0 that means removal of the element
          STATEV(4) = 0

       ELSE
C         set field variable (1)=0
          FIELD(1) = 0
C         save Solution-dependent state variable (4) =1 that means the element is not removed
          STATEV(4) = 1

       ENDIF

      RETURN
      END
```

VUSDFLD subroutine developed to implement Void Growth Model fracture criterion in Abaqus/Explicit.

```fortran
C --------------------Subroutine variables ----------------------
      subroutine vusdfld(
1   nblock, nstatev, nfieldv, nprops, ndir, nshr,
2   jElem, kIntPt, kLayer, kSecPt,
3   stepTime, totalTime, dt, cmname,
4   coordMp, direct, T, charLength, props,
5   stateOld,
6   stateNew, field )
C
      include 'vaba_param.inc'
C
      dimension jElem(nblock), coordMp(nblock,*),
1         direct(nblock,3,3), T(nblock,3,3),
2         charLength(nblock), props(nprops),
3         stateOld(nblock,nstatev),
4         stateNew(nblock,nstatev),
5         field(nblock,nfieldv)
      character*80 cmname
C
C   Local arrays from vgetvrm are dimensioned to
C    maximum block size (maxblk)
C
      parameter( nrData=6 )
      character*3 cData(nblock,nrData)
      dimension rData(nblock*nrData), jData(nblock*nrData)
      dimension eqps(nblock)
      dimension stress(nblock*nrData)
      dimension stresses(nblock,nrData)


C -------------------------- Current values of variables -----------------------


C -------------------------- Call current values of PEEQ------------------------
      call vgetvrm( 'PEEQ', eqps, jData, cData, jStatus )
C -------------------------- Call current values of stress----------------------
      call vgetvrm( 'S', stress, jData, cData, jStatus )
      stresses = reshape(stress, (/nblock, nrData/))


C -- A loop to obtain PEEQ, stress, pressure, and triaxiality for each element----
```

```fortran
      do k = 1, nblock

C     EPL is element's PEEQ
      EPL = eqps(k)

C     Sij is element's stress components
      S11 = stresses(k,1)
      S22 = stresses(k,2)
      S33 = stresses(k,3)
      S12 = stresses(k,4)
      S13 = stresses(k,5)
      S23 = stresses(k,6)
C     Hydrostatic Pressure
      PT = -(stresses(k,1)+stresses(k,2)+stresses(k,3))/3.0

C     Von Mises stress

      MS = SQRT( 0.5*((stresses(k,1)-stresses(k,2))**2+(stresses(k,1)
     1 -stresses(k,3))**2+(stresses(k,2)-stresses(k,3))**2+6*
     2 (stresses(k,4)**2+stresses(k,5)**2+stresses(k,6)**2)))

C     Triaxiality only for tensile elements (MS>0)

      IF(MS .GT. (0))THEN

          TR = -PT/MS
C         Save triaxiality in Solution-dependent state variable (2)
          stateNew(k,2)=TR
      ELSE
C         For compression element DVGI is zero, so triaxiality is not important assume to be 0
          TR=0
          stateNew(k,2)=TR
      ENDIF

C ------------------------Calculate increment of values------------------------

C     For elements in the plastic range
      IF(EPL .GT. (0))THEN
C         DEPL is the increment in PEEQ
C         stateOld(k,1) is PEEQ from previous time increment of analysis
          DEPL=ABS(EPL-stateOld(k,1))
C         Save PEEQ in Solution-dependent state variable (1)
          stateNew(k,1)=EPL
```

105

```fortran
C        If triaxiality is positive (tension)
         IF (TR .GE. (0))THEN
C         DVGI is the increment in VGI
         DVGI=DEPL*exp(1.5*ABS(TR))
C        save VGI in Solution-dependent state variable (3)
C        stateOld(k,3) is VGI from previous time increment of analysis
         stateNew(k,3)=stateOld(k,3)+DVGI

         ELSE
C        If triaxiality is negative (compression)
C        No change in VGI
         DVGI=0
C        save VGI in Solution-dependent state variable (3)
         stateNew(k,3)=stateOld(k,3)+DVGI
         ENDIF

      ELSE
C        If the plastic strain was 0 then the VGI is zero.
C        save VGI in Solution-dependent state variable (3)
         stateNew(k,3)=0

      ENDIF

C --------------------------- Element removal -----------------------------------

C      If VGI>VGIcritical=3.09 (this value must be calibrated for material)
       IF(stateNew(k,3) .GT. (3.09))THEN
C         set field variable (1)=1
         field(k,1) = 1
C         save Solution-dependent state variable (4) =0 that means removal of the element
         stateNew(k,4) = 0

         ELSE
C         set field variable (1)=0
         field(k,1) = 0
C         save Solution-dependent state variable (4) =1 that means the element is not removed
         stateNew(k,4) = 1

         ENDIF

      end do

      RETURN
      END
```

Appended papers

Paper I:
Performance of welded flange plate joints between steel beams and box columns without continuity plates

Performance of welded flange plate joints between steel beams and box columns without continuity plates

Mohammad Ali Mahdavipour, Songxiong Ding & Dmitry Vysochinskiy
Department of Engineering Sciences, University of Agder, Grimstad, Norway

ABSTRACT: In this paper, the cyclic performance of welded flange plate beam-to-box column connections was studied with focus on joints without continuity plates. The effect of continuity plates elimination on the stiffness and strength of these joints was investigated by a series of numerical analyses. In addition, new reinforcement details with Vertical Edge Stiffeners (VES) were proposed to reduce the plastic deformation demand on Completed Joint Penetration welds (CJPs). Results showed that continuity plates are important elements for the strength and stiffness of this kind of joint. In absence of continuity plates, all plastic deformations concentrated on the CJPs welds and column wall that could initiate undesirable modes of fracture. Finally, plastic deformation demand on the joints revealed that using vertical edge stiffeners transferred the plastic strain concentration from CJPs to beam plastic hinge.

1 INTRUDUCTION

Using built-up box columns in 3D frames is common when structures become taller and rolled wide-flange sections are not available or optimum. Box columns have high flexural resistance around both main axes and provide also more torsional stiffness because of their closed section (Sherman, 1996). Despite these two advantages, the performance of beam connection to box column is very sensitive to details of reinforcement due to low out-of-plane stiffness of the column walls. The most prevalent reinforcement used in previous research and codes is transverse stiffener or continuity plate (Aisc, 2016, Chen et al., 2004, Farooghi Mehr and Ghobadi, 2017). Previous experimental and numerical studies showed that without continuity plates, the joint capacity of moment transferring can be affected significantly due to out-of-plane deformations in the wall plates of the column (Anderson and Linderman, 1991). However, using continuity plates is expensive and sometimes difficult to implement and inspect. This difficulty is related to the connection between the last face of the column and continuity plates where regular welding procedures are not applicable in a closed section.

One of the first comprehensive studies was carried out by Anderson & Linderman (1991) to investigate this particular type of joint. Eleven specimens from A36 steel grade with wide-flange beams and box columns were tested. Test results showed when the thickness of continuity plates is less than beam flange thickness, buckling of continuity plates would be probable under ultimate loads. It was also concluded that plastic hinge cannot form in the connected beam when the width-to-thickness ratio of column walls without continuity plates is large.

Chen, et al. (2004) also carried out six full-scale tests on the steel bolted web and welded flange (BWWF) connections between wide-flange beams and box columns under cyclic load, with focus on rib reinforcement. Results showed that welding continuity plates inside the box column is vital to the integrity of the joint.

Kim et al. (2003) experimentally and numerically investigated the behavior of the connections between steel beams and box columns with pre-Northridge details. The outcomes indicated that brittle fracture in Complete Joint Penetration welds (CJPs) under cyclic load was the main fracture mode of the tested specimens. Column type, continuity plates and geometry of joint were argued as decisive factors for determination of fracture locus in such joints.

Kiamanesh et al. (2010) used 20 numerical models to investigate the effect of internal and external stiffeners on the connection hysteresis, load transfer mechanism, and stress distribution. This study showed that when the continuity plates are in the place, the main mechanism of the moment transferring from beam to column is the top flange plate.

Another experimental and numerical study was carried out by Cholami et al. (2013) on seismic performance of WFP (Welded Flange Plates) connections between steel I-beams and box columns. In this study, three full-scale joints were tested under AISC-341 cyclic test protocol (Fig. 1) to investigate the effect of the flange plates and fillet welds geometry on the performance of the joints. All three specimens met the criteria for special moment-resisting frames according to AISC-341 (AISC, 2016). Plastic deformations only developed in the plastic hinge area in the beams. The results showed that the panel zones and continuity plates experienced deformations in the elastic range
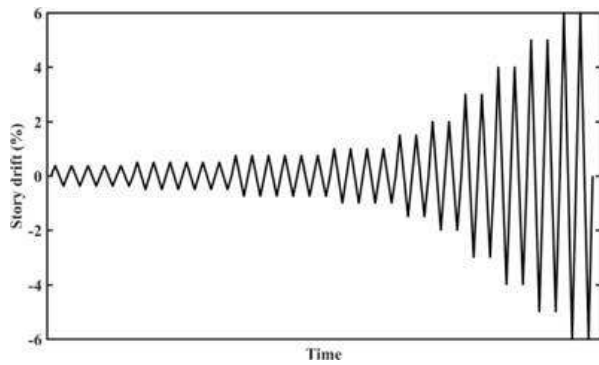
Figure 1. Cyclic loading sequence prescribed by AISC seismic provisions for beam-to-column connections testing (AISC, 2016).

only. On the other hand, WFP connection is a common practice in moment-resisting joints for steel frames because of flexibility in changing the width and length of flange plates, and larger dimensional tolerances in construction. Because of these advantages, this paper focused on this kind of connection.

2 OBJECTIVE AND SCOPE

Considering difficulties and limitations related to the construction and inspection of continuity plates, this article presents the cyclic performance of unstiffened beam-to-box column joints with WFP connection. FEM models were created to investigate the joints stiffness and strength in absence of the continuity plates. New details (configuration) of joints in replacement of continuity plates were proposed in order to retain strength and stiffness of joints. In this method, the flange plates were considered to have width equal to column, and two Vertical Edge Stiffeners (VES) were added to release plastic strain concentration from CJP welds. Numerical models were validated by experimental outcomes for a benchmark joint.

3 JOINT MODELS

To investigate the cyclic performance of unstiffened WFP connections between I-beams and box columns, a joint studied by Cholami et al. (2013) was selected as benchmark. It was constructed with an I-beam ($380 \times 200 \times 8 \times 12$ mm) and a box column ($400 \times 400 \times 20$mm) with dimensions as shown in Figure 2. All parts were made from ST37 steel with mechanical properties as given in Table 1. Loading sequence as prescribed by AISC seismic provisions (Fig.1) was used to study the cyclic behavior of this joint (AISC, 2016). The hysteresis curve of the tested specimen is shown in Figure 3.

In order to study the effect of continuity plates elimination and the newly proposed details, four numerical models were created with ABAQUS /CAE.

The notation of models and geometry of flange plates are listed in Table 2. The first model (S-WFP200-CP) is the model of benchmark joint and

Table 1. Mechanical properties of steel used in the benchmark joint (Gholami et al., 2013).

	σ_y^*	ε_y^*	σ_u^{**}	ε_u^{**}
	Mpa	%	Mpa	%
Beam flange	300	0.150	430	18
Beam web	310	0.155	400	17
Column plates	290	0.145	390	15
Top flange plate	310	0.155	450	18
Bottom flange plate	290	0.145	390	15

*σ_y and ε_y are yield stress and strain; σ_u and ε_u are ultimate stress and strain.
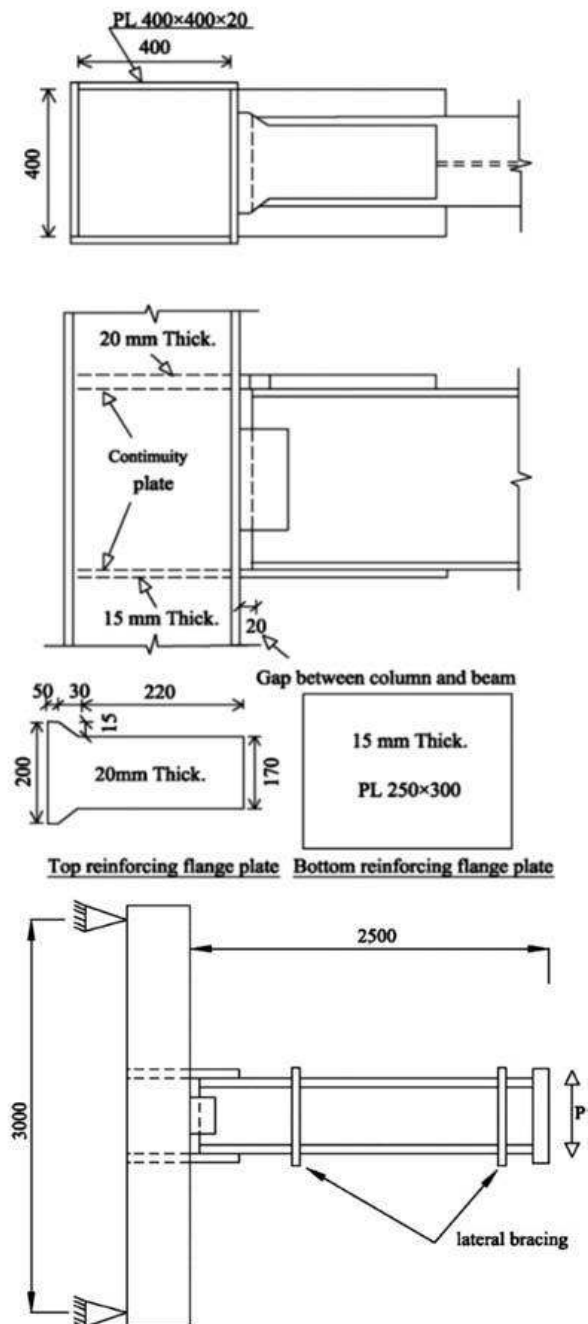
Figure 2. Scheme of the test setup and geometry of benchmark joint tested by Cholami et al. (2013).

1180
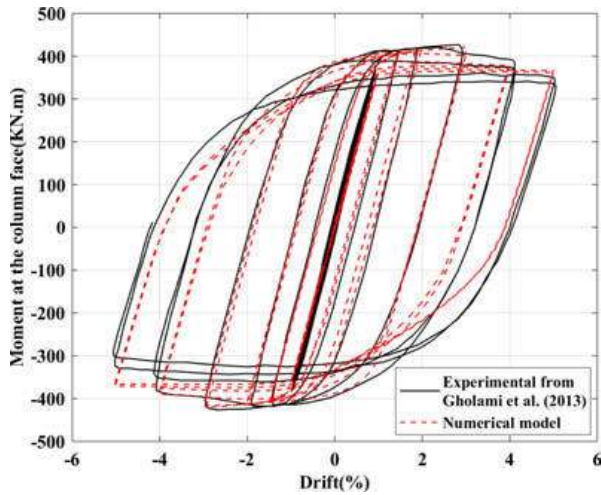
Figure 3. Comparison between numerical (present study) and experimental (Cholami et al., 2013) hysteresis curves for the benchmark joint.

Table 2. Geometrical features of studied joints.

Specimen	flange plate width (B_{fp}) mm	flange plate length (L_{fp}) mm
S-WFP200-CP*	200	300
S-WFP200	200	300
S-WFP400	400	470
S-WFP400-VES**	400	470

* The benchmark joint with continuity plates.
** Joint with vertical edge stiffeners.

other three models were created without continuity plates and by different flange plate width (B_{fp}=200,400 mm). Since the angle of tapering region in the top plate must be smaller than 30° (INBC, 2014), the length of the flange plates (L_{fp}) also was increased. Other properties implemented in these three joints were similar to those for the benchmark joint model. Model S-WFP400-VES is the same as the model S-WFP400, but with two additional vertical edge stiffeners (VESs, t=20mm) that were welded to column edges and flange plates. In fact, these two plates are expected to mitigate stress and strain concentration of CJP welds (see Figure 4 for details of vertical edge stiffeners in the joint). These new components can be easily welded to bottom flange plate and the column edges before column installation. After column and beam installation in the right position, the top flange plate also can be welded to these two plates by CJP welds. As a result, all welds can be performed in good circumstance and they are still in access for inspection.

To create numerical models, solid brick elements (C3D8R) were utilized, with finer meshes close to the center of the joints, and the locus of the plastic hinge in the beam, while in other regions coarser meshes was used as shown in Figure 5.
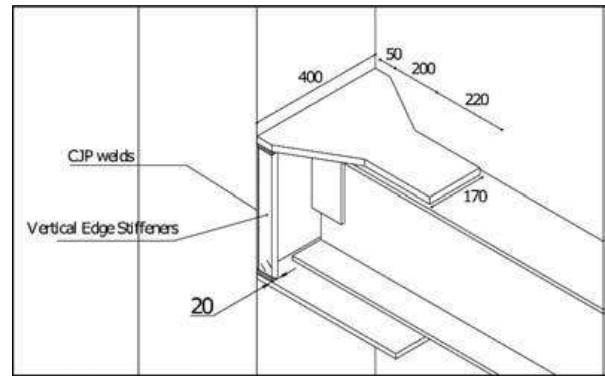
Figure 4. Details of vertical edge stiffeners (VESs) used to release stress and strain concentration in the place of CJP welds (all dimensions are in mm).
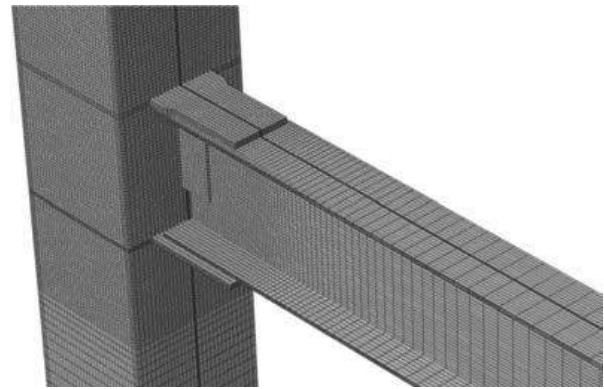
Figure 5. FEM model and mesh configuration for the benchmark joint (S-WFP200-CP).

Bilinear kinematic hardening combined with von Mises yield criterion was used to model plasticity in steel based on the material properties as presented in table 1. Kinematic hardening also was applied to consider steel hardening under cyclic loads. Welding details were ignored in the numerical models. Boundary conditions were simulated the same as the test condition, with the hinges at the ends of the column and sufficient lateral bracing in the beam.

Hysteresis curves as extracted from each model were compared with that from benchmark joint to investigate the performance of each model. furthermore, equivalent plastic strain (PEEQ) was used as a representative parameter for plastic damages. This parameter indicates the cumulative plastic strain demand in the components. When the initial equivalent plastic strain is zero, the PEEQ can be calculated by integrating plastic strain (based on Mises plasticity) on the analysis time history (t) as follows (Dassault Systèmes, 2016):

$$PEEQ = \int_0^t \varepsilon_{eq} dt \qquad (1)$$

Where ε_{eq} = Equivalent Von Mises strain.

Figure 3 compares the numerical and experimental hysteresis curves for benchmark joint (S-WFP200-CP). It shows a good agreement between the numerical model outcomes and experimental results. Figure 6

1181
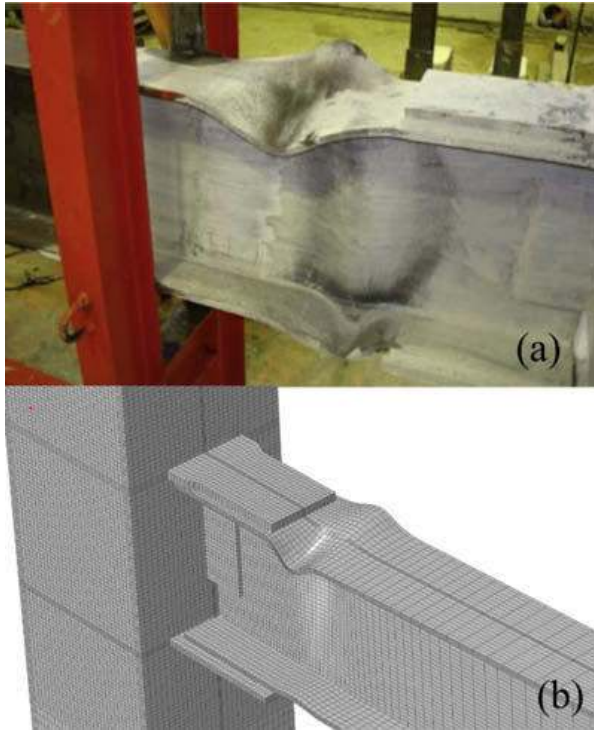
Figure 6. Benchmark joint deformed shape (a) experimental (Gholami et al., 2013) (b) numerical (present study).
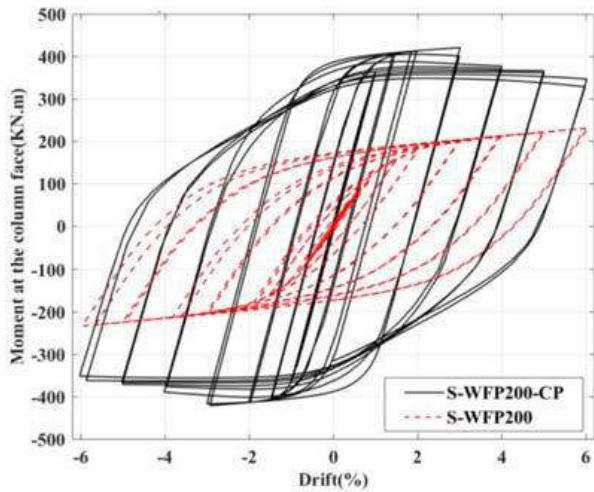
Figure 7. Hysteresis curves of S-WFP200 and S-WFP200-CP (benchmark) specimens.

also shows the deformed shape of the beam as simulated in S-WFP200-CP model, which is close to the deformed shape of this specimen as seen in experiment.

4 RESULTS

Figures 7-9 compare the cyclic performance of modified joints (without continuity plates) with the benchmark joint. As can be seen in Figure 7, the modified joint S-WFP200 (with flange plate width smaller than column width (B_{fp} =200 mm)), exhibited a significant loss in both strength and stiffness. Joint S-WFP200
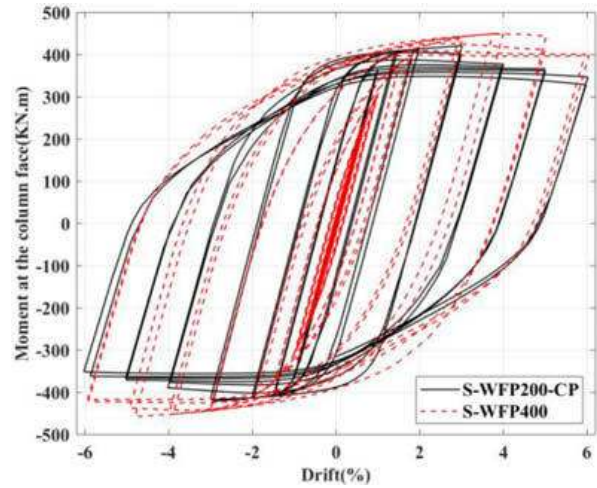
Figure 8. Hysteresis curves of S-WFP400 and S-WFP200-CP (benchmark) specimens.
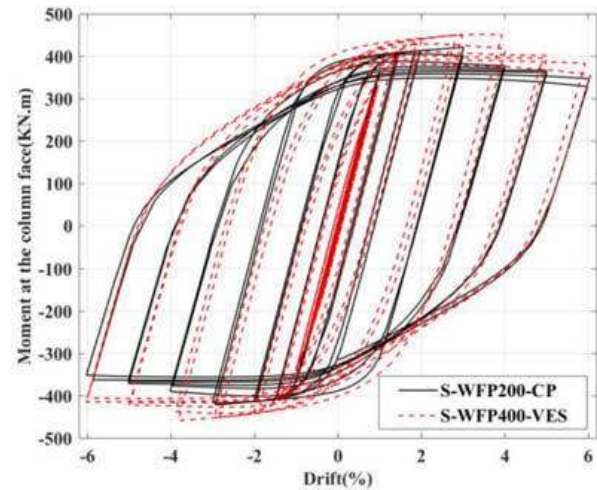
Figure 9. Hysteresis curves of S-WFP400-VES and S-WFP200-CP (benchmark) specimens.

showed 45% and 61% decrement in the maximum strength and initial stiffness of the joint respectively. In terms of plastification mode as shown in Figure 11 for the PEEQ, in S-WFP200 joint no plastic deformation developed in the beam while a large amount of plastic strain concentration was formed on the CJPs and column walls (maximum PEEQ=4.4). This concentration might lead to weld fracture, punching fracture or lamellar tearing in the column wall. It is worth mentioning that all plastic deformations concentrated on the beam in the benchmark joint (see Fig.10) that is a desirable mode of energy dissipation in steel moment-resisting frames.

In comparison with S-WFP200 joint, in S-WFP400 and S-WFP400-VES specimens (B_{fp} is the same as column width=400 mm), stiffness and strength are approximately equal to benchmark joint (Figs 8-9). In fact, S-WFP400 joint provided about 7% more capacity and almost equal stiffness in comparison with benchmark joint, however the maximum PEEQ (5.37) remained at the location of connection between flange plates and column walls (Fig. 12). In comparison, in

1182
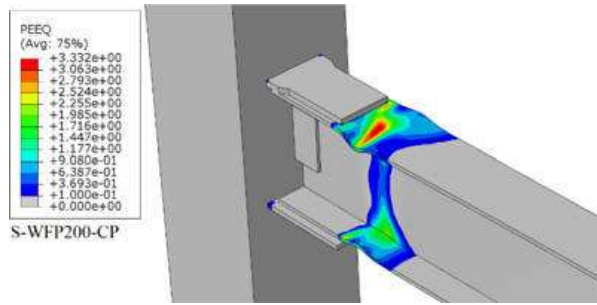
Figure 10. PEEQ distribution in S-WFP200-CP (benchmark joint).
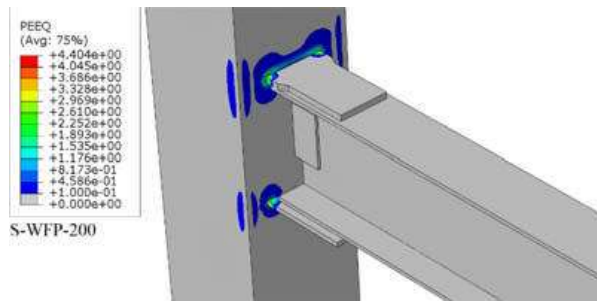
Figure 11. PEEQ distribution in S-WFP200.
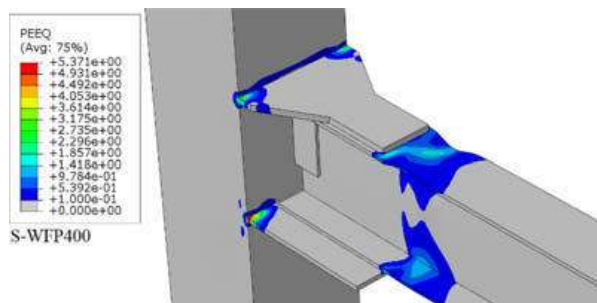
Figure 12. PEEQ distribution in S-WFP400.
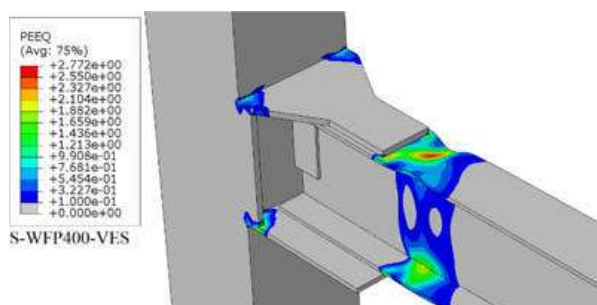
Figure 13. PEEQ distribution in S-WFP400-VES.

S-WFP400-VES joint (with VESs), the stiffness and capacity of the joint was 7% more than the benchmark joint, while its maximum PEEQ (2.77) occurred in the beam (Fig. 13). It is noted that this value is approximately half of that corresponding value in S-WFP400. It is obvious that by using vertical edge stiffeners, most of the plastic deformations migrated from CJP welds to the beam plastic hinge.

5 CONCLUSIONS

In this investigation, the aim was to assess the cyclic performance of WFP moment-resisting connections between steel I-beams and box columns without continuity plates. Hysteresis curves of the studied joints without continuity plates demonstrated that the continuity plates are decisive elements to determine the stiffness and strength of such joints. Moreover, the obtained results showed that in absence of continuity plates, the locus of plastification and fracture of the joints could be completely different from similar joints with continuity plates. When the width of the flange plates was smaller than column width, all plastic deformations concentrated on CJPs. In situation that the width of flange plate was taken equal to column width, the joint exhibited the strength and stiffness approximately equal to the benchmark joint, however, the maximum plastic deformation demand was still on the CJP welds. To cope with this issue, new details with vertical edge stiffeners were proposed to release stress and strain concentration from CJP welds. The results showed that using the proposed details is an effective method to release plastic deformations on CJP welds in joints without continuity plates. This conclusion can be drawn from maximum PEEQ that occurred on the beam plastic hinge instead of CJP welds.

REFERENCES

AISC 2016. Seismic provisions for structural steel buildings (AISC 341–16). American Institute of Steel Construction.

Anderson, J. C. & Linderman, R. R. 1991. Steel beam to box column connections. Los Angeles, California: Department of Civil Engineering University of Southern California.

Chen, C. C., Lin, C. C. & Tsai, C. L. 2004. Evaluation of reinforced connections between steel beams and box columns. *Engineering structures,* 26, 1889–1904.

Dassault Systèmes 2016. Abaqus/CAE User's Manual.

Farooghi Mehr, S. M. R. & Ghobadi, M. S. 2017. Seismic performance of retrofitted WFP connections joined to box column using ribs. *Journal of Constructional Steel Research,* 137, 297–310.

Gholami, M., Deylami, A. & Tehranizadeh, M. 2013. Seismic performance of flange plate connections between steel beams and box columns. *Journal of Constructional Steel Research,* 84, 36–48.

INBC 2014. Iranian National Building Code (INBC), Part 10: Steel Structures. Ministry of Roads and Urban Development.

Kiamanesh, R., Abolmaali, A. & Ghassemieh, M. 2010. The effect of stiffeners on the strain patterns of the welded connection zone. *Journal of Constructional Steel Research,* 66, 19–27.

Kim, T. 2003. *Experimental and analytical performance evaluation of welded steel moment connections to box or deep W-shape columns.* Doctor of Philosophy, University of California, Berkeley.

Sherman, D. R. 1996. Designing with structural tubing. *Engineering Journal,* 33, 101–109.

Paper II:

Effect of the joint strength on the performance of ordinary moment-resisting frames under a progressive collapse situation

EASD Procedia

EFFECT OF THE JOINT STRENGTH ON THE PERFORMANCE OF ORDINARY MOMENT-RESISTING FRAMES UNDER A PROGRESSIVE COLLAPSE SITUATION

Mohammad Ali Mahdavipour[1], Dmitry Vysochinskiy[1]

[1] Department of Engineering Sciences, University of Agder
Jon Lilletuns vei 9, 4879 Grimstad, Norway
e-mail: {ali.mahdavipour, dmitry.vysochinskiy} @uia.no

Keywords: Progressive collapse, Panelzone, Column removal, Ductile fracture.

Abstract. In standard design procedures of steel structures, buildings are usually designed for gravity and seismic load rather than a progressive collapse situation. When a structure is located in a low seismic zone, the codes have dictated fewer requirements regarding the beam-to-column strength ratio and the panelzone strength. In this study, a frame subassembly from an 8-story ordinary steel moment-resisting structure with different strength of exterior joints was investigated by numerical models under a column removal situation. The results revealed that although the beam-to-column strength ratio and the panelzone strength are generally less critical parameters in the seismic design of ordinary moment-resisting frames, they can have a notable effect on the fracture pattern and the capacity of the structure under a progressive collapse. Hence a special consideration about the joints strength is needed when a structure is aimed to be designed for a progressive collapse situation.

1 INTRODUCTION

Progressive collapse is known as a rapid dynamic process that usually initiates from a local failure and propagates element-by-element to a global or partial collapse of the structure [1-4]. When a column is removed within a story of a steel structure, several sequential mechanisms act against the unbalanced vertical load. At very early stages, the beams and connections are under shear actions. In a subsequent stage as vertical displacement increases, the flexural moment at the beams becomes the dominant resisting mechanism in the frame. Finally, if the connections are ductile enough to undergo large deformations and adapt to a new configuration, the catenary action will be activated as the last resisting mechanism [1-3]. Since catenary action plays the main role in the frame resistance in progressive collapse, enough ductility of steel joints is required to develop catenary forces in the beams; otherwise, the premature global collapse of a multi-story steel structure might occur.

On the other hand, the standard design procedures of steel structures have been developed mostly for other dynamic loads like seismic load rather than a progressive collapse situation. Although the design methodology for seismic load and the progressive collapse is different, the seismic details in the steel structures would influence the performance of the connections and structures under a progressive collapse situation.

Two critical parameters of the seismic design of moment-resisting frames are the beam-to-column strength ratio and the panelzone strength. The codes [5, 6] have determined a maximum level of beam-to-column strength ratio to prevent plastic hinge formation in the columns and reduce the potential of the column-sway collapse. This limit is not obligatory for low-dissipative structures (ordinary moment frames) that are usually designed in a low-seismic zone [5, 6].

So far, the progressive collapse of steel structures has been investigated in many experimental and numerical studies [3, 7-16]; however, there are a few research studies to focus on the effect of the beam-to-column strength ratio and the panelzone strength, especially in ordinary moment frames that the strong-column-weak-beam criterion is usually neglected.

Kim and Kim [17] studied moment-resisting structures with both weak and strong panelzones by using macro-scale numerical models. The results of the nonlinear dynamic analyses showed that the influence of panelzone is dependent on the location of the removed column. The panelzone deformation could be notable if an exterior joint is engaged in the progressive collapse mechanism, while when all joints are interior, the effect of the panelzone deformation on the performance of the frame is not significant. For structures designed for high seismic load, it was also indicated that the panelzone consideration had little effect on the overall performance of the structure. In contrast, the performance of low-rise structures designed only for gravity loads could significantly be affected by the deformation of the panelzones, especially at the exterior bays. It was also reported that excessive panelzone distortion decreased the ductility demand of the beams in some cases.

In a similar study, Kordbagh and Mohammadi [18] investigated special moment-resisting frames under corner and middle column removal scenarios. The results revealed that considering panelzone in the structure with I-section columns notably increased the maximum and permanent vertical displacement of the frame, especially when the removed column was an exterior one. As a general conclusion, the panelzone effect must be considered for progressive collapse evaluation of moment-resisting structures if the panelzones were designed only for minimum requirements recommended by building codes.

Most of the previous studies used macro-level models to evaluate the effect of the beam-to-column strength ratio and the panelzone strength. Such models are not able to provide details about other level phenomena like the joints fracture mode and local plastic deformations.

2   OBJECTIVE AND SCOPE

In this paper, a frame subassembly from an exterior bay of an 8-story moment-resisting structure located in a low-seismic zone was studied under a column removal situation. In such structures, the beam-to-column strength ratio limit is usually ignored due to low seismic hazard. Therefore, two configurations of the selected subassembly with different beam-to-column strength ratios (and different panelzone strength) were investigated by nonlinear finite element simulations. A calibrated plasticity model in conjunction with a ductile damage initiation criterion was used to predict the performance of the subassemblies. These two subassemblies were compared in terms of the capacity and the pattern of ductile fracture.

3   DESCRIPTION OF THE FRAME SUBASSEMBLIES

An 8-story building with a steel moment-resisting system designed for a low-seismic area (e.g., Norway) with 0.1g design ground acceleration was selected as a case study. In terms of geometry, the structure was considered with four equal bays of 5 m (see Fig. 1(a)). Also, each story was assumed to be 3m in height. Besides seismic loads, the structure was designed for 30 kN/m and 12 kN/m uniformly distributed dead and live loads, respectively. The frame was designed according to EC8 [6] for a low ductility class with a behavior factor (q) equal to 2. In this ductility class controlling the strong-column-weak-beam criterion is not obligatory. It is worth mentioning that in the design process of this frame, strength criteria were dominant in the design of the sections, and the size of the beams was constant over the height of the building. All elements were selected from S355J2 structural steel with 355 MPa nominal yield strength. Welded Unreinforced Flange-Welded web (WUF-W) connections described in Fig. 1(c) were employed as the moment-resisting connections to resist lateral seismic loads. The weld access holes with the geometry adapted from AWS D1.8, 2016 [19] was implemented in the web of the beams to provide enough space for the flange Complete Joint Penetration welds (CJPs).
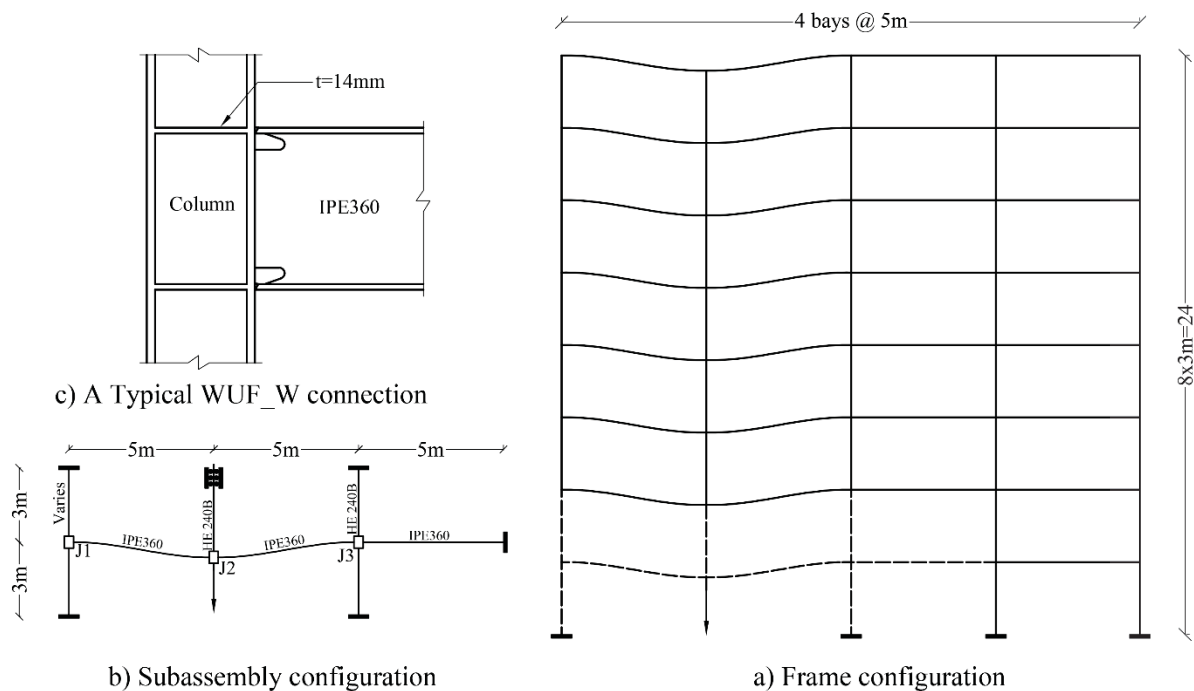
Figure 1: Configuration of a) the studied 8-story moment-resisting frame b) the subassembly c) Welded Unreinforced Flange-Welded web (WUF-W) connections.

Since analyzing the whole of the structure at the micro-level is challenging in terms of computational time and effort, a subassembly of the frame located at the first story as shown in Fig.1(b) was chosen for the finite element analyses. As it is apparent in this figure, this subassembly included three joints (J1, J2, and J3) connected by beams and columns with boundary conditions applied at the interface points between the subassembly and the rest of the frame. This subassembly was selected because the asymmetric strength of the joint J1 and J3 can also provide more detailed information regarding the effects of the beam-to-column joint strength. The previous studies also indicated that in this scenario, the panelzones have the most influence [17].

All design sections were the same in two subassemblies except the left column cross section that varies between HE180B and HE240B to study the effect of the beam-to-column strength ratio and the panelzone strength of the exterior joint. It should be noted that Subassembly-1 is from the original design of the frame that HE180B section was adequate as the left column for applied loads. On the other hand, in Subassembly-2, HE240B as the left column is a conservative design compared to the original frame.

4   NUMERICAL MODELS

4.1 Material model

Ductile fracture is known as a continuous process in which nucleation, growth, and coalescence of microvoids in ductile metals lead to form a new free surface in the material. Based on the prior studies [20-24], ductile fracture initiation is a function of equivalent plastic strain, stress triaxiality, strain rate, and Lode angle; however, the later one is less important when the structure is under tension load (positive triaxiality) [24, 25]. So far, several fracture models have been developed and utilized for predicting and evaluating the ductile fracture in steel structures. Some of these models are more complicated to be implemented (e.g., the Gurson-Tvergaard-Needleman model has over ten parameters for a single material [26]). Some other models (e.g., Johnson-Cook [20] and Bai-Wierzbicki [25]) are more appropriate for engineering applications where the uniaxial test is a standard test.

In this study, a phenomenological ductile damage model for predicting the onset of ductile fracture [27, 28] was used to investigate the fracture pattern of the studied subassemblies. In this model, it is assumed that the equivalent plastic strain at the onset of damage (ε_D^{pl}), is a function of stress triaxiality and strain rate [27]:

$$\varepsilon_D^{pl}(\eta, \dot{\varepsilon}^{pl}) \tag{1}$$

Where $\eta = {}^{\sigma_m}\!/_{\sigma_{eq}}$ is the stress triaxiality, σ_m is hydrostatic pressure and σ_{eq} is Mises equivalent stress. $\dot{\varepsilon}^{pl}$ also denotes the strain rate. Based on this definition, the damage variable can be defined as follows [7]:

$$D = \int \frac{d\varepsilon^{pl}}{\varepsilon_D^{pl}(\eta, \dot{\varepsilon}^{pl})} \tag{2}$$

This damage variable is an incremental state variable that increases monotonically with plastic deformations (ε^{pl}) to reach D=1 which indicates the fracture initiation. To use this model, a fracture strain curve in the space of ε^{pl}-η is needed. This curve was obtained by performing uniaxial tests under different triaxiality states for steel grade S355J2, as shown in Fig. 2. The described ductile fracture criterion was used in conjunction with the Mises plasticity and a linear isotropic hardening rule as the material model. To calibrate the stress-strain behavior of the

S355J2 material, five round smooth samples were tested under the uniaxial tensile test. Fig.3 shows the geometry of the samples.
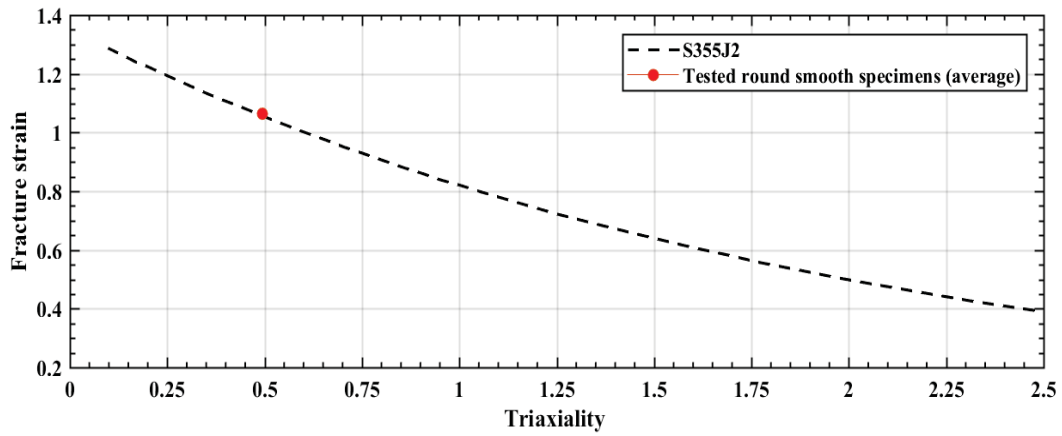
Figure 2: Fracture strain curve for S355J2 at different triaxiality.The curve adapted from [29].
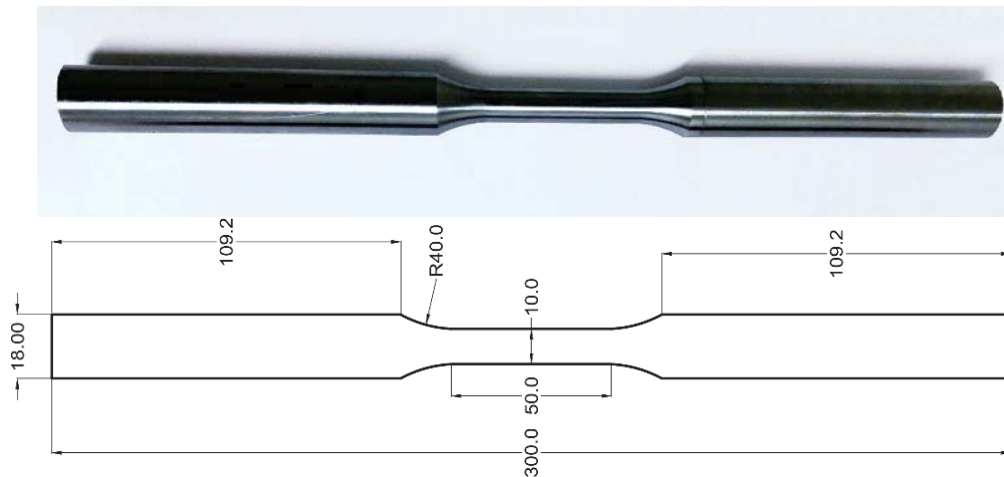
Figure 3: The geometry of round smooth tensile specimens.

All specimens were taken from a flat plate with 25mm thickness in the rolling direction. It should be noted that the effect of the strain rate was outside of the scope so that all tests were conducted at a strain rate of 0.002 mm/mm/s.

A 50mm axial extensometer and a digital image correlation system (DIC) were used to measure the elongation of the gage length. Using DIC can provide the fracture strain of each sample precisely. For example, as shown in Fig. 4, the fracture strain was 1.047 and 1.075 in sample MU1 and MU4, respectively. The engineering stress-strain curves for all tested samples are illustrated in Fig. 5.

To calibrate the ductile damage model an average fracture strain of all five samples ($\bar{\varepsilon}_f = 1.064$) was used. The point corresponding to the average fracture strain and triaxiality of the samples is plotted in Fig. 2 to validate the curve at least at one point. Since the stress triaxiality is varying after the necking of the samples, an average value was obtained ($\bar{\eta} = 0.49$) from the numerical simulation. Fig. 2 indicates a good agreement between the curve and experimental results for round smooth bar samples (plotted by a red circle).
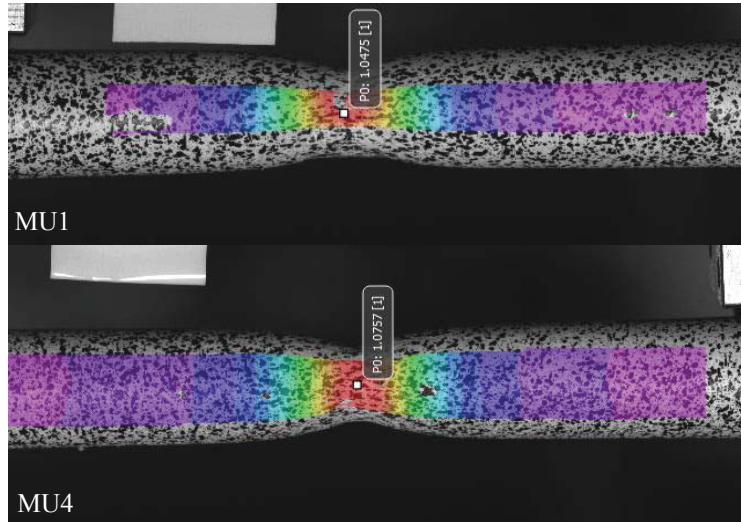
Figure 4: Fracture strain of samples MU1 and MU4 extracted from DIC.
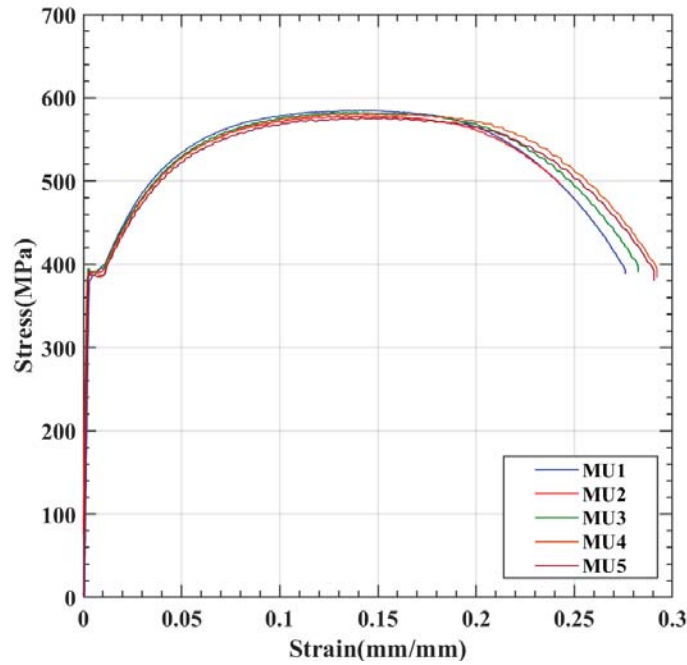
Figure 5: Engineering stress-strain curves for tested round smooth bar samples.

To use the test data in the material plasticity model, true stress-strain curves are required. Before the necking that the uniaxial state is governed, the true strain and stress can be obtained as follows:

$$\varepsilon_t = \ln (\varepsilon_e + 1)$$

$$\sigma_t = (1 + \varepsilon_e)\sigma_e$$

(3)

Where ε_t and σ_t are true strain and stress respectively, while ε_e and σ_e denote engineering values.

After necking, these relations are invalid due to stress triaxiality and strain localization. Therefore, a linear transition was assumed between the ultimate and the fracture point. The fracture strain could be obtained by DIC; however, the equivalent true fracture stress also

should be calculated to consider the triaxial stress state. Bridgman proposed an approximate conversion from a triaxial stress state into an equivalent stress σ_{eff} by using the geometry of the samples as follows [30]:

$$\sigma_{eff} = \frac{\sigma_t}{(1 + \frac{4R}{D}) \times ln(1 + \frac{D}{4R})} \tag{4}$$

Where D is the diameter of the sample, and R is the radius of curvature at the fracture point. These two parameters can be measured at the fracture point by image processing (e.g., See Fig. 6 for sample MU1).
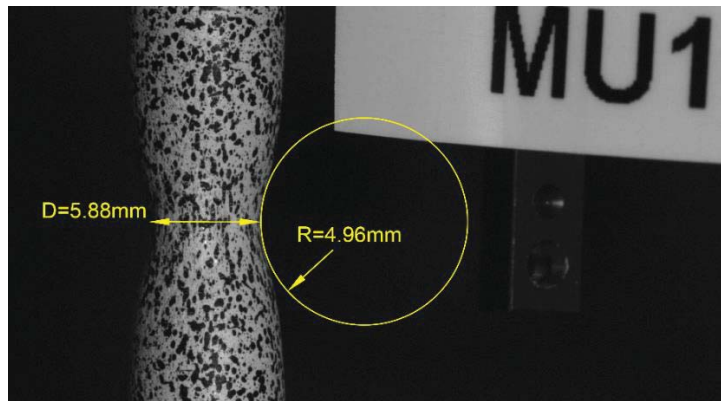
Figure 6: The diameter of the sample and the radius of curvature at the fracture point for sample MU1.

The calibrated material plasticity and damage model verified by numerical models. For instance, Fig. 7 compares the experimental and numerical force-displacement curves for the MU1 specimen. As this figure shows, there is a good agreement between numerical and experimental curves.
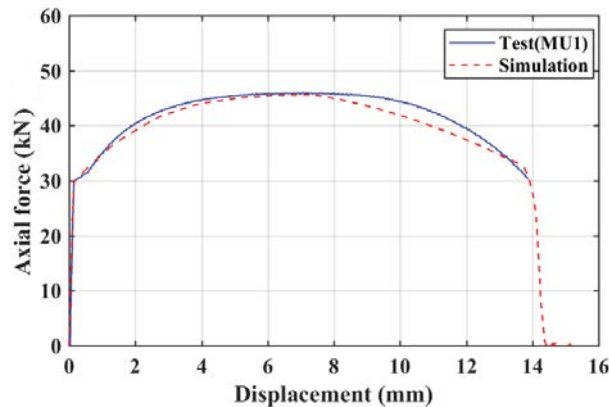
Figure 7: Ductile damage model verification for sample MU1.

4.2 Finite element models of the subassemblies

To predict the ductile fracture of two pre-described subassemblies, nonlinear finite element models were created in Abaqus/CAE. The explicit solver was employed due to its efficiency in conducting and converging extreme nonlinear behavior, particularly when a fracture and material separation are simulated. The simulations were implemented as a quasi-static to find the

capacity of the subassemblies and track the fracture behavior of the components under incremental displacement imposed at the point of the removed column.

For all nonlinear parts around the beam-to-column joints, the eight-node solid brick elements with reduced integration points (C3D8R) with a fine mesh were applied for the discretization of the models (see Fig. 8). These fine-meshed domains were assumed to have a length at least equal to the depth of beam or column that is known as the most probable place for plastic hinges formation. In these areas, the thickness of beams flanges and webs divided into at least four layers of element.

On the other hand, the middle parts of the beams and columns were modeled by a coarse mesh to reduce the time of analyses. To make an appropriate transition between the fine-meshed and the coarse-meshed areas a combination of C3D8R and six-node wedge element (C3D6) was used as shown in Fig. 8. It is worth mentioning that in numerical models, the properties of the welds were ignored.

An incremental displacement was applied to the removed column at joint J2, and the boundary conditions were defined as shown in Fig. 1(b). Also, it was supposed that beams flanges and columns at the joint level are laterally braced due to the slab system and secondary beams.
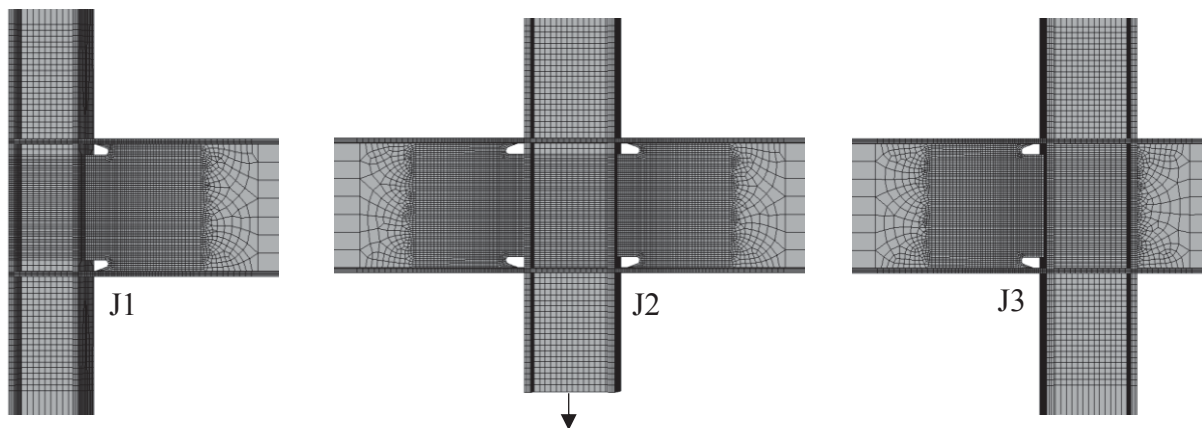
Figure 8: Finite element discretization of subassemblies with a fine mesh around the joints.

5 RESULTS

Fig. 9 compares the force-vertical displacement of two described subassemblies. Comparing of the subassemblies can be done in different aspects and parameters. In terms of yielding strength, both subassemblies provided approximately similar global yielding strength; however, due to the panelzone distortion in the Subassembly-1 with HE180B column, the panelzone in J1 was the first component that experienced plastic deformations, while the beam in this joint had a limited plastic strain even at the last step of the analysis. Moreover, this panelzone distortion imposed the maximum equivalent plastic strain (PEEQ) in the upper column of the joint J1. Forming plastic hinge and excessive lateral deformation of the column can increase the potential of post-yield buckling of the column under axial loads. In contrast, in the other subassembly (with HE240B column) the panelzone yielded after some plastification in the beam so that in the last step of the analysis, the maximum PEEQ occurred in the beam area while the upper column exhibited a low amount of plastic deformations.

Before any fracture initiation in the subassemblies, the Subassembly-2 with stronger joint J1 provided significantly more vertical strength. For example, in the vertical displacement of 877mm that is corresponding to the onset of fracture in the bottom flange of the joint J2 in the

Subassembly-2, the vertical strength of this subassembly was about 44% more than Subassembly-1.
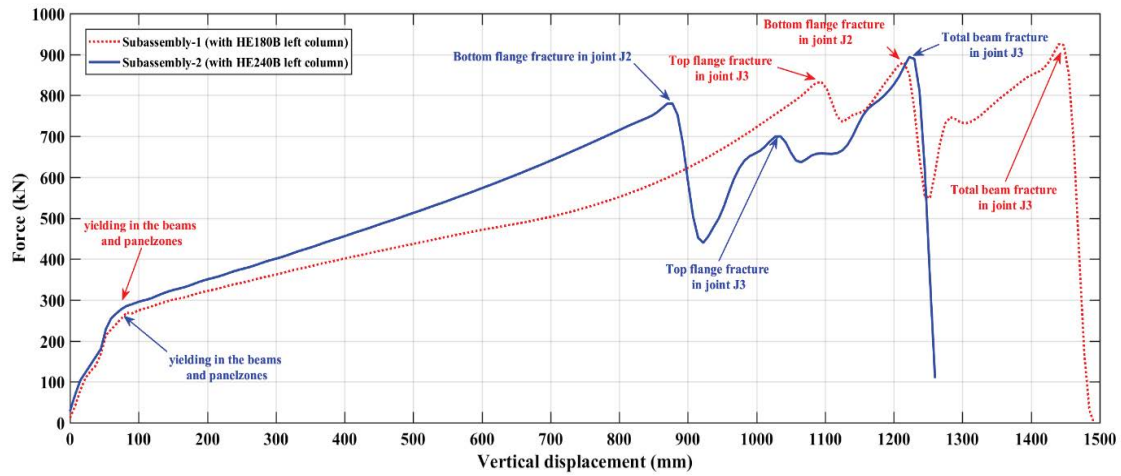
Figure 9: Vertical force-displacement curves for two studied frame subassemblies.
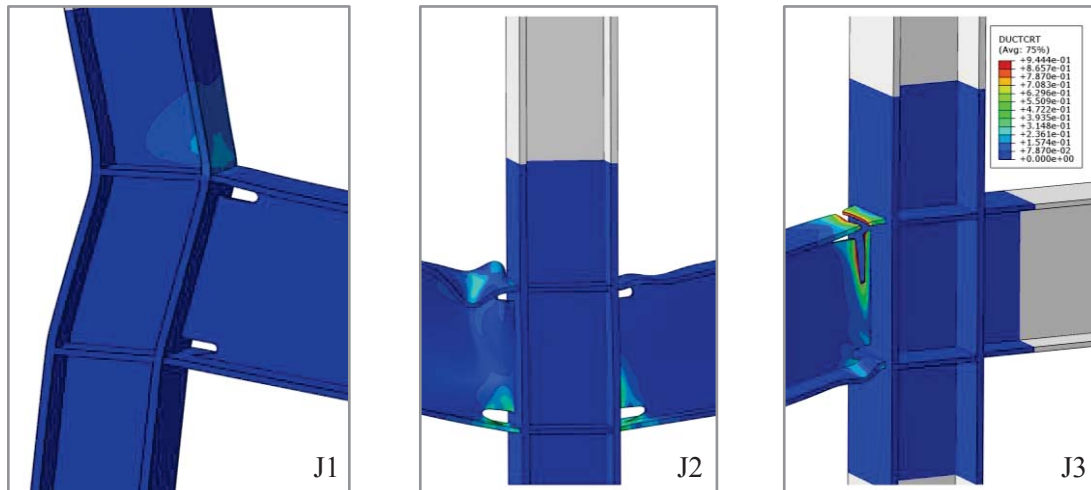
Figure 10: Distribution of ductile damage variable (D) at different joints in Subassembly-1 (ductile fracture initiated and developed firstly in J3)

In terms of ductile fracture initiation pattern, as shown in Fig.10 for the Subassembly-1, due to unbalanced stiffness and catenary action in the two sides beams, the fracture firstly initiated at the top flange of the beam in J3 joint and then developed to the web of the beam. When the right beam lost some amount of its stiffness, the fracture also initiated at the bottom flange in the other side beam in the joint J2.

On the other hand, the Subassembly-2 exhibited a vice-versa fracture initiation pattern. In other words, due to the stronger J1 joint, the stiffness and catenary action is more balanced than the Subassembly-1. As Fig.11 indicates the fracture initiated at the left beam of the joint J2. By developing the crack in the beam web and decreasing the beam stiffness, the J3 joint finally experienced the fracture at the top flange of the beam.

An interesting trend can be drawn from Fig.9 although the complete fracture of beams for both subassemblies happened in joint J3 and the cap vertical forces of both subassemblies are approximately similar, the Subassembly-1 exhibited larger vertical displacement than the Subassembly-2. This extra displacement caused by the excessive distortion of joint J1 (less stiffness) that delayed the activation of the catenary action in the beams. As a result, a weak panelzone

can significantly increase the vertical displacement demand of the frames and have to be considered in the frame analysis.

In addition, if the maximum vertical displacement demand obtained from the nonlinear dynamic analysis of the frame under similar column removal scenario was less than vertical displacement corresponding to ductile fracture initiation of subassemblies (in the capacity curves), using a simplified material model like a bilinear model can provide valid results in nonlinear dynamic analysis of the frame.

All these conclusions were made based on the assumption that welds material possesses higher toughness than base metal and the welds are without defects and significant stress and strain concentration.
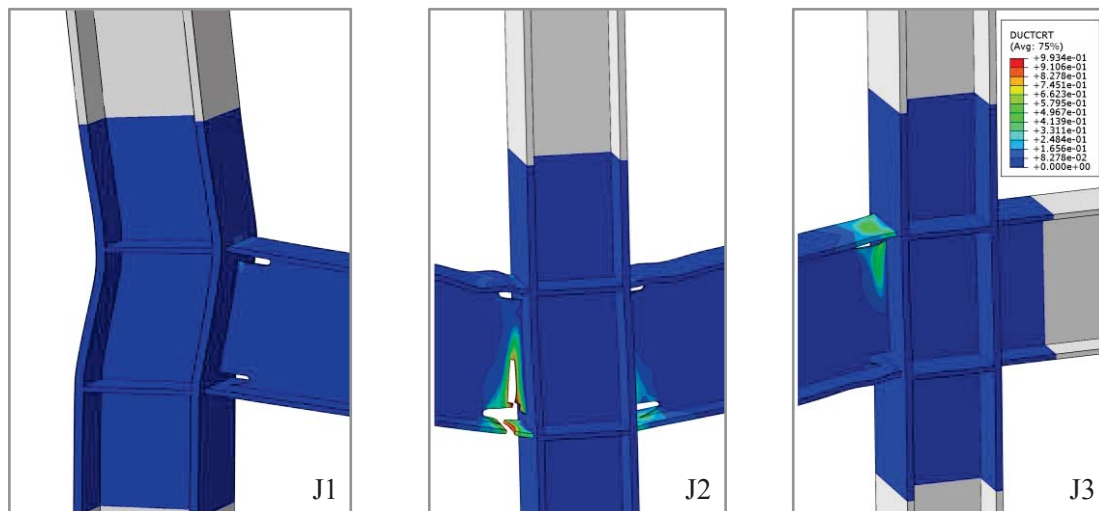
Figure 11: Distribution of ductile damage variable (D) at different joints in Subassembly-2 (ductile fracture initiated and developed firstly in J2)

6   CONCLUSIONS

A frame subassembly from an 8-story ordinary steel moment-resisting structure was studied for a column removal situation. The capacity and the fracture pattern of the subassembly obtained for different exterior joint strength. Based on the results from numerical models, the following conclusions can be drawn:

- The strength of the exterior joints in outer bays of such structures can significantly affect the fracture pattern and the capacity of the frame under a column removal situation.

- When an exterior weak joint was used, excessive plastic deformation of the panelzone led to an unbalanced state in catenary action so that the asymmetric force induced the fracture at the end of the right beam near to the interior joint. In contrast, when a stronger exterior joint was used, the rigidity of the panelzone led to make a balanced state in catenary action so that the fracture occurred at the left beam near to the middle joint that the column was removed.

- Before any fracture initiation, the vertical strength of the specimen with a stronger exterior joint showed about 44% more strength than the model with a weaker exterior joint; however, the maximum resisted vertical force for both models was approximately similar.

- In general, although the beam-to-column strength ratio and the panelzone strength usually are less critical in the standard procedure of design of moment-resisting structures in a low seismic zone, special consideration is needed when such structures are also designed for a progressive collapse situation.

REFERENCES

[1] Ellingwood BR, Smilowitz R, Dusenberry DO, Duthinh D, Lew HS, Carino NJ. Best practices for reducing the potential for progressive collapse in buildings. 2007.

[2] General Services Administration. Alternate path analysis & design guidelines for progressive collapse resistance. 2013.

[3] Sadek F, Main JA, Lew HS, Robert SD, Chiarito VP, El-Tawil S. An experimental and computational study of steel moment connections under a column removal scenario (NIST Technical Note 1669). National Institute of Standards and Technology; 2010.

[4] American Society of Civil Engineers. ASCE Standard ASCE/SEI 7-10: Minimum Design Loads and Associated Criteria for Buildings and Other Structures. Reston, Virginia2010.

[5] AISC. Seismic provisions for structural steel buildings (ANSI/AISC 341-10). Chicago(IL): American Institute of Steel Construction; 2010.

[6] European Committee for Standardization. Eurocode 8: Design of structures for earthquake resistance-part 1: general rules, seismic actions and rules for buildings (EN 1998-1). European Committee for Standardization,Brussels2004

[7] Botez M, Bredean L, Ioani A. Improving the accuracy of progressive collapse risk assessment: Efficiency and contribution of supplementary progressive collapse resisting mechanisms. Computers & Structures. 2016;174:54-65.

[8] Jiang B, Li G-Q, Usmani A. Progressive collapse mechanisms investigation of planar steel moment frames under localized fire. Journal of Constructional Steel Research. 2015;115:160-8.

[9] Jiang J, Li G-Q. Disproportionate collapse of 3D steel-framed structures exposed to various compartment fires. Journal of Constructional Steel Research. 2017;138:594-607.

[10] Khandelwal K, El-Tawil S. Collapse behavior of steel special moment resisting frame connections. Journal of Structural Engineering. 2007;133:646-55.

[11] Khandelwal K, El-Tawil S. Pushdown resistance as a measure of robustness in progressive collapse analysis. Engineering Structures. 2011;33:2653-61.

[12] Khandelwal K, El-Tawil S, Kunnath SK, Lew H. Macromodel-based simulation of progressive collapse: Steel frame structures. Journal of structural engineering. 2008;134:1070-8.

[13] Kim T, Kim J. Collapse analysis of steel moment frames with various seismic connections. Journal of Constructional Steel Research. 2009;65:1316-22.

[14] Rahnavard R, Fard FFZ, Hosseini A, Suleiman M. Nonlinear analysis on progressive collapse of tall steel composite buildings. Case studies in construction materials. 2018;8:359-79.

[15] Li L, Wang W, Teh LH, Chen Y. Effects of span-to-depth ratios on moment connection damage evolution under catenary action. Journal of Constructional Steel Research. 2017;139:18-29.

[16] Li L, Wang W, Chen Y, Lu Y. Experimental investigation of beam-to-tubular column moment connections under column removal scenario. Journal of Constructional Steel Research. 2013;88:244-55.

[17] Kim T, Kim J. Progressive collapse-resisting capacity of steel moment frames considering panel zone deformation. Advances in Structural Engineering. 2009;12:231-40.

[18] Kordbagh B, Mohammadi M. Influence of panel zone on progressive collapse resistance of steel structures. Journal of Performance of Constructed Facilities. 2018;32:04018014.

[19] American Welding Society (AWS) D1 Committee on Structural Welding. Structural welding code-seismic supplement (AWS D1.8/D1.8M:2016). MA: American Welding Society; 2016.

[20] Hancock J, Mackenzie A. On the mechanisms of ductile failure in high-strength steels subjected to multi-axial stress-states. Journal of the Mechanics and Physics of Solids. 1976;24:147-60.

[21] Johnson GR, Cook WH. Fracture characteristics of three metals subjected to various strains, strain rates, temperatures and pressures. Engineering fracture mechanics. 1985;21:31-48.

[22] McClintock FA. A criterion for ductile fracture by the growth of holes. Journal of applied mechanics. 1968;35:363-71.

[23] Rice JR, Tracey DM. On the ductile enlargement of voids in triaxial stress fields. Journal of the Mechanics and Physics of Solids. 1969;17:201-17.

[24] Bao Y, Wierzbicki T. On fracture locus in the equivalent strain and stress triaxiality space. International Journal of Mechanical Sciences. 2004;46:81-98.

[25] Bai Y, Wierzbicki T. A new model of metal plasticity and fracture with pressure and Lode dependence. International journal of plasticity. 2008;24:1071-96.

[26] Jia L-J, Ge H. Ultra-Low Cycle Fatigue Failure of Metal Structures Under Strong Earthquakes: Springer; 2018.

[27] Dassault Systèmes. Abaqus analysis user's manual. Simulia Corp. Providence, RI, USA2013.

[28] Hooputra H, Gese H, Dell H, Werner H. A comprehensive failure model for crashworthiness simulation of aluminium extrusions. International Journal of Crashworthiness. 2004;9:449-64.

[29] Hradil P, Talja A. Ductility limits of high strength steels. Research report VTT; 2016.

[30] Öchsner A. Continuum Damage and Fracture Mechanics: Springer; 2016.

Paper III:

A DIC-based alternative approach to calibrate ductile fracture criterion

A DIC-based alternative approach to calibrate ductile fracture criterion

Mohammad Ali Mahdavipour[1], Dmitry Vysochinskiy[2]

[1,2]Department of Engineering Sciences, University of Agder, Grimstad, Norway

[1]ali.mahdavipour@uia.no

[2]dmitry.vysochinskiy@uia.no

1. Abstract

In the case of ductile fracture modeling, the common calibration procedure typically utilizes uniaxial tensile tests to calibrate the constitutive model and employs notched tensile specimens to calibrate the fracture criterion. However, in many situations, e.g., weldments, the production of uniaxial specimens can be challenging due to the limited length of the test material or complicated geometry. In addition, the digital image correlation (DIC) technique is becoming more widely available and can provide engineers with more informative material testing. The presented paper proposes a DIC-based approach that allows calibrating both the constitutive model and the fracture parameters from a single set of flat notched specimens. To validate the proposed approach, the void growth model (VGM) was selected as the fracture criterion. Then the results from common and proposed calibration approaches were compared using tested specimens manufactured from S355J2 structural steel as a case study. Results showed that the material model calibrated by both approaches could successfully predict experimental fracture strain in notched specimens. However, the proposed approach could estimate the equivalent stress with higher accuracy than the common approach, particularly at large plastic deformations. It was also indicated that the proposed approach calibrated the critical void growth index with lower dispersion. The experimental and numerical studies carried out in this paper supported the proposed approach as a viable alternative to calibrate ductile fracture parameters without producing uniaxial specimens.

KEYWORDS

Digital image correlation; ductile fracture; weld; constitutive model; void growth model

2. Introduction

To simulate the structural failure under excessive plastic strain (ductile fracture), finite element (FE) simulations require both adequate and accurate constitutive models and ductile fracture criteria of all involved materials (i.e., base metal, weld, and heat-affected zone). Since the prediction errors can be caused by both the inherent properties of the model as well as inaccurate calibration, it is useful to distinguish between an adequate and an accurate model. Simply put, an adequate material model refers to a model that can appropriately simulate different phenomena involved in the physical process of steel plasticity and ductile fracture, while an accurate model is an adequate model that has been properly calibrated, implemented, and validated.

Previous studies (Kanvinde and Deierlein 2006; Kanvinde and Deierlein 2007; Kiran and Khandelwal 2014; Liao et al. 2012; Liao et al. 2015; Wang et al. 2011) demonstrated that void growth model (VGM) as a micromechanical fracture criterion is an adequate model to predict the ductile fracture of steel structures under monotonic tensile loads (i.e., stress triaxiality ratio (η) > 0.33). Since the VGM uses the history of strain and stress to evaluate the fractured state, it is also a preferred model for situations with significant geometry changes or triaxiality variation (Kanvinde and Deierlein 2004; Kiran and Khandelwal 2014). Because of this feature, VGM is better suited to simulate material separation through finite element removal technique in comparison to the basic critical strain criterion (Saykin et al. 2020). At the same time, VGM has only one calibration parameter (critical void growth index, $VGI_{critical}$) which makes the calibration process less complicated than other advanced models, e.g., Gurson-Tvergaard-Needleman (GTN), which requires several parameters for a single material (Tvergaard and Needleman 1984).

To calibrate the VGM, complementary finite element models of tested smooth-notched tensile (SNT) specimens should be analyzed up to the test fracture elongation (Δ_f). Since the final calibration of $VGI_{critical}$ is based on the numerical responses, the accuracy of the constitutive model can play a substantial role. The constitutive model includes the elastic properties, yield stress, and a strain hardening evolution rule to define the equivalent stress ($\bar{\sigma}$) as a function of equivalent strain ($\bar{\varepsilon}$).

The constitutive model of steel material is usually calibrated based on standard uniaxial tensile tests (hereafter is called common approach); however, in many

situations, the production of uniaxial specimens can be impractical due to the limited length of test material and complicated part geometry, e.g., weldments.

To the best of the authors' knowledge, there are few studies (Murata et al. 2018; Shi and Chen 2018; Tu et al. 2016; Tu et al. 2017; Wang et al. 2011; Zhang et al. 2002) in the literature that deal with the calibration of true stress-strain curves without uniaxial specimens. In these studies, notched specimens were typically used through an inverse analysis to calibrate the true stress-strain curves. In notched specimens, plastic deformations only develop in the notched zone taken from a specified metal region like a weld. Although these investigations reported many interesting results, they are limited to the round bar configuration of test specimens. However, the flat configuration is more desirable in many structural applications, particularly for plate-shaped and hollow steel sections.

In this study, an alternative approach was proposed in which both the constitutive model and VGM were calibrated based on a single set of flat notched specimens. In this approach, a two-segment exponential strain hardening evolution rule was fitted on each notched specimen individually. To make this fitting feasible, a transitional strain point between two segments was introduced, which can be measured by a digital image correlation (DIC) system. Then, the constitutive model and VGM fracture criterion were calibrated based on both proposed and common approaches for mild steel S355J2. In addition, pull-plate tests and simulations were performed as local representatives of the bolted and reduced beam section (RBS) connections to qualify the proposed approach as an alternative calibration procedure to calibrate the ductile fracture in steel structures.

3. Void Growth Model

In the fracture process of many conventional steel materials, void growth and coalescence are the most dominant phases of fracture initiation. In contrast, the effect of the nucleation process is negligible (Anderson 2005; Kanvinde and Deierlein 2004). Rice and Tracey (1969) developed an analytical relation for the void growth rate of a spherical void in an elastic-perfectly plastic material under plastic strain and a triaxial stress state as follows:

$$\frac{dR}{R} = Ce^{1.5\eta}d\bar{\varepsilon}_p \qquad (1)$$

where R is the radius of a spherical void, $\bar{\varepsilon}_p$ and η are the equivalent plastic strain and the stress triaxiality ratio, respectively. The stress triaxiality ratio is defined as the ratio of hydrostatic stress (σ_m) to equivalent stress ($\bar{\sigma}$). In this relation, the

exponent of *1.5* was obtained based on theoretical derivations done by Rice and Tracey (1969). Also, *C* is a material-dependent parameter that controls the void growth rate. Then fracture is physically postulated to initiate when the size of voids exceeds a critical value (Kanvinde and Deierlein 2006). Based on this postulation, the VGM fracture criterion can be formulated mathematically by the following expression (Kanvinde and Deierlein 2006):

$$VGI = \int_0^{\bar{\varepsilon}_p} e^{1.5\eta} d\bar{\varepsilon}_p > VGI_{critical} \qquad (2)$$

The left-hand side of this expression is an explicit integration of η with respect to $\bar{\varepsilon}_p$ over the loading history, which is named void growth index (VGI). The critical void growth index (i.e., $VGI_{critical}$) on the right-hand side is assumed to be a material property that can be calibrated based on the test results of SNT specimens and complementary finite element analyses (Kanvinde and Deierlein 2006). Once the displacement of SNT specimens in FE models reaches the fracture displacement observed in the test (Δ_f), the integral gives $VGI_{critical}$ (usually at the center of the specimen). Therefore, in the VGM calibration procedure the constitutive model must be calibrated in advance.

In FE simulations, a numerical integration method such as the trapezoidal rule must be utilized to implement Eq. 2 in models. Therefore, enough small incremental time steps are required to ensure accuracy in the VGI evaluation. Otherwise, the trapezoidal integral might give inaccurate results, especially when the stress triaxiality changes at a high rate due to geometrical nonlinearity. Since explicit solver usually enforces small incremental time steps, this solver can do the numerical integration accurately.

In addition, to quantify ductile fracture initiation as a global behavior and release from single point behavior, a length-scale parameter needs to be defined to collect multiple single-material point failures (Kanvinde and Deierlein 2004). For this reason, the characteristic length (ℓ^*) is defined as a length scale, and ductile crack is assumed to initiate once the VGI exceed $VGI_{critical}$ over this length (Kanvinde and Deierlein 2006). ℓ^* for a specific steel material can be determined based on fractography, but a common range of 0.1 to 0.4 mm has been reported by other researchers (Kanvinde and Deierlein 2006; Kiran and Khandelwal 2014; Liao et al. 2012).

4. Constitutive model calibration

For continuum mechanical modeling of solid structures, the material behavior must be implemented in numerical models in terms of the constitutive model that defines stress (σ) as a function of strain (ε) (Öchsner 2016).

$$\sigma = f(\varepsilon) \qquad (3)$$

In the linear elastic region, this relation can be defined by Hooke's law in 3-dimensional space, while for the plastic region, the constitutive model is described by a yield criterion (e.g., von Mises) and a strain hardening evolution rule that reflects the influence of material hardening on the yield condition (Öchsner 2016). The strain hardening evolution ($H(\bar{\varepsilon}_p)$) rule can be described mathematically as the derivative of equivalent stress ($\bar{\sigma}$) with respect to the equivalent plastic strain $(\bar{\varepsilon}_p)$ as follows:

$$H(\bar{\varepsilon}_p) = \frac{d\sigma(\bar{\varepsilon}_p)}{d\bar{\varepsilon}_p} \qquad (4)$$

In this study, the constitutive model was calibrated based on two approaches. In the first approach (i.e., common approach), the calibration was done based on standard uniaxial tensile tests. However, in the proposed approach, SNT specimens were employed to calibrate the true stress-strain curve.

4.1. Common approach

As shown in Fig. 1, before the onset of necking in a uniaxial tensile specimen, the stress is in a uniaxial state, and strain is distributed uniformly within the gauge length. As a result, the true stress and strain before the necking of the specimen can be directly calculated based on the engineering stress and strain obtained from the test. The true uniaxial strain can be expressed as:

$$\varepsilon^t = ln\,(1 + \varepsilon^e) \qquad (5)$$

and by assuming volume constancy and uniform distribution of strain along the gauge length, the true stress can be calculated by:

$$\sigma^t = \sigma^e(1 + \varepsilon^e) \qquad (6)$$

where σ^t and ε^t are true uniaxial stress and strain, respectively. σ^e and ε^e also refer to the engineering values of stress and strain.
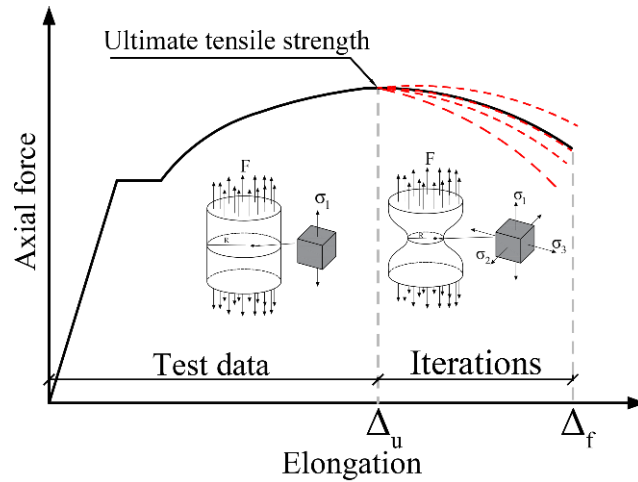
Fig. 1. An illustration of the calibration process of the material constitutive model based on uniaxial specimens.

After the ultimate elongation (Δ_u) neck geometry changes the stress state to a triaxial state (see Fig. 1). Therefore, assumptions made for Eqs. 5 and 6 are no longer valid, and an equivalent stress-strain relationship is required for the post-necking simulation. Several methods such as analytical approaches and experimental-numerical iterative techniques were proposed to characterize the post-necking hardening rule for uniaxial specimens. Bridgman correction (Bridgman 2013) is an analytical method that proposes a stress correction factor based on the stress triaxiality in the necked area. The correction factor is determined by the neck geometrical features like minimum cross-sectional radius and the radius of the neck curvature. Previous studies on metal demonstrated that Bridgman's correction is not very accurate to identify the stress flow under large strains (Barton et al. 1991; Tu et al. 2020), and the corrected stress using this method showed overestimated results compared to stress obtained by an inverse analysis (Murata et al. 2018). It was also concluded that the ability of Bridgman's method to predict stress triaxiality depends on the material properties (Alves and Jones 1999). Last but not least, Bridgman's correction has been developed for round bar specimens, while flat specimens are more applicable for structural steel members that are usually produced in the form of rolled flat sections (plates, I, and H beams). That is why the experimental-numerical iterative techniques have been developed to calibrate the material post-necking hardening evolution rule in ductile metals. In such methods, material parameters are calibrated in an iterative optimization process to find the best match between numerical and experimental quantities like force-displacement curves (Tu et al. 2020). However, due to the inhomogeneous stress state and its interaction with geometrical nonlinearity

(necking) in large plastic strains, using this method on standard uniaxial specimens can increase the potential of nonunique calibration (Cooke and Kanvinde 2015). In other words, different definitions of the material model can produce the same goodness of fit between numerical and experimental global results, while the local responses like plastic strains can be varied up to 50% compared to the actual material strain (Cooke and Kanvinde 2015).

As described later, since the flat specimens were used in this study, an experimental-numerical iterative technique was employed to calibrate the post-necking hardening evolution rule on uniaxial specimens. For this purpose, an exponential post-necking strain hardening evolution rule was used in which the hardening can be written in the form of an exponential function of equivalent plastic strain ($\bar{\varepsilon}_p$) as follows:

$$H(\bar{\varepsilon}_p) = k_0 e^{-n_0 \bar{\varepsilon}_p} \qquad (7)$$

where two calibration parameters k_0 and n_0 were adjusted in the calibration process. It is worth mentioning that this exponential form of hardening evolution, which has been proposed by Voce (1948), can provide a better fit for materials when the stress reaches a saturation stress at large strains (Jun et al. 2017; Tu et al. 2020) and when compared to unsaturated models like Hollomon's power law (Hollomon 1945).

To evaluate the accuracy of each iteration, the Mean Absolute Percentage Error (MAPE) was calculated based on the force-displacement curves, which were resulted from the test and FE models. The MAPE is expressed as follows:

$$MAPE = \frac{1}{N} \sum_{i=1}^{N} \left| \frac{F_{test} - F_{FEM}}{F_{test}} \right| \qquad (8)$$

where F_{test} and F_{FEM} are experimental and numerical forces for a given displacement point. N also denotes the number of displacement points where the curves are discretized for comparison. In this study, MAPE was obtained based on 25 uniformly distributed points from ultimate displacement (Δ_u) to the fracture displacement (Δ_f). The maximum acceptable MAPE can be assumed based on the required accuracy for a particular application also available computational resources. In this study, the computational resource was not restricted, and a 0.01 value of MAPE was considered as the acceptable calibration error. This value can provide a 1% matching deviation on average that indicates an accurate match. It must be noted if MAPE cannot converge to a smaller value than this accepted limit after adequate iterations, it means that the selected hardening rule cannot provide

the specified accuracy level. Once the plastic flow curves were calibrated based on each uniaxial specimen, an average curve is calculated and applied in numerical models of SNT specimens to calibrate the fracture criterion.

4.2.Proposed approach

In the proposed approach, both the constitutive model and the fracture criterion were calibrated for notched specimens individually. Fig. 2 illustrates the proposed calibration procedure. In contrast to uniaxial specimens, in the notched specimens, stress is in a triaxial state, and the strain is localized in the notches from the beginning of the test. As a result, the iterative calibration of the hardening evolution rule must be done for all plastic strain ranges (from yielding to fracture). In this study, a two-segment exponential function was employed for the hardening evolution rule. Previous studies on similar models (e.g., two-term Voce model (Voce 1948)) showed that using two segments for the hardening rule provides more flexibility in calibration and more accurate matching between experimental and numerical results (Hertelé et al. 2011; Khadyko et al. 2014; Qin et al. 2017; Vysochinskiy 2014). As it is illustrated in Fig. 2(c), these two segments of the hardening evolution function ($H(\bar{\varepsilon}_p)$) intersect each other at a point that is named the transitional strain ($\varepsilon_{(Trans)}$). This hardening evolution function can be written as follows:

$$H(\bar{\varepsilon}_p) = \begin{cases} k_1 e^{-n_1 \bar{\varepsilon}_p} & for \ \bar{\varepsilon}_p \leq \varepsilon_{(Trans)} \\ k_2 e^{-n_2 \bar{\varepsilon}_p} & for \ \bar{\varepsilon}_p \geq \varepsilon_{(Trans)} \end{cases} \tag{9}$$

where k_1, n_1 and k_2, n_2 are considered as material calibration parameters for the first and second segments, respectively. These parameters can be adjusted based on an iterative optimization process to find the best match between numerical and experimental force-displacement curves. In accordance with the form of the force-displacement curves for SNT specimens (see Fig. 2(a)), $\varepsilon_{(Trans)}$ was phenomenologically assumed to be equal to the strain corresponding to the cap point of the curves measured by DIC. This assumption is consistent with Zhang et al. (2002) 's findings that the true strain at maximum load is independent of the notch geometry. As shown in Fig. 2(b), for smooth-notched round bar specimens, there is only one strain value in the minimum section due to axisymmetric geometry. However, for double-edge-notched flat specimens, the strain is distributed non-uniformly over the notch cross section. Thus, the strain measured by DIC must be averaged as the transitional strain. It must be noted although strain

is a local response that can vary in the volume of material, this definition makes a connection between global and local responses by assuming an average strain for the minimum section of the specimen. In addition to the plastic hardening rule, numerical models require the elastic modulus and yield stress of each notched specimen. These parameters were estimated based on iterative analyses of the specimens considering a simple elastic-perfectly plastic constitutive model.

5. Material description

To make a valid comparison, one needs reference material for which both the common approach and the proposed approach could be applied. Furthermore, it is desirable to have as little variation between tests as possible. Welds are subjected to large variations in mechanical properties due to uncertain solidification conditions and thermal processing history. Therefore, weld material is not suitable reference material. On the other hand, rolled profiles have well-controlled thermal history and microstructure, and a single profile is large enough to produce all the samples required and keep the variation of material properties at a minimum. Thus, S355J2 structural steel grade was selected as a case study material. S355J2 is known as a variant of S355 that can absorb a minimum of 27 J of energy in low temperatures (-20° C) based on the V-notch impact tests (European Committee for Standardization 2004).

Cap point

P_u

Axial force

Δ_u Δ_f

Elongation

(a) Force-elongation curve

From DIC

True longitudinal strain

Averaged $\varepsilon_{(Trans)}$ from DIC

w

0   Distance   w

Smooth-notched flat specimen

$\varepsilon_{(Trans)}$

Smooth-notched bar specimen
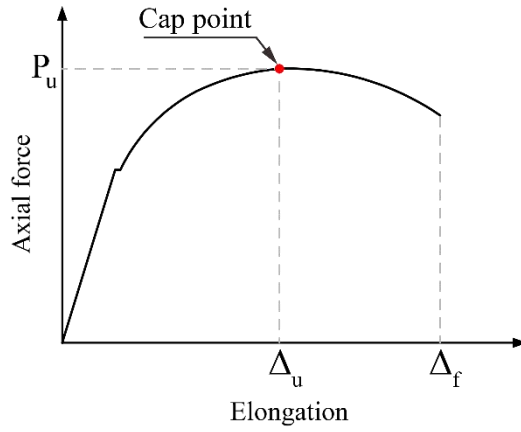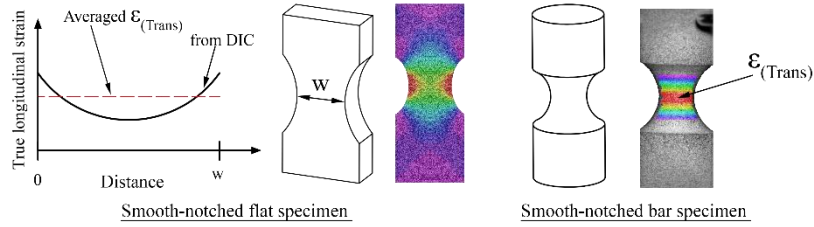
(b) Transitional strain at the cap point

$H(\bar{\varepsilon}_p) = k_1 * exp(-n_1 * \bar{\varepsilon}_p)$

$H(\bar{\varepsilon}_p)$

Transition point

$H(\bar{\varepsilon}_p) = k_2 * exp(-n_2 * \bar{\varepsilon}_p)$

0

0   $\varepsilon_{(Trans)}$

Equivalent plastic strain ($\bar{\varepsilon}_p$)
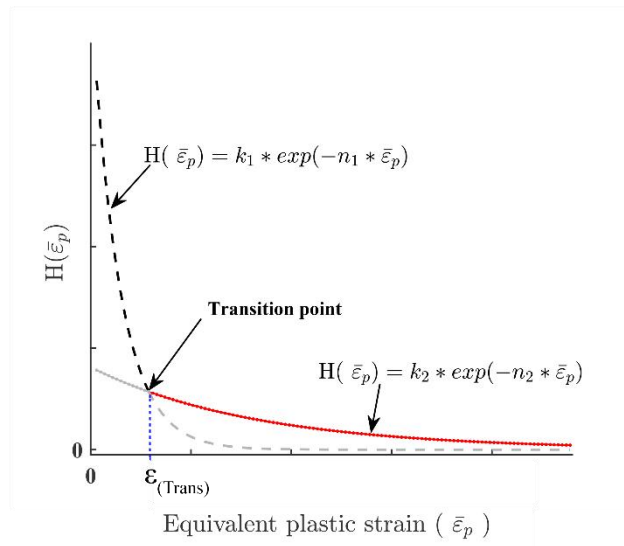
(c) Two-segment exponential strain hardening

Fig. 2. The calibration procedure of the constitutive model for notched specimens was performed based on a two-segment strain hardening evolution rule (the proposed approach).

6. Experimental program

6.1. Material tests

Two sets of flat specimens (named flange and web sets) were cut from the flanges and the web of an IPE200 steel beam manufactured by S355J2 steel grade. Since the beam flange and web thicknesses were limited, a flat configuration was selected instead of round bar specimens. Fig. 3 illustrates the geometry of tested specimens. The nominal thickness of the specimens was 8.1 and 5.3 mm for flange and web set, respectively. However, the actual thicknesses were measured for each specimen individually. In each set, three uniaxial and six double-edge-notched tensile specimens with three different notch radius sizes (NR=12.5, 6.25, and 3 mm) were tested (a total of nine specimens for each set). In addition, a notation system was defined to refer to each specimen. In this system, letters "U" and "N" denote unnotched (uniaxial) and notched specimens, respectively. The notch radius comes immediately after the letter "R" for notched specimens. Also, the letters "F" or "W" means the flange or web set, respectively. Finally, the test number was noted in the parentheses (e.g., UF(1) and NR3-F(1)).
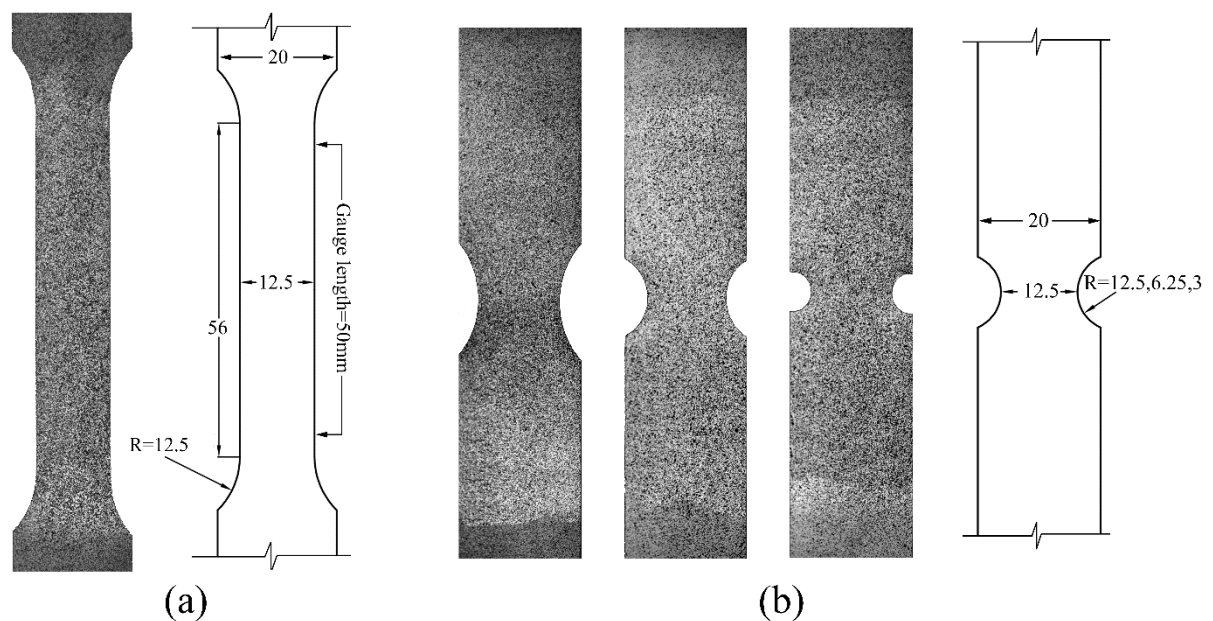
Fig. 3. The geometry of flat specimens taken from the flange and web of an IPE200 (S355J2): a) uniaxial tensile specimen b) double-edge-notched tensile specimens with 12.5, 6.25, and 3 mm of notch radius (all dimensions are in mm and the total length of the specimens was 250 mm)

All tests were performed by a 250 kN uniaxial test machine equipped with hydraulic grips. A physical extensometer with a 50 mm gauge length was attached to the specimens to measure the elongation and remove the machine compliance

error (deformations originated from machine parts, load cell, and grips slippage). In addition to the physical extensometer, a 3D digital image correlation system was used as a non-contact and full-field measurement device that can derive the deformation and strain field on the surface of the specimen based on the images captured by a stereo camera system. Fig. 4 shows the test setup configuration.

It should be noted that the VGM is independent of the strain rate in the formulation. In addition, the control of the strain rate after necking is too complicated due to strain localization. Because of these, the effect of the strain rate was set aside from the scope of this study, and all the tests were performed by 0.1 mm/s speed of the actuator.
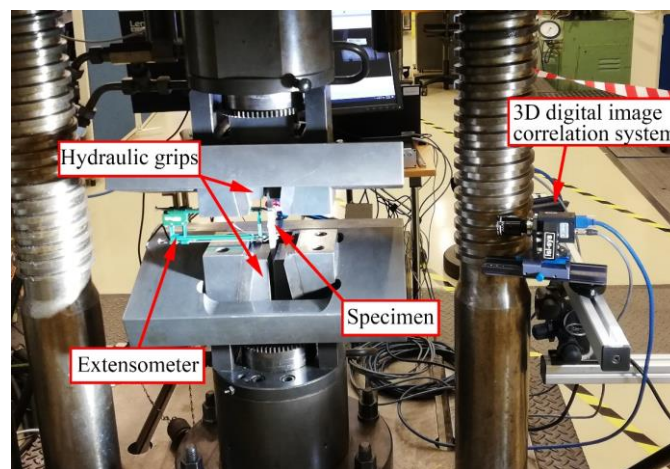
Fig. 4. The test setup configuration.

6.2. Component tests

To validate and compare the material models calibrated by two studied approaches, four pull-plate specimens were tested. These specimens were taken from the flange of the same IPE200 beam used in the material testing. The configuration of the tested plates is shown in Fig. 5. The first two specimens (S-1 and S-2) are local representatives of the steel components in the bolted structures, while the other specimens (S-3 and S-4) are similar to beam flanges in RBS connections. Different arrangements of drilled holes in S-1 and S-2 specimens were designed to provide different fracture patterns. Specimens S-3 and S-4 are also different in the geometry of the reduced section. While a round cut was used in the S-3 specimen, the plate was cut by a dog-bone configuration in the S-4 specimen (with a 30 mm uniform reduced section). The elongation was measured by virtual extensometers with different gauge lengths (L_g) defined by DIC, as shown in Fig. 5. It is worth mentioning that these tests were performed using the same displacement rate that was used in the material testing.
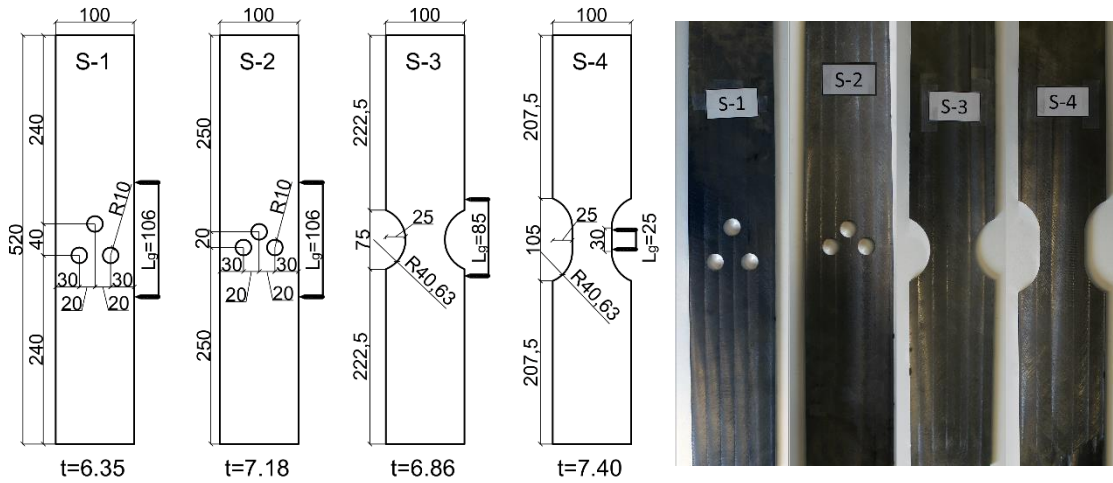
Fig. 5. Configuration of the pull-plate test specimens taken from IPE200 specimens (all dimensions are in mm)

7. Numerical models

The finite element model of each tested specimen was analyzed by Abaqus explicit solver. Because of the symmetry of the material specimens, only one-quarter of their geometry was modeled to reduce the computational time. C3D8R eight-node brick element with reduced integration point was used to discretize the geometry of specimens. The only integration point of the C3D8R element is located in the middle of the element (Dassault Systèmes 2014). To calibrate the constitutive model, the uniform length of the uniaxial specimens and the notches in the double-edge-notched specimens were meshed with 0.5 and 0.2 mm mesh sizes. For VGM calibration, only 0.2 mm mesh size was considered in the notches, which is comparable with the characteristic length (ℓ^*) of the mild steel (Kanvinde and Deierlein 2006; Liao et al. 2012) (see Fig. 6(a) for an example of the mesh configuration).

To ensure the mesh quality in the strain localized places (necks in the uniaxial tensile specimens and notches in the notched specimens), mesh size was controlled and updated during analyses by using an adaptive meshing technique. This adaptive meshing technique creates a new mesh and remaps solution variables from the old mesh to the new mesh with an advection process to maintain the quality of the mesh during the deformation history (Dassault Systèmes 2014). The main parameter of the algorithm is the frequency that controls both mesh quality and computational efficiency (Dassault Systèmes 2014). In this study, adaptive meshing was performed every ten increments to ensure high mesh quality in the critical locations of the specimens.

It is worth mentioning that the constitutive model and fracture criterion were calibrated based on von Mises yield criterion associated with isotropic hardening. Although the von Mises yield criterion is pressure-independent, it is known as a simple but acceptable yield criterion for most structural applications.

The full geometries of pull-plate tests were simulated numerically based on the average stress-strain curve and $VGI_{critical}$ calibrated by the proposed and common approaches. The finite element discretization and adaptive meshing technique described in the numerical model for the material specimens were also used for modeling pull-plate tests but with a larger mesh size (i.e., 1 mm, see Fig. 6(b)). This element size was selected based on a sensitivity study (Kanvinde and Deierlein 2007) on similar specimens, demonstrating that the stress and strain in the reduced sections are subjected to a relatively low gradient when no sharp crack or flaw exists. As a result, the micromechanical fracture models can be applied by a rather coarse mesh (Kanvinde and Deierlein 2007). In these numerical models, an element removal technique was also employed to model the fracture propagation through the plates. In this technique, once the VGI value was larger than $VGI_{critical}$ for a given element it was removed from the model.

Since Abaqus does not offer the VGM as a built-in fracture criterion, a VUSDFLD user subroutine was developed to implement the VGM in the numerical models. This subroutine is called in each time increment to calculate the VGI for all integration points.

As shown in Fig. 6(a), the boundary conditions of specimens were modeled as fully restrained at one end while the other end was pulled up to have gauge elongation equal to the test. In addition, the symmetry boundary condition was modeled in material specimens about the symmetry planes that cut the geometry into a quarter.
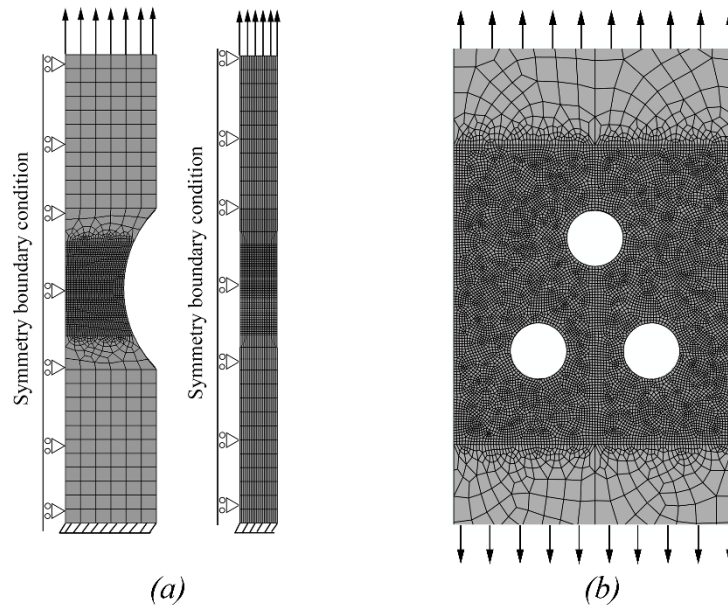
Fig. 6. Mesh configuration in numerical models: a) smooth-notched specimen (R=12.5 mm) with 0.2 mm mesh size, b) pull-plate test S-1 with 1 mm mesh size.

8. Results and discussion

8.1. Constitutive model calibration results

8.1.1. Common approach

Fig. 7 compares the numerical and experimental force-displacement curves of UF(1) and UW(1) specimens. In addition, all calibrated parameters on all uniaxial specimens are listed in Table 1. The calibration was done based on a 0.5 mm mesh size along with the described adaptive meshing technique. After calibration of the hardening parameters, all models were also analyzed with the same calibrated parameters but with 0.2 mm mesh size to evaluate the effect of mesh size on the global and local responses of the specimens. These curves demonstrate that for S355J2 steel, the exponential post-necking hardening rule can simulate the force-displacement response of the specimens accurately (MAPE<0.01).
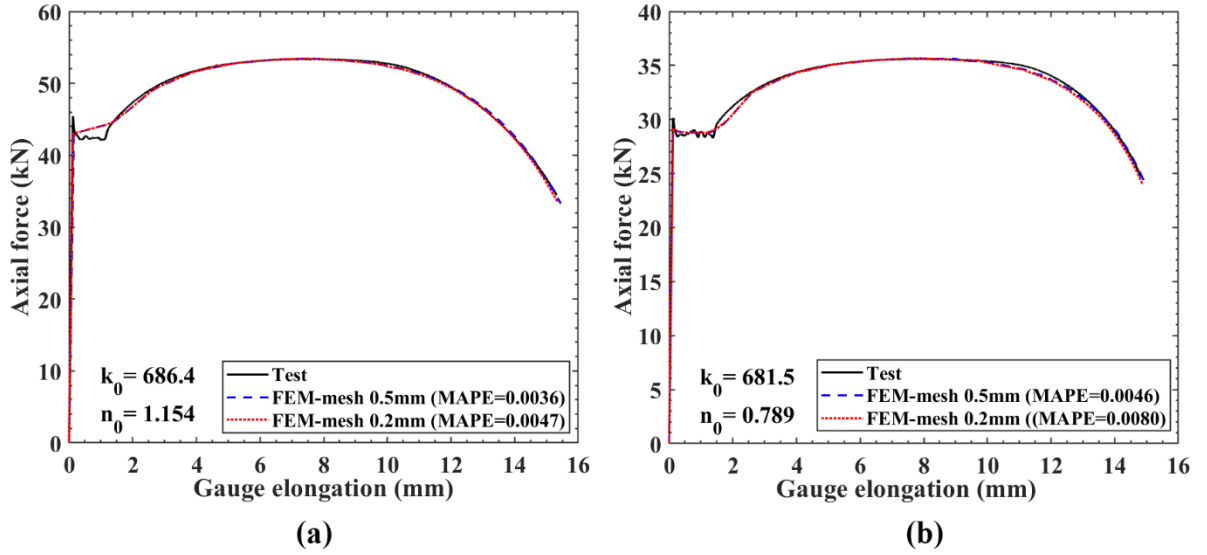
Fig. 7. Comparison between numerical and experimental force-displacement curves for uniaxial specimens: a) UF(1), b) UW(1).

Table 1. Material parameters obtained based on the tested uniaxial specimens and the common calibration approach.

Specimen	Elastic modulus (MPa)	Yield stress (MPa)	Ultimate Eng. stress (MPa)	Ultimate true stress (MPa)	Ultimate true strain (mm/mm)	Post-necking hardening parameters (the common approach)		MAPE for two mesh sizes	
						k_0	n_0	0.5 mm	0.2 mm
UF(1)	191424	429.2	533.01	616.1	0.145	686.4	1.154	0.0036	0.0047
UF(2)	184174	443.7	550.01	630.8	0.137	696.4	1.364	0.0045	0.0052
UF(3)	204211	446.9	558.9	644.6	0.143	795.3	1.355	0.0056	0.0062
UW(1)	192239	438.4	536.2	616.8	0.140	681.5	0.789	0.0046	0.0080
UW(2)	192301	443.4	544.2	622.2	0.134	699.8	0.696	0.0029	0.0049
UW(3)	209556	429.1	542.2	625.0	0.142	800.0	1.231	0.0035	0.0066
Mean (CV%)	195651 (4.8)	438.5 (1.8)	544.1 (1.7)	625.9 (1.7)	0.140 (2.9)	726.6 (7.6)	1.098 (26.2)	0.0041 (23.6)	0.0059 (21.2)

Comparison between the numerical curves obtained by two different mesh sizes (0.5 mm and 0.2 mm) indicates that the global force-displacement response of the specimens is almost nonsensitive to the mesh size. The MAPE values for different mesh sizes showed that using a 0.2 mm mesh size changed the MAPE values slightly so that they remained smaller than the accepted value (0.01). Fig. 8 compares the mesh quality of specimen UF(1) with and without the adaptive meshing technique at a displacement corresponding to the test fracture displacement. This figure demonstrates the efficiency of the adaptive meshing technique to keep the quality of the mesh almost the same as the undeformed mesh, while the non-adaptive mesh caused a large element distortion in the necked area.

Consequently, as indicated in Fig. 9, the local strain responses in the neck region of the uniaxial tests were affected negligibly by element size when the adaptive meshing technique was applied. Therefore, the models with the adaptive meshing technique can be a solution to reduce the computational time of the calibration process without significant loss of accuracy. The mesh size is more important when an explicit solver is used in which the stable time increment is directly connected to the minimum size of the elements.

(a)   (b)   (c)
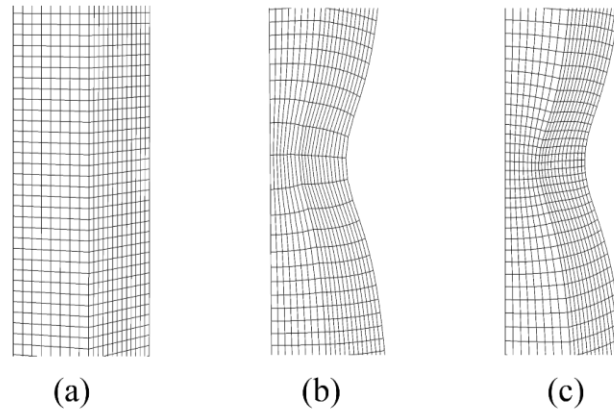
Fig. 8. The mesh of UF(1) specimen with 0.5 mm of element size: a) undeformed mesh, b) deformed mesh without adaptive meshing technique, c) deformed mesh with adaptive meshing technique.
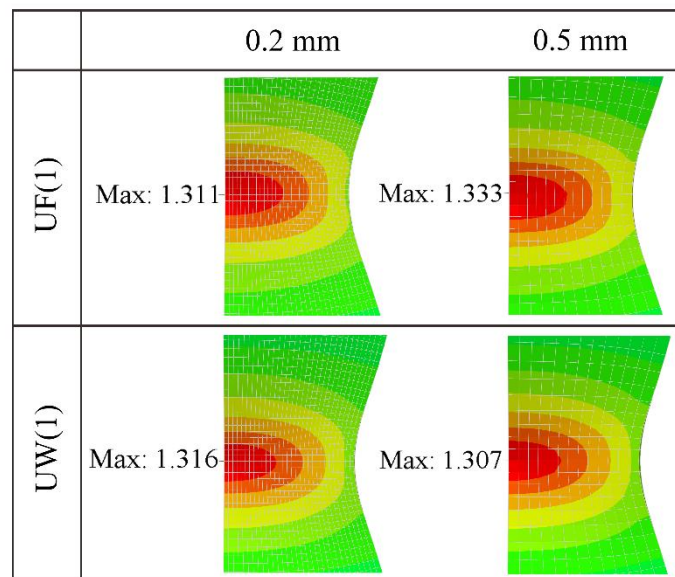
Fig. 9. Negligible effect of the element size on the surface true longitudinal strain at the fracture displacement of the specimens UF(1) and UW(1).

8.1.2. Proposed approach

Fig. 10 compares the force-strain curves obtained based on the physical extensometer and a virtual extensometer defined by DIC. As it is evident before the ultimate point that strain is distributed uniformly and the engineering strain is independent of the gauge length, two measuring techniques gave similar results,

which validates DIC measurements. However, after this point, the curves diverged because of the different gauge lengths.

Figs. 11(a) and 12(a) show the field of surface true longitudinal strain in the notch area of the tested specimens for flange and web sets, respectively. These values were measured by DIC for the cap point of the force-displacement curve (see Fig. 2(a)). The true longitudinal strain is the total true plastic and elastic strain along the loading direction. Because of the symmetry, only half the width of the specimens is illustrated in these figures. In addition, the extracted strain profiles in the minimum section of the notches are drawn in Figs. 11(b) and 12(b). As these figures indicate, smaller notches exhibited lower strain at the center of the specimens while the strain at the root of the notches increased significantly compared to large notches. In other words, the smaller notches caused a more non-uniform strain distribution on the notch section.
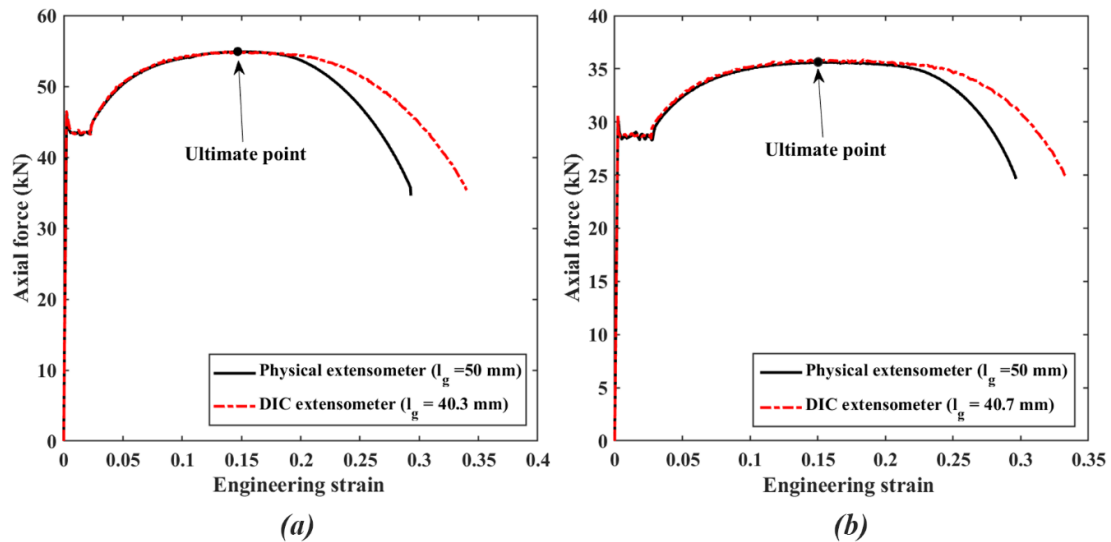
Fig. 10. DIC validation based on physical extensometer for two uniaxial tensile specimens: a) UF(2), b) UW(2).

Based on the strain profile measured by DIC, $\varepsilon_{(Trans)}$ was calculated for each notched specimen. Then the hardening parameters were calibrated based on the proposed approach. The calibration results are listed in Table 2. In this table, the total MAPE of notched specimens is also reported for two studied calibration approaches. It is worth mentioning that the total MAPE was calculated based on 50 displacement points uniformly distributed from the yielding point to the fracture point.
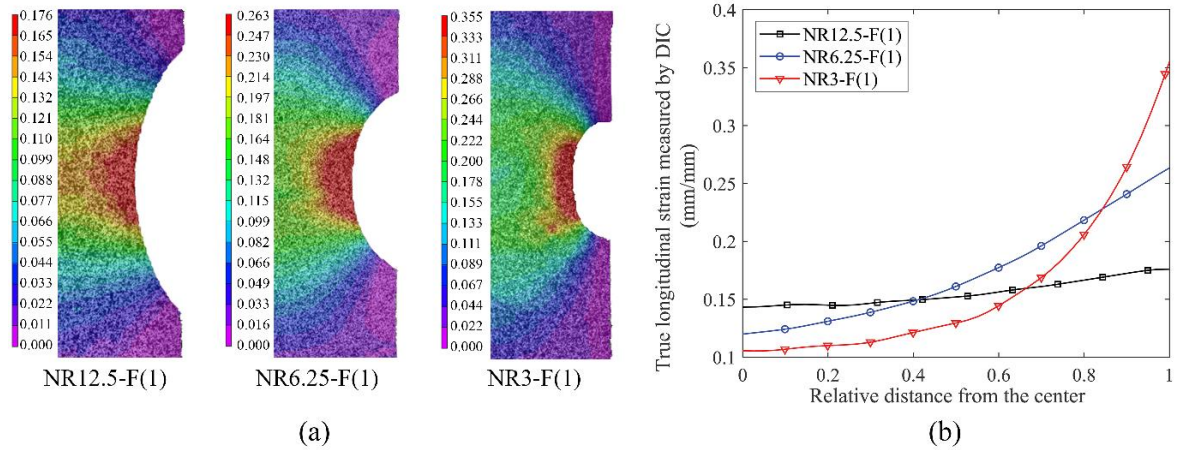
Fig. 11. Local responses of notched specimens (flange set) measured by DIC for the cap point of the force-displacement curves: a) Surface true longitudinal strain field, b) Surface true longitudinal strain profile in the minimum section.
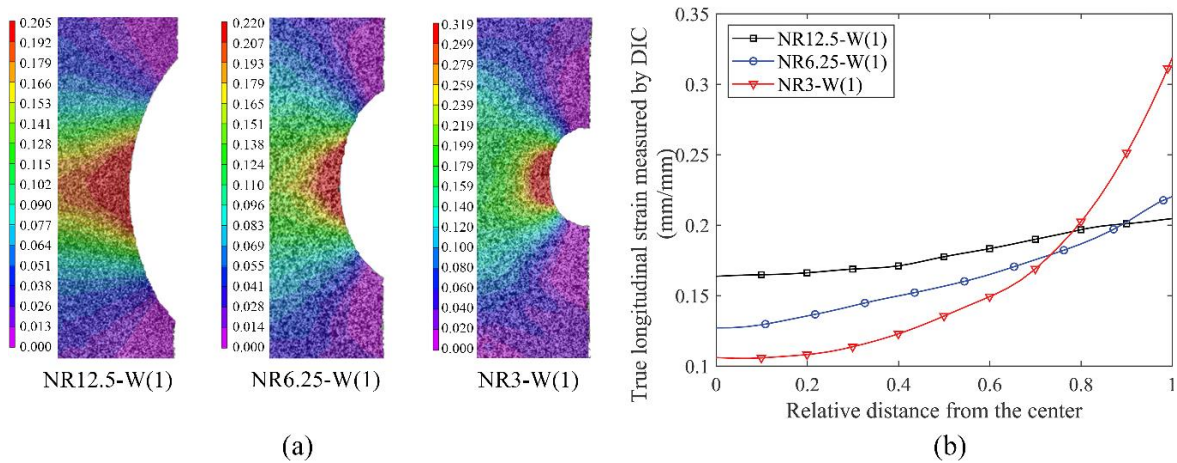
Fig. 12. Local responses of notched specimens (web set) measured by DIC for the cap point of the force-displacement curves: a) Surface true longitudinal strain field, b) Surface true longitudinal strain profile in the minimum section.

Fig. 13 also visualizes the numerical and experimental force-displacement curves for some of the studied specimens as examples. As this figure shows, numerical models in which the material hardening evolution was calibrated based on the proposed approach showed a close agreement with the experimental curves (0.0062 total MAPE on average). In contrast, although in the common approach, the constitutive model was calibrated accurately to simulate uniaxial specimens, the results for the notched specimens showed notable deviations from experiments (0.0321 MAPE on average). These deviations are more considerable after the cap point and vary from one specimen to another due to uncertainties. Such deviations also can be seen between experimental and numerical curves obtained by other researchers (Liao et al. 2012; Wang et al. 2011).
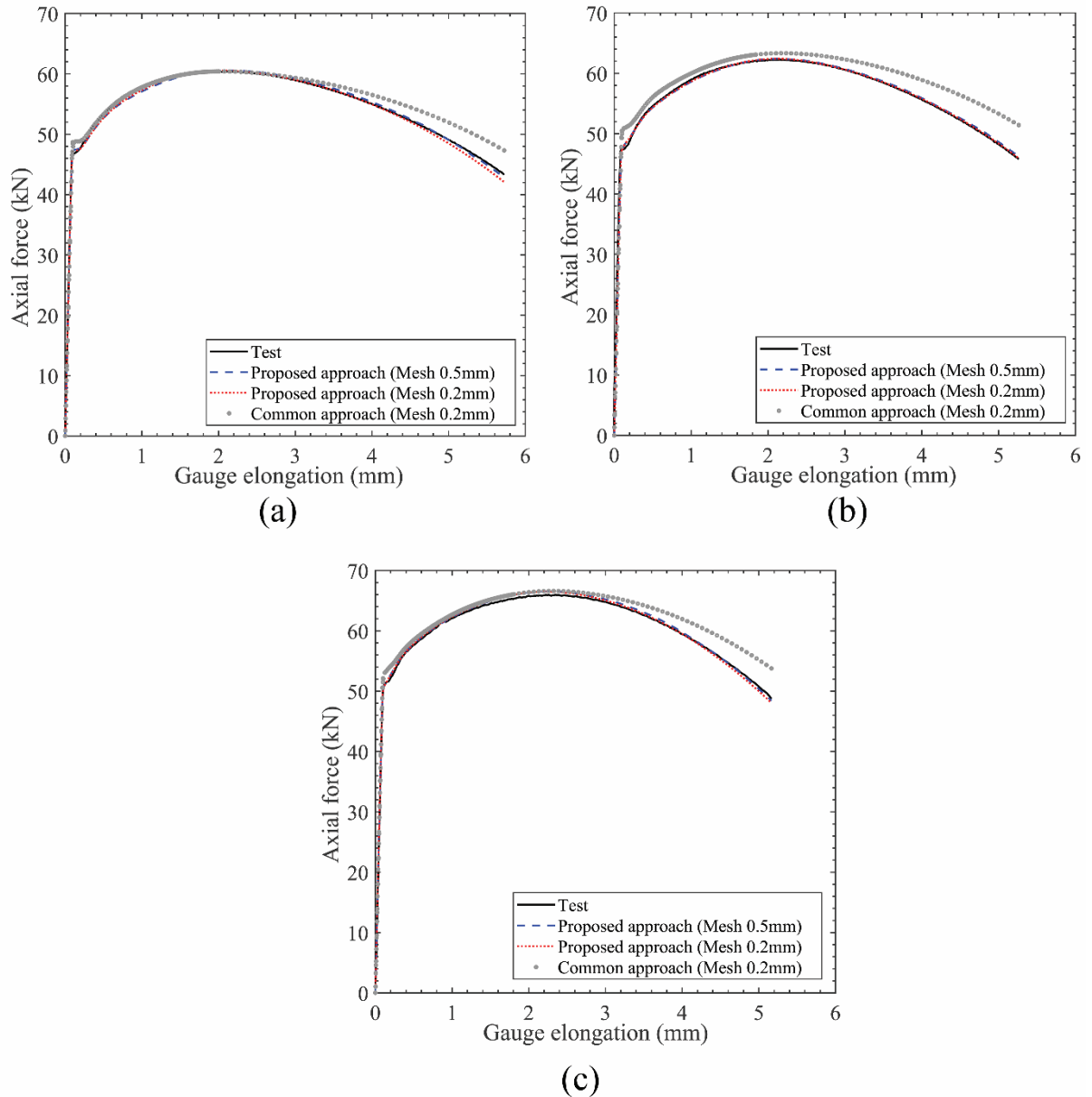
Fig. 13. Comparison between numerical and experimental force-displacement curves of notched specimens: a) NR12.5-F(1), b) NR6.25-F(1), and c) NR3-F(1).

In Fig. 13, the numerical curves obtained by the proposed approach are presented for two sizes of the mesh (0.5 and 0.2 mm). As it is evident, changing the mesh size in this range (0.5-0.2 mm) had a negligible influence on the global responses of the specimens. In addition, Fig. 14 compares the surface true longitudinal strain measured by DIC and obtained from numerical models at the middle point of the specimens. Based on this figure for the notch local strain, the common and proposed approaches provided an almost identical fracture strain by a 5.6% and 5.4% error relative to the DIC, respectively. As a result, the main difference between these two calibration approaches is evaluating the equivalent stress. This can be observed in the average stress-strain curves shown in Fig. 15. As this figure

shows, the common method overestimated the equivalent stress in the post-necking region, which was also demonstrated in the simulation of the pull-plate tests.
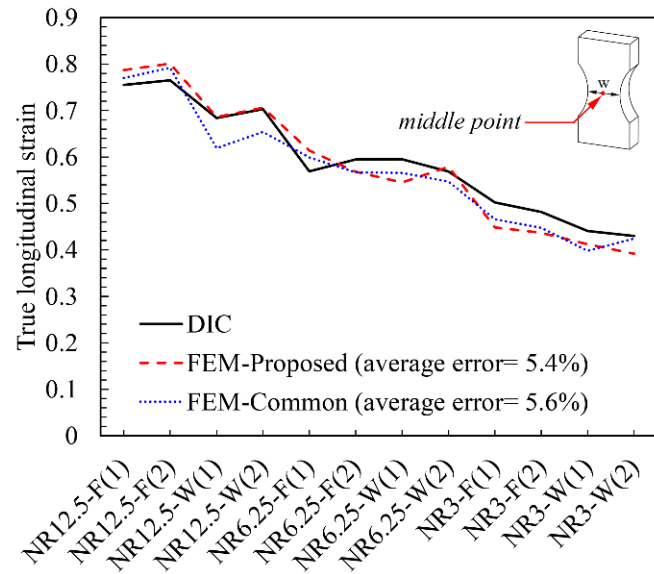
Fig. 14. The surface true longitudinal strain at the fracture displacement of double-notched flat specimens at the middle point.
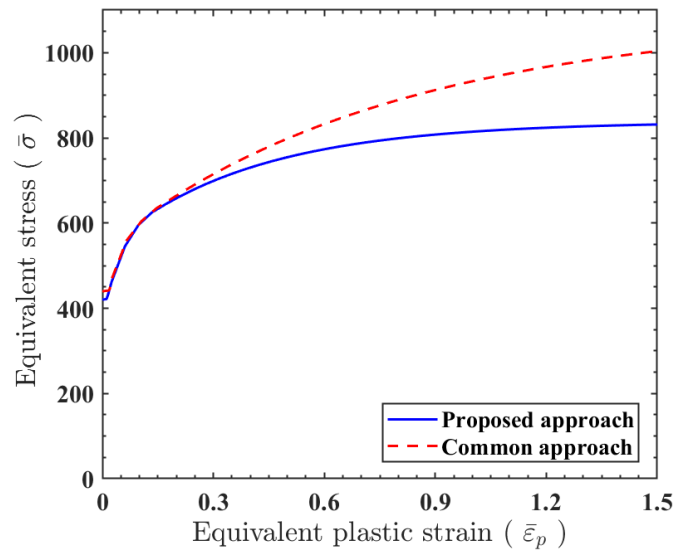
Fig. 15. Average plastic flow curves used in numerical simulation of the pull-plate tests obtained by the proposed and common calibration approaches.

Table 2. Calibration outputs of the proposed and common calibration approaches.

Specimen	Hardening parameters (proposed approach)				$\varepsilon_{(Trans)}$ measured by DIC	Total MAPE		$VGI_{critical}$	
	k_1	n_1	k_2	n_2		Proposed approach	Common approach	Proposed approach	Common approach
NR12.5-F(1)	4656	14.59	837	2.66	0.155	0.0065	0.0221	3.32	2.56
NR12.5-F(2)	4500	14.25	812.5	2.44	0.130	0.0051	0.0305	3.30	2.65
NR6.25-F(1)	4500	14.75	650.0	2.00	0.173	0.0027	0.0431	2.87	2.28
NR6.25-F(2)	4437	14.81	790.62	2.98	0.169	0.0063	0.0320	3.09	2.11
NR3-F(1)	4500	14.25	819.9	2.55	0.174	0.0061	0.0287	3.02	2.48
NR3-F(2)	4000	14.0	950	3.0	0.159	0.0038	0.0311	2.99	2.39
NR12.5-W(1)	4718	15.31	1000	3.25	0.180	0.0040	0.0281	2.95	1.78
NR12.5-W(2)	4600	15.0	814	3.5	0.136	0.0067	0.0386	3.29	1.66
NR6.25-W(1)	4500	14.25	987	4.02	0.162	0.0099	0.0322	3.62	1.77
NR6.25-W(2)	4000	14.0	950	3.25	0.151	0.0085	0.0338	3.10	1.70
NR3-W(1)	4531	14.94	650	2.62	0.157	0.0078	0.0347	2.79	1.73
NR3-W(2)	4562	14.69	893	3.5	0.172	0.0071	0.0307	2.80	1.81
Mean (CV%)	4458.7 (5.1)	14.57 (2.9)	857.9 (11.8)	3.06 (15.2)	0.160 (9.6)	0.0062 (33.2)	0.0321 (16.4)	3.09 (8.0)	2.08 (18.1)

8.1.3. Sensitivity to transitional strain

Like other measuring techniques, DIC also has inherent uncertainties in measuring and averaging the strain. The accuracy of DIC is generally dependent on different factors like image quality, quality of paint and speckles, and quality of lighting (Sutton et al. 2009). In addition, DIC can only measure the surface strain field. As a result, some errors are inevitable in estimating transitional strain $\varepsilon_{(Trans)}$. For this reason, a sensitivity analysis was done to investigate the effect of the deviation of transitional strain on the calibration accuracy. After the calibration of model parameters (k_1, n_1, k_2, n_2) the transitional strain was intentionally changed, and the global and local responses of the numerical model were compared to the test. Figs. 16(a) and 16(b) describe the trend of MAPE and surface true longitudinal strain with respect to the deviation of $\varepsilon_{(Trans)}$ for notched specimens taken from the beam flange. As it is evident from Fig. 16(a), over a ±15% range of deviation, the MAPE changed negligibly, and almost for all specimens, it was under the maximum allowable value (0.01) defined in the calibration procedure. Fig. 16(b) also shows a plateau in local response in this range of $\varepsilon_{(Trans)}$. Therefore, a rough estimation of transitional strain would be sufficient for accurate calibration of the two-segment exponential hardening rule. In these figures, the values corresponding to zero deviation denote the MAPE and strain obtained based on the actual transitional strains, which were measured by DIC.
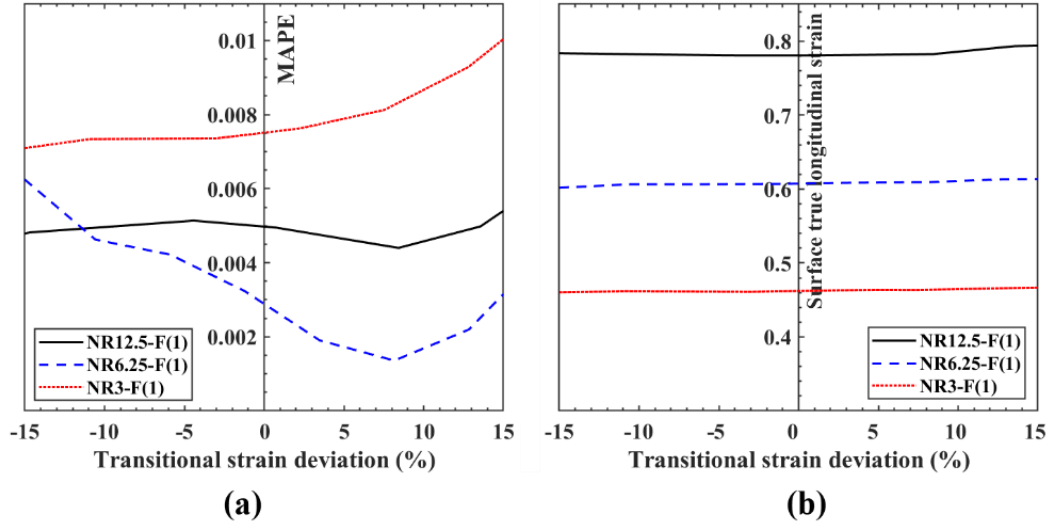
Fig. 16. Variation of the global and local responses for up to ±15% deviation of $\varepsilon_{(Trans)}$: a) MAPE, b) the surface true longitudinal strain at the fracture displacement.

8.2. VGM calibration results

Once the constitutive model was calibrated by two described approaches, the VGI for the material points of each notched specimen was calculated based on Eq. 2 by using the developed VUSDFLD user subroutine. Table 2 lists the calibrated $VGI_{critical}$ for both approaches. These values were the maximum value of VGI at the notch section in a displacement corresponding to the test fracture displacement. For specimens with 12.5 and 6.25 mm of notch radius, this maximum occurred in the center of the specimens, while in the specimens with 3 mm of the notch radius, the fracture initiated at a point between the center and the notch root. This can be justified based on extremely non-uniform strain distribution on the notch of these specimens (see Figs. 11(b) and 12(b)).

As Table 2 reports, the mean value of $VGI_{critical}$ calibrated by the proposed approach is 3.09, which is about 48% more than average $VGI_{critical}$ calibrated by the common approach (2.08). This difference cannot be used to compare the accuracy of the approaches; however, it proves that calibration of VGM and the constitutive model can be meaningfully correlated. In other words, $VGI_{critical}$ calibrated based on each approach must be used by the corresponding constitutive model to have an accurate prediction of the fracture. This can also be interpreted as the nonunique calibration of the VGM.

In terms of dispersion, when the proposed approach was used, the coefficient of variation of $VGI_{critical}$ was almost 8%, while values calibrated by the common approach exhibited about 18% of dispersion. These coefficients demonstrate that

the proposed calibration approach is less subjected to calibration errors and uncertainties.

9. Results validation

The numerical models calibrated by two calibration procedures were compared to predict fracture of the pull-plate tests. Figs. 17 and 18 compare the numerical and experimental force-elongation curves of the tested specimens. It is apparent from these figures that the proposed approach showed a closer agreement between the numerical and experimental force-displacement curves. The accuracy of two calibrated material models can be compared in terms of force and displacement corresponding to the fracture initiation. Based on these curves, the fracture initiation displacement predicted by the proposed approach indicated a 4.8% average absolute error compared to the test. This error was 7.0% for the common approach. However, the average absolute error in the fracture initiation force predicted by the common approach was 10.8%, which is more than twice the average absolute error, which was obtained from the proposed approach (4.6%). It must be noted that for all pull-plate tests, the material model calibrated by both approaches overestimated the fracture forces.

The numerical curves after fracture initiation also indicate an acceptable accuracy in predicting fracture propagation through the plates. In addition, the comparison between the numerical and experimental fractured pattern of specimens in Figs. 17 and 18 demonstrates the ability of VGM to predict fracture initiation and propagation when it is integrated by the adaptive meshing and element removal techniques. Such a model is advantageous to evaluate the performance of the steel structure under extreme loads.

Besides improving the accuracy, the numerical and experimental results validated the proposed approach as an alternative for calibration of the material model, which only required flat SNT specimens. Therefore, it can be applied for situations with a limited material length or complicated geometry (e.g., weldments) that the production of uniaxial specimens is impractical.
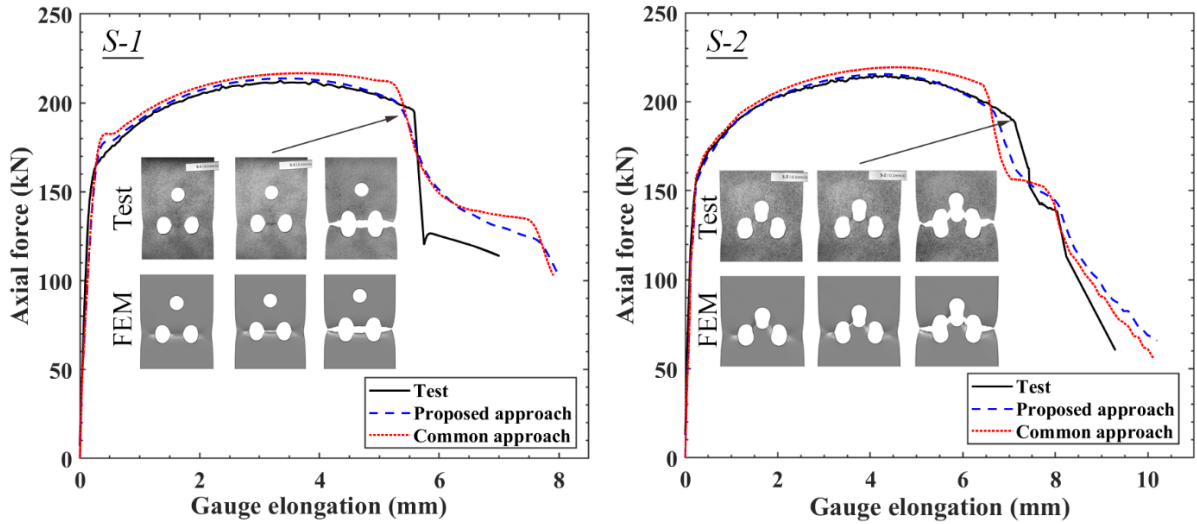
Fig. 17. Numerical and experimental force-elongation curves of S-1 and S-2 specimens.
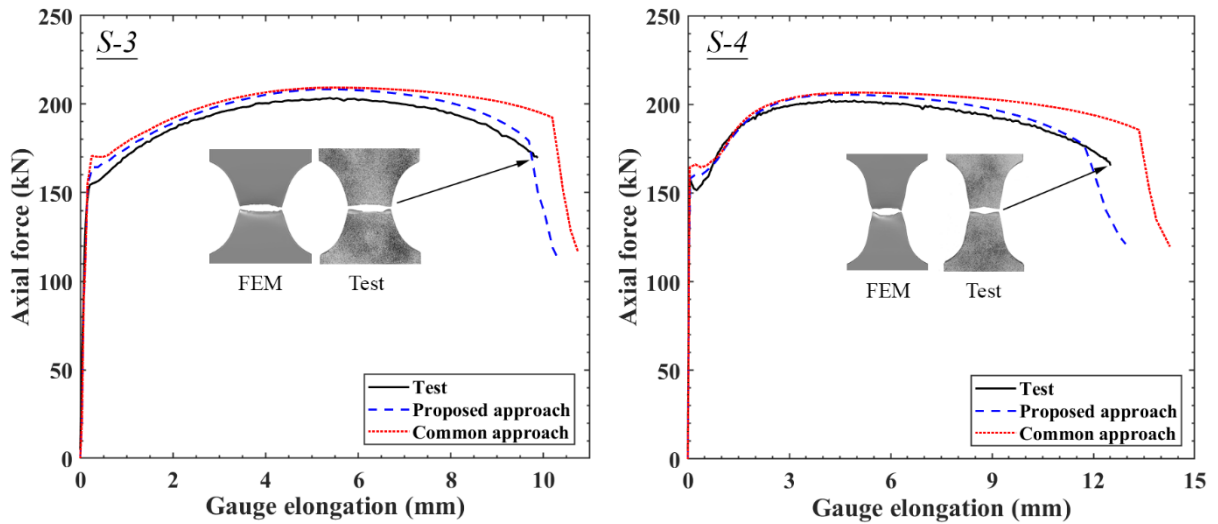
Fig. 18. Numerical and experimental force-elongation curves of S-3 and S-4 specimens.

10. Conclusion

The common approach to calibrate the ductile fracture criteria utilizes two sets of tests. Uniaxial tensile tests are employed to calibrate the constitutive model, and notched tensile specimens are used to calibrate the fracture criterion. This calibration process is not applicable when the length of material is limited (e.g., welds) or the geometry of parts is complicated to produce uniaxial specimens.

To overcome this problem, an alternative calibration approach was presented based on a two-segment exponential hardening evolution rule. In this approach, both the constitutive model and VGM can be calibrated by a single set of notched specimens. The approach utilizes the digital image correlation system as a strain field measurement technique to estimate the transitional strain ($\varepsilon_{(Trans)}$) that denotes the transition point between two segments of the hardening rule. The common and proposed calibration approaches were compared for S355J2 steel as

a case study material. The following conclusions were drawn from the experimental and numerical studies carried out in this paper:

- It was shown that the numerical models calibrated by the proposed approach could provide a tighter fit between the experimental and numerical force-displacement curves of double-edge-notched specimens during the calibration process. The total mean absolute percentage error was 0.62% for the proposed approach and 3.21% for the common approach on average. The proposed approach also indicated better prediction in pull-plate tests. This approach predicted fracture initiation force of four pull-plate tests with a 4.6% average error. In comparison, the common approach led to a 10.8% average error, which is about twice the proposed method. Therefore, it was concluded that the proposed method could estimate the equivalent stress more precisely compared to the common method.

- In terms of predicting local strain, numerical models calibrated based on both approaches could successfully predict the strain measured by DIC in flat notched specimens with nearly the same accuracy.

- The mean value of $VGI_{critical}$ calibrated by the proposed approach was 3.09, which is about 48% more than average $VGI_{critical}$ calibrated by the common approach (2.08). These values indicate a meaningful correlation between the VGM and the constitutive model that also can be understood as the nonunique calibration of the VGM.

- In terms of dispersion, when the proposed approach was used, the coefficient of variation of calibrated $VGI_{critical}$ was almost 8%, while the common approach led to about 18% of dispersion in this parameter. These values also indicate that the proposed calibration approach is less subjected to calibration errors and uncertainties.

- Finally, presented results supported the proposed calibration approach as a practical alternative to calibrate ductile fracture criterion when producing uniaxial tension specimens is difficult. In addition, because the proposed approach synchronizes the calibration of the constitutive model and fracture criterion, it can capture the correlation between them. This feature is beneficial to address the variation of the material parameters in probabilistic-mechanical analyses. On the contrary, the common approach lacks this feature, and the calibration of the

constitutive model and fracture criterion are two unsynchronized processes.

Although the proposed approach would need more computational resources to do iterations and relies on the use of field strain measurements from a digital image correlation (DIC) system, the fast advancement of computer technology and the development of open-source digital image correlation platforms will make using this approach feasible in design and research projects that the fracture performance of steel structures is under investigation.

11.References

Alves, M. l., and Jones, N. (1999). "Influence of hydrostatic stress on failure of axisymmetric notched specimens." *Journal of the Mechanics and Physics of Solids*, 47(3), 643-667.

Anderson, T. L. (2005). *Fracture mechanics: fundamentals and applications*, CRC press.

Barton, D., Sturges, J., Mirza, M., and Church, P. (1991). "Deformation and Fracture; Modelling Techniques to Take Account of Strain-Rate Behaviour and Stress State." *Le Journal de Physique IV*, 1(C3), C3-931-C933-936.

Bridgman, P. W. (2013). *Studies in large plastic flow and fracture: with special emphasis on the effects of hydrostatic pressure*, Harvard University Press.

Cooke, R., and Kanvinde, A. (2015). "Constitutive parameter calibration for structural steel: Non-uniqueness and loss of accuracy." *Journal of Constructional Steel Research*, 114, 394-404.

Dassault Systèmes (2014). *ABAQUS Analysis User's Manual (Version 6.14)*, Dassault Systèmes Simulia Corp., Providence, RI.

European Committee for Standardization (2004). "Standard for hot-rolled structural steel. Part 2 - Technical delivery conditions for non-alloy structural steels (EN 10025-2:2004).", CEN, Brussels, Belgium.

Hertelé, S., De Waele, W., and Denys, R. (2011). "A generic stress–strain model for metallic materials with two-stage strain hardening behaviour." *International Journal of Non-Linear Mechanics*, 46(3), 519-531.

Hollomon, J. H. (1945). "Tensile deformation." *Aime Trans*, 12(4), 1-22.

Jun, C., Li, F.-g., and SUN, Z.-k. (2017). "Tensile stress–strain behavior of metallic alloys." *Transactions of Nonferrous Metals Society of China*, 27(11), 2443-2453.

Kanvinde, A., and Deierlein, G. (2004). "Micromechanical simulation of earthquake-induced fracture in structural steel." *Rep. No.145*, The John A. Blume Earthquake Engineering Center, Stanford.

Kanvinde, A., and Deierlein, G. (2006). "The void growth model and the stress modified critical strain model to predict ductile fracture in structural steels." *Journal of Structural Engineering*, 132(12), 1907-1918.

Kanvinde, A., and Deierlein, G. (2007). "Finite-element simulation of ductile fracture in reduced section pull-plates using micromechanics-based fracture models." *Journal of Structural Engineering*, 133(5), 656-664.

Khadyko, M., Dumoulin, S., Børvik, T., and Hopperstad, O. S. (2014). "An experimental–numerical method to determine the work-hardening of anisotropic ductile materials at large strains." *International Journal of Mechanical Sciences*, 88, 25-36.

Kiran, R., and Khandelwal, K. (2014). "Experimental studies and models for ductile fracture in ASTM A992 steels at high triaxiality." *Journal of Structural Engineering*, 140(2), 04013044.

Liao, F., Wang, W., and Chen, Y. (2012). "Parameter calibrations and application of micromechanical fracture models of structural steels." *Structural engineering and mechanics*, 42(2), 153-174.

Liao, F., Wang, W., and Chen, Y. (2015). "Ductile fracture prediction for welded steel connections under monotonic loading based on micromechanical fracture criteria." *Engineering Structures*, 94, 16-28.

Murata, M., Yoshida, Y., and Nishiwaki, T. (2018). "Stress correction method for flow stress identification by tensile test using notched round bar." *Journal of Materials Processing Technology*, 251, 65-72.

Öchsner, A. (2016). "Continuum damage mechanics." *Continuum Damage and Fracture Mechanics*, Springer, 65-84.

Qin, J., Holmedal, B., Zhang, K., and Hopperstad, O. S. (2017). "Modeling strain-path changes in aluminum and steel." *International Journal of Solids and Structures*, 117, 123-136.

Rice, J. R., and Tracey, D. M. (1969). "On the ductile enlargement of voids in triaxial stress fields." *Journal of the Mechanics and Physics of Solids*, 17(3), 201-217.

Saykin, V. V., Nguyen, T. H., Hajjar, J. F., Deniz, D., and Song, J. (2020). "The effect of triaxiality on finite element deletion strategies for simulating collapse of full-scale steel structures." *Engineering Structures*, 210, 110364.

Shi, G., and Chen, Y. (2018). "Investigation of ductile fracture behavior of lap-welded joints with 460 MPa steel." *Advances in Structural Engineering*, 21(9), 1376-1387.

Sutton, M. A., Orteu, J. J., and Schreier, H. (2009). *Image correlation for shape, motion and deformation measurements: basic concepts, theory and applications*, Springer Science & Business Media.

Tu, H., Schmauder, S., and Weber, U. (2016). "Simulation of the fracture behavior of a S355 electron beam welded joint by cohesive zone modeling." *Engineering Fracture Mechanics*, 163, 303-312.

Tu, S., Ren, X., He, J., and Zhang, Z. (2020). "Stress–strain curves of metallic materials and post-necking strain hardening characterization: A review." *Fatigue & Fracture of Engineering Materials & Structures*, 43(1), 3-19.

Tu, S., Ren, X., Nyhus, B., Akselsen, O. M., He, J., and Zhang, Z. (2017). "A special notched tensile specimen to determine the flow stress-strain curve of hardening materials without applying the Bridgman correction." *Engineering Fracture Mechanics*, 179, 225-239.

Tvergaard, V., and Needleman, A. (1984). "Analysis of the cup-cone fracture in a round tensile bar." *Acta metallurgica*, 32(1), 157-169.

Voce, E. (1948). "The relationship between stress and strain for homogeneous deformation." *Journal of the Institute of Metals*, 74, 537-562.

Vysochinskiy, D. (2014). "Formability of aluminium alloy subjected to prestrain by rolling." Norwegian University of Science and Technology.

Wang, Y., Zhou, H., Shi, Y., and Xiong, J. (2011). "Fracture prediction of welded steel connections using traditional fracture mechanics and calibrated micromechanics based models." *International Journal of Steel Structures*, 11(3), 351.

Zhang, Z., Hauge, M., Thaulow, C., and Ødegård, J. (2002). "A notched cross weld tensile testing method for determining true stress–strain curves for weldments." *Engineering fracture mechanics*, 69(3), 353-366.

Paper IV:
Developing fracture-based fragility curves for steel components in corrosive environments

Developing fracture-based fragility curves for steel components in corrosive environments

Mohammad Ali Mahdavipour[1], Dmitry Vysochinskiy[2]

[1] Ph.D. Research Fellow, Department of Engineering Sciences, University of Agder, Jon Lilletuns vei 9, 4879, Grimstad, Norway, Email: ali.mahdavipour@uia.no

[2]Associate Professor, Department of Engineering Sciences, University of Agder, Jon Lilletuns vei 9, 4879, Grimstad, Norway, Email: dmitry.vysochinskiy@uia.no

Abstract

Under excessive plastic deformations, pitting corrosion accelerates ductile fracture initiation in steel components. Because of the stochastic and time-dependent nature of corrosion in steel material, the integrity of the steel components must be evaluated through a rational procedure in which corrosion uncertainties are considered to estimate the probability of failure for future events. Previous studies developed fragility curves to predict the capacity of global structures under uniform corrosion. However, for steel structures subjected to pitting corrosion, the local effect of corrosion is substantial and is also challenging to implement in the global model of structures. In this study, the concept of fracture-based fragility curves was developed at the component level by micromechanical modeling of different random pitting morphologies at a given intensity level of pitting corrosion. For this purpose, a unique meshing technique was employed to implement random pitting morphologies in numerical models. A demonstration study on a single-sided corroded plate revealed that random morphologies at an identical corrosion intensity level led to a notable dispersion in the failure elongations. The proposed fragility curves could address this effect on the probability of failure of the specimen. Therefore, decision-makers can reliably utilize such curves in a comprehensive risk-based corrosion management framework to evaluate the risk of failures and determine proper treatment strategies.

KEYWORDS

Fragility curve; pitting corrosion; steel marine structure; ductile fracture; excessive plastic deformation; probability of failure

1. Introduction

Many of the worlds' structures like bridges, jetties, offshore facilities are subjected to aggressive environments. For these structures, structural integrity and safety must be demonstrated concerning the interaction of possible loading scenarios and the corrosion deterioration (DNV GL 2015a). Because of the stochastic and time-dependent nature of corrosion in steel material, this interactional effect must be studied through a comprehensive risk-based corrosion management framework (DNV GL 2015a).

In a risk-based corrosion management procedure, the risk is identified based on the potential threats and consequences of the current and future corrosion to the structural integrity (DNV GL 2015a). In this procedure, the analysis of the likelihood of failures and their consequences to the whole system plays a central role in performing a quantitative risk assessment (DNV GL 2015a). Based on such evaluated likelihoods, the risk managers can choose proper treatment techniques to upgrade existing structures to fulfill principal criteria, e.g., health and safety, economy, environment, etc. (DNV GL 2015a). Furthermore, the risk evaluation of failure in the design phase of new structures subjected to corrosion is also essential to facilitate an optimal selection of corrosion prevention, inspection, and monitoring methods based on the structure's performance for future events.

In order to perform corrosion risk evaluations, fragility curves are viable statistical tools because they quantify the failure of the aged structures in terms of probability. Fragility curves have been widely employed for the assessment of various structures subjected to corrosion. Ghosh and Padgett (2010); Guo and Zhang (2019), and Yang et al. (2021) developed fragility curves for different aged reinforced concrete structures under seismic loads. In these studies, the corrosion was considered as a uniform reduction in the sectional area of the rebars. Jahanitabar and Bargi (2018); (Yang et al. 2019), and (Yeter et al. 2020) conducted similar studies to develop seismic fragility curves for steel structures affected by uniform corrosion.

All the above-mentioned studies used the concept of fragility curves to predict the capacity of an aged structure at the global level. This approach is mainly applicable to structures with uniform corrosion, that the effect of corrosion deterioration can be implemented in macro models or simplified shell models by reducing the section of the corroded members. However, for steel structures subjected to pitting corrosion, the local effect of corrosion is substantial. Modeling this local effect in the global structures is challenging due to numerical models and computational

resources limitations. This issue will be more challenging when structures are under extreme loads that cause excessive plastic deformations. In such a scenario, corrosion pits act as local concentrators that magnify the local plastic strain and stress triaxiality (Cerit 2013; Ji et al. 2015; Pidaparti and Patel 2008; Turnbull et al. 2010). This magnification can accelerate ductile fracture initiation in steel components (Bao and Wierzbicki 2004; Hancock and Mackenzie 1976; Johnson and Cook 1985; McClintock 1968; Rice and Tracey 1969) and can reduce their ductility significantly. In addition, previous studies (Ahmmad and Sumi 2010; Songbo et al. 2021; Wang et al. 2018a; Wang et al. 2017; Xu et al. 2016; Zhao et al. 2020) indicated that a three-dimensional representation of the pit geometry associated with a micromechanical fracture criterion is required to accurately capture the local effects of pitting on the ductile fracture of a component. In such numerical models, a fine discretization of the corrosion spatial geometry must be utilized to predict the local responses properly (Ahmmad and Sumi 2010; Songbo et al. 2021; Wang et al. 2018a; Wang et al. 2017). As a result, fragility curves obtained based on the macro modeling approach or shell modeling with an equivalent thickness cannot properly describe the effect of the random pitting in the prediction of failure of the structures (Wang et al. 2018b).

The limitations mentioned above motivated the authors to introduce fracture-based fragility curves at the component level of corroded steel structures subjected to marine environments. For a given intensity level of pitting corrosion, the fragility curves were produced by micromechanical modeling of different random pitting morphologies. In this connection, pitting morphologies were generated randomly based on the probability distributions of pit characteristics and were implemented based on a proposed meshing technique. The developed fragility curves are capable to reliably assess the integrity of steel components under large plastic deformations where ductile fracture is a probable failure mode. As a result, the proposed approach can be extended to real scenarios like a ship collision, an unexpected element removal, or a dropped heavy object in which excessive plastic deformations are expected. Under those circumstances, each component contributes to the reliability or failure of the system (Lemaire 2013). Therefore, the component fragility curves enable engineers to characterize the most critical failure scenario based on combinations of component failures (Lemaire 2013).

It is worth mentioning that proposed fragility curves are applicable for both general and pitting corrosion or a combination of them; however, in this study, only the

pitting corrosion was considered that is believed to be the main source of the corrosion uncertainties.

2. Methodology

Fig. 1 illustrates an overview of the risk-based corrosion management procedure consists of three main modules. These modules form a life cycle in which a continuous assessment is done to keep the risk of corrosion updated and accordingly to determine the expected life of the facilities and revise the remediation strategy (DNV GL 2015a). In the corrosion module, a long-term evolution rule for different types of corrosion (i.e., uniform and pitting corrosion) associated with the probability distributions of the corrosion characteristics, e.g., pit depth and shape, are provided (Melchers 2021; Shekari et al. 2017). As shown in Fig. 2.a, based on the output of the corrosion module, one can determine the severity of the corrosion in terms of corrosion Intensity Measure (IM) for a given time of exposure (t_1). The IM parameter must be defined based on the dominant corrosion parameters that affect the failure of the components. Additionally, the probability distributions of the corrosion parameters are provided for this specific time of exposure (t_1). Based on these probability distributions for an assumed level of corrosion intensity measure $(IM = im_1)$, various pitting morphologies can be considered. Consequently, the variation of pitting morphology can affect the Engineering Demand Parameter (EDP) in which the component fails. EDP is a structural response quantity that can be used to estimate the failure or damage state of a component (Whittaker et al. 2004). In this study, numerical models associated with a micromechanical fracture criterion were analyzed for different stochastic morphologies of pitting corrosion to quantify the probability of failure.

As illustrated schematically in Fig. 2.b, a fragility curve is a cumulative probability distribution function in which the probability of failure for a determined engineering demand parameter (edp_1) can be written as follows:

$$F(edp_1) = P_f(EDP > edp_1 | IM = im_1) \qquad (1)$$

Where $F(edp_1)$ denotes the probability of failure when EDP exceeds edp_1. The right-hand term $P_f(EDP > edp_1 | IM = im_1)$ is calculated from stochastic analyses of the structural component subjected to a set of random pitting morphologies generated for a predefined level of intensity measure $(IM = im_1)$. This concept is common practice in earthquake engineering to consider the

uncertainties associated with the frequency content of different ground motions (Deylami and Mahdavipour 2016; Mahdavipour and Deylami 2014).
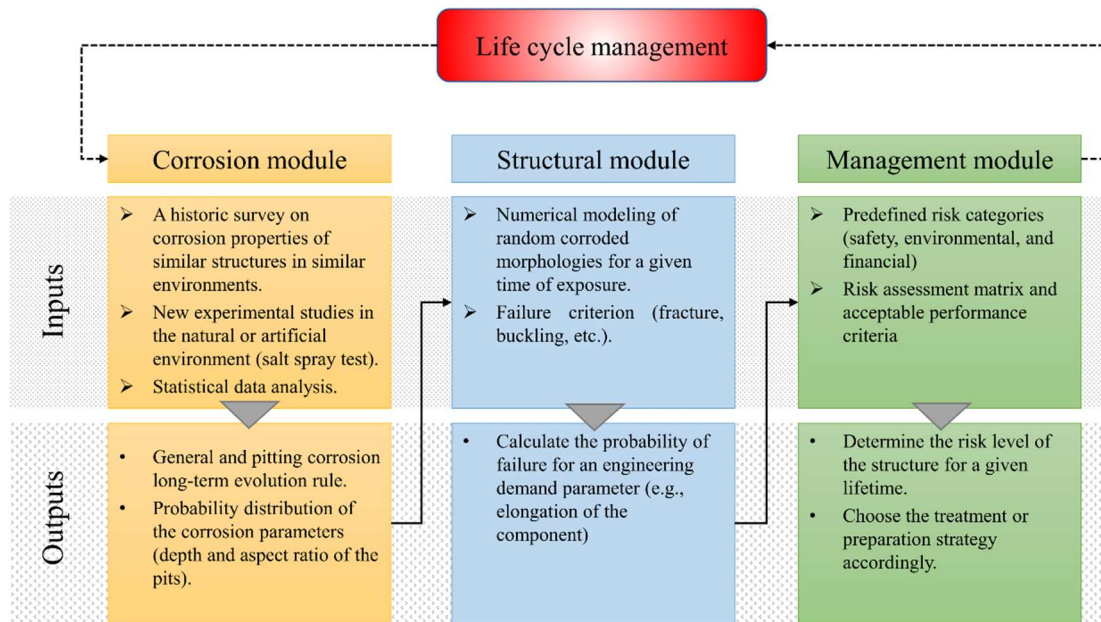
Fig. 1. An overview of the risk-based corrosion management procedure (this study is focused on the structural module).
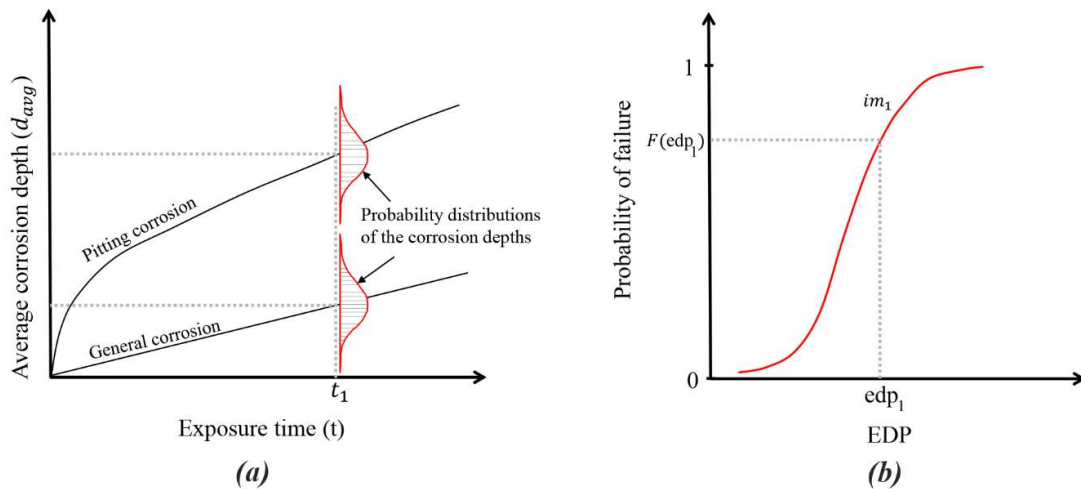
Fig. 2. a) An illustration of the long-term evolution rule and the probability distribution of corrosion parameters, b) an illustration of the concept of fragility curve.

Based on the outputs of the structural modules, decision-makers utilize risk management methods to assess the most critical scenarios in terms of principal criteria, e.g., health and safety, economy, environment, and accordingly prescribe remedies for an expected lifetime (DNV GL 2015a). It is worth mentioning that doing the whole cycle described in Fig. 1 requires a variety of data gathered for a particular project. This study is devoted to making advancements in the structural modules. For this reason, the output of the corrosion module was determined from

relevant literature. Then the fragility curves were developed to scrutinize the effect of involved parameters on the failure probability of components.

2.1. Intensity measure of corrosion

An Intensity Measure (IM) definition is required to describe the severity of future corrosion and involve all influential parameters in the assessment process. For uniform corrosion, the main parameter that can specify the intensity of corrosion is the average corrosion depth, while in pitting corrosion, using one parameter cannot accurately describe the intensity level of the corrosion. One of the conventional IMs is Degree of Pitting (DOP) that provides information about the surficial intensity of pits by calculating the ratio of the corroded area (A_c) to the total area of the original member (A_t) (Huang et al. 2010; Wang et al. 2020; Wang et al. 2014) as follows:

$$DOP(\%) = \frac{A_c}{A_t} \times 100\% \qquad (2)$$

DOP is silent about the pitting depth; however, pit depth was indicated as an influential parameter on the ductility of the tensile components (Sheng and Xia 2017; Xu et al. 2016). Therefore, in this study, an integrated $IM[DOP, d_{avg}]$ was used that consists of both Degree of Pitting (DOP) and average pitting depth (d_{avg}). This definition is also consistent with standard methods (ASTM 2005; International Organization for Standardization 2020) proposed for the rating of pitting corrosion.

2.2. Engineering demand parameter

The selection of a proper EDP depends on the nature of the load and the probable failure mode of the component. For example, when the fracture of a tensile member is under investigation, axial elongation of the component can be considered as EDP; however, it must be selected appropriately for other types of components, e.g., steel joints under bending or a compression member. In these components, joint rotation and compressive load can be considered as describing structural responses related to the component failure or damage state.

2.3. Pitting characteristics

Previous studies (Duddu 2014; Xu et al. 2016) showed that when corrosion pits are significantly developed into the thickness of members, the pits can be simplified by semi-ellipsoids. By this simplification, the effect of the pit geometry

can be implemented in finite element models as were done by many other authors (Cerit 2013; Cerit et al. 2009; Huang et al. 2010; Wang et al. 2018a; Yan et al. 2019; Zhang et al. 2015; Zhao et al. 2020).

In this study, a semi-ellipsoidal shape was also assumed as an acceptable geometry to implement pits in the finite element models. Based on this geometry, to characterize a pit, one needs to specify its coordinates (x and y), depth (d), and aspect ratio (AR). AR is defined as the ratio between the pit width (w) and the pit depth ($AR=w/d$) that affects local responses in the pit, i.e., plastic strain and stress triaxiality (Cerit 2013; Cerit et al. 2009; Wang et al. 2018a). These parameters illustrated in Fig.4 can randomly be generated based on the probability distributions of the pit characteristics. Fig. 3 describes the procedure to generate a random pattern based on an assumed time of exposure (t_1) that intensity of the corrosion is $IM[DOP_{(t_1)}, d_{avg(t_1)}]$.
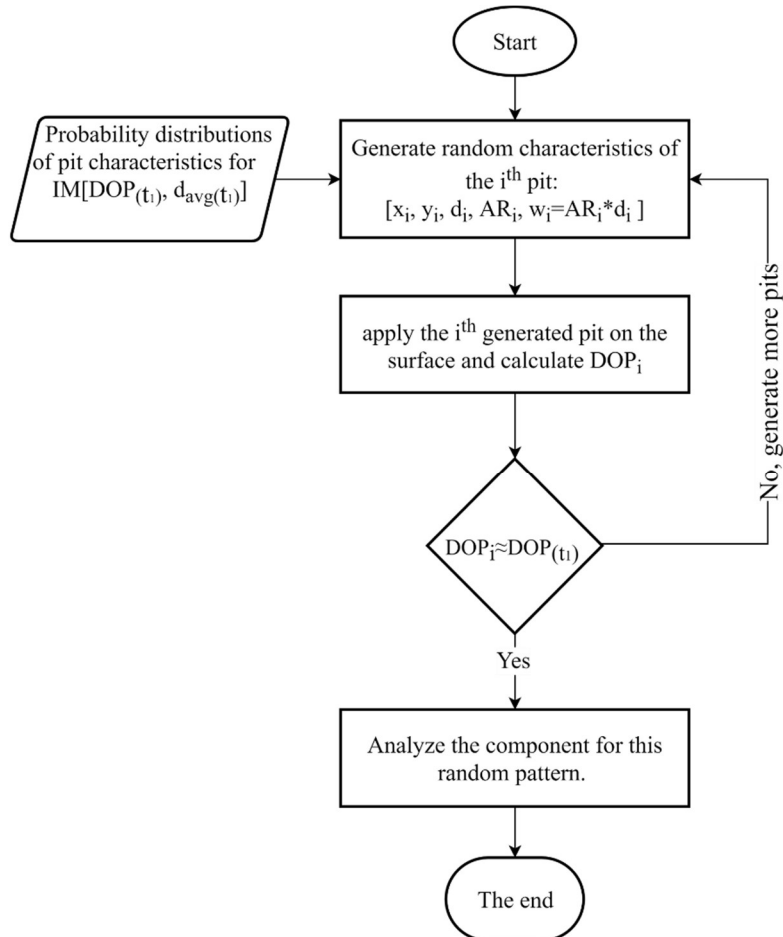

Fig 3. The procedure of random pitting pattern generation for $IM[DOP_{(t_1)}, d_{avg(t_1)}]$.

2.4. Numerical modeling of the random pitting

To evaluate the failure of a component under externally applied load, the finite element model of the component must be analyzed for each generated random

pattern. In this study, a carving technique was proposed to implement different pitting patterns into the numerical models. More details about this technique and also material modeling are presented in the following sections.

2.4.1. Pitting pattern discretization

The meshing technique and proper type of elements to implement corrosion pits depend on the nature of the problem. Previous studies indicated that for steel members under compression where the main failure is a global or local buckling, shell elements are adequate (Wang et al. 2018b; Wang et al. 2014; Zhao et al. 2018; Zhao et al. 2021). The effect of random pitting morphologies can be implemented by changing the thickness of the shell element in the location of the pits (Wang et al. 2018b; Wang et al. 2014; Zhao et al. 2018; Zhao et al. 2021). Alternatively, when the component is under tensile load and fracture is the most dominant failure mode, using solid elements with fine mesh is required to predict the fracture initiation. In contrast to shell elements, solid elements can properly capture the effect of triaxiality and interaction between pits.

On the other hand, for solid elements, implementing a random pattern of semi-ellipsoidal pits in the geometry of components is a demanding task. When the geometry is complicated, and hexahedral elements are employed, the standard meshing techniques provided by numerical software solutions often need manual partitioning and seeding to have a proper mesh quality. The manual meshing techniques are inefficient in implementing a random pitting morphology with lots of different random pits. In most cases, these meshing techniques can lead to divergence or a low-quality mesh. This can be more problematic in this study in which multiple random patterns are under investigation. One possibility is to use tetrahedral elements that support fully automatic tetrahedral meshers (Dassault Systèmes 2014). But for the same degree of freedom and amount of discretization through the thickness of a member, one needs significantly more tetrahedral elements compared to hexahedrons (Wang et al. 2017).

Moreover, the first-order tetrahedral elements are insufficiently accurate for structural calculations (Dassault Systèmes 2014), and the second-order formulation must be chosen that even needs more computational resources. In contrast, developed reduced integration hexahedral elements can significantly increase computational efficiency without losing accuracy (Dassault Systèmes 2014). Therefore, various techniques were employed to implement random pitting corrosion with hexahedral elements (Ahmmad and Sumi 2010; Wang et al. 2014;

Wang et al. 2017). These techniques are mainly developed based on third-party software or code that might be unavailable to the community. In this study, the pits were implemented on the component's geometry by carving the pits on an intact mesh. The geometry of the intact component was discretized with eight-node brick elements with reduced integration (C3D8R). Then the pits were implemented by removing nodes and associated elements located inside the pits. Fig. 4 illustrates this approach to implement the geometry of a single pit on a steel plate.

For micromechanical modeling of ductile fracture, a fine mesh size comparable with the characteristic length (ℓ^*) of the mild steel is required to calculate the local response and the fractured state accurately (Kanvinde and Deierlein 2006; Liao et al. 2012). The characteristic length is defined as a length scale that ductile crack is assumed to initiate once the fracture criteria exceed the critical value over that length (Kanvinde and Deierlein 2006). This mesh refinement must be used over the most critical region of the component due to the unknown locus of fracture initiation. By using such fine mesh, a stepwise representation of pits created by carving on the intact mesh can predict relatively similar local results compared to pits implemented by geometry. This can be tested through a standard mesh sensitivity analysis for a single pit penetrated into the component.
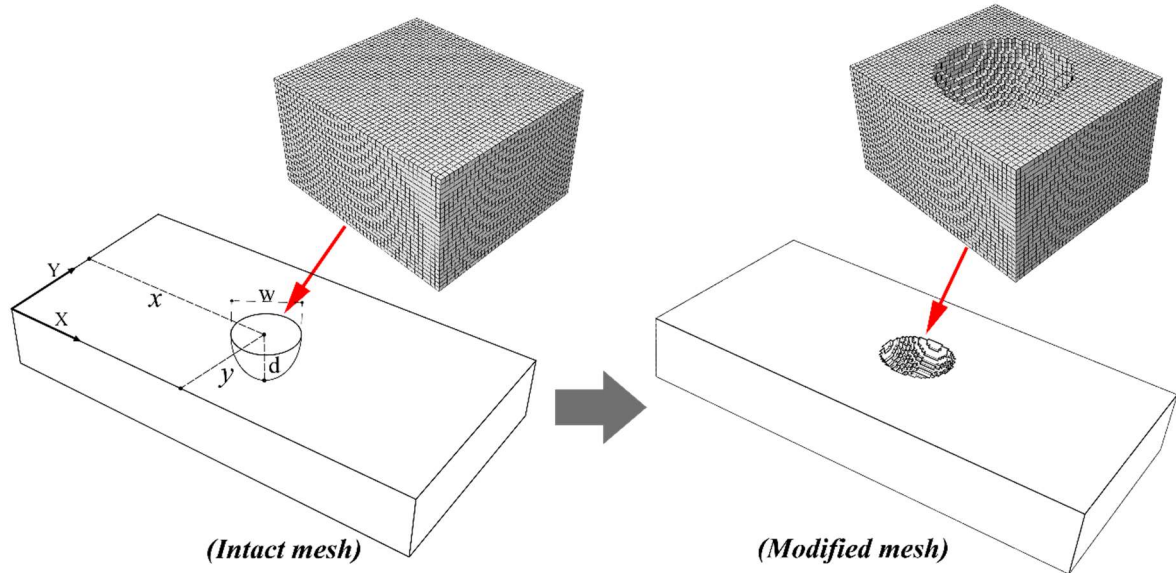
Fig. 4. The geometry of a random pit is implemented by carving on the intact mesh.

2.4.2. Material modeling

The Void Growth Model (VGM) was selected as a micromechanical ductile fracture criterion in which an explicit continuous integration of the stress triaxiality ratio (η) with respect to equivalent plastic strain ($\bar{\varepsilon}_p$) is performed (Kanvinde and Deierlein 2006). Based on the VGM, the fracture initiates when the size of voids

exceeds a threshold value (Kanvinde and Deierlein 2006). Therefore, the criterion can be formulated as follows (Kanvinde 2017):

$$VGI = \int_0^{\bar{\varepsilon}_p} e^{1.5\eta}.d\bar{\varepsilon}_p > VGI_{critical} \qquad (3)$$

The left-hand side of this relation is the Void Growth Index (VGI) that is calculated by an explicit integration of stress triaxiality ratio (η) with respect to equivalent plastic strain history ($\bar{\varepsilon}_p$) (Kanvinde and Deierlein 2006; Kanvinde and Deierlein 2007). The critical void growth index ($VGI_{critical}$) on the right-hand side can be considered as a material parameter that is calibrated based on the smooth-notched tensile specimens and complementary finite element analyses (Kanvinde and Deierlein 2006; Kanvinde and Deierlein 2007).

Besides the fracture criterion, an element removal technique was used to model the fracture propagation through the components that remove elements with VGI larger than $VGI_{critical}$. It was indicated that the VGM can effectively be used to simulate material separation through finite element removal techniques (Saykin et al. 2020).

3. A Case study

To present a demonstration of the described method, fracture-based fragility curves were extracted for a simple pulling dogbone specimen under different intensity levels of pitting corrosion. This plate can be considered as a local representative of an actual steel component.

3.1. Specimen geometry

Fig. 5 shows the geometry of the intact specimen. It was assumed that only the uniform reduced length (30x50mm) is under corrosion attack. The corrosion outside of this region is not critical due to the larger cross-sectional area. The plate was taken from an IPE 200 steel beam flange and machined into a 7.4 mm thickness (Mahdavipour and Vysochinskiy 2021).
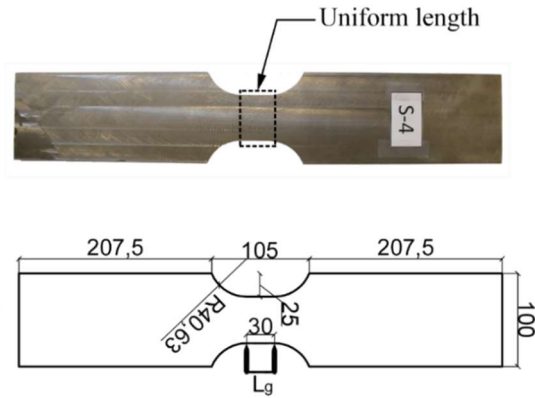
Fig. 5. The geometry of the intact tensile plate from S355J2 steel material (all dimensions are in mm and the thickness of the plate is 7.4mm) (Mahdavipour and Vysochinskiy 2021).

3.2. Specimen material

The specimen was fabricated from European steel grade S355J2 (European Committee for Standardization 2004). Fig. 6.a presents the plastic flow curve of S355J2 calibrated by Mahdavipour and Vysochinskiy (2021). This flow curve was employed with von Mises yield criterion and associated isotropic hardening to simulate material plasticity (Mahdavipour and Vysochinskiy 2021). The calibration of the VGM for S355J2 steel based on notched specimens also showed an average of 3.09 for $VGI_{critical}$ (Mahdavipour and Vysochinskiy 2021). In terms of elastic properties, Young's modulus (E) and Poisson's ratio (v) were assumed to be 191 GPa and 0.3, respectively. Fig. 6.b compares the numerical and experimental force-elongation of the intact specimen. This figure indicates a good agreement between numerical and experimental results. More validation tests also can be found in (Mahdavipour and Vysochinskiy 2021).
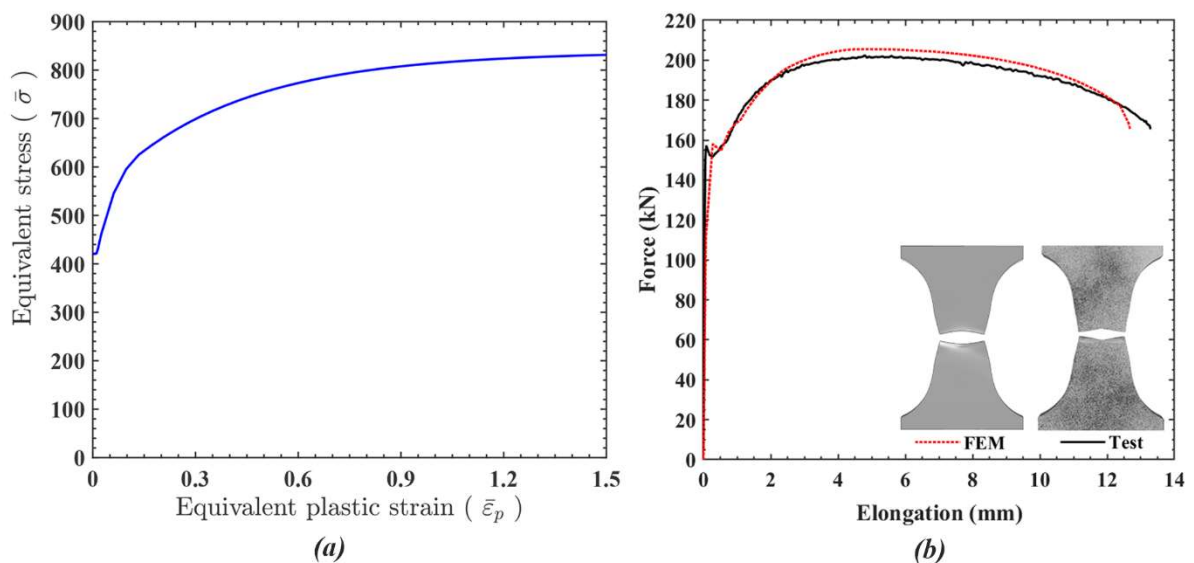
Fig. 6. a) Plastic flow curve of S355J2 used in numerical models (Mahdavipour and Vysochinskiy 2021), b) A comparison between numerical curve obtained in this study and experimental curve reported by (Mahdavipour and Vysochinskiy 2021).

3.3. Numerical modeling of specimen

Abaqus finite element software based on an explicit integration scheme was used to model intact and corroded specimens. A VUSDFLD user subroutine was developed to employ VGM as a fracture criterion in the numerical models.

Since guidelines like DNVGL-CG-0172 and DNVGL-CG-0182 (DNV GL 2015b; DNV GL 2016) define 60%-70% of the original plate thickness as a minimum acceptable remaining thickness without repair, 3 mm was considered as the maximum pit depth when pitting intensities were defined. In other words, repairing is necessary when pits are penetrated more than 3 mm in the studied plate. Based on this limitation, a standard mesh sensitivity analysis for a single pit with a 3 mm depth penetrated at the center of the plate was carried out. The pit was implemented by carving on the intact mesh with different sizes (0.7-0.3 mm) also by direct implementation of the geometry of the pit. Fig. 7 compares the *VGI* distribution in the pit for different mesh sizes.

The results indicate that by decreasing the mesh size from 0.4 mm to 0.3 mm, the maximum *VGI* changed less than 1%. This slight variation implies that mesh size is converged, and using 0.4 mm mesh size is adequate to evaluate local response in the pit domain. On the other hand, the element size must also be comparable with the typical characteristic length (ℓ^*) of mild steels that is reported from 0.4 mm to 0.2 mm (Kanvinde and Deierlein 2006; Liao et al. 2012). Based on these two factors, a 0.3 mm mesh size was selected for the discretization of the uniform length of the specimen; however, this element size must be reverified if thicker plates with deeper pits are under investigation.

As Fig.7 indicates, the maximum *VGI* obtained from carving on 0.3 mm mesh size showed less than 7% difference with the pit implemented by geometry. It must be remembered that using ideal smooth semi-ellipsoidal pits in itself is a simplification of the overall geometry of pits; however, the natural pits can have irregular surfaces. Therefore, this difference should not be interpreted as an absolute error but indicate that carving pits can predict the local effect of pit reasonably. It is also worth mentioning that although the carved pit could capture the maximum *VGI* observed in the pit, the *VGI* distribution fluctuates due to the stepwise nature of the carving approach (see Fig. 4). Since the maximum *VGI* controls the fracture initiation, the form of distribution is less influential on the final pit fracture behavior. Fig. 8 shows the final mesh configuration of the intact specimen as well as presents an example of a carved mesh for a random pitting pattern.
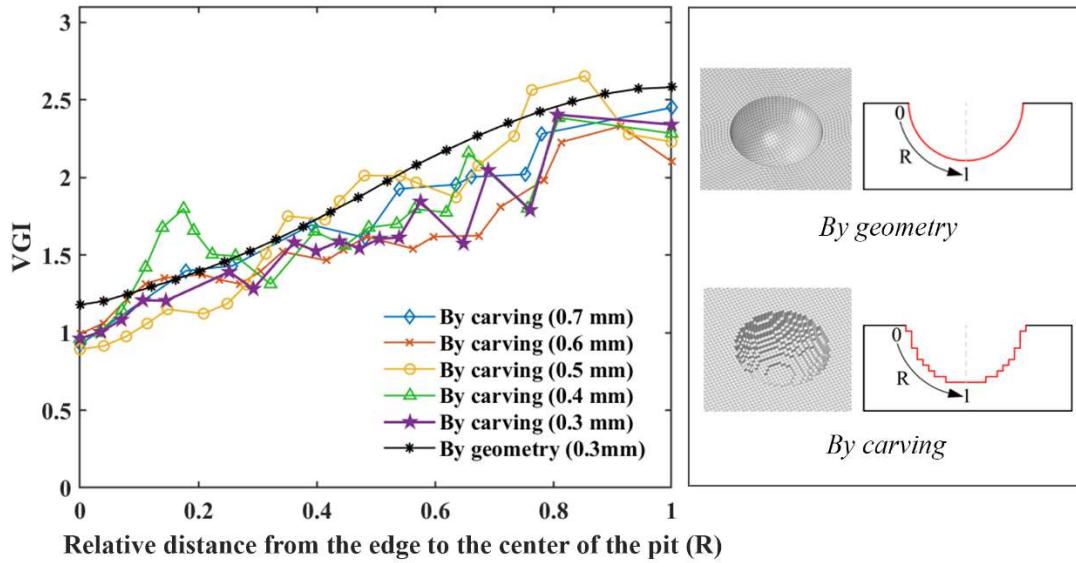
Fig. 7. Sensitivity of the VGI to the mesh size for a single pit carved at the center of the plate.
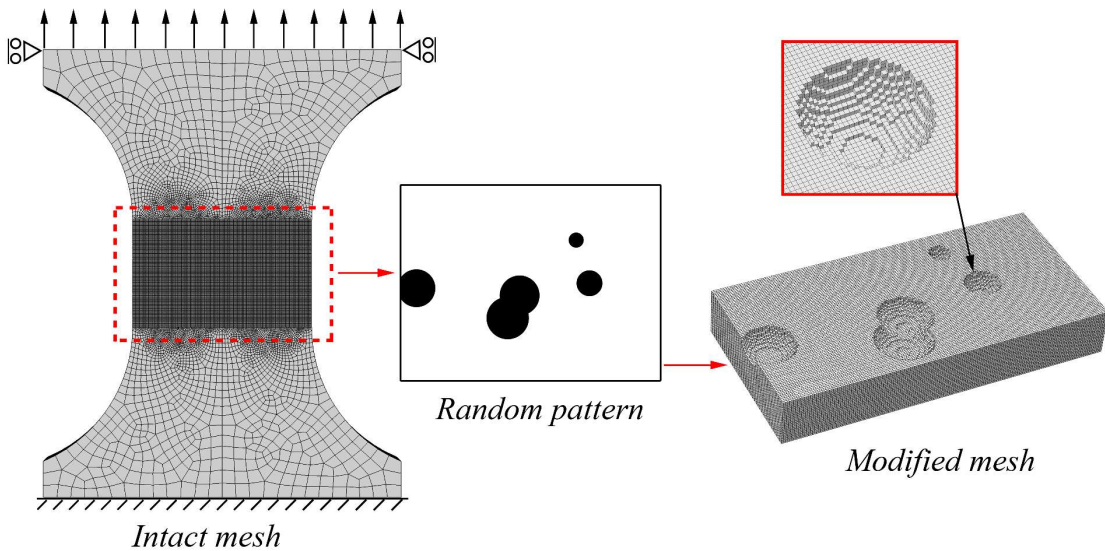
Fig. 8. An illustration of the implementation of a random pitting pattern by carving on the intact mesh.

3.4. Selected pitting IMs

Based on IM definition, nine different levels of IM were considered as listed in Table 1. Fifty random pitting morphologies were generated for each level based on the probability distribution of the pitting characteristics. The number of realizations discussed later by statistical analyses of the simulation results. It must be noted these predefined levels of intensity were selected only to extend the methodology into an application based on *DOPs* smaller than 50%. This limitation was adapted from reputable guidelines (DNV GL 2015; DNV GL 2016) that consider *DOPs* greater than 50% as uniform corrosion. As mentioned before, in an actual project, the target level of pitting corrosion is defined and updated

through a life cycle assessment based on the corrosion evolution rules, periodic inspections, and an expected lifespan, as described in Fig. 1.

Table 1. Matrix of predefined levels of intensity measure of pitting corrosion, $IM[DOP, d_{avg}]$.

		d_{avg}		
		1 mm	2 mm	3 mm
DOP	5%	IM[5%, 1mm]	IM[5%, 2mm]	IM[5%, 3mm]
	10%	IM[10%, 1mm]	IM[10%, 2mm]	IM[10%, 3mm]
	30%	IM[30%, 1mm]	IM[30%, 2mm]	IM[30%, 3mm]

3.5. Selected EDP

Since the specimen is under tensile load and the fracture is the failure mode, the elongation in the uniform length was considered as EDP. Fig. 5 shows the 30 mm of gage length that the elongation was measured for the intact and corroded plates. Based on this parameter, the failure elongation was determined as an elongation in which the strength of the plate dropped sharply. It is important to realize that for other types of components, e.g., connections, finding an obvious point that shows failure is difficult due to structural redundancy and alternative paths to transfer the applied load to other parts. In such cases, a certain amount of strength reduction can be recognized as the failure point.

3.6. Distribution of the pit characteristics

As described in Fig. 3, random pit generation was executed based on the probability distributions of the pit characteristics. These distributions were obtained based on a literature survey on pitting corrosion in mild steel. The position vector (x, y) of each pit center was generated based on uniform distribution (Xia et al. 2021). In this connection, overlapping of the pits was also allowed to consider the intersection of pits and create a larger area of wall thinning. Statistical analyses on naturally and artificially corroded structures showed that the pit depth and aspect ratio follow lognormal distribution (Wang et al. 2018b; Xia et al. 2021). The average pit depth is a time-dependent parameter estimated for a specific environment and expected exposure time. As noted in Table 1, three different average pit depths were assumed ($d_{avg} =$ 1mm, 2mm, 3mm). The logarithmic standard deviation of the depth of the pits ($\sigma_{\ln(d)}$) was observed from 0.1 to 0.5 without an obvious trend of change during the time of exposure (Xia et al. 2021). Therefore, a 0.3 constant logarithmic standard deviation of pit depth was considered for all average pit depths in this study. The *AR* is also time-dependent

so that during the time of exposure, the pits change from shallow-wide pits (AR=60) into deep-narrow pits (AR=5) (Xia et al. 2021). Since well-penetrated pits are the most influential pits on ductile fracture (Wang et al. 2018a; Xu et al. 2016), a 5:1 width to depth ratio was assumed as the average aspect ratio (AR_{avg}) with a 0.6 logarithmic standard deviation ($\sigma_{\ln(AR)}$) (Xia et al. 2021). It is worth mentioning that the logarithmic standard deviation of AR was also reported unchanged during the exposure time (Xia et al. 2021). It is also important to realize that although the selected averages and standard deviations do not imply a specific real situation, they are reasonable values adopted to expand the methodology into an application. All these distributions are summarized as follows:

$$
\begin{cases}
x = Uniform\ [x_1\ \ x_2] \\
y = Uniform\ [y_1\ \ y_2] \\
d = Lognormal\ (d_{avg}, \sigma_{\ln(d)})\ \ where\ \ \ d_{avg} = 1mm, 2mm, 3mm\ ;\ \sigma_{\ln(d)} = 0.3 \\
AR = Lognormal\ (AR_{avg}, \sigma_{\ln(AR)})\ \ where\ \ \ AR_{avg} = 5:1\ ;\ \sigma_{\ln(AR)} = 0.6 \\
w = d \times AR
\end{cases}
$$
$$(4)$$

Where x_1, x_2, y_1 and y_2 specify the plate boundaries.

4. Results and discussion

For each nine intensity measures listed in Table 1, the intact mesh of the specimen was modified and analyzed for fifty randomly generated pitting morphologies. Fig 9 shows the force-elongation curves for IM[5%, 2mm], IM[10%, 2mm] and IM[30%, 2mm]. The ultimate and failure points of each curve are highlighted in this figure. In addition, the failure elongation of the intact specimen is also provided for better comparison.

The distribution of the highlighted points indicates that different random pitting morphologies with an identical intensity measure could change the capacity and deformability of the specimen. Statistical parameters for ultimate load and failure elongation are listed in Table 2.

4.1. Effect of random pitting on the ultimate load

Based on the obtained coefficients of variation, the ultimate load of the specimen experienced less than 6.5% of dispersion. Low dispersion indicates that details of pitting corrosion have a negligible effect on the ultimate load variation. As a result, a simplified method without pitting details can be employed to predict the ultimate load. The average reduction in ultimate load is 23.5% in the worst case (i.e.,

IM[30%,3mm]). Fig. 10 also indicates that the decrease in the ultimate capacity of the specimen is correlated with both d_{avg} and DOP by -0.52 and -0.72 correlation coefficients, respectively. These coefficients imply a meaningful correlation between these parameters.

4.2. Effect of random pitting on the failure elongation

According to Table 2, the failure elongation exhibited 12.6%-30.2% of dispersion due to variation of pitting pattern. This dispersion demonstrates the effect of pitting details on the ductility of the specimen by triggering the fracture initiation and propagation in different modes. Fig. 12 illustrates the most dominant modes that pitting affected fracture initiation and propagation. As shown in this figure, the fracture initiated at the centroid of the cross-section of the intact specimen and propagated towards the edges. Based on these results, the most critical section with the highest VGI demand is the center of the intact specimen. In some patterns, the fracture initiation was triggered by the occurrence of pits (not necessarily deep pits) at this critical location. In some other patterns, a deep pit was generated based on the described probability distributions for pit characteristics (refer to Eq. 4). This deep pit produced higher triaxiality and reduced the fracture strain so that an accelerated fracture initiated at the root of the pit and propagated through the plate. In addition, as Fig. 12 illustrates, the interaction between neighboring pits and interaction between pits and the edge of the plate could also expedite the fracture initiation. In some realizations, a combination of these modes was observed. These results indicate, if a simplified method rather than solid modeling is used, that method must address all these possible effects of pitting appropriately.

Fig. 11 indicates that the reduction in deformability of specimen is correlated with both d_{avg} and DOP by -0.75 and -0.33 correlation coefficients, respectively. Therefore, deeper and denser pitting patterns led to more reduction in failure elongation; however, the effect of d_{avg} was more significant. This correlation also highlights the use of the integrated IM that identifies the level of the pitting corrosion based on both degree of pitting (DOP) and pit average depth (d_{avg}). According to Table 2, for the greatest intensity measure, i.e., IM[30%,3mm], the elongation reduced by 66% on average compared to the intact specimen. This reduction rate is an extreme deterioration in terms of deformability.

Table 2. Statistical parameters of the ultimate load and failure elongation.

Pitting intensity	Ultimate load				Failure elongation			
	Average (kN)	Standard deviation (kN)	Coefficient of variation (%)	Average reduction of the ultimate load (%)	Average (mm)	Standard deviation (mm)	Coefficient of variation (%)	Average reduction of the failure elongation (%)
IM[5%,1mm]	202.5	0.76	0.37	1.4	10.7	1.52	14.2	13.6
IM[5%,2mm]	199.2	2.32	1.16	3.1	8.1	1.65	20.4	34.6
IM[5%,3mm]	194.6	4.11	2.11	5.3	6.1	1.45	23.8	50.7
IM[10%,1mm]	199.8	1.06	0.53	2.76	9.8	1.34	13.7	20.8
IM[10%,2mm]	193.5	3.18	1.64	5.85	7.1	1.5	21.1	42.6
IM[10%,3mm]	185.9	6.32	3.40	9.55	5.3	1.42	26.8	57.2
IM[30%,1mm]	190.3	2.01	1.06	7.39	8.8	1.11	12.6	28.9
IM[30%,2mm]	174.9	6.72	3.84	14.9	5.8	1.34	23.1	53.2
IM[30%,3mm]	157.1	10.06	6.41	23.5	4.2	1.27	30.2	66.1

IM[5%,2mm]

IM[10%,2mm]

IM[30%,2mm]
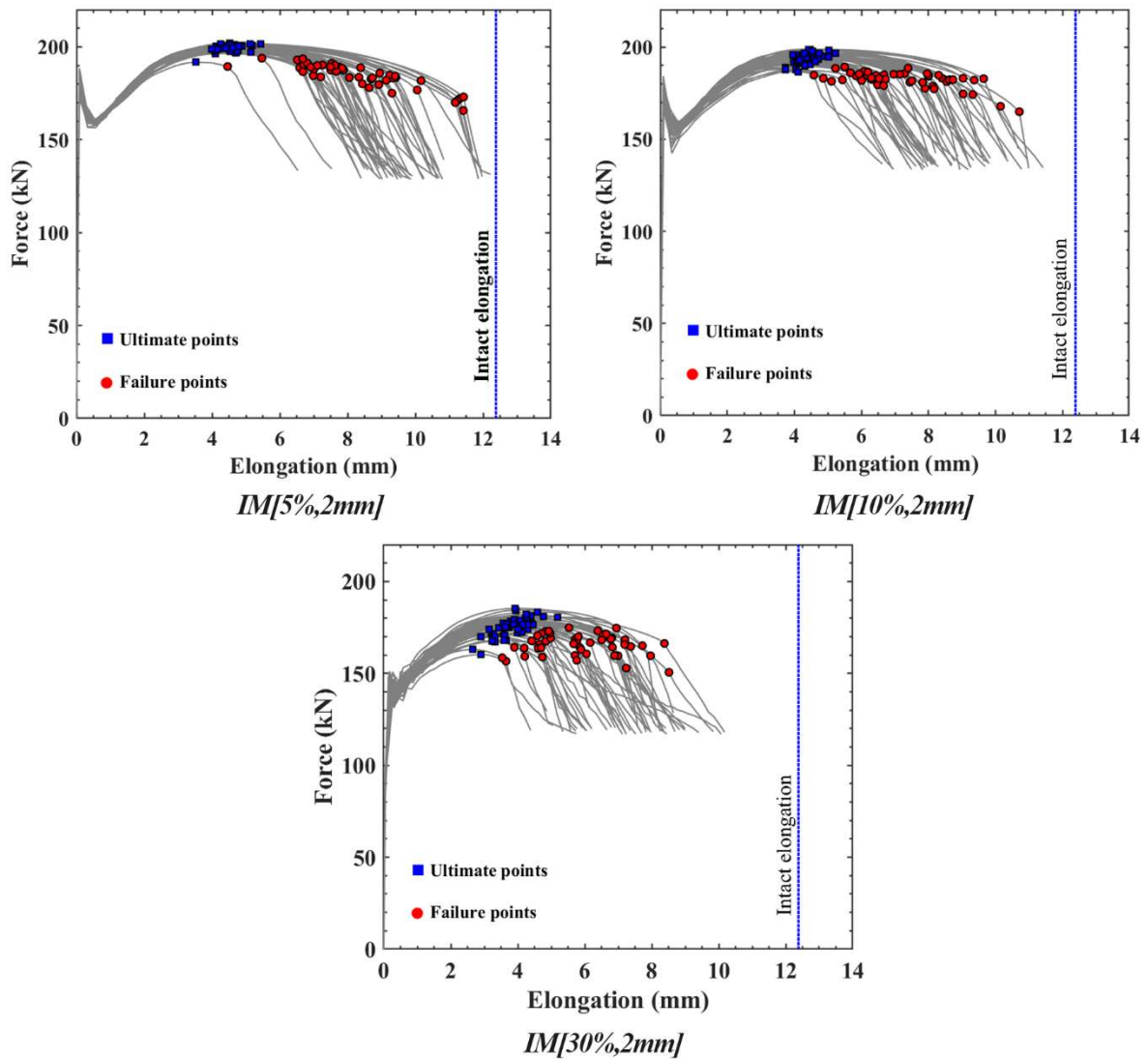
Fig. 9. Force-elongation curves for 2 mm average pit depth and different DOPs.
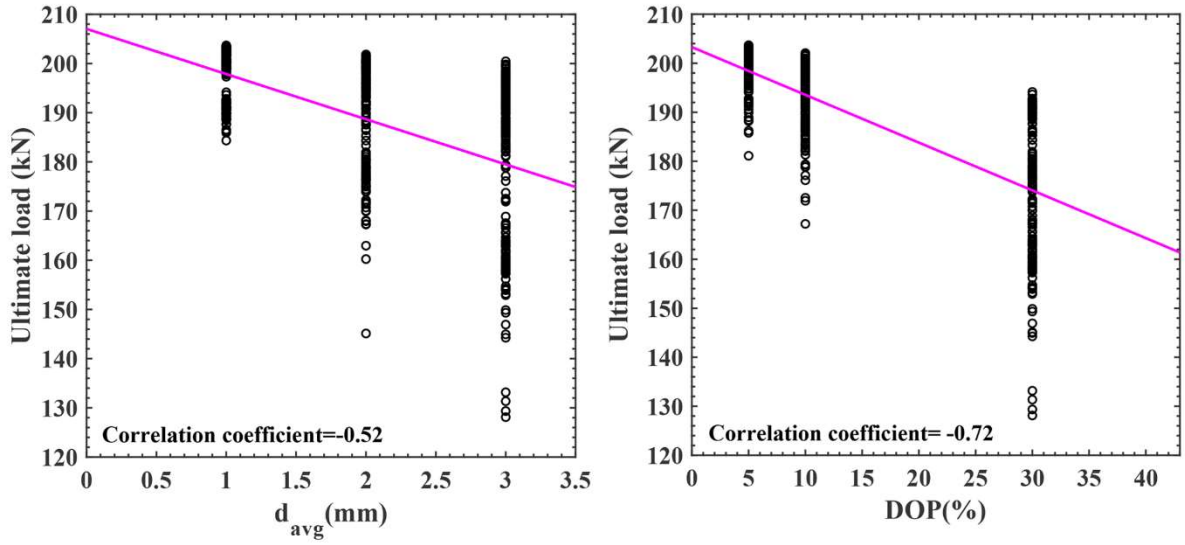
Fig. 10. The ultimate load is correlated with DOP and d_{avg}.
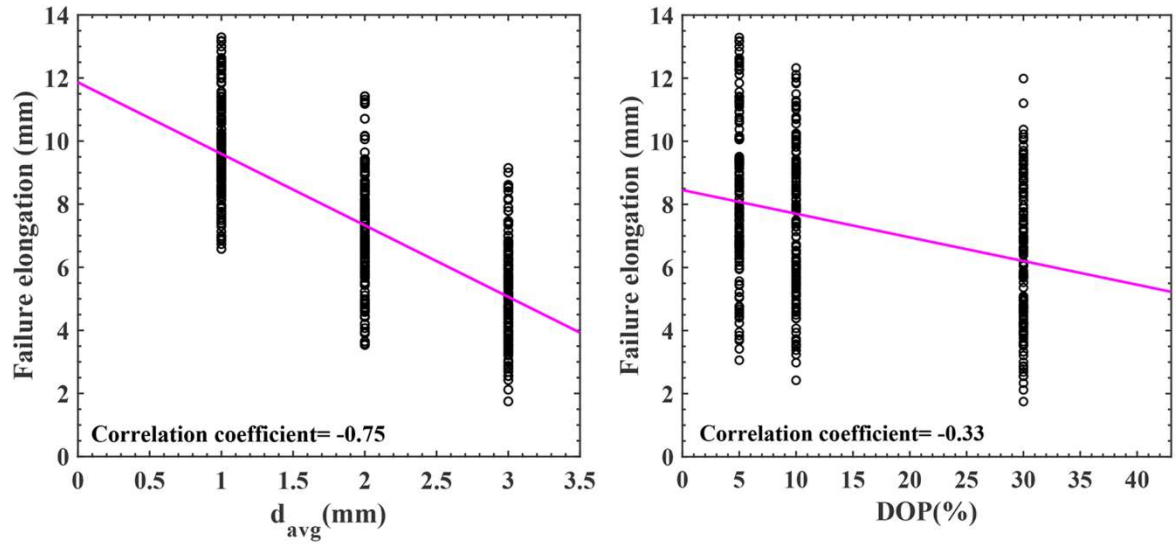
Fig. 11. The failure elongation is correlated with DOP and d_{avg}.
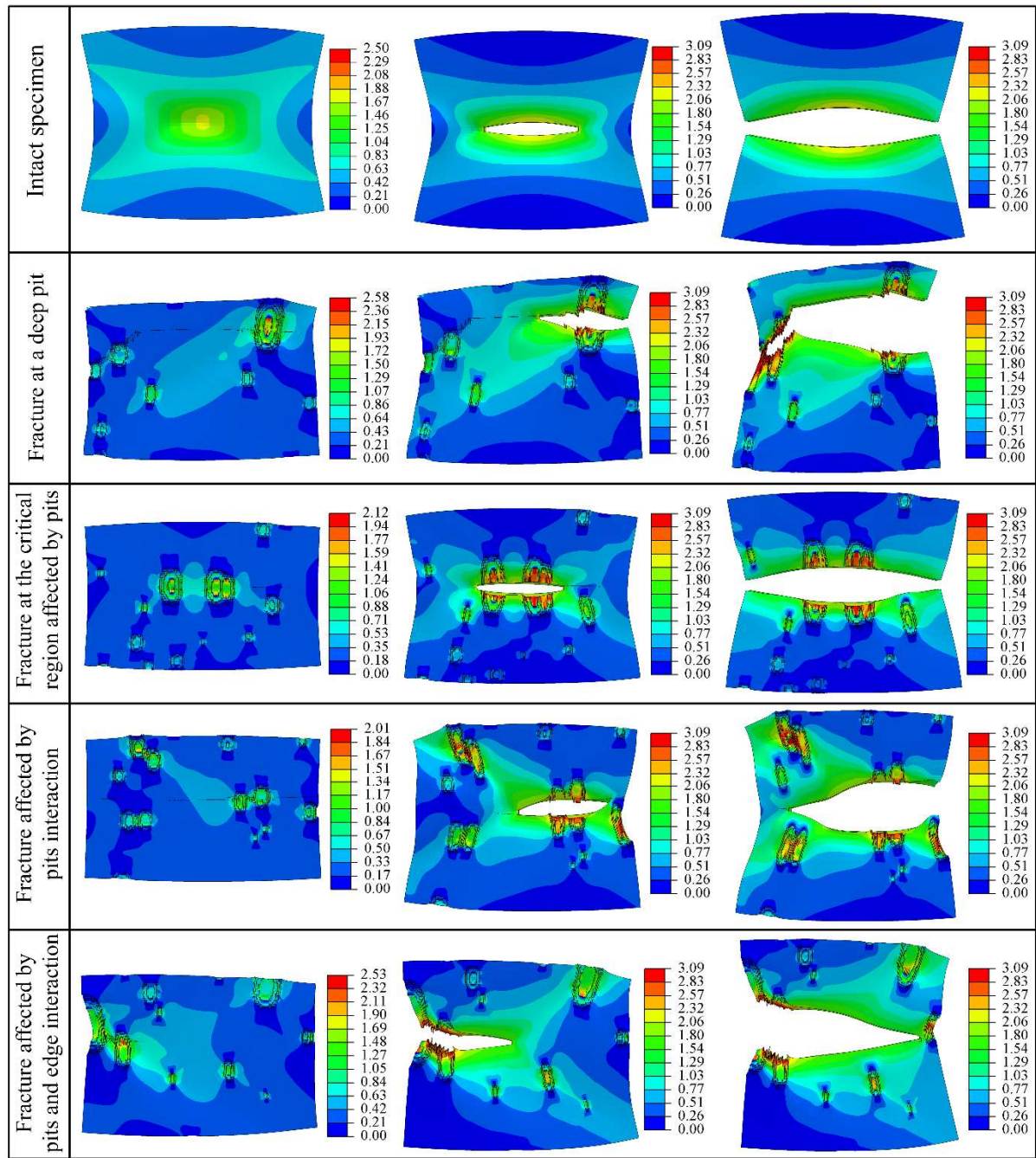
Fig. 12. Different modes of fracture initiation were observed under the effect of pitting corrosion. Contours show the VGI distribution.

4.3. Component fragility curves

Empirical Cumulative Distribution Function (ECDF) was calculated based on the fifty failure elongations for each intensity measure. These fragility curves provide the probability of failure for a given elongation as described in Eq. 1. Fig. 13 shows these fragility curves for a given *DOP* and different d_{avg} (1 mm, 2 mm, and 3 mm). Large Differences between these curves denote the significant effect of pitting characteristics on the deformability of the specimen. It is worth mentioning that

for using these curves, the demand elongation of the component must be estimated based on the analysis of the global structure. It must also be reminded that for a specific environment and exposure time, only one fragility curve is required to use in the risk-based corrosion management procedure as described in Fig. 1.

To compare these ECDFs with Lognormal, Normal, and Weibull (two-parameter) distributions, two-sample Kolmogorov–Smirnov (K-S) tests at a 5% significance level were used. K-S is a common nonparametric test method to check whether two datasets of samples are describing the same probability distribution or not (Sprent and Smeeton 2016). The goodness of fit was evaluated based on the K-S output parameters (statistic and P-value). These results indicated a better fit for all curves when a Lognormal distribution was used. The fitted Lognormal curves are also presented in Fig. 13.

(DOP=5%)

(DOP=10%)

(DOP=30%)

Fig. 13. Fragility curves obtained for various DOP and d_{avg} (dotted curves denote fitted lognormal distributions)

4.4. Number of random morphologies

Using more random morphologies can help enhance the accuracy of the ECDFs of the failure elongation; meanwhile, it can increase the computational time and cost. In this study, fifty random pitting morphologies were initially evaluated; however, the failure elongation resulted from numerical models showed that using fewer pa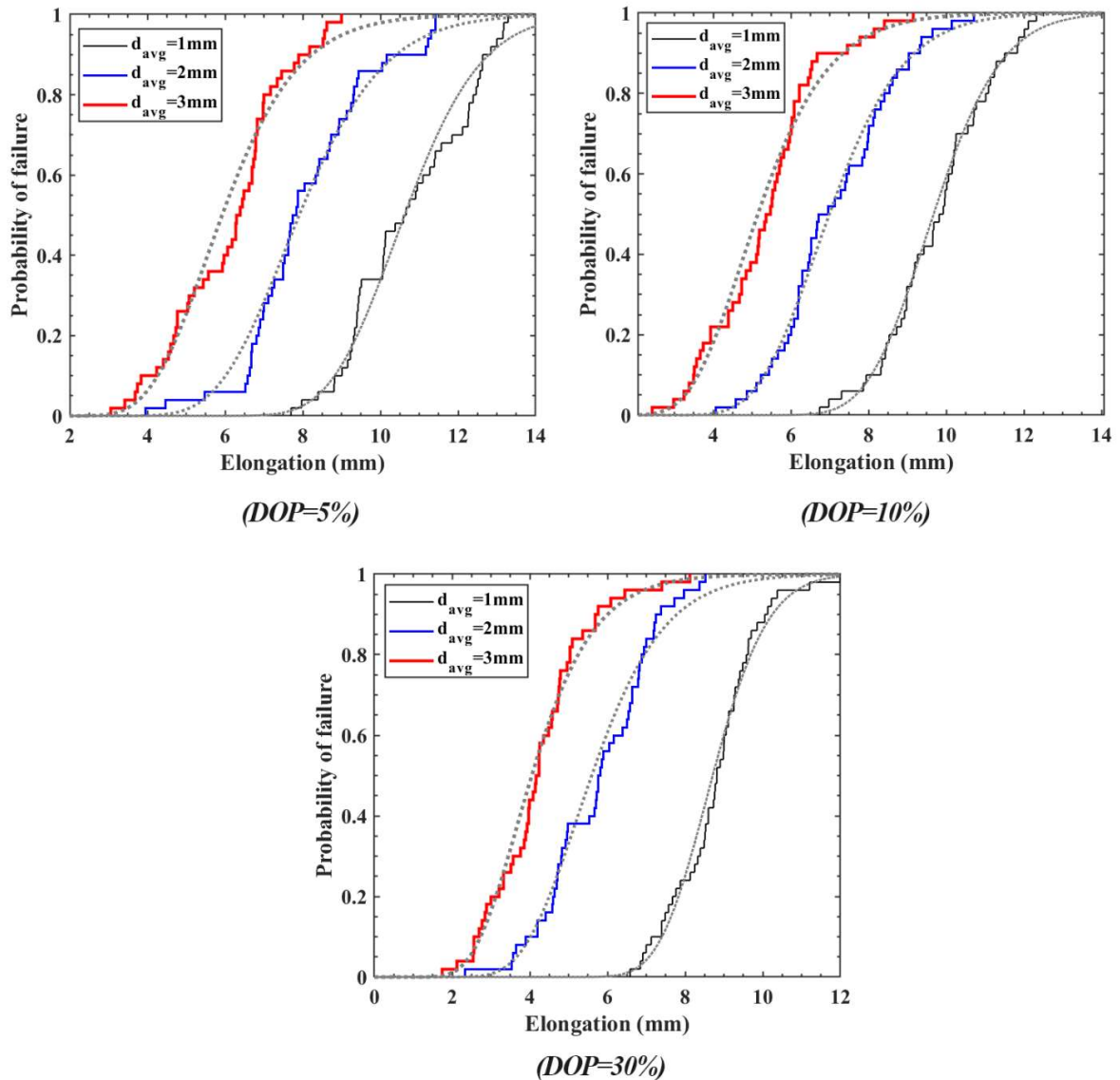tterns also can predict the results with the approximately same distribution. For this reason, the ECDFs of datasets with fewer pitting morphologies (i.e., 5, 10, 20, 30, and 40) were compared to the ECDF from fifty morphologies. The results of the two-sample K-S test at a 5% significance level for all intensity measures indicate that twenty random morphologies can describe the ECDFs as almost accurate as fifty random morphologies.

5. Conclusions

Steel structures can experience excessive plastic deformations during their lifetime due to extreme events. Under a corrosive environment, the interaction of pitting corrosion and plastic deformation can affect the integrity of the steel components because of an accelerated ductile fracture. Therefore, pitting corrosion must be addressed appropriately to evaluate structural capacity and ductility during corrosion risk management procedures.

This study proposed fracture-based fragility curves as tools that provide the probability of failure for a given intensity level of the pitting corrosion. A two-parameter intensity measure was defined to describe the severity of the pitting corrosion based on the degree of pitting and the average depth of pits. For a predefined intensity level, the fragility curves can be obtained by analyzing the failure of steel components for various random pitting patterns generated according to the probability distributions of the pit characteristics (location, depth, aspect ratio). A demonstration study on a tensile plate subjected to single-sided pitting corrosion at different levels of intensity measure showed that the developed fragility curves are powerful tools to consider the morphology-to-morphology uncertainties in structural evaluations.

According to obtained fragility curves, both degrees of pitting (DOP) and the average depth of pits are influential on the probability of failure. However, the effect of average depth was more significant. It was observed that for a given intensity level of corrosion, the variation on the failure elongation of the plate could exceed 30%. In comparison, the dispersion in ultimate load was limited to 6.4%. The significant variation of failure elongation was derived from different

modes that corrosion pits triggered fracture initiation in various random morphologies. The interaction of two pits, the interaction between pits and the edge of the plate, and the existence of a well-penetrated pit are the most dominant modes that corrosion pits accelerate the ductile fracture initiation. In contrast, the low variation in ultimate load demonstrated that pitting details is less critical in predicting the ultimate capacity of the components.

In addition, the effect of the number of random morphologies on the fragility curves was investigated by Kolmogorov–Smirnov tests. The results revealed that using twenty random morphologies is adequate to describe the fragility curves of the studied specimen; however, this number can vary by specimen configuration. Therefore, the number of random morphologies for other specimen configurations must be determined based on a similar procedure to capture all possible fracture initiation modes.

The proposed method coupled with corrosion data and risk management procedures can be used for the life cycle evaluation of new or existing steel structures under excessive plastic deformations and corrosive environments. However, the main challenge regarding the applicability of the method is the considerable required computational resources. This is mainly attributable to the fine mesh of solid elements used for ductile fracture prediction. Future studies must move towards an optimal modeling technique in which all described effects of random pits can be involved in the failure of steel components with less computational effort.

6. References

Ahmmad, M. M., and Sumi, Y. (2010). "Strength and deformability of corroded steel plates under quasi-static tensile load." *Journal of marine science and technology*, 15(1), 1-15.

ASTM (2005). "Standard guide for examination and evaluation of pitting corrosion (G46-94)." ASTM International.

Bao, Y., and Wierzbicki, T. (2004). "On fracture locus in the equivalent strain and stress triaxiality space." *International Journal of Mechanical Sciences*, 46(1), 81-98.

Cerit, M. (2013). "Numerical investigation on torsional stress concentration factor at the semi elliptical corrosion pit." *Corrosion Science*, 67, 225-232.

Cerit, M., Genel, K., and Eksi, S. (2009). "Numerical investigation on stress concentration of corrosion pit." *Engineering failure analysis*, 16(7), 2467-2472.

Dassault Systèmes (2014). *ABAQUS Analysis User's Manual (Version 6.14)*, Dassault Systèmes Simulia Corp., Providence, RI.

Deylami, A., and Mahdavipour, M. (2016). "Probabilistic seismic demand assessment of residual drift for Buckling-Restrained Braced Frames as a dual system." *Structural Safety*, 58, 31-39.

DNV GL (2015a). "Risk based corrosion management (DNVGL-RP-C302)." DNV GL AS.

DNV GL (2015b). "Thickness diminution for mobile offshore units (DNVGL-CG-0172)." DNV GL AS.

DNV GL (2016). "Allowable thickness diminution for hull structure (DNVGL-CG-0182)." DNV GL AS.

Duddu, R. (2014). "Numerical modeling of corrosion pit propagation using the combined extended finite element and level set method." *Computational Mechanics*, 54(3), 613-627.

European Committee for Standardization (2004). "Standard for hot-rolled structural steel. Part 2 - Technical delivery conditions for non-alloy structural steels (EN 10025-2:2004).", CEN, Brussels, Belgium.

Ghosh, J., and Padgett, J. E. (2010). "Aging considerations in the development of time-dependent seismic fragility curves." *Journal of Structural Engineering*, 136(12), 1497-1511.

Guo, X., and Zhang, C. (2019). "Seismic fragility analysis of corroded chimney structures." *Journal of Performance of Constructed Facilities*, 33(1), 04018087.

Hancock, J., and Mackenzie, A. (1976). "On the mechanisms of ductile failure in high-strength steels subjected to multi-axial stress-states." *Journal of the Mechanics and Physics of Solids*, 24(2-3), 147-160.

Huang, Y., Zhang, Y., Liu, G., and Zhang, Q. (2010). "Ultimate strength assessment of hull structural plate with pitting corrosion damnification under biaxial compression." *Ocean Engineering*, 37(17-18), 1503-1512.

International Organization for Standardization (2020). "ISO 11463: Corrosion of metals and alloys - Guidelines for the evaluation of pitting corrosion."

Jahanitabar, A. A., and Bargi, K. (2018). "Time-dependent seismic fragility curves for aging jacket-type offshore platforms subjected to earthquake ground motions." *Structure and Infrastructure Engineering*, 14(2), 192-202.

Ji, J., Zhang, C., Kodikara, J., and Yang, S.-Q. (2015). "Prediction of stress concentration factor of corrosion pits on buried pipes by least squares support vector machine." *Engineering Failure Analysis*, 55, 131-138.

Johnson, G. R., and Cook, W. H. (1985). "Fracture characteristics of three metals subjected to various strains, strain rates, temperatures and pressures." *Engineering fracture mechanics*, 21(1), 31-48.

Kanvinde, A. (2017). "Predicting fracture in civil engineering steel structures: State of the art." *Journal of Structural Engineering*, 143(3), 03116001.

Kanvinde, A., and Deierlein, G. (2006). "The void growth model and the stress modified critical strain model to predict ductile fracture in structural steels." *Journal of Structural Engineering*, 132(12), 1907-1918.

Kanvinde, A., and Deierlein, G. (2007). "Finite-element simulation of ductile fracture in reduced section pull-plates using micromechanics-based fracture models." *Journal of Structural Engineering*, 133(5), 656-664.

Lemaire, M. (2013). *Structural reliability*, John Wiley & Sons.

Liao, F., Wang, W., and Chen, Y. (2012). "Parameter calibrations and application of micromechanical fracture models of structural steels." *Structural engineering and mechanics*, 42(2), 153-174.

Mahdavipour, M., and Deylami, A. (2014). "Probabilistic assessment of strain hardening ratio effect on residual deformation demands of Buckling-Restrained Braced Frames." *Engineering structures*, 81, 302-308.

Mahdavipour, M. A., and Vysochinskiy, D. (2021). "Using a DIC-based approach to enhance the calibration accuracy of the void growth model ductile fracture criterion." Unpublished manuscript, University of Agder

McClintock, F. A. (1968). "A criterion for ductile fracture by the growth of holes." *Journal of applied mechanics*, 35(2), 363-371.

Melchers, R. E. (2021). "New insights from probabilistic modelling of corrosion in structural reliability analysis." *Structural Safety*, 88, 102034.

Pidaparti, R. M., and Patel, R. R. (2008). "Correlation between corrosion pits and stresses in Al alloys." *Materials Letters*, 62(30), 4497-4499.

Rice, J. R., and Tracey, D. M. (1969). "On the ductile enlargement of voids in triaxial stress fields." *Journal of the Mechanics and Physics of Solids*, 17(3), 201-217.

Saykin, V. V., Nguyen, T. H., Hajjar, J. F., Deniz, D., and Song, J. (2020). "The effect of triaxiality on finite element deletion strategies for simulating collapse of full-scale steel structures." *Engineering Structures*, 210, 110364.

Shekari, E., Khan, F., and Ahmed, S. (2017). "Probabilistic modeling of pitting corrosion in insulated components operating in offshore facilities." *ASCE-ASME J Risk and Uncert in Engrg Sys Part B Mech Engrg*, 3(1).

Sheng, J., and Xia, J. (2017). "Effect of simulated pitting corrosion on the tensile properties of steel." *Construction and Building Materials*, 131, 90-100.

Songbo, R., Ying, G., Chao, K., Song, G., Shanhua, X., and Liqiong, Y. (2021). "Effects of the corrosion pitting parameters on the mechanical properties of corroded steel." *Construction and Building Materials*, 272, 121941.

Sprent, P., and Smeeton, N. C. (2016). *Applied nonparametric statistical methods*, CRC press.

Turnbull, A., Wright, L., and Crocker, L. (2010). "New insight into the pit-to-crack transition from finite element analysis of the stress and strain distribution around a corrosion pit." *Corrosion Science*, 52(4), 1492-1498.

Wang, H., Xu, S., Wang, Y., and Li, A. (2018a). "Effect of pitting degradation on ductile fracture initiation of steel butt-welded joints." *Journal of Constructional Steel Research*, 148, 436-449.

Wang, R., Guo, H., and Shenoi, R. A. (2020). "Compressive strength of tubular members with localized pitting damage considering variation of corrosion features." *Marine Structures*, 73, 102805.

Wang, R., Shenoi, R. A., and Sobey, A. (2018b). "Ultimate strength assessment of plated steel structures with random pitting corrosion damage." *Journal of Constructional Steel Research*, 143, 331-342.

Wang, Y., Wharton, J. A., and Shenoi, R. A. (2014). "Ultimate strength analysis of aged steel-plated structures exposed to marine corrosion damage: A review." *Corrosion Science*, 86, 42-60.

Wang, Y., Xu, S., Wang, H., and Li, A. (2017). "Predicting the residual strength and deformability of corroded steel plate based on the corrosion morphology." *Construction and Building Materials*, 152, 777-793.

Whittaker, A., Deierlein, G., Hooper, J., and Merovich, A. (2004). "Engineering demand parameters for structural framing systems." *Report number: ATC-58-2*, 2.

Xia, M., Wang, Y., and Xu, S. (2021). "Study on surface characteristics and stochastic model of corroded steel in neutral salt spray environment." *Construction and Building Materials*, 272, 121915.

Xu, S., Wang, H., Li, A., Wang, Y., and Su, L. (2016). "Effects of corrosion on surface characterization and mechanical properties of butt-welded joints." *Journal of Constructional Steel Research*, 126, 50-62.

Yan, Y., Shao, B., Zhou, X., Song, S., Zhou, X., and Yan, X. (2019). "A study on the influence of double ellipsoidal pitting corrosion on the collapsing strength of the casing." *Engineering Failure Analysis*, 100, 11-24.

Yang, J., Guo, T., Luo, D., and Liu, Z. (2021). "Multiscale Modeling and Seismic Fragility Analysis of Corroded Precast Concrete Frame." *Journal of Performance of Constructed Facilities*, 35(1), 04020128.

Yang, Y., Wu, Q., He, Z., Jia, Z., and Zhang, X. (2019). "Seismic Collapse Performance of Jacket Offshore Platforms with Time-Variant Zonal Corrosion Model." *Applied Ocean Research*, 84, 268-278.

Yeter, B., Tekgoz, M., Garbatov, Y., and Soares, C. G. (2020). "Fragility analysis of an ageing monopile offshore wind turbine subjected to simultaneous wind and seismic load." *Safety in Extreme Environments*, 1-16.

Zhang, J., Liang, Z., and Han, C. (2015). "Effects of ellipsoidal corrosion defects on failure pressure of corroded pipelines based on finite element analysis." *International Journal of Electrochemical Science*, 10, 5036-5047.

Zhao, Z., Liang, B., Liu, H., and Wu, X. (2018). "Influence of pitting corrosion on the bending capacity of thin-walled circular tubes." *Journal of the Brazilian Society of Mechanical Sciences and Engineering*, 40(11), 1-12.

Zhao, Z., Zhang, H., Xian, L., and Liu, H. (2020). "Tensile strength of Q345 steel with random pitting corrosion based on numerical analysis." *Thin-Walled Structures*, 148, 106579.

Zhao, Z., Zheng, C., Zhang, J., Liang, B., and Zhang, H. (2021). "Influence of random pitting corrosion on moment capacity of thin-walled circular tubes subjected to compression force." *International Journal of Pressure Vessels and Piping*, 189, 104260.

Paper V:

Micromechanical modeling of corroded steel joints under excessive plastic deformations

Micromechanical Modeling of Corroded Steel Joints Under Excessive Plastic Deformations

Mohammad Ali Mahdavipour[1], Dmitry Vysochinskiy[2]

[1] Ph.D. Research Fellow, Department of Engineering Sciences, University of Agder, Jon Lilletuns vei 9, 4879, Grimstad, Norway, Email: ali.mahdavipour@uia.no

[2] Associate Professor, Department of Engineering Sciences, University of Agder, Jon Lilletuns vei 9, 4879, Grimstad, Norway, Email: dmitry.vysochinskiy@uia.no

Abstract

Under excessive plastic deformations, pitting corrosion can accelerate ductile fracture initiation in steel structures. For an accurate numerical prediction of ductile fracture in corrosion pits, a micromechanical fracture criterion along with a fine three-dimensional solid meshing is required. Previous studies on this topic are limited to simple plates; however, for a more detailed component, e.g., steel beam-to-column joint, implementing the pit geometry on the global model of the joint is challenging in terms of meshing and computational time. In this paper, two-level numerical modeling was employed to reduce the complexity of the problem. In this technique, submodels with refined mesh are used to perform micromechanical simulations and assess the ductility degradation of joints. For a case study joint, it was found that the pits near the edge of the web and flange plates are the most critical and can reduce the fracture initiation displacement of the joint by about 25%. On the other hand, the pits located on the edges of plates or far from the edges caused a negligible reduction in the fracture initiation displacement of the joint. These results suggest two-level numerical modeling as a viable technique to facilitate micromechanical simulation of pitting corrosion in corroded steel joints.

KEYWORDS

Ductile fracture; corrosion pit; steel joint; void growth model; plastic deformation; submodeling

1. Introduction

Progressive collapse is defined as an unpredicted extreme situation in which a local failure leads to a disproportionate global or partial collapse of a structure (Adam et al. 2018; GSA 2016; Sadek et al. 2010). In frame structures, columns carry the most gravity loads, and their removal is the most critical progressive collapse scenario (Adam et al. 2018; GSA 2016; Sadek et al. 2010). In steel structures, the unbalanced loads due to column removal are transferred by alternative paths provided by adjacent beams and joints (Sadek et al. 2010). These components are supposed to develop shear, flexural, and catenary resisting actions until the system reaches a new equilibrium (Adam et al. 2018; Sadek et al. 2010). Therefore, they are normally designed and constructed so that critical zones (i.e., plastic hinges) can sustain excessive plastic deformations before the loss of integrity. As also observed in experiments (Lew et al. 2013; Wang et al. 2021), the ductile fracture is the main failure mode of joints under this loading scenario. To ensure sufficient ductility of steel components, design codes (AISC 2016a; AISC 2016b) define protected zones and requirements to avoid pre-existing notches on them. A notch located in a protected zone can cause stress and strain concentration and accelerate fracture in a local spot. Despite codes requirements, notches can also appear due to pitting corrosion under an aggressive environment. Pitting corrosion is one of the main forms of corrosion that initiates and propagates locally in steel structures located in a corrosive environment (Bardal 2004; Pedeferri 2018). Various structures, including industrial steel structures located in coastal areas, LPG terminals located on jetties, topsides of offshore facilities, can be subjected to pitting corrosion. These corroded structures can also experience extreme events like a column removal due to a ship or vehicle collision (see Fig. 1), a localized fire, an explosion caused in industrial facilities by gas pipe fracture, or a leakage of combustible liquids (Adam et al. 2018). The collapse of these facilities must be investigated under the coupled effect of the pitting corrosion and excessive plastic deformations to avoid disasters in terms of casualties, economy, and environment (DNV GL 2015).

In general, the location of pits is extremely stochastic and difficult to predict (Bardal 2004; Pedeferri 2018). In addition, localized penetration and high cathodic to anodic area ratio increase the penetration speed so that pitting corrosion can affect a large portion of metal thickness in a short time (Pedeferri 2018). Depending on the geometry of pits, they can increase the plastic strain and stress

triaxiality (Cerit 2013; Cerit et al. 2009; Ji et al. 2015; Pidaparti and Patel 2008; Turnbull et al. 2010; Wang et al. 2018) that are known as two influential parameters for ductile fracture initiation in metals (McClintock 1968; Rice and Tracey 1969). Ductile fracture initiation at the root or wall of a corrosion pit can be followed by ductile tearing that pushes the crack front at high-stress levels and increases the chance of failure by cleavage fracture and unstable crack propagation (Petti and Dodds Jr 2005; Wang et al. 2018). In most cases, no adequate information is available on the effect of localized corrosion on overall member ductility. Therefore, finite element analysis (FEA) is usually performed (International Standards Organization 2008). Previous studies on simple tensile plates (Ahmmad and Sumi 2010; Songbo et al. 2021; Wang et al. 2018; Wang et al. 2017; Xu et al. 2016; Zhao et al. 2020) indicated that when the ductile fracture of steel components is under investigation, a three-dimensional representation of the pit geometry associated with a micromechanical fracture criterion is needed to assess the structural integrity. A fine discretization of the corrosion geometry must be utilized in such numerical models to predict the local responses on the pits properly (Ahmmad and Sumi 2010; Songbo et al. 2021; Wang et al. 2018; Wang et al. 2017). However, to the authors' knowledge, no study has quantified the effect of pitting corrosion on the ductility of steel joints under a column removal scenario. Steel joints possess more sophisticated geometries than simple plates and can produce more complicated stress and strain distributions. The solid meshing of the complex geometry of a joint and analyzing it for various pitting scenarios could be challenging, particularly when a micromechanical fracture criterion is employed. In addition, multiple zones in joints can experience excessive plastic deformations that all must be investigated for fracture.

This study aims to reduce the difficulties regarding meshing and micromechanical simulation of the corroded joints using a two-level numerical modeling technique. This technique was used through a parametric numerical study to assess the effect of an isolated corrosion pit on the ductile fracture initiation of a case study joint. Based on such analyses, one can determine which pit (with a certain geometry and location) can be considered critical and must be treated to avoid joint collapse for probable future events.
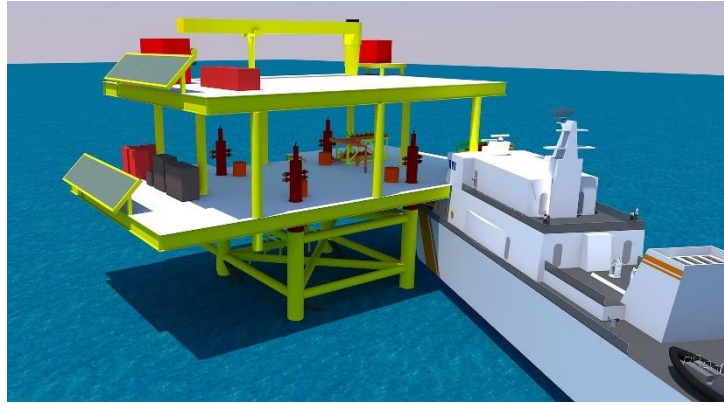
Fig. 1. A collision between a vessel and a steel production platform can lead to a progressive collapse.

2. Methodology

When the ductile fracture is the failure mode of steel components, micromechanical fracture modeling predicts fracture more accurately than traditional fracture mechanics (Wang et al. 2011). Micromechanical models are able to simulate the fundamental mechanisms of fracture by utilizing the modern computational capacity to predict localized stresses and strains (Kanvinde and Deierlein 2004). However, when a notch like a corrosion pit exists, these models require fine solid meshing around the pit domain to accurately capture localized stresses and strains (Ahmmad and Sumi 2010; Songbo et al. 2021; Wang et al. 2018; Wang et al. 2017; Xu et al. 2016; Zhao et al. 2020).

On the other hand, the meshing convergence and computational time would be challenging if the overall three-dimensional model of a steel component (e.g., a joint) is used to implement pits. One possibility to refine the mesh in the pit domain is to use tetrahedral elements that support fully automatic tetrahedral meshers (Dassault Systèmes 2014). However, for the same degree of freedom and the same amount of layers of elements through the thickness of a member, one needs significantly more tetrahedral elements compared to hexahedrons (Wang et al. 2017). Moreover, the first-order tetrahedral elements are not sufficiently accurate for structural calculations, particularly when large plastic strains are involved (Dassault Systèmes 2014). As a result, the second-order formulation must be chosen that even needs more computational resources. In contrast, developed reduced integration hexahedral elements can remarkably increase computational efficiency without significant loss of accuracy (Dassault Systèmes 2014). Finally, it is worth mentioning that before fracture initiation, modeling details of a local region around the pit has a negligible effect on the overall solution of the joint.

This study utilized two-level numerical modeling to overcome difficulties associated with modeling pits in complicated geometries. First, as described in Fig. 2, the nonlinear finite element analysis of the joint (not corroded) is carried out at the global level without pit implementation. Then based on the outcomes of this model and submodeling technique, critical regions are studied for fracture modeling and pit existence. Submodeling is a technique to investigate a local region with a more refined mesh based on the interpolation of the solution from a relatively coarse mesh in the global model (Hirai et al. 1984; Kardak 2015; Mao and Sun 1991; Marenić et al. 2010; Narvydas and Puodziuniene 2014). This technique effectively obtains the solution with a higher resolution in the local region of interest, e.g., a corrosion pit (Liu et al. 2021; Mao and Sun 1991; Verma et al. 2019).

There are two common submodeling techniques. In the displacement-based method, the boundary conditions of the submodel are nodal displacements extracted from the global model. The second method is called stress-based submodeling that stresses or tractions from the integration points are transmitted to the submodel as boundary conditions. The displacement-based submodeling method is preferred for large displacement problems because boundary conditions calculated using displacement can converge faster than the stress field (Sun and Mao 1988). In addition, Narvydas and Puodziuniene (2014) demonstrated that displacement-based submodeling is less sensitive to the mesh density of the global model and can provide higher accuracy than the stress-based method.

Like other finite element methods, this technique is also subjected to numerical errors classified into two main categories: Discretization errors and boundary condition errors. Discretization errors are inherent in the determination of responses with the finite element method (Oñate 2013). Since using a fine mesh in submodels is controlled by micromechanical modeling, the discretization errors in the submodels might be less critical. As a result, most of the discretization errors are originated from the global model and must be kept within a reasonable range to calculate boundary responses accurately for the submodels (Kardak 2015). This error can be controlled by refining the mesh until further refinement causes no significant change in the nodal displacement output of the global model (Kardak 2015; Oñate 2013).

Besides the discretization errors, the submodeling technique is also affected by boundary condition errors (Cormier et al. 1999; Kardak 2015; Mao and Sun 1992). As illustrated in Fig. 2, mesh refinement in submodels creates additional degrees

of freedom at boundaries that do not exist in the global model (Sun and Mao 1988). The global solution only provides displacements at the nodes of the original coarse mesh. Consequently, the displacement boundary conditions for new nodes in submodels must be derived based on the shape function of the original elements in the global model (Sun and Mao 1988). This interpolation can induce error in the boundary condition of the submodels. Therefore, the global mesh size adequacy must be checked for proper transmission of displacements into submodels. In order to evaluate the amount of these errors, the boundary responses of the submodels are compared to the corresponding region in the global model. In addition, to reduce the effect of the boundary condition errors on the local notch, the submodel region must be sufficiently taken away from the region of interest. Sun and Mao (1988) suggested this distance at least one coarse element in the global model.

It is worth mentioning that submodeling is a one-directional boundary condition exchanging from the global to the submodel with no feedback from the submodel to the global model (Mora et al. 2020; Narvydas and Puodziuniene 2014; Verma et al. 2019). Therefore, for the displacement-based submodeling, it is essential to ensure that the stiffness of the submodel is the same as the corresponding region in the global model (Narvydas and Puodziuniene 2014). However, the stiffness can be different due to mesh refinement if the global mesh is significantly coarser than the submodel. In addition, when the fracture is under investigation, the stiffness of the submodel changes due to fracture development and material separation. In consequence, boundary conditions provided by the global model are not realistic for the post-fracture analysis of the submodel.

Since this study is limited to fracture initiation in joints, the submodel stiffness is not affected by local fracture propagation. Therefore, displacement-based solid-to-solid submodeling was considered to transmit the nodal displacements from the global model to the submodels as boundary conditions. Based on this technique and the procedure described in Fig. 2, various pit location scenarios were analyzed for a case study joint. Then, the fracture initiation displacement of each corroded scenario was compared with the intact submodel as a benchmark to quantify the joint degradation in terms of fracture initiation.
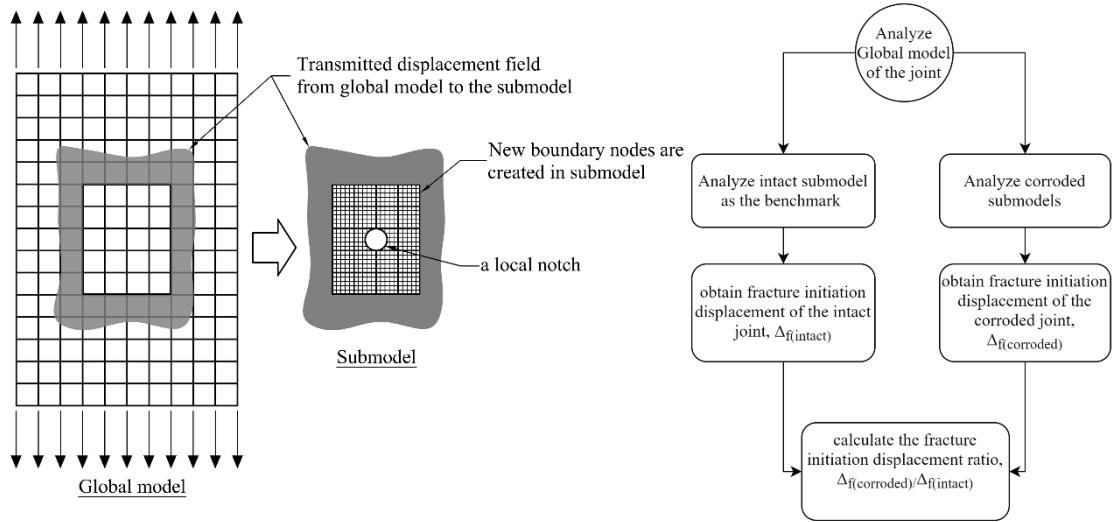
Fig. 2. An illustration of two-level finite element modeling and the procedure for micromechanical modeling of the corroded joints.

2.1. Micromechanical fracture criterion

Calibrated material constitutive model and fracture criterion are required to predict the nonlinear behavior and fracture initiation in steel material. In this study, the void growth model (VGM) was selected to characterize the ductile fracture initiation. Based on the theoretical studies done by Rice and Tracey (1969) on the processes of void growth and coalescence, Kanvinde and Deierlein (2006) used VGM as a micromechanical fracture criterion. In VGM, an explicit continuous integration of the stress triaxiality ratio (η) with respect to equivalent plastic strain ($\bar{\varepsilon}_p$) is done. These two parameters are known as the main influential parameters on the ductile fracture of metals under monotonic tensile loads (i.e., $\eta > 0.33$) (McClintock 1968; Rice and Tracey 1969). For situations with large geometry or triaxiality variation, VGM is a more appropriate criterion than instantaneous criteria in which only the current values of stress and strain are used (Kanvinde and Deierlein 2004). VGM has only one calibration parameter, i.e., the critical void growth index. Therefore, the model offers a good compromise between accuracy and complexity compared to other models like Gurson-Tvergaard-Needleman (GTN) with more parameters for a single material (Jia and Ge 2019).

Based on the VGM, the fracture initiates when the size of voids exceeds a critical value (Kanvinde and Deierlein 2006) that can mathematically be written as follows:

$$VGI = \int_0^{\bar{\varepsilon}_p} e^{1.5\eta} . d\bar{\varepsilon}_p > VGI_{critical} \qquad (1)$$

The left-hand side of this inequality is known as the Void Growth Index (VGI) that is an integration of η with respect to $\bar{\varepsilon}_p$. The critical void growth index ($VGI_{critical}$) on the right-hand side can be understood as a material property that is calibrated based on the smooth-notched tensile specimens and complementary finite element analyses (Kanvinde and Deierlein 2006). It is worth mentioning that to evaluate the fractured state based on a representative volume rather than a single point; the VGI is typically compared with $VGI_{critical}$ over a characteristic length (ℓ^*) of the mild steel that is reported 0.4-0.1 mm (Kanvinde and Deierlein 2006; Liao et al. 2012).

3. Case study

To present a demonstration of the described method, a sub-assemblage of a typical welded beam-to-column steel joint with an isolated corrosion pit was investigated under a column removal scenario. More details about this case study are presented in the following subsections.

3.1. Sub-assemblage description

As described in Fig. 3, the sub-assemblage was composed of two half-span beams and one column which moves vertically in the middle. This configuration has been widely used in different numerical and experimental studies (Adam et al. 2018) to simulate the effect of interior column removal. Based on this configuration, the inflection points are assumed at the middle of the beam span and modeled as pin supports (See Fig. 3).

A Welded Unreinforced Flange-Welded web (WUF-W) joint was selected in which rolled IPE360 steel beams were framed into a HE200M column by double-beveled tee welds and extra fillet welds as described in Fig. 4. Studies showed that adding an extra fillet weld effectively reduces fracture potential in the butt welds in moment-resisting joints (Chi et al. 2000). This weld configuration was selected to ensure that the weld is well-reinforced and does not fracture before the base metal, as the fracture of welds is outside the scope of this study. All steel members were fabricated from S355J2 steel grade that is known as a variant of S355 absorbing a minimum of 27J of energy in low temperatures (-20°C) based on the V-notch impact tests (European Committee for Standardization 2004). Weld access holes were used to perform the welds based on AWS D1.8, 2016 recommendation (American Welding Society (AWS) D1 Committee on Structural

Welding 2016). Fig. 4 illustrates the geometry of the weld access holes and continuity plates used in the studied joint.
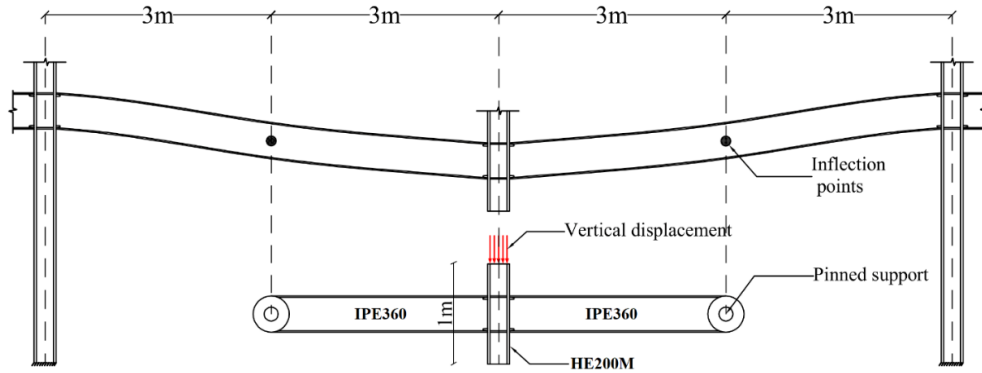

Fig. 3. The configuration of joint sub-assemblage under a column removal scenario.
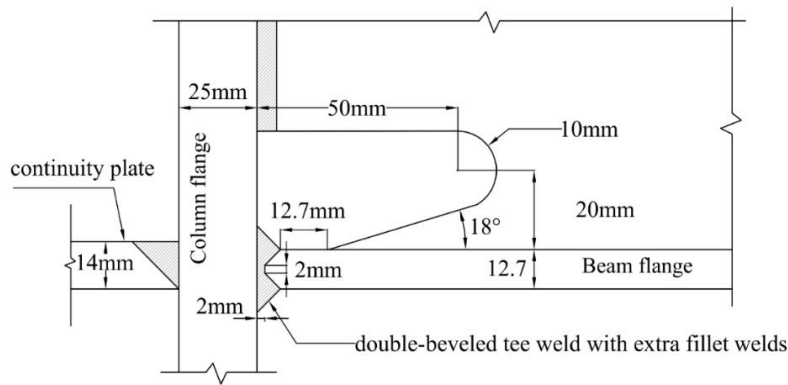

Fig. 4. Welding configuration and the weld access hole geometry of the studied joint.

3.2. Pit characteristics

Previous studies on corrosion pits (Duddu 2014; Xu et al. 2016) indicated that when they are significantly developed into the thickness of plates, the pits can be approximated by a semi-ellipsoid, as shown in Fig. 5. Many authors (Cerit 2013; Cerit et al. 2009; Huang et al. 2010; Wang et al. 2018; Yan et al. 2019; Zhang et al. 2015; Zhao et al. 2020) implemented pitting corrosion in numerical models based on this approximation. In this study, also a semi-ellipsoidal shape was assumed to be an acceptable morphology to implement pits in numerical models. Other possible pit geometries like narrow crack-shaped pits that increase the chance of brittle fracture were not considered in this research.
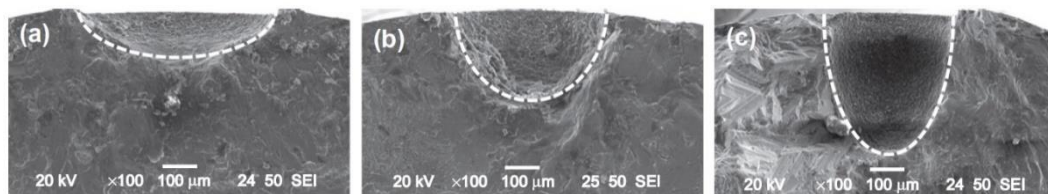

Fig. 5. Typical morphology of corrosion pits obtained by Scanning Electron Microscope (SEM) (Cerit 2013, with permission): (a) a wide semi-ellipsoidal pit, (b) a semi-spherical pit, and (c) a narrow semi-ellipsoidal pit.

The joint was studied for different scenarios of a single pit penetrated in critical regions of the described joint. According to Table 1, all pit scenarios can be classified into three categories based on the pit location relative to the free edge of the web or flange plate. In the edge pit category, the pit cut the free edge of the plates, and it was assumed that the pit center coincides with the edge line. In the near-edge category, the pit penetrates close to the free edge of the plates so that a ligament is formed between the pit and the edge. In this category, the effect of edge ligament was studied for three different ligament lengths ($l_e = t/12, t/6$, and $t/4$), where t is the plate thickness. The rest of the pit scenarios are in the far-edge category in which the pit is located far from the free edges of the plates.

All these pit categories were also investigated for different geometrical parameters. According to Table 1, two values of pit depth were studied in which the pit penetrated to 50% and 25% of plate thickness (t). The plate thickness was 12.7 mm and 8 mm for the flange and the web of the beam (IPE360), respectively. In addition, for each depth, three different pit aspect ratios ($AR = 1, 0.5, 0.25$) were studied. This geometrical parameter is defined as the ratio between the pit radius and the pit depth ($AR = r/d$) and can affect local responses in the pit, i.e., plastic strain and stress triaxiality (Cerit 2013; Cerit et al. 2009; Ji et al. 2015; Pidaparti and Patel 2008; Turnbull et al. 2010; Wang et al. 2018). According to this definition, for a given pit depth, a smaller AR denotes a narrower pit. Fig. 6 illustrates schematically all different pit characteristics investigated in this study.

Based on the FEA of the intact joint as presented later, the most critical places in the flange and the web of the beam with higher equivalent plastic strain were identified and considered as submodels. Then, the isolated pit was moved in those areas according to predefined grids. For the tensile flange, the pit was assumed to penetrate the outer fiber of the flange by various location scenarios, as described in Fig. 7. This grid was defined above the weld access hole for the web of the beam, as illustrated in Fig. 8. The above-described pitting matrix includes 582 pitting scenarios which are different in terms of location, depth, and aspect ratio.
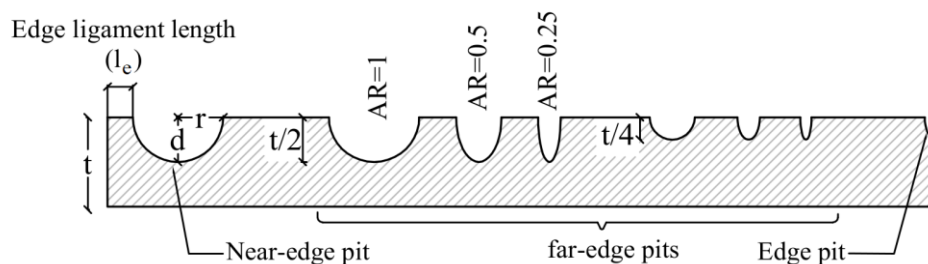

Fig. 6. An illustration of different investigated characteristics of the corrosion pit.

Table 1. Isolated pit characteristics matrix.

notation	pit depth (d)	location	pit aspect ratio (AR)	edge ligament length (l_e)
P1	$t/2$ *	far-edge	1	-
			0.5	-
			0.25	-
		near-edge	1	$t/12, t/6, t/4$
			0.5	$t/12, t/6, t/4$
			0.25	$t/12, t/6, t/4$
		edge	1	-
			0.5	-
			0.25	-
P2	$t/4$	far-edge	1	-
			0.5	-
			0.25	-
		near-edge	1	$t/12, t/6, t/4$
			0.5	$t/12, t/6, t/4$
			0.25	$t/12, t/6, t/4$
		edge	1	-
			0.5	-
			0.25	-
* t is 12.7mm for the flange plate and 8mm for the web plate.				

(a) edge and far-edge pit   (b) near-edge pit

Fig. 7. Pit location grid on the flange of the beam (all dimensions are in mm).

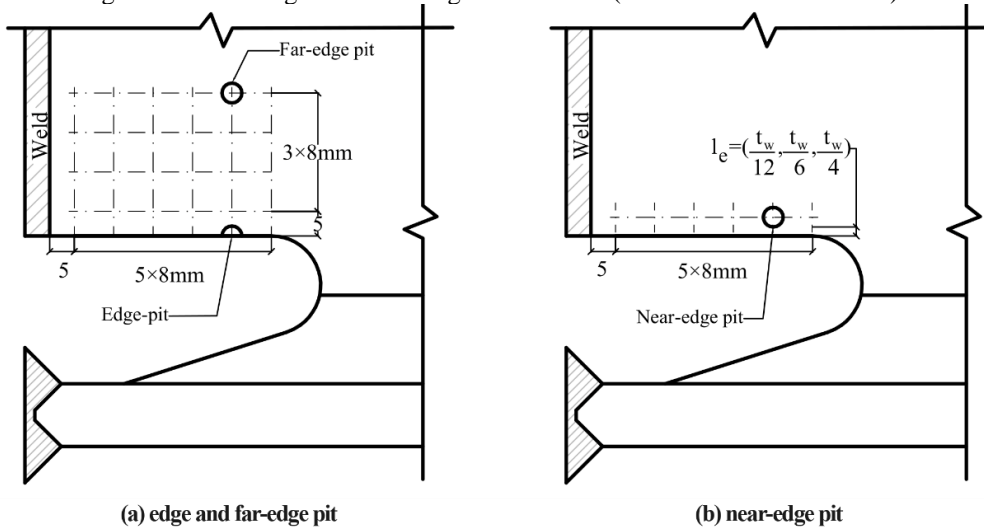
(a) edge and far-edge pit   (b) near-edge pit
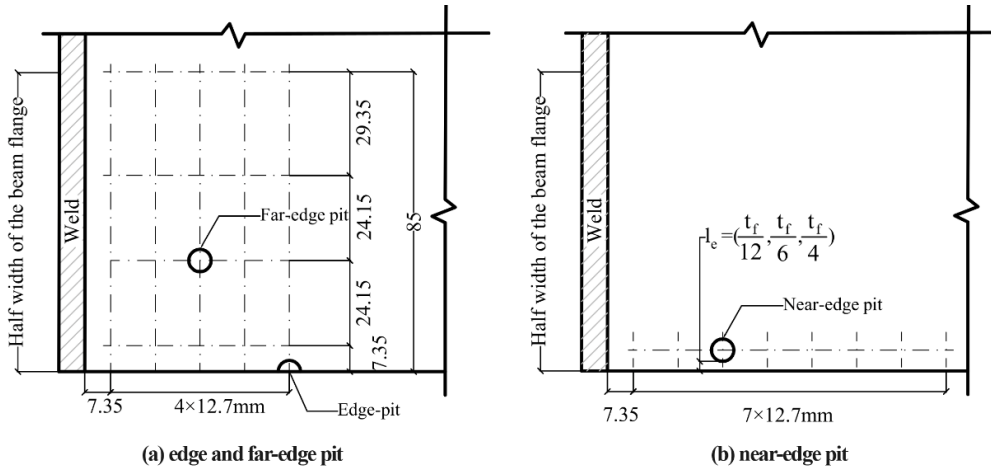
Fig. 8. Pit location grid on the web of the beam (all dimensions are in mm).

3.3. Finite element modeling

Abaqus finite element software was used based on an implicit integration scheme to simulate the global model and submodels. Eight-node brick elements with reduced integration (C3D8R) were used to discretize the geometry of models. This element is a general-purpose linear brick element with only one integration point at the center, significantly reducing computational time compared to fully integrated elements (Dassault Systèmes 2014). In addition, due to the reduced integration point, this element is not subjected to the shear locking phenomenon observed in fully integrated elements (Dassault Systèmes 2014).

Fig. 9 illustrates different mesh refinements used to discretize the geometry of the global model and submodels of the joint. To predict the fracture initiation in the intact submodel, a 1 mm mesh size was used (see Fig. 9.e). Previous studies (Kanvinde and Deierlein 2007; Mahdavipour and Vysochinskiy 2021) showed that elements larger than the material's characteristic length (ℓ^*) can predict fracture initiation accurately when there is no sharp notch. However, in submodels with corrosion pit, a very fine mesh (0.3-0.2 mm) was employed for the pits and surrounding areas, as shown in Fig. 9. This mesh size is approximately one-tenth of pit depth and is also comparable with the characteristic length of the mild steel (Kanvinde and Deierlein 2006; Liao et al. 2012). Similar mesh density was also used by (Wang et al. 2018). The other regions of the submodels were discretized by 3 mm mesh size as was used for the global model.

For the global model discretization, a 3 mm mesh density was employed at the critical region of the beam (near to the column face). The number of layers of elements through the thickness of plates in the global model was selected based on a standard mesh sensitivity analysis. For this purpose, the global model was analyzed for 3, 5, 7, and 9 layers of elements through the plates. Fig. 10.a compares the longitudinal nodal displacements across the beam flange where the boundary condition of the intact submodel was defined. These curves were obtained for 377 mm of joint vertical displacement corresponding to fracture initiation displacement of the intact submodel, as described later. According to these curves, nodal displacement in the global model changed only 0.21% in maximum when the number of layers increased from seven to nine. As a result, mesh refinement converged, and seven layers were selected to extract the submodels' boundary conditions.

To ensure that the mesh refinement in submodels did not change the stiffness significantly, the stress in the boundary of the intact submodel and global model are compared in Fig. 10.b. These curves were obtained for the same amount of joint vertical displacement (377 mm). This comparison indicated that the maximum difference between stress profiles in the submodel and global model is about 3%. This value implies that the boundary condition was transmitted from the global model to the submodel with an acceptable level of boundary condition error. Because of the symmetry of the sub-assemblage, only half geometry was modeled, and symmetric boundary condition was applied on the symmetry plane, as shown in Fig. 9. Boundary conditions were assigned to the Reference Points (RP) defined at the ends of the beam and the column. These reference points were constrained to the section nodes by kinematic coupling constraints. All these reference points were also restrained for out-of-plane movements. As shown in Fig. 9, the column removal was modeled by a static vertical displacement acting on *RP2*. It is important to realize that progressive collapse is a nonlinear dynamic phenomenon in nature. However, this study focused on capacity evaluation rather than demand assessment. Therefore, static push-down analysis was employed as a standard method recommended by reputable guidelines (GSA 2016) and (DoD 2009) that was also used in the recent open literature (Adam et al. 2018; Daneshvar and Driver 2019; Lee et al. 2021; Qian et al. 2020; Qiu et al. 2020; Wang et al. 2020).

The geometry of all welds was modeled to have realistic stress and strain distribution on the beam. All weld profiles were attached to the beam and column by tie constraints to simulate no relative motion between them (Dassault Systèmes 2014).
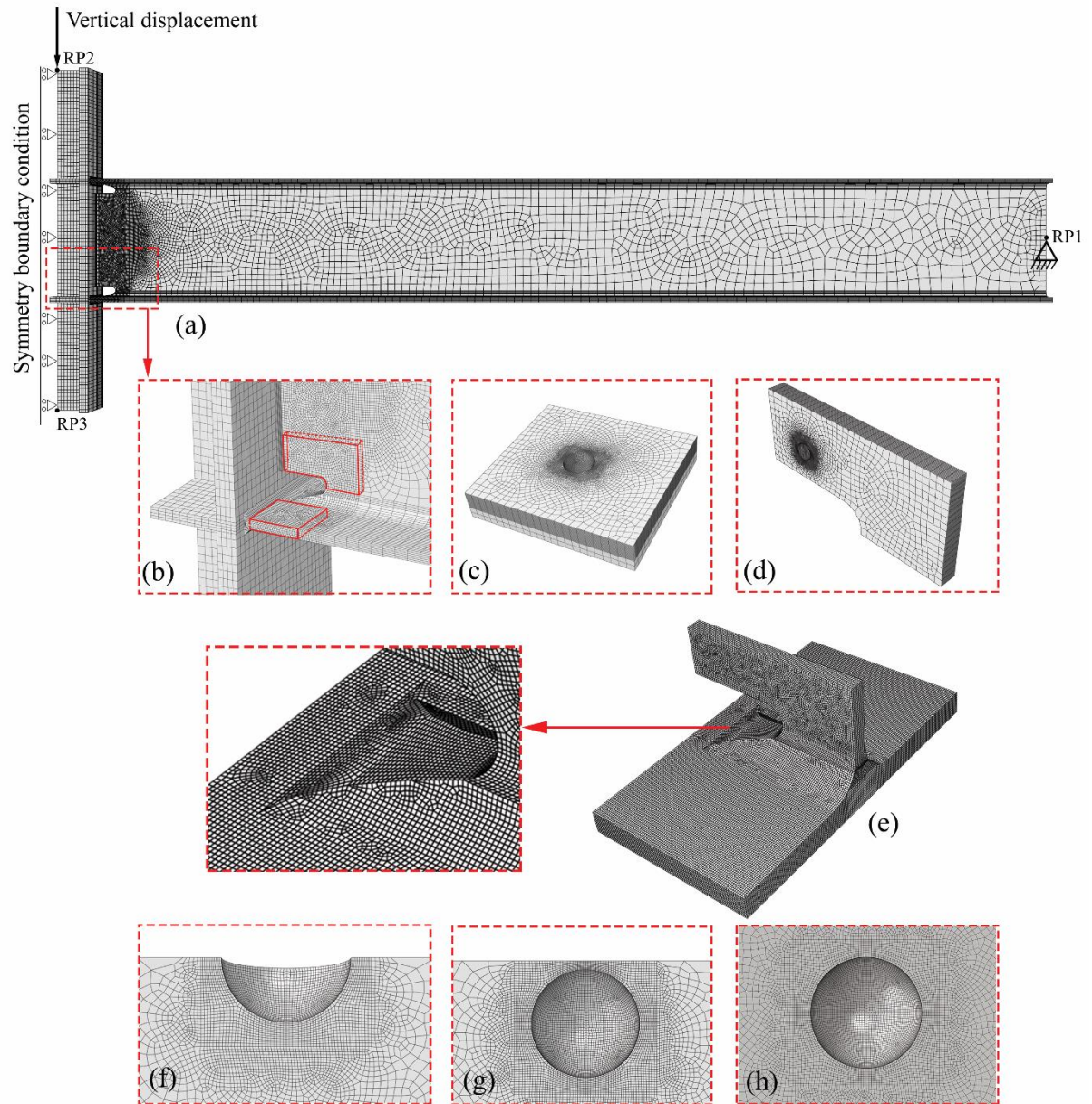
Fig. 9. Finite element modeling details: a) the global model of the joint and applied boundary conditions, b) mesh refinement in the global model, c) a submodel from the beam flange, d) a submodel from the beam web, e) Intact submodel and mesh configuration, f) mesh configuration of an edge pit, g) mesh configuration of a near-edge pit, h) mesh configuration of a far-edge pit.
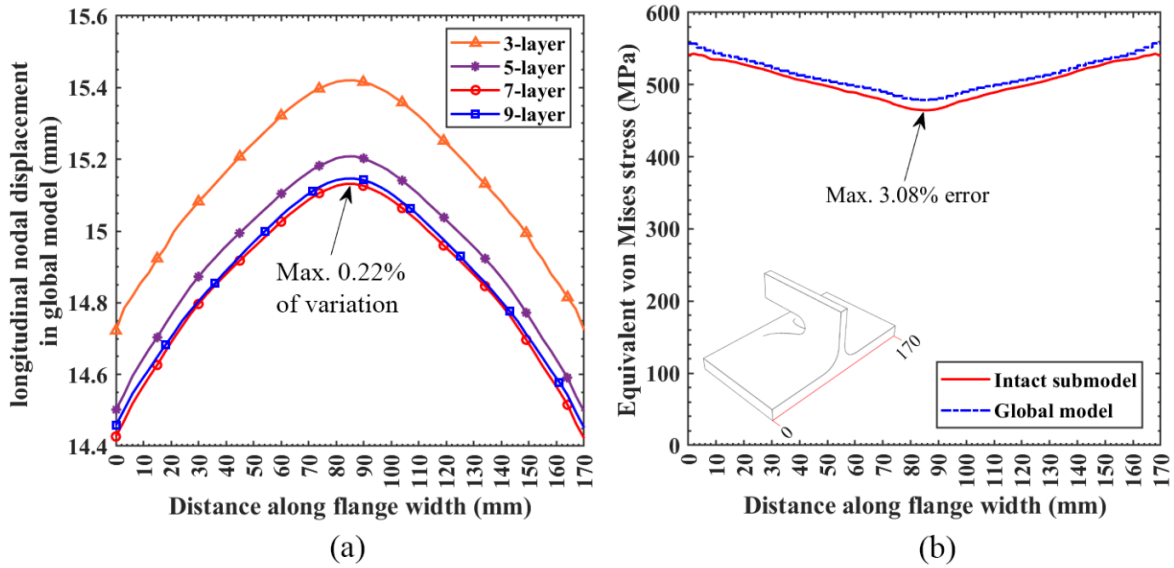
Fig. 10. Mesh sensitivity analysis result at the boundary of submodel region: a) Longitudinal nodal displacement of global model converged by using seven layers of elements through the thickness of the plates, b) Comparison between stress values obtained from the global model and submodel.

3.4. Calibrated material properties

Material nonlinear behavior of the joint was simulated by von Mises yield criterion associated with isotropic hardening. Fig. 11 illustrates the average plastic flow curves used for base metal (S355J2) calibrated by Mahdavipour and Vysochinskiy (2021). Calibrated $VGI_{critical}$ was also averaged 3.09 for this steel grade (Mahdavipour and Vysochinskiy 2021). The weld plastic flow curve adapted from (Tu 2017) is also shown in Fig. 11; however, the fracture of welds was not modeled. In addition, the average of Young's modulus (E) and Poisson's ratio (ν) was assumed to be 200 GPa and 0.3, respectively.
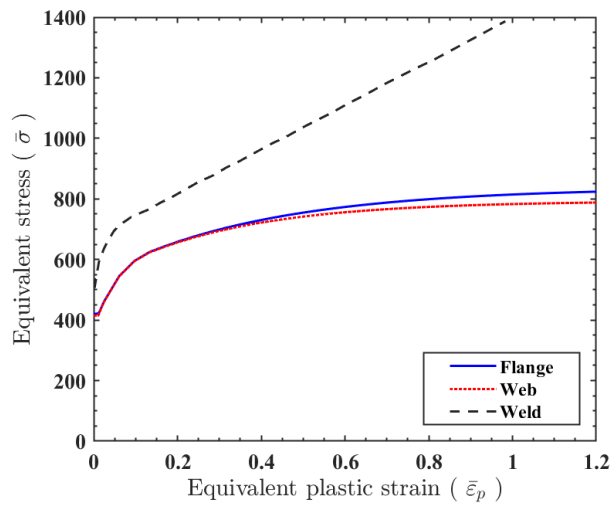

Fig. 11. Plastic flow curves used in the numerical models (Mahdavipour and Vysochinskiy 2021; Tu 2017).

Fig. 12 compares numerical and experimental force-displacement and fracture patterns of two pull-plate tests with different hole configurations (Mahdavipour and Vysochinskiy 2021). As this figure indicates, the above-described material model could predict the fracture of the tested specimens accurately. More information about these validation tests is available in (Mahdavipour and Vysochinskiy 2021).

It is worth mentioning that the VGM is not a built-in fracture criterion in Abaqus. Therefore, a USDFLD user subroutine was developed to implement the VGM in the numerical models. This subroutine was called at each time increment to calculate the VGI for all integration points.
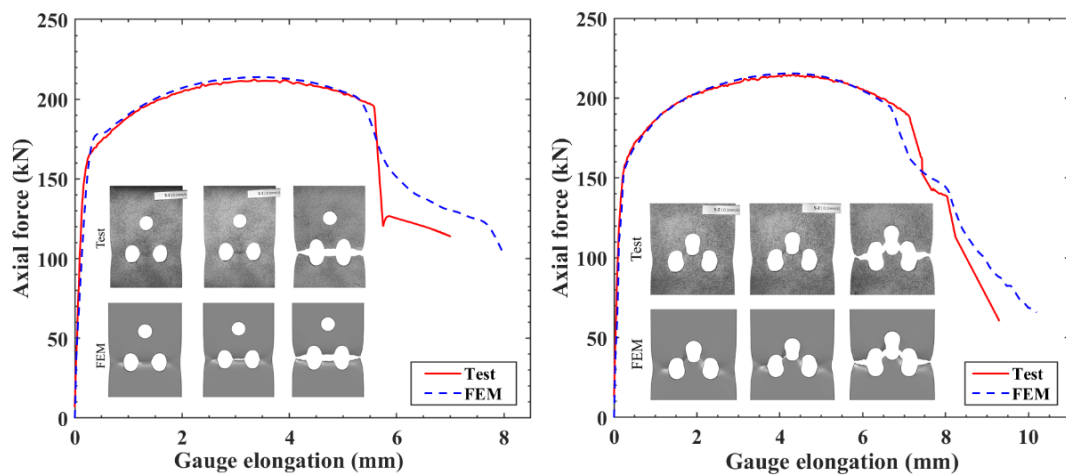

Fig. 12. Material model validation for two pull-plate specimens fabricated from S355J2 with different hole configurations (Mahdavipour and Vysochinskiy 2021).

4. Results and discussion

In this section, the joint vertical displacement corresponding to fracture initiation of the intact submodel (uncorroded) was considered as the benchmark value (hereafter is called fracture initiation displacement, $\Delta_{f(intact)}$). Then the corroded submodels with different described pit scenarios were investigated up to this displacement. Indeed, if a corrosion pit can initiate fracture by less vertical displacement of the joint, that is a deteriorating factor in terms of ductile fracture initiation.

4.1. Result of the intact joint

Fig. 13 shows the equivalent plastic strain ($\bar{\varepsilon}_p$) distribution and the fracture location predicted for the intact submodel. As indicated in this figure, the fracture occurred at the root of the weld access hole (center of the flange). The same pattern of fracture initiation was reported in similar types of joints studied by other

researchers (Sadek et al. 2010; Wang et al. 2021). Fig. 14 shows the vertical force-displacement curve of the intact joint up to the fracture initiation displacement ($\Delta_{f(intact)}$=377 mm). Beyond this displacement, the effect of the corrosion pit is less important because the intact joint is already fractured.
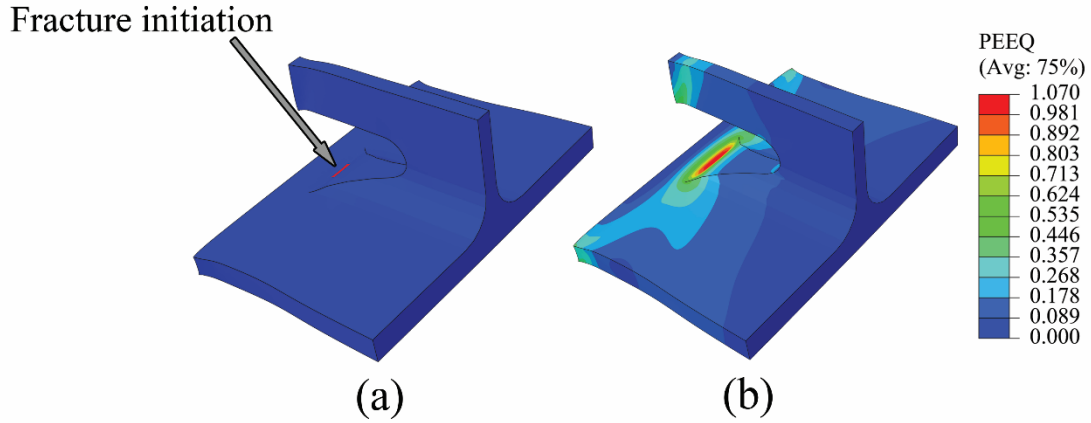

Fig. 13. Intact submodel to predict the fracture initiation of the uncorroded joint: a) mesh configuration b) location of fracture initiation, c) distribution of equivalent plastic strain ($\bar{\varepsilon}_p$).
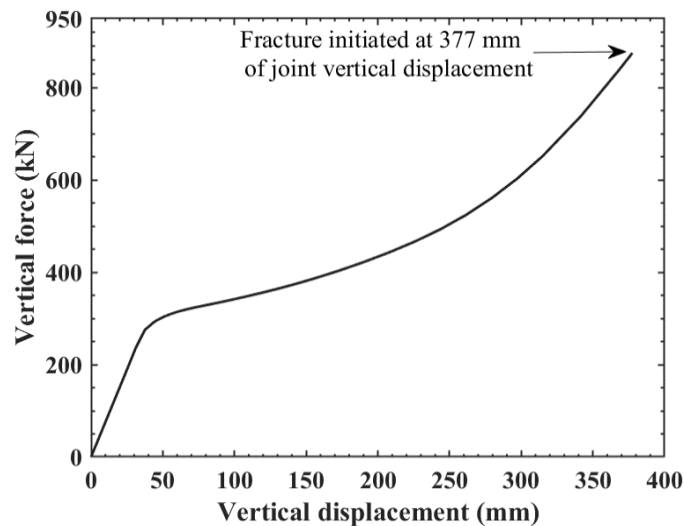

Fig. 14. The vertical force-displacement curve of the intact joint up to the fracture initiation displacement.

4.2. Result of the corroded joint

All submodels with an isolated corrosion pit were analyzed up to the fracture initiation displacement of the intact joint. Based on the results, dissimilar patterns of fracture initiation were observed in different pit categories. For the far-edge pits, the maximum VGI occurred at the root of the pits, and the ductile crack was initiated at this location. The near-edge pits fractured in the ligament between the pit and the free edge of the plates. The maximum VGI in the edge pits was observed on the wall; however, no fracture was observed for this pit category. Fig. 15 shows

examples of the VGI distribution and fracture initiation pattern of these three categories of pits.
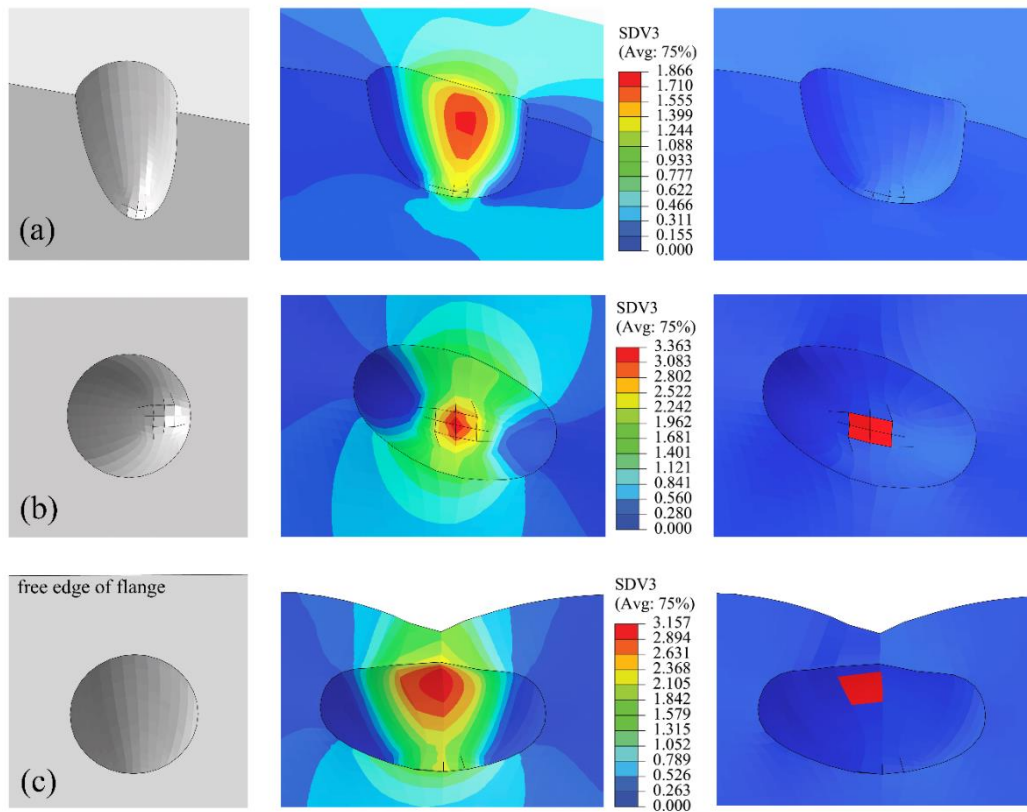

Figure 15. Examples of the VGI distribution and fracture initiation pattern: a) an edge pit without fracture initiation, b) a far-edge pit with fracture initiation at the root of the pit, c) a near-edge pit with fracture initiation at its ligament.

4.2.1. Edge and far-edge pits

Fig. 16 and 17 present the VGI ratio for the edge and far-edge pits in different locations. VGI ratio is defined as the maximum VGI normalized by $VGI_{critical}$. The VGI ratios larger than 1.0 are filled by gray color to denote locations with fracture initiation. Important to realize that ratios larger than 1.0 are physically impossible. However, in these figures, larger values were also used to make a more sensible comparison between different locations in terms of VGI demand. All these distributions of VGI ratio were obtained for a vertical displacement corresponding to the fracture initiation displacement of the intact joint ($\Delta_{f(intact)}$). According to these figures, the VGI ratio is lower than 1.0 for all free edges of the plates. It means that no edge pit was fractured before the intact joint fracture. As a result, such pits can be classified as noncritical pits for the fracture initiation of the joint. In contrast, the far-edge pits experienced VGI ratios larger the 1.0 in the region close to the butt welds and around the middle of the flange. Based on these distributions, no far-edge pit fractured in the distance larger than $2t_f$ from the

weld. For far-edge pits located on the web of the beam also a rectangular bounded by a distance less than $2t_w$ from the weld and about $3t_w$ from the weld access hole can be identified as the critical region. These values also indicate that the submodels were selected large enough to capture all critical places for fracture initiation of the pit. Fig. 16 and 17 also reveal more details about the effect of different pit geometrical characteristics (depth and aspect ratio). As a general trend, when the aspect ratio (AR) decreased, or the depth of pits (d) increased, the pits at the same location showed a higher VGI ratio. In other words, the gray areas which show the fractured state were larger for narrower and deeper pits (e.g., pits in the flange with $d = t_f/2$ and $AR =0.25$ were the most critical).

Although these figures are beneficial for identifying the critical locations with high potential of fracture initiation, they do not provide enough information about the reduction in the fracture initiation displacement of the joint. For this purpose, a scatter plot was drawn in Fig. 18 in which the ratio between fracture initiation displacement of the corroded joint and the intact joint $(\Delta_{f(corroded)}/\Delta_{f(intact)})$ is shown for all fractured far-edge pits. The points shown in this figure are classified based on the pit aspect ratio and location. Obviously, the pit fracture can reduce the fracture displacement of the joint by 11% in maximum; however, the average value for all fractured pits denotes less than 5% reduction that is negligible. Based on these ratios, one might conclude that edge and far-edge pits by the described characteristics would not affect the joint integrity significantly.

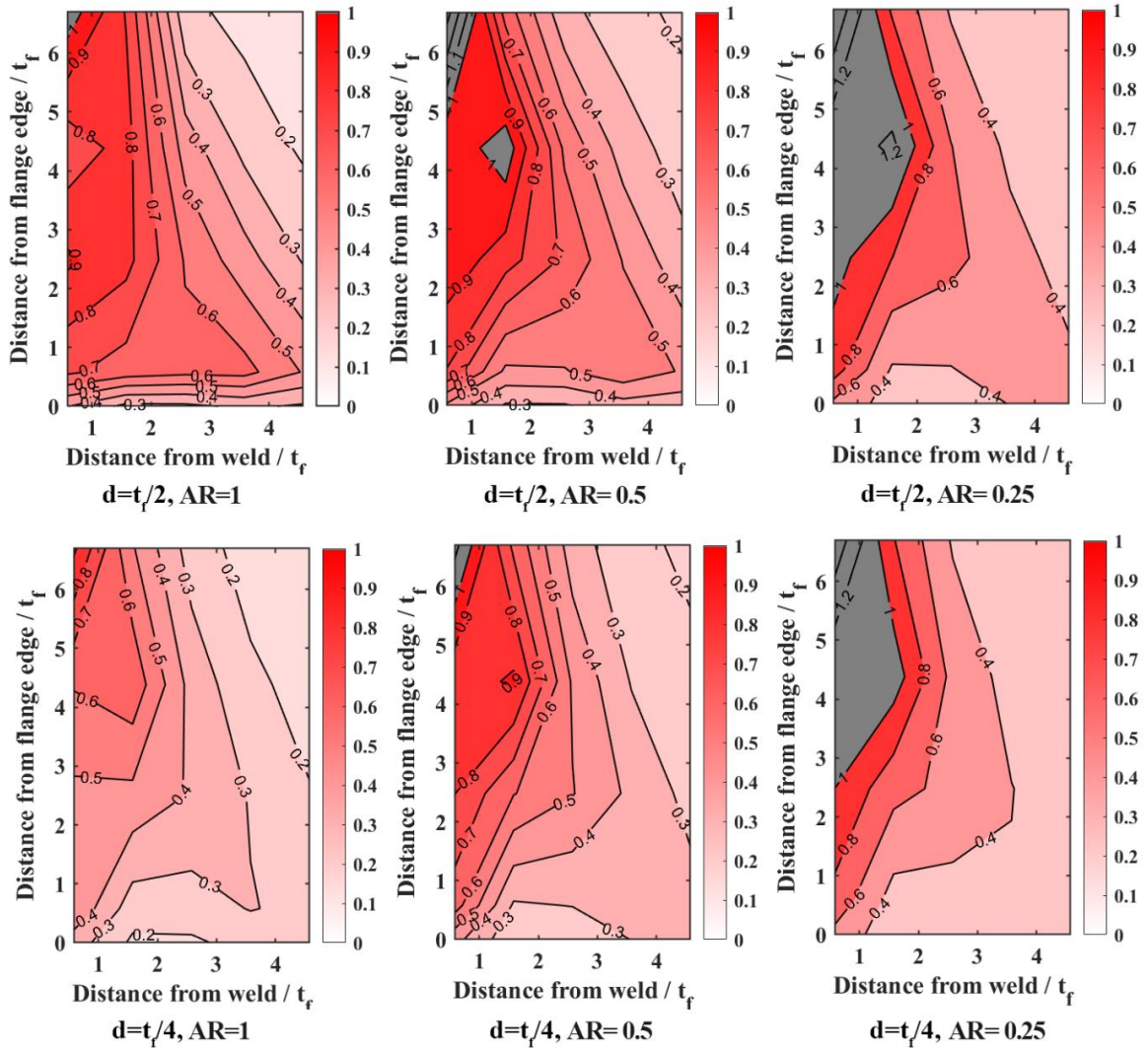Figure 16. Distribution of the VGI ratio on the half flange of the beam for different depths and aspect ratios of the pit.

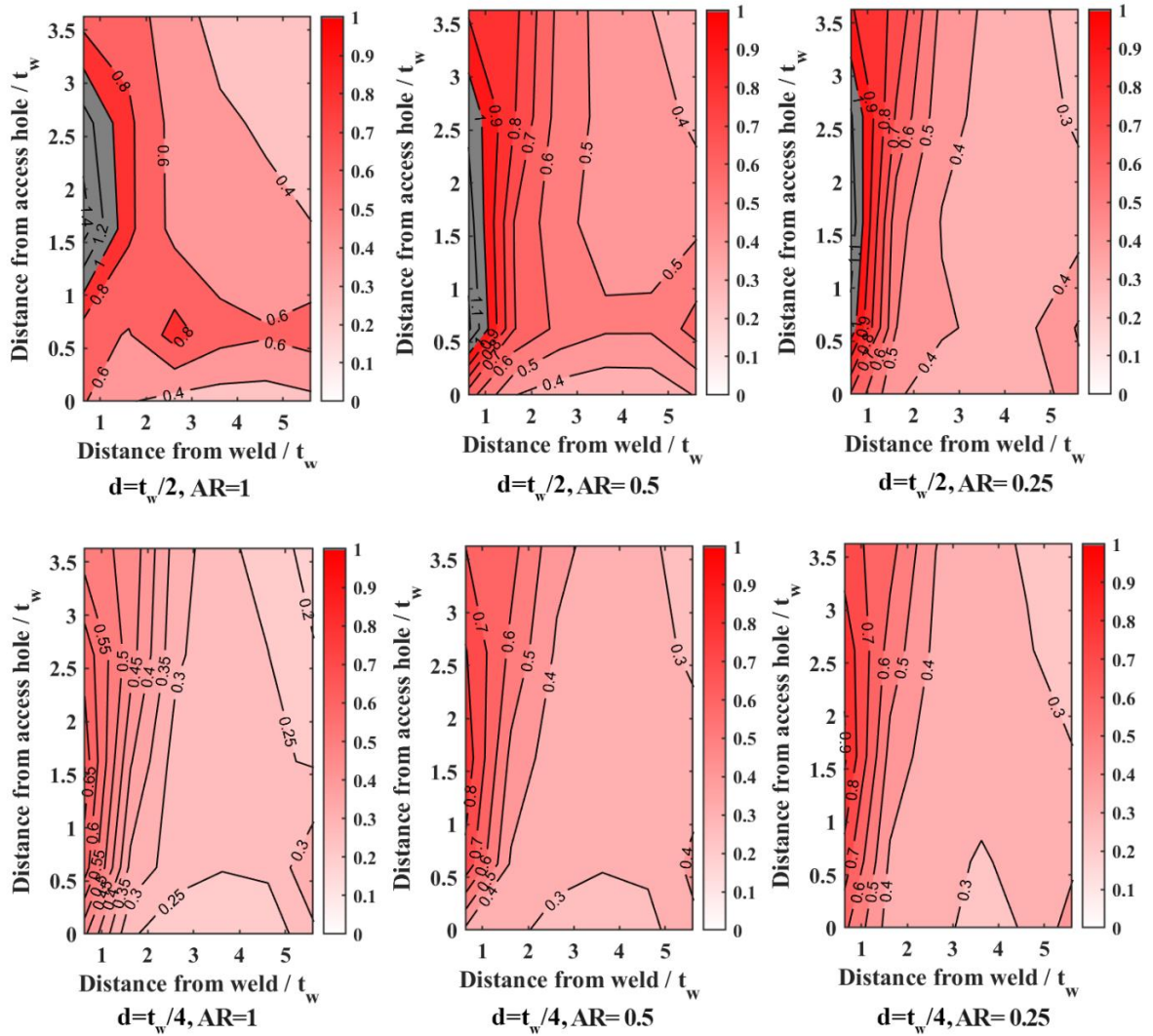Figure 17. Distribution of the VGI ratio on the web of the beam for different depths and aspect ratios of the pit.

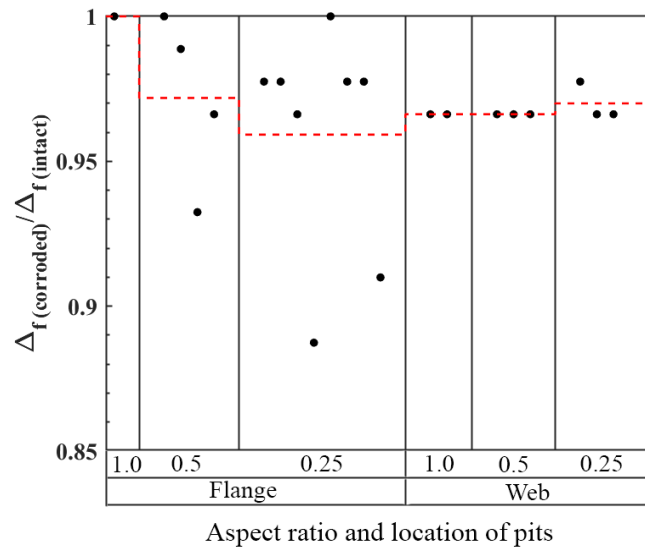Aspect ratio and location of pits

Figure 18. The ratio of fracture initiation displacement of the joint subjected to an isolated far-edge pit (the dashed line denotes the average ratio).

4.2.2. Near-edge pits

As described, the near-edge pits penetrate close to the free edge of the flange or weld access hole, and a ligament is formed between the pit and the edge of the plates (see Fig. 6). This ligament can act as a notch concentrating local stress and strain and starts ductile fracture when the joint sustains excessive plastic deformations. Fig. 19 shows the VGI ratio for the near-edge pits with $d = t_f/2$ and different aspect ratios (AR) and ligament lengths (l_e) as a portion of the flange thickness (t_f). The pits arrangement is shown in Fig. 7.b. The dashed lines in Fig. 19 indicate the fracture initiation threshold (VGI ratio=1). Based on this figure, one can determine a $7t_f$ (or equally about 0.25 of the beam depth) distance from the butt weld as a critical zone for the fracture initiation of the near-edge pits in the flange. In this zone, the fracture initiation in the ligaments could occur earlier than the fracture of the intact joint. However, it also depended on the ligament length (l_e). For example, almost all pits within this zone that also possessed a narrow ligament ($l_e = t_f/12$) experienced fracture before the intact joint while none of the pits with $l_e = t_f/4$ exceeded the fracture threshold. As this figure indicates, in general, a smaller AR increased the VGI ratio in the ligament but for some pits (e.g., pits with $l_e = t_f/12$) this rule is not the case. Indeed, the AR changes both the elevation and plan geometry of ligaments vice versa. Smaller AR (narrower pit) provides less metal between the pit wall and the flange edge while at the same time it increases the surrounding metal due to a smaller radius. The same results were obtained for the near-edge pits on the web of the beam as described in Fig. 8.b. Based on the results, the whole straight edge of the weld access hole was critical, and fracture initiated in most of the pits located in this region with a displacement smaller than the intact joint. To quantify the reduction in the fracture initiation displacement of the joint, a scatter plot of the ratio of fracture initiation displacement of the corroded joint and the intact joint ($\Delta_{f(corroded)}/\Delta_{f(intact)}$) is shown in Fig. 20 for all fractured near-edge pits. As this figure shows, the fracture was initiated with less than 75% of the joint vertical displacement for some near-edge pit scenarios. One may conclude if the initiated crack propagates as a ductile tearing and in the form of an unstable crack propagating could make a significant reduction (more than 25%) in the joint ductility. These results highlight the importance of inspection, monitoring, and treatment of such pits. It should be noted that increasing the pit size during the time of exposure can change a far-edge pit into a near-edge pit. More exposure time also can reduce the ligament of an

existing near-edge pit. Such a pit development near the edge of the plates would play a key role in the final ductility of the joint.
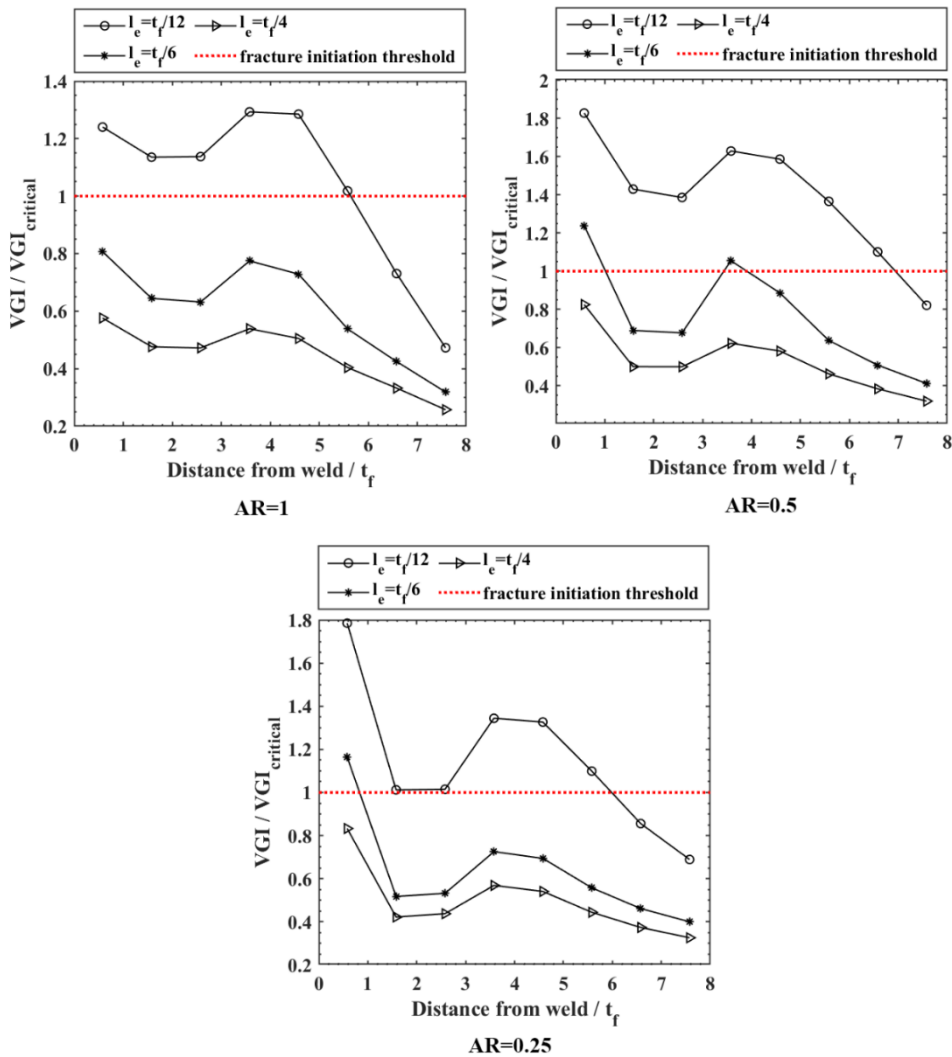

AR=1

AR=0.5

AR=0.25

Figure 19. VGI ratio of the flange near-edge pits with $d = t_f/2$ (at the fracture initiation displacement of the intact joint).

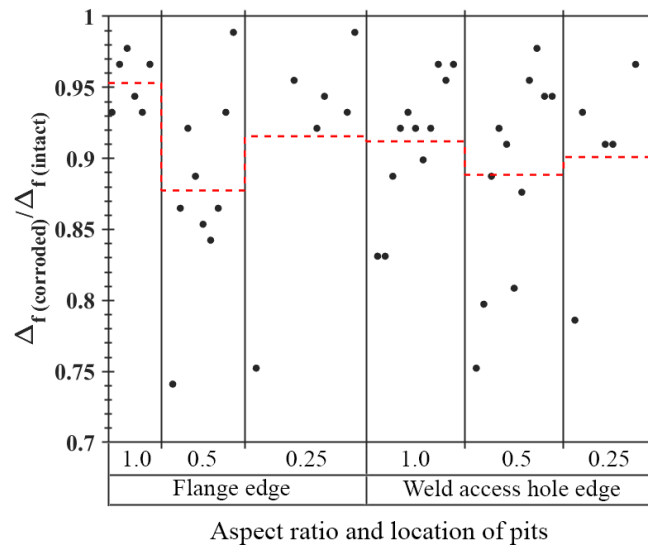

Aspect ratio and location of pits

Figure 20. The fracture initiation displacement ratio of the joint subjected to an isolated near-edge pit (the dashed line denotes the average ratio).

5. Conclusions

Despite code requirements regarding protection methods to avoid pitting corrosion, it is still happening in steel structures located in aggressive environments. Furthermore, many aged facilities that are kept in operation beyond their design life can also be subjected to extreme events like a column removal scenario. In such a situation, the interaction between excessive plastic deformations and pitting localization can lead to ductility degradation by an accelerated fracture initiation. Therefore, evaluation of the pitting effect on the structural integrity of steel joints could be vital for the performance of the global structure under future events.

On the other hand, accurate numerical prediction of ductile fracture in corrosion pits requires a micromechanical fracture criterion and a fine three-dimensional solid mesh in the pit domain. However, for complicated geometry of beam-to-column joints implementing the pit geometry on the overall model of the joint and achieving proper mesh configuration is challenging and time-consuming.

In this study, two-level numerical modeling was employed to overcome these challenges. In this technique, a global model was used to carry out the nonlinear finite element analysis of the overall joint. Then various pit scenarios were investigated by micromechanical simulations on submodels taken from the critical regions of the joint.

This approach was examined through a parametric numerical study performed on a typical welded steel beam-to-column joint with an isolated corrosion pit and under a column removal scenario. The critical pitting scenarios were identified by comparing the fracture initiation of the corroded joint with the intact joint (uncorroded). Fracture initiation in the joint was studied for three categories of pits specified based on their location relative to the free edge of plates (edge, near-edge, and far-edge pits). Besides the location of the pit, the geometrical properties of the pit (depth and aspect ratio) were also investigated. For this purpose, two depths of pit penetration ($t/2$ and $t/4$) and three values of pit aspect ratio (1, 0.5, and 0.25), and also three values of edge ligament length ($t/12, t/6,$ and $t/4$) were considered. In total, 582 submodels subjected to an isolated pit were analyzed. Based on the numerical outcomes of the case study joint, the main conclusions that can be drawn are:

- No edge pit was fractured before the intact joint fracture. As a result, such pits can be considered noncritical for the ductility of the joint.

- Far-edge pits close to the butt welds in both flange and web exhibited the fracture initiation earlier than the intact joint. However, the reduction in fracture displacement was minor (11% in maximum). As a result, such isolated pits also can be skipped due to their insignificant effect.
- Near-edge pits were identified as the most critical pits that can accelerate the fracture initiation of the joint compared to two other categories, particularly when they form a narrow ligament between the pit and the free edge of plates. The result showed that the fracture initiation displacement of the intact joint was reduced by about 25% when near-edge pits existed. If the initiated ductile crack propagates in the form of ductile tearing and unstable crack propagation, it can significantly reduce the joint ductility. These results highlight the importance of inspection, monitoring, and treatment of near-edge pits or far-edge pits that can change into a near-edge pit during the exposure time.
- Regarding geometrical parameters, the results showed that when the aspect ratio decreased (narrower pit) or the pit's depth increased, there was an increased tendency to fracture.

These results suggest the two-level numerical modeling as a capable technique to facilitate micromechanical simulation of pitting corrosion in complicated components under excessive plastic deformations. Based on this technique, engineers can scrutinize the behavior of corroded joints to find a proper treatment strategy.

6. Limitation and future work

This study is limited to an isolated pit. In a real situation, distribution of pits along with uniform corrosion can occur. As a result, the joint fracture behavior must also be investigated for a reduction of the cross-section area and interaction between pits. Future studies should consider a more realistic distribution of pits and involve more aspects of the problem, such as the joint size effect, structural details, and pitting corrosion of the welds. A procedure can be made to consider all these factors efficiently in the inspection, monitoring, and treatment of such joints to avoid their collapse for a prolonged lifetime.

7. References

Adam, J. M., Parisi, F., Sagaseta, J., and Lu, X. (2018). "Research and practice on progressive collapse and robustness of building structures in the 21st century." *Engineering Structures*, 173, 122-149.

Ahmmad, M. M., and Sumi, Y. (2010). "Strength and deformability of corroded steel plates under quasi-static tensile load." *Journal of marine science and technology*, 15(1), 1-15.

AISC (2016). "Prequalified connections for special and intermediate steel moment frames for seismic applications (AISC 358-16)." American Institute of Steel Construction, Chicago.

AISC (2016). "Seismic provisions for structural steel buildings (AISC 341-16)." American Institute of Steel Construction, Chicago.

American Welding Society (AWS) D1 Committee on Structural Welding (2016). "Structural welding code-seismic supplement (AWS D1.8/D1.8M:2016)." American Welding Society, MA.

Bardal, E. (2004). *Corrosion and protection*, Springer, London.

Cerit, M. (2013). "Numerical investigation on torsional stress concentration factor at the semi elliptical corrosion pit." *Corrosion Science*, 67, 225-232.

Cerit, M., Genel, K., and Eksi, S. (2009). "Numerical investigation on stress concentration of corrosion pit." *Engineering failure analysis*, 16(7), 2467-2472.

Chi, W.-M., Deierlein, G. G., and Ingraffea, A. (2000). "Fracture toughness demands in welded beam-column moment connections." *Journal of structural engineering*, 126(1), 88-97.

Cormier, N., Smallwood, B., Sinclair, G., and Meda, G. (1999). "Aggressive submodelling of stress concentrations." *International Journal for Numerical Methods in Engineering*, 46(6), 889-909.

Daneshvar, H., and Driver, R. G. (2019). "One-sided steel shear connections in progressive collapse scenario." *Journal of Architectural Engineering*, 25(2), 04019009.

Dassault Systèmes (2014). *ABAQUS Analysis User's Manual (Version 6.14)*, Dassault Systèmes Simulia Corp., Providence, RI.

DNV GL (2015). "Risk based corrosion management (DNVGL-RP-C302)." DNV GL AS.

DoD (2009). "Design of buildings to resist progressive collapse (UFC 4-023-03)." Department of Defence,, Washington, DC.

Duddu, R. (2014). "Numerical modeling of corrosion pit propagation using the combined extended finite element and level set method." *Computational Mechanics*, 54(3), 613-627.

European Committee for Standardization (2004). "Standard for hot-rolled structural steel. Part 2 - Technical delivery conditions for non-alloy structural steels (EN 10025-2:2004).", CEN, Brussels, Belgium.

GSA (2016). "Alternate path analysis & design guidelines for progressive collapse resistance." General Services Administration.

Hirai, I., Wang, B. P., and Pilkey, W. D. (1984). "An efficient zooming method for finite element analysis." *International Journal for Numerical Methods in Engineering*, 20(9), 1671-1683.

Huang, Y., Zhang, Y., Liu, G., and Zhang, Q. (2010). "Ultimate strength assessment of hull structural plate with pitting corrosion damnification under biaxial compression." *Ocean Engineering*, 37(17-18), 1503-1512.

International Standards Organization (2008). "Petroleum and natural gas industries-fixed steel offshore structures, ISO 19902." *International Organization for Standardization.*

Ji, J., Zhang, C., Kodikara, J., and Yang, S.-Q. (2015). "Prediction of stress concentration factor of corrosion pits on buried pipes by least squares support vector machine." *Engineering Failure Analysis*, 55, 131-138.

Jia, L.-J., and Ge, H. (2019). *Ultra-low-Cycle Fatigue Failure of Metal Structures Under Strong Earthquakes*, Springer.

Kanvinde, A., and Deierlein, G. (2004). "Micromechanical simulation of earthquake-induced fracture in structural steel." *Rep. No.145*, The John A. Blume Earthquake Engineering Center, Stanford.

Kanvinde, A., and Deierlein, G. (2006). "The void growth model and the stress modified critical strain model to predict ductile fracture in structural steels." *Journal of Structural Engineering*, 132(12), 1907-1918.

Kanvinde, A., and Deierlein, G. (2007). "Finite-element simulation of ductile fracture in reduced section pull-plates using micromechanics-based fracture models." *Journal of Structural Engineering*, 133(5), 656-664.

Kardak, A. A. (2015). "On an effective submodeling procedure for stresses determined with finite element analysis." Doctorate of Philosophy, Louisiana State University.

Lee, S.-Y., Noh, S.-Y., and Lee, D. (2021). "Comparison of progressive collapse resistance capacities of steel ordinary and intermediate moment frames considering different connection details." *Engineering Structures*, 231, 111753.

Lew, H. S., Main, J. A., Robert, S. D., Sadek, F., and Chiarito, V. P. (2013). "Performance of steel moment connections under a column removal scenario. I: Experiments." *Journal of Structural Engineering*, 139(1), 98-107.

Liao, F., Wang, W., and Chen, Y. (2012). "Parameter calibrations and application of micromechanical fracture models of structural steels." *Structural engineering and mechanics*, 42(2), 153-174.

Liu, J., Liu, Y., Liu, L., Yu, Y., and He, X. (2021). "Submodeling method to study the residual stress of TBCs near the interfacial asperity on a vane." *Engineering Failure Analysis*, 122, 105220.

Mahdavipour, M. A., and Vysochinskiy, D. (2021). "Using a DIC-based approach to enhance the calibration accuracy of the void growth model ductile fracture criterion." Unpublished manuscript,University of Agder

Mao, K., and Sun, C. (1991). "A refined global-local finite element analysis method." *International journal for numerical methods in engineering*, 32(1), 29-43.

Mao, K., and Sun, C. (1992). "Error estimators using global–local methods." *International Journal for numerical methods in Engineering*, 35(3), 589-599.

Marenić, E., Skozrit, I., and Tonković, Z. (2010). "On the calculation of stress intensity factors and J-integrals using the submodeling technique." *Journal of pressure vessel technology*, 132(4).

McClintock, F. A. (1968). "A criterion for ductile fracture by the growth of holes." *Journal of applied mechanics*, 35(2), 363-371.

Mora, D., Garrido, O. C., Mukin, R., and Niffenegger, M. (2020). "Fracture mechanics analyses of a reactor pressure vessel under non-uniform cooling with a combined TRACE-XFEM approach." *Engineering Fracture Mechanics*, 238, 107258.

Narvydas, E., and Puodziuniene, N. "Applications of sub-modeling in structural mechanics." *Proc., Proceedings of 19th International Conference. Mechanika, Kaunas, Lithuania*, 172-176.

Oñate, E. (2013). *Structural analysis with the finite element method. Linear statics: volume 2: beams, plates and shells*, Springer Science & Business Media.

Pedeferri, P. (2018). *Corrosion Science and Engineering*, Springer, Switzerland.

Petti, J. P., and Dodds Jr, R. H. (2005). "Ductile tearing and discrete void effects on cleavage fracture under small-scale yielding conditions." *International Journal of Solids and Structures*, 42(13), 3655-3676.

Pidaparti, R. M., and Patel, R. R. (2008). "Correlation between corrosion pits and stresses in Al alloys." *Materials Letters*, 62(30), 4497-4499.

Qian, K., Lan, X., Li, Z., Li, Y., and Fu, F. (2020). "Progressive collapse resistance of two-storey seismic configured steel sub-frames using welded connections." *Journal of Constructional Steel Research*, 170, 106117.

Qiu, L., Lin, F., and Wu, K. (2020). "Improving progressive collapse resistance of RC beam–column subassemblages using external steel cables." *Journal of Performance of Constructed Facilities*, 34(1), 04019079.

Rice, J. R., and Tracey, D. M. (1969). "On the ductile enlargement of voids in triaxial stress fields." *Journal of the Mechanics and Physics of Solids*, 17(3), 201-217.

Sadek, F., Main, J. A., Lew, H. S., Robert, S. D., Chiarito, V. P., and El-Tawil, S. (2010). "An experimental and computational study of steel moment connections under a column removal scenario." *NIST Technical Note*, 1669.

Songbo, R., Ying, G., Chao, K., Song, G., Shanhua, X., and Liqiong, Y. (2021). "Effects of the corrosion pitting parameters on the mechanical properties of corroded steel." *Construction and Building Materials*, 272, 121941.

Sun, C., and Mao, K. (1988). "A global-local finite element method suitable for parallel computations." *Computers & structures*, 29(2), 309-315.

Tu, H. (2017). *Numerical simulation and experimental investigation of the fracture behaviour of an electron beam welded steel joint*, Springer.

Turnbull, A., Wright, L., and Crocker, L. (2010). "New insight into the pit-to-crack transition from finite element analysis of the stress and strain distribution around a corrosion pit." *Corrosion Science*, 52(4), 1492-1498.

Verma, A. S., Vedvik, N. P., Haselbach, P. U., Gao, Z., and Jiang, Z. (2019). "Comparison of numerical modelling techniques for impact investigation on a wind turbine blade." *Composite Structures*, 209, 856-878.

Wang, F., Yang, J., and Pan, Z. (2020). "Progressive collapse behaviour of steel framed substructures with various beam-column connections." *Engineering Failure Analysis*, 109, 104399.

Wang, H., Huo, J., Liu, Y., Wang, N., and Elchalakani, M. "Experimental and numerical study on impact behavior of beam-column substructures of steel frame." *Proc., Structures*, Elsevier, 14-29.

Wang, H., Xu, S., Wang, Y., and Li, A. (2018). "Effect of pitting degradation on ductile fracture initiation of steel butt-welded joints." *Journal of Constructional Steel Research*, 148, 436-449.

Wang, Y., Xu, S., Wang, H., and Li, A. (2017). "Predicting the residual strength and deformability of corroded steel plate based on the corrosion morphology." *Construction and Building Materials*, 152, 777-793.

Wang, Y., Zhou, H., Shi, Y., and Xiong, J. (2011). "Fracture prediction of welded steel connections using traditional fracture mechanics and calibrated micromechanics based models." *International Journal of Steel Structures*, 11(3), 351.

Xu, S., Wang, H., Li, A., Wang, Y., and Su, L. (2016). "Effects of corrosion on surface characterization and mechanical properties of butt-welded joints." *Journal of Constructional Steel Research*, 126, 50-62.

Yan, Y., Shao, B., Zhou, X., Song, S., Zhou, X., and Yan, X. (2019). "A study on the influence of double ellipsoidal pitting corrosion on the collapsing strength of the casing." *Engineering Failure Analysis*, 100, 11-24.

Zhang, J., Liang, Z., and Han, C. (2015). "Effects of ellipsoidal corrosion defects on failure pressure of corroded pipelines based on finite element analysis." *International Journal of Electrochemical Science*, 10, 5036-5047.

Zhao, Z., Zhang, H., Xian, L., and Liu, H. (2020). "Tensile strength of Q345 steel with random pitting corrosion based on numerical analysis." *Thin-Walled Structures*, 148, 106579.